Dissertation

submitted to the
Combined Faculties of the Natural Sciences and Mathematics
of the Ruperto-Carola-University of Heidelberg, Germany
for the degree of
Doctor of Natural Sciences

Put forward by
Thomas Ding, M.Sc.
born in Heidelberg

Oral examination: January 24th, 2018

Quantum dynamics in weak and strong fields measured by XUV nonlinear spectroscopy

Referees: **Prof. Dr. Thomas Pfeifer**
Prof. Dr. Andreas Wolf

Quantendynamik in schwachen und starken Feldern gemessen mit nichtlinearer XUV Spektroskopie—Im Rahmen dieser Arbeit wurde die Dynamik von fundamentalen nichtlinearen Prozessen im Neonatom in zweierlei Hinsicht untersucht. Zum einen wurden Korrelationen zwischen elektronischen Anregungen im extrem-ultravioletten (XUV) Spektralbereich auf ihren natürlichen Zeitskalen vermessen. Dafür wurde das Konzept der transienten Absorptionsspektroskopie, das auf der Verwendung von höherer harmonischen (HHG) Strahlung mit Attosekundenpulsdauern und einem einzigen zeitverzögerten, moderat-intensiven nahinfraroten Puls beruht, um einen perturbativen nahinfraroten Puls erweitert, mit dem Ziel, zeitaufgelöste Spektroskopie nach der Vierwellenmisch-Technik durchzuführen. Dadurch konnten die Kopplungsdynamiken zwischen Zuständen mit unterschiedlichen Paritäten aufgespürt werden. Während der erste Teil dieser Arbeit sequentielle Prozesse mit mehreren schwachen und moderat-intensiven kohärenten Feldern untersucht, wird im zweiten Teil die Auswirkung intensiver, partiell-kohärenter Strahlung betrachtet. Für diesen Zweck wurde eine neuartige Beamline entwickelt und am Freieelektronenlaser in Hamburg (FLASH) aufgebaut, um erste Pump-Probe Experimente mit XUV-Pulsen nach der transienten Absorptionsmethode durchzuführen. Die Messungen zeigten zum einen die pulsversatz- und intensitätsabhängige Kontrolle von sequentiellen Ionisationsprozessen, aber auch spektrale Verstärkungseffekte durch Kohärenz und Signaturen, die auf starke Kopplung zwischen gebundenen Zuständen im doppeltionisierten Neonatom hindeuten. Für die Interpretation der Daten wurden numerische quantenmechanische Modellrechnungen durchgeführt. Zukünftige Anwendungen beinhalten die zweidimensionale Spektroskopie mit HHG und FLASH Pulsen mit dem Ziel, elektronische Prozesse in Molekülen elementspezifisch zu untersuchen.

Quantum dynamics in weak and strong fields measured by XUV nonlinear spectroscopy—In this work fundamental nonlinear dynamics inside the neon atom are studied in two respects: At first, correlations between electronic inner-shell excitations in the extreme-ultraviolet (XUV) spectral range are probed on their natural sub-femtosecond time scale. To this end, the concept of attosecond transient absorption with a high-harmonic generated (HHG) attosecond and a single time-delayed moderately strong near-infrared (NIR) pulse was extended by a third, perturbative NIR pulse to perform time-resolved four-wave-mixing spectroscopy. This allowed to retrieve coupling dynamics between states of odd and even parity in a two-dimensional spectral representation. While the first part of this work explores the sequential interaction of several weak and moderately strong, fully coherent laser pulses with the target neon, the second part addresses the impact of strong, partially-coherent fields delivered by the XUV free-electron laser in Hamburg (FLASH). For this purpose, a novel beamline setup was developed and assembled at FLASH which allowed to perform first XUV-pump—XUV-probe transient absorption measurements. The measurements revealed the time-delay and intensity-dependent control of sequential ionization processes, coherence-enhancement effects, and strong-coupling signatures of bound—bound transitions in doubly-ionized neon. For the interpretation of the experimental results numerical simulations based on quantum mechanical few-level models were employed. Future applications of this method involve the two-dimensional spectroscopy both with HHG and FLASH pulses to probe site-specific information of electronic processes in molecules.

List of Publications

Parts of this work have been published or prepared in the following references:

T. Ding, C. Ott, A. Kaldun, A. Blättermann, K. Meyer, V. Stooß, M. Rebholz, P. Birk, M. Hartmann, A. Brown, H. Van Der Hart, and T. Pfeifer.
Time-resolved four-wave-mixing spectroscopy for inner-valence transitions.
Opt. Lett. **41** 709–712 (2016).

T. Ding, A. Blättermann, V. Stooß, C. Ott, K. Meyer, A. Kaldun, M. Rebholz, P. Birk, M. Hartmann, L. Aufleger, A. Brown, H. Van Der Hart, and T. Pfeifer.
Towards two-dimensional spectroscopy on inner-shell transitions with XUV and soft-X-ray pulses.
International Conference on Ultrafast Phenomena, OSA Technical Digest (online) (Optical Society of America, 2016), paper UF1A.2.

Further publications with own contributions:

A. Kaldun, C. Ott, A. Blättermann, M. Laux, K. Meyer, T. Ding, A. Fischer, and T. Pfeifer
Extracting Phase and Amplitude Modifications of Laser-Coupled Fano Resonances.
Phys. Rev. Lett. **112**, 103001 (2014).

A. Blättermann, C. Ott, A. Kaldun, T. Ding, and T. Pfeifer.
Two-dimensional spectral interpretation of time-dependent absorption near laser-coupled resonances.
J. Phys. B: At. Mol. Opt. Phys. **47** 124008 (2014).

C. Ott, A. Kaldun, L. Argenti, P. Raith, K. Meyer, M. Laux, Y. Zhang, A. Blättermann, S. Hagstotz, T. Ding, R. Heck, J. Madroñero, F. Martín, and T. Pfeifer.
Reconstruction and control of a time-dependent two-electron wave packet.
Nature **516**, 374–378 (2014).

Z. Q. Yang, D. F. Ye, T. Ding, T. Pfeifer, and L. B. Fu.
Attosecond XUV absorption spectroscopy of doubly excited states in helium atoms dressed by a time-delayed femtosecond infrared laser.
Phys. Rev. A **91**, 013414 (2015).

A. Blättermann, C. Ott, A. Kaldun, T. Ding, V. Stooß, M. Laux, M. Rebholz, and T. Pfeifer.
In situ characterization of few-cycle laser pulses in transient absorption spectroscopy.
Opt. Lett. **40** 3464–3467 (2015).

V. Stooß, A. Kaldun, C. Ott, A. Blättermann, T. Ding, T. Pfeifer.
Sub-cycle symmetry breaking of atomic bound states interacting with a short and strong laser pulse in a time-domain picture.
arXiv:1506.01182v2 (2016).

Contents

Chapter 1

Introduction

Light, matter, and their interaction are integral parts of modern science and technology with the invention of the laser [1] as one of the most groundbreaking scientific achievements of the last century. Using lasers, scientists have trapped [2] and cooled [3] matter down to temperatures close to absolute zero where it may turn into a state called Bose-Einstein condensate [4,5]. But also the other extreme, namely super-hot and dense matter which is believed to exist in the core of stars has been created in laser laboratories [6]. Highly stable lasers operate atomic clocks and provide the standards for frequency and time [7]. With the advent of short-pulsed mode-locked [8–10] lasers the way was paved for high-precision spectroscopy with frequency combs [11] and time-resolved spectroscopy on extraordinary time scales to image chemical reactions [12,13]. Certainly, this list of achievements driven by lasers is by far not complete and there is no foreseeable end of this progress. The tenor of this opening paragraph is: Understanding and controlling light—matter interaction presents an ongoing revolution in contemporary science and technology.

What is a laser? Laser is an acronym for *light amplification by stimulated emission of radiation*. Simply put, a gain medium capable of being energetically pumped and population inverted amplifies incident radiation via stimulated emission. The gain medium is enclosed by a highly reflective cavity that redirects the radiation through the medium for the repetitive amplification. One remarkable characteristic of laser radiation is *coherence*, i.e., the presence of a fixed phase relationship of the emitted light waves. Coherence is the key ingredient that made the above mentioned scientific achievements possible.

The main theme of this thesis is the time-resolved spectroscopy of quantum systems. The motion of a quantum system is dictated by the energy level spacing between a pair of quantum states. For instance, nuclear motion within molecules involves quantum states which are spaced by milli-electronvolts (meV) energies. The corresponding time scale is on the order of a few hundreds of femtoseconds ($1\,\mathrm{fs} = 10^{-15}\,\mathrm{s}$). Electronic dynamics inside atoms or molecules are associated with energy level spacings on the order of electronvolts (eV) and take place on even faster, sub-fs time scales. Following such dynamics in real time demands laser pulses with commensurately short temporal durations.

Nowadays, with state-of-the-art laser sources, time-resolved spectroscopy may be called a matter of routine. However, currently available, fully coherent laser sources are typically limited to radiation wavelengths in the infrared, visible, and ultraviolet spectral regions. The extension of well-established spectroscopic techniques into the extreme-ultraviolet (XUV) and even x-ray spectral region is, in principle, possible with the use of novel, laser-like radiation sources based on (i) non-linear processes to create very high harmonics—known as high-harmonic generation (HHG) [14–16]—and (ii) free-electron lasers (FELs) [17]. The pulses delivered by HHG sources exhibit a high degree of coherence and sub-fs temporal durations. The drawback of HHG is the perturbatively low field intensity. In contrast, FELs deliver pulses at extremely high intensities, which however are lacking in temporal duration and—if generated through self-amplified spontaneous emission (SASE)—are statistically fluctuating in phase. SASE-FEL pulses are said to be partially coherent [18].

Various time-resolved spectroscopy concepts have been developed addressing different aspect of quantum dynamics. Regardless of the specific laser pulse parameters and properties, the general scheme is the same for all of them [13]: At first, dynamical processes are initiated within the target system under study by the so-called pump pulse. After a well-defined time delay, the so-called probe pulse interacts with the sample in order to interrogate those dynamics. Detection methods are available either directly, in the time-domain, measuring fragmented ionization products for instance by using reaction microscopes [19–21] or streak cameras [22]. Or, by means of spectral-domain methods based on (transient) photo-absorption which allows to retrieve dynamic information indirectly, for instance from characteristic fingerprint signatures of spectral lineshapes [23]. Pump-probe spectroscopy with fully coherent (stimulated-emission based) laser sources opened the field of “femtosecond photo-chemistry” [12, 13], which was honored by the Nobel prize in 1999 [24]. Nowadays, major effort is put into pump-probe approaches involving XUV attosecond pulses obtained from HHG in combination with femtosecond infrared/visible pulses in order to track the dynamics of electrons inside atoms [25]. In parallel, first single-color pump-probe experiments based on intense SASE-FEL radiation in the XUV spectral range have been realized, as exemplified for instance by the measurement of electron rearrangement dynamics [26] and interatomic Coulombic decay [27]. The probably most complete time-resolved spectroscopy approach is the implementation of *coherent two-dimensional spectroscopy* [28] which measures non-linear four-wave-mixing signals as a function of two pulse delays. In this way, energy transfer from quantum coherence excitations can be mapped, which for instance allowed to study the quantum mechanical nature of photosynthesis [29]. Once two-dimensional spectroscopy is implemented in the XUV and x-ray spectral region, the element-selective (by exciting spatially localized inner-shell transitions) spectroscopy of coherent coupling dynamics in molecules will be possible [30, 31]. First attempts are being made [32, 33], however the full implementation of XUV two-dimensional spectroscopy is technically highly demanding and still not yet realized so far.

In this work novel XUV *non-linear* time-resolved spectroscopy methods involving weak-field HHG and strong-field FEL pulses are developed to explore the sequential interaction of multiple photons with a target on a fundamental level. The methods are based on (attosecond) transient absorption, which so far has only been employed using an attosecond HHG and a single near-infrared femtosecond pulse. Several aspects are investigated: Firstly, the *coherent* (phase-sensitive) non-linear light—matter interaction in an excited bound-state system with HHG and moderately strong near-infrared pulses. Secondly, the *incoherent* non-linear light—matter interaction of sequential double ionization in intense XUV SASE-FEL fields. And thirdly, the *partially coherent* excitation of bound—bound transitions with strong XUV SASE-FEL fields. For those studies, the paradigmatic few-electron target system neon is chosen. The neon level scheme allows for 2s inner-shell XUV-excited states of opposite parity which can be resonantly coupled by one near-infrared photon—an ideal spectroscopic test ground for first proof-of-principle time-resolved multi-wave-mixing experiments with HHG pulses. Moreover, neon is appropriate for experiments on sequential double ionization, as it exhibits large XUV photoionization cross sections both in its neutral and first ionic charge states. In the doubly ionized neon atom, the resonant and coherent excitation of bound—bound transitions is possible.

The following scientific questions are asked:

- How can coherent higher-order coupling pathways be controlled and retrieved?
- To what extent can sequential double-ionization be controlled?
- What is the impact of strong SASE pulses on bound—bound transitions?
- Which role plays the SASE-coherence spikes in transient absorption spectroscopy?

Despite its complexity neon is still tractable by theoretical means. The presented work may serve as a benchmark to test existing theory. For this work, the observed phenomena were understood with the help of numerical calculations based on few-level models.

This thesis is structured as follows: Chapter 2 provides the basics for the content of this work. The focus is placed on the theoretical concepts which are the basis of the presented simulations. In chapter 3 the light sources of this work are introduced. Chapter 4 provides details about the experimental setup, the design of which is an integral part of this work. Chapter 5 contains the experimental part on the HHG-based transient absorption experiments with multiple pulses, while in chapter 6 the strong-field transient absorption experiments with strong-field XUV SASE pulses are described. Finally, the results are summarized in chapter 7 and an outlook is given.

In this thesis atomic units (a.u.) are used, where not otherwise stated. Atomic units are natural units defined relative to the properties of the hydrogen atom and are commonly used to simplify mathematical expressions. That means, the elementary electron charge e, the electron mass m_e, the Bohr radius a_0, Planck's reduced constant $\hbar$, and Coulomb's coupling constant $(4\pi\varepsilon_0)^{-1}$ are all set to unity

$$\mathrm{e} = m_\mathrm{e} = \mathrm{a}_0 = \hbar = (4\pi\varepsilon_0)^{-1} = 1. \tag{1.1}$$

Furthermore relevant for this work are the atomic units of energy, $E_\mathrm{a.u.} \approx 27.211\,\mathrm{eV}$, and time $t_\mathrm{a.u.} \approx 24.189\,\mathrm{as}$.

Chapter 2

Theoretical background

2.1 Ultra-short laser pulses

Light has a wave character. Its propagation through and the interaction with matter is governed by Maxwell's electromagnetic theory. The most basic solution of the electromagnetic wave equation is that of a plane wave described by a space- and time-dependent electric field:

$$\mathbf{E}(\mathbf{x},t) = \mathcal{E}_0 \mathrm{e}^{(\mathrm{i}\omega t - \mathbf{x}\cdot\mathbf{k})}. \tag{2.1}$$

Here, ω is the angular frequency (henceforth frequency) and $\mathbf{k}$ is the wave vector. Building on the usual non-relativistic dipole approximation (i.e. $\mathbf{x}\cdot\mathbf{k} \ll 1$) in all considerations of this work, the spatial dependence and the magnetic-field component coupled to the electric field will be neglected.

Eq. (2.1) describes the ideal case of a single-frequency continuous wave (CW) of infinite duration. (Short-)pulsed light fields are characterized by a continuum of frequencies which, according to Fourier's theorem, can be constructed as

$$\widetilde{E}(\omega) = \mathcal{F}\{E(t)\} = \frac{1}{\sqrt{2\pi}} \int_{-\infty}^{\infty} E(t)\mathrm{e}^{-\mathrm{i}\omega t}\mathrm{d}t. \tag{2.2}$$

The operator $\mathcal{F}$ denotes the complex Fourier transform and $\widetilde{E}(\omega)$ is a complex-valued function, symbolized by the tilde. The electric field in the time domain, $E(t)$, being in principle a measurable quantity, is assumed to be real-valued. Given $\widetilde{E}(\omega)$, $E(t)$ can be obtained from the inverse Fourier transform ($\mathcal{F}^{-1}$):

$$E(t) = \mathcal{F}^{-1}\left\{\widetilde{E}(\omega)\right\} = \frac{1}{\sqrt{2\pi}} \int_{-\infty}^{\infty} \widetilde{E}(\omega)\mathrm{e}^{\mathrm{i}\omega t}\mathrm{d}\omega. \tag{2.3}$$

Only when weak interactions with a physical system are considered and the rotating wave approximation (RWA) is valid, a complex representation will be used for the E-field also in the time domain, allowing only the slowly oscillating frequency terms to enter the Hamiltonian for light—matter interaction.

The quantity that an experimental spectrometer measures is the power-spectral density

$$I(\omega) \propto |\widetilde{E}(\omega)|^2. \tag{2.4}$$

In the time domain the (spatio-)temporal intensity profile $I(t) = [E(t)]^2$ irradiated by a laser can be measured in W/cm^2 units.

For the mathematical description of ultra-short laser pulses it is convenient to approximate the experimental envelope function by a Gaussian

$$E_\mathrm{G}(t) = \mathcal{E}_0 \, \mathrm{e}^{-(t/t_\mathrm{G})^2}. \tag{2.5}$$

with the peak field strength $\mathcal{E}_0$. This definition uses the Gaussian standard deviation related to the full width at half maximum (FWHM) of the peak intensity ($\mathcal{E}_0^2$) via

$$t_\mathrm{G} = \frac{t_\mathrm{FWHM}}{\sqrt{2\ln 2}}. \tag{2.6}$$

The temporal pulse duration t_FWHM and the spectral bandwidth $\Delta\omega_\mathrm{FWHM}$ are linked to each other by the uncertainty principle of Fourier's analysis, which provides a lower limit to their product

$$t_\mathrm{FWHM} \cdot \Delta\omega_\mathrm{FWHM} \geq 2\pi c_\mathrm{G}. \tag{2.7}$$

The constant c_G depends on the exact pulse shape. For Gaussian pulses, as defined in Eq. (2.5), $c_\mathrm{G} = 2\ln 2/\pi \approx 0.441$. Similar relations of this form [Eq. (2.7)] can be found for other pulse profiles than the Gaussian, see e.g. Ref. [34]. It can be concluded that the shortest possible pulse duration of a laser system (that is, when equality in Eq. (2.7) is reached) is generally limited by the spectral bandwidth. Accordingly, in this case the pulses are termed bandwidth-limited. However, due to dispersion effects during the generation process itself, or while traveling through ambient air, and/or due to reflections off optical components, short laser pulses accumulate a time- and frequency-dependent phase, $\phi(t)$ and $\varphi(\omega)$, respectively, which may lead to temporal broadening and pulse durations much larger than the possible bandwidth limit.

The time-dependent phase $\phi(t)$ can be expanded into

$$\phi(t) = \phi_\mathrm{CEP} + \frac{\partial \phi}{\partial t} t + \widetilde{\phi}(t) \tag{2.8}$$

where the constant term ϕ_CEP is the so-called carrier-envelope phase (CEP) offset between the pulse envelope and the electric-field oscillation with a carrier frequency ω_C, which is obtained from the second term, $\partial\phi/\partial t = \omega_\mathrm{C}$. The term $\widetilde{\phi}(t)$ contains only the higher-order contributions in time. For $\widetilde{\phi}(t) \neq 0$ the phase $\phi(t)$ is changing with time and the inequality in Eq. (2.7) holds.

Also the spectral phase $\varphi(\omega)$ can be expanded into a Taylor series

$$\varphi(\omega) = \sum_{n=0}^{\infty} \frac{(\omega-\omega_0)^n}{n!} \left.\frac{\partial^n \varphi}{\partial \omega^n}\right|_{\omega_0} = \sum_{n=0}^{\infty} \frac{(\omega-\omega_0)^n}{n!} D_n \tag{2.9}$$

where D_n are the dispersion coefficients and determined by evaluating the n*th*-derivative of $\varphi(\omega)$ with respect to ω at ω_0. The zero*th*-order term, D_0, is again the carrier-envelope offset phase, D_1 describes a temporal delay, called group delay (GD), and D_2, the so-called group-delay dispersion (GDD), changes the instantaneous frequency linearly in time (linear chirp) and causes temporal broadening. The changes in the frequency caused by the third- and higher-order dispersion effects (D_n for $n \geq 3$) may lead to temporal beating patterns across the pulses (non-linear chirp).

Further details about the mathematical treatment of ultra-short laser pulses can be found in many textbooks, e.g. [34, 35]. In this thesis, dispersion effects beyond $n \geq 2$ will not be considered as the detailed temporal and spectral pulse structures are of minor importance for the experimental and theoretical methods. It can be concluded from the above considerations, that for coherent laser pulses the phase behavior plays a role of paramount importance for the pulse characteristics, in particular in the presence of dispersion in experimental setups. The influence of the random phase of partially-coherent [18], SASE-grown (self-amplified spontaneous emission) pulses on the temporal and spectral pulse properties will be discussed in chapter 6.2 in the context of free-electron laser (FEL) applications.

2.2 Light—atom interaction

This section deals with the theoretical concepts and formalisms for the description of the interaction between an atomic (or ionic) quantum system and light. How the quantum system responds and behaves in the presence of the radiation field depends on many parameters concerning the system and the field. A variety of quantum mechanical interaction pathways are possible leading to the transition between bound excited states, laser-dressed states, or ionization just to mention a few of them. Not pretending to be complete, within the scope of this section only the key aspects of light—atom interaction for the presented studies will be discussed. The focus will be placed on the quasi-resonant interaction of a quantum system with light and the resulting bound—bound quantum transitions in the two limiting cases: The weak-field limit and the strong-field limit.

In the weak-field limit, time-dependent perturbation theory is applicable and the conventional picture of absorption or emission of a photon in a quantum transition holds. Besides transitions between bound states, also the transition from a bound state to a free (continuum) state, i.e. ionization, can be described. In the limit of strong laser fields the situation changes. As it will be discussed, in this case coherent Rabi oscillations can be excited which cannot be understood by perturbation theory. The strong-field concept is more general and, in principle, can be seen as a unified approach also applicable for weak and intermediate field strengths. However, the advantage of time-dependent perturbation theory is that it allows to treat the interaction with several laser pulses as a series of individual (time-ordered) transition steps each followed by free propagation of the unperturbed (field-free) system. This is in particular instrumental for multi-dimensional spectroscopy studies which aim to unravel the involved light—matter interaction pathways in Hilbert (or Liouville) space of a complex (higher-order) problem.

2.2.1 The weak-field limit: Perturbation theory

In general, time-dependent perturbation theory considers physical phenomena that can be formulated by the Hamiltonian

$$\hat{\mathbf{H}}(t) = \hat{\mathbf{H}}_0 + \lambda \hat{\mathbf{H}}_{\mathrm{int}}(t) \tag{2.10}$$

with a time-independent unperturbed part, $\hat{\mathbf{H}}_0$, and a comparatively small time-dependent perturbation, $\lambda \hat{\mathbf{H}}_{\mathrm{int}}(t)$. The solutions of $\hat{\mathbf{H}}_0$—the eigenstates $|\phi_j\rangle$ and the energy eigenvalues E_j—are usually accurately known. When subject to perturbation (here in terms of a light field), $\lambda \hat{\mathbf{H}}_{\mathrm{int}}(t)$, the system either absorbs or emits energy in form of a photon and undergoes a transition from one (unperturbed) eigenstate to another. The main task of time-dependent perturbation theory is the determination of the respective transition probability assuming the main part of the wave function remains in the initial (ground) state.

Perturbation theory applies in the limit of low laser intensities (weak-field limit) when the laser-field strength is much lower than the binding potential. This is clearly the case for high-harmonic generated XUV pulses (field strengths typically on the order 10^{-5} a.u.) in interaction with rare-gas atoms. At field-strengths above 0.01 a.u. ($10^{13}\,\mathrm{W/cm^2}$ intensity regime), which can be reached with both strong-field light sources used in this work the Ti:sapphire-based femtosecond NIR laser and the XUV free-electron laser in Hamburg (FLASH), perturbation theory might already fail (note that 1 a.u. reflects the electric-field strength due to the nucleus in ground-state hydrogen according to Bohr's classical model). In the strong-field limit the eigenstates of the coupled system—the "laser-dressed" atom—have to be considered in order to allow significant changes in the spectroscopic structure. This will be discussed in the following section.

Starting with the Hamiltonian as in Eq. (2.10), solutions to the time-dependent Schrödinger equation

$$\mathrm{i}\hbar \frac{\partial |\Psi(t)\rangle}{\partial t} = \left[\hat{\mathbf{H}}_0 + \lambda \hat{\mathbf{H}}_{\mathrm{int}}(t)\right] |\Psi(t)\rangle \tag{2.11}$$

can be expanded in an orthonormal set $\{|\phi_j\rangle\}$

$$|\Psi(t)\rangle = \sum_j c_j \exp(-\mathrm{i}\omega_j t)\, |\phi_j\rangle . \tag{2.12}$$

The eigenfunctions $|\phi_j\rangle$ represent vectors in a j-dimensional state space in $\mathbb{C}^j$ and, in principle, also incorporate spatial ("x") dependence. The x-dependence will not be explicitly defined. It can be ignored for the few-level model calculations as only the dynamical behavior of the expansion coefficients c_j is considered and all x-dependent quantities such as dipole matrix elements are fed into the numerical models.

The expansion coefficients c_j in Eq. (2.12) are constant with time for $\lambda = 0$. When exposed to perturbation, $\lambda \neq 0$, the coefficients are permitted to vary in time, i.e. $c_j \equiv c_j(t)$. The main idea behind time-dependent perturbation theory is that the time-dependent variation of $c_j(t)$ due to $\lambda \hat{\mathbf{H}}_{\text{int}}(t)$, in other words $\partial_t c_j(t)$, should be small.

Substituting Eq. (2.12) in Eq. (2.11), the differential equation whose solution provides the expansion coefficient can be derived as

$$\mathrm{i}\hbar \frac{\partial c_k(t)}{\partial t} = \sum_j \langle \phi_k | \lambda \hat{\mathbf{H}}_{\text{int}}(t) | \phi_j \rangle c_j(t) \exp(\mathrm{i}\omega_{kj} t) \tag{2.13}$$

where $\omega_{kj} = (E_k - E_j)/\hbar$ is the transition frequency from $|\phi_j\rangle$ to $|\phi_k\rangle$. Eq. (2.13) is still exact. The perturbative approximation is introduced by expanding the coefficient in powers of the perturbation parameter λ

$$c_j(t) \approx c_j^{(0)}(t) + \lambda c_j^{(1)}(t) + \lambda^2 c_j^{(2)}(t) + \cdots . \tag{2.14}$$

Substituting this expansion into Eq. (2.13), collecting equal powers of λ, and integrating over time yields a recursive scheme for next-to-leading-order corrections. The coefficient in order $n+1$ is obtained by

$$c_k^{(n+1)}(t) = -\frac{\mathrm{i}}{\hbar} \int_0^t \mathrm{d}t' \, \langle \phi_k | \hat{\mathbf{H}}_{\text{int}}(t') | \phi_j \rangle c_j^{(n)}(t') \exp(\mathrm{i}\omega_{kj} t'). \tag{2.15}$$

The probability of finding the system in state $|\phi_k\rangle$ at time t is given by the squared modulus of the $c_k(t)$ coefficient

$$P_k(t) = |c_k(t)|^2. \tag{2.16}$$

To proceed further it is helpful to consider only two states, say $|0\rangle$ and $|1\rangle$, with $\omega_1 > \omega_0$, and assume the system is initially ($t = 0$) prepared in the state $|0\rangle$, while $|1\rangle$, the final state, is vacant, i.e. written in zero*th* order:

$$c_0^{(0)}(0) = 1, \qquad c_1^{(0)}(0) = 0. \tag{2.17}$$

These assumptions have to be fed into Eq. (2.15). Now an electric field $E(t) = E_{\mathrm{G}}(t)\cos(\omega_{\mathrm{C}} t)$ shall play the role of the perturbation parameter λ and the perturbative interaction is written as

$$\lambda \hat{\mathbf{H}}_{\text{int}}(t) = \hat{d} \cdot E(t) = \hat{d} \cdot \frac{E_{\mathrm{G}}(t)}{2} \cdot (\mathrm{e}^{\mathrm{i}\omega_{\mathrm{C}} t} + \mathrm{e}^{-\mathrm{i}\omega_{\mathrm{C}} t}). \tag{2.18}$$

where $\hat{d}$ is the electric dipole operator, -e$\hat{x}$, associated with the transition matrix element between state $|0\rangle$ and $|1\rangle$

$$d_{10} \equiv -\mathrm{e} \langle 1 | x | 0 \rangle . \tag{2.19}$$

According to Eq. (2.15) the first-order transition amplitude is given by

$$c_1^{(1)}(t) = -\frac{\mathrm{i}}{\hbar} d_{10} \cdot c_0^{(0)} \int_0^t dt' \frac{E_{\mathrm{G}}(t)}{2} \cdot (\mathrm{e}^{\mathrm{i}(\omega_1 - \omega_0 + \omega_{\mathrm{C}})t'} + \mathrm{e}^{\mathrm{i}(\omega_1 - \omega_0 - \omega_{\mathrm{C}})t'}). \tag{2.20}$$

This is the point at which the rotating wave approximation (RWA) can be made. Assuming the carrier frequency ω_{C} is close to resonance with the transition $\omega_1 - \omega_0 \equiv \omega_{10}$, i.e. $\omega_{10} \approx \omega_{\mathrm{C}}$, the first phase term in Eq. (2.20) with frequency $\omega_{10} + \omega_{\mathrm{C}}$ oscillates so rapidly compared with the second term (and any other relevant time variations of the considered problem) that it can be assumed to average to zero over a short time scale. In this way it is argued that the first term can be neglected. For numerical calculations within the framework of time-dependent perturbation theory of this work, the RWA is applied by eliminating the positive-frequency phase term of the electric field. In other words, the electric field is written in complex form: $E_{\mathrm{G}}(t)\exp(-\mathrm{i}\omega_{\mathrm{C}} t)$.

The discussion so far has been based on the assumption $\omega_1 > \omega_0$, where ω_1 is the final state energy, which described the special case of (stimulated) *absorption* of a photon. However, Eq. (2.15) is general and also describes the inverse scenario—*stimulated emission* of a photon—if the perturbation causes a transition from the higher ($|1\rangle$) to the lower state ($|0\rangle$). In this case, the field is defined by a positive-frequency phase term, i.e. $E_{\mathrm{G}}(t)\exp(\mathrm{i}\omega_{\mathrm{C}} t)$, within the RWA.

In general, the time integration of Eq. (2.20) evaluated in the limit of large times ($t \to \infty$) allows to derive the transition rate [36]

$$W_{kj} = \frac{|c_1^{(k)}(t)|^2}{t} = \frac{2\pi}{\hbar^2} |d_{kj}|^2 \frac{\mathcal{E}_0^2}{4}\, \delta(\omega_k - \omega_j \pm \omega_{\mathrm{C}}) \tag{2.21}$$

i.e. the number of transitions per unit interaction time from state $|\phi_j\rangle$ to $|\phi_k\rangle$ induced by the applied perturbation. For this derivation, a monochromatic field was assumed with a peak field strength $\mathcal{E}_0$. The above formula is the ordinary form of *Fermi's golden rule*. The Dirac δ-function guarantees for energy conservation between initial and final state and makes the transition rate zero for $\omega_k - \omega_j \neq \omega_{\mathrm{C}}$ and infinite for $\omega_k - \omega_j = \pm\omega_{\mathrm{C}}$ (for the two cases when the final state has higher energy than the initial state, $\omega_k - \omega_j = +\omega_{\mathrm{C}}$, and when the final state has lower energy than the initial one, so that $\omega_k - \omega_j = -\omega_{\mathrm{C}}$). The squared matrix element $|d_{kj}|^2$ has the characteristic of a cross section. However, Eq. (2.21) only has physical meaning when a distribution of final states is considered to which transitions can occur. In this case, the "total" transition rate is written as the sum over all possible final states

$$W_j = \sum_k \frac{2\pi}{\hbar^2} |d_{kj}|^2 \frac{\mathcal{E}_0^2}{4}\, \delta(\omega_k - \omega_j \pm \omega_{\mathrm{C}}) = \frac{2\pi}{\hbar^2} |d_{kj}|^2 \rho(\omega_f), \tag{2.22}$$

which involves the density of final states

$$\rho(\omega_f) = \sum_k \delta(\omega_f - \omega_k) \tag{2.23}$$

evaluated at the final energy $\omega_f = \omega_j \pm \omega_{\mathrm{C}}$ and assuming d_{kj} is constant over the considered states. Eq. (2.22) is often referred to as the general form of Fermi's rule with a density of states function $\rho(\omega_f)$ incorporating the local final-state phase-space properties of the considered problem. It applies for the rate of transition to a (quasi-discrete) bound final state, to a set of final states which are part of a (flat) continuum, and to various other types of transition or scattering mechanisms in the field of atomic, nuclear, and solid-state physics.

A detailed introduction to perturbation theory and the treatment of related problems can be found in many textbooks. Here, the main references are [36, 37].

2.2.2 The strong-field limit: Rabi oscillations

In the foregoing section the light—atom interaction was discussed in the limit of weak laser fields assuming small changes in a two-level system's quantum state population (i.e. $c_0(t) \approx 1$ and $c_1(t) \approx 0$ for all t). In this picture the system either absorbs a photon from a light field and undergoes a transition from state $|0\rangle \rightarrow |1\rangle$, or it emits a photon to the light field and the reverse transition process takes place. Such perturbative transition steps serve as "time starters" in many time-resolved numerical simulations for experiments with attosecond HHG-pump pulses.

Now the more general case in which a significant fraction of population is transferred between the involved quantum states will be considered. This condition applies when strong laser pulses interact with a quantum system. The new phenomenon that becomes apparent in the strong-field limit and that cannot be accounted for by perturbation theory is the coherent coupling of the quantum state coefficients between the upper and lower levels by the light field so that population can oscillate back and forth. This is commonly known as Rabi oscillations [38]. These oscillations can beat with the fundamental transition frequency of a given spectral line resulting in side bands in the absorption/emission spectrum of that line, which is known as Autler-Townes or AC-Stark effect [39].

For the theoretical description of these effects again a quantum two-level system with energy levels E_0 and E_1, where $E_1 > E_0$, will be considered. It is convenient to assume the interaction with a monochromatic electric field,

$$E(t) = \mathcal{E}_0 \cos(\omega_C t) = \frac{\mathcal{E}_0}{2} \cdot (\mathrm{e}^{\mathrm{i}\omega_C t} + \mathrm{e}^{-\mathrm{i}\omega_C t}), \tag{2.24}$$

with a real-valued amplitude $\mathcal{E}_0$ (i.e. assuming linear field polarization) whose carrier frequency ω_C is in, or close to, resonance with the transition frequency $\omega_{10} = (E_1 - E_0)/\hbar$, i.e. $\omega_C \approx \omega_{10}$. As in the previous section, the objective is to solve the time-dependent Schrödinger equation

$$i\hbar \frac{\partial}{\partial t} |\Psi(t)\rangle = \hat{\mathbf{H}} |\Psi(t)\rangle \tag{2.25}$$

with Hamiltonian

$$\hat{\mathbf{H}} = \hat{\mathbf{H}}_0 + \hat{\mathbf{H}}_{\text{int}}(t) \tag{2.26}$$

accounting for the field-free two-level system $\hat{\mathbf{H}}_0$ and the light—atom interaction $\hat{\mathbf{H}}_{\text{int}}(t) = \hat{d} \cdot E(t)$ with the dipole-moment operator $\hat{d}$. Assuming the general solution for the two-level system

$$|\Psi(t)\rangle = c_0(t)\mathrm{e}^{-\mathrm{i}\omega_0 t} |\phi_0\rangle + c_1(t)\mathrm{e}^{-\mathrm{i}\omega_1 t} |\phi_1\rangle , \tag{2.27}$$

Schrödinger's equation provides two differential equations in the form of Eq. (2.13) from the previous section

$$\begin{aligned}\dot{c}_0(t) &= -\mathrm{i}\frac{\mathcal{E}_0\, d_{01}}{2\hbar}\left(\mathrm{e}^{\mathrm{i}(\omega_\mathrm{C}-\omega_{10})t}+\mathrm{e}^{-\mathrm{i}(\omega_\mathrm{C}+\omega_{10})t}\right)c_1(t)\\ \dot{c}_1(t) &= -\mathrm{i}\frac{\mathcal{E}_0\, d_{10}}{2\hbar}\left(\mathrm{e}^{-\mathrm{i}(\omega_\mathrm{C}-\omega_{10})t}+\mathrm{e}^{\mathrm{i}(\omega_\mathrm{C}+\omega_{10})t}\right)c_0(t)\end{aligned} \tag{2.28}$$

The upper equation describes the emission of a photon and the associated temporal changes in the $c_0(t)$ amplitude, while the lower one describes the absorption of a photon and the temporal variation of $c_1(t)$. The interaction matrix elements [cf. Eq. (2.13)] were evaluated by

$$\langle\phi_1|\,\hat{\mathbf{H}}_\mathrm{int}(t)\,|\phi_0\rangle = d_{10}\cdot\frac{\mathcal{E}_0}{2}\,(\mathrm{e}^{\mathrm{i}\omega_\mathrm{C}t}+\mathrm{e}^{-\mathrm{i}\omega_\mathrm{C}t}) \tag{2.29}$$

where $d_{10}\equiv -\mathrm{e}\,\langle\phi_1|x|\phi_0\rangle$ is the dipole matrix element for the transition $|0\rangle\rightarrow|1\rangle$. Since dipole transition matrix elements represent measurable quantities, they are taken to be real-valued ($d_{10}=d_{10}^*$), which implies that $d_{10}=d_{01}$.

Invoking the rotating wave approximation (RWA), which means that fast phase terms (with frequency $\omega_\mathrm{C}+\omega_{10}$) are discarded, the coupled differential equations (2.28) simplify to

$$\begin{aligned}\dot{c}_0(t) &= -\frac{\mathrm{i}}{2}\Omega_\mathrm{R}\,\mathrm{e}^{\mathrm{i}\Delta\cdot t}\,c_1(t)\\ \dot{c}_1(t) &= -\frac{\mathrm{i}}{2}\Omega_\mathrm{R}\,\mathrm{e}^{-\mathrm{i}\Delta\cdot t}\,c_0(t)\end{aligned} \tag{2.30}$$

where the field—transition frequency offset, the so-called detuning, was introduced as $\Delta=\omega_\mathrm{C}-\omega_{10}$. The pre-factor in Eq. (2.28) includes the light—atom interaction energy in frequency units, $\Omega_\mathrm{R}\equiv|d_{10}\mathcal{E}_0/\hbar|$, which is commonly referred to as the *Rabi frequency* [38].

The analytical solution of Eqs. (2.30) is

$$\begin{aligned}c_0(t) &= \mathrm{e}^{-\frac{\mathrm{i}}{2}\Delta\cdot t}\left\{\left[\cos\left(\frac{\Omega t}{2}\right)+\mathrm{i}\frac{\Delta}{\Omega}\sin\left(\frac{\Omega t}{2}\right)\right]c_0(0)-\mathrm{i}\frac{\Omega_\mathrm{R}}{\Omega}\sin\left(\frac{\Omega t}{2}\right)c_1(0)\right\}\\ c_1(t) &= \mathrm{e}^{\frac{\mathrm{i}}{2}\Delta\cdot t}\left\{-\mathrm{i}\frac{\Omega_\mathrm{R}}{\Omega}\sin\left(\frac{\Omega t}{2}\right)c_0(0)+\left[\cos\left(\frac{\Omega t}{2}\right)-\mathrm{i}\frac{\Delta}{\Omega}\sin\left(\frac{\Omega t}{2}\right)\right]c_1(0)\right\}\end{aligned} \tag{2.31}$$

with the so-called generalized Rabi frequency given by $\Omega=\sqrt{\Omega_\mathrm{R}^2+\Delta^2}$. This means, in the case of vanishing detuning ($\Delta=0$) and if the system is in state $|0\rangle$ at $t=0$ so that $c_0(0)=1$ and $c_1(0)=0$, the corresponding probabilities for finding the system in state $|0\rangle$ or $|1\rangle$ are given by

$$\begin{aligned}P_0(t) &= |c_0(t)|^2=\cos^2\left(\frac{\Omega_\mathrm{R}\,t}{2}\right)\\ P_1(t) &= |c_1(t)|^2=\sin^2\left(\frac{\Omega_\mathrm{R}\,t}{2}\right).\end{aligned} \tag{2.32}$$

The physical meaning is that in the presence of a strong laser field the quantum system oscillates back and forth between the two levels at Rabi cycles of period $T = 2\pi/\Omega_{\mathrm{R}}$. The Rabi frequency Ω_{R} is a measure for the interaction strength. If detuning is present ($\Delta \neq 0$), faster oscillations but with lower amplitude are expected [cf. Eqs. (2.31)]. It is intuitive that the oscillatory response of a strongly driven system can only be achieved if the system's lifetime due to decoherence or decay mechanisms (which thus far has been assumed to be infinitely long), as well as the laser coherence time are comparable, or ideally longer than the Rabi cycling period. This presents several complications for the use of ultra-short strong-field laser pulses, such as those delivered by free-electron laser (FEL) sources, to control the oscillatory population transfer between two energy levels from the sub-valence shell of an atomic system. To compete with the fast autoionization and Auger lifetimes of ∼1-100 fs and, in particular, with the short coherence times provided by the naturally partially-coherent SASE-FEL pulses (∼2–3 fs at FLASH in 2016), coupling laser intensities of at least $10^{13}\,\mathrm{W/cm^2}$ are necessary (assuming dipole transition matrix elements of 1 a.u.). Hence, so far, only a few experiments have demonstrated that a strong SASE pulse can induce Rabi cycling on an inner-shell transition [40,41].

For attosecond transient absorption spectroscopy (ATAS) experiments the frequency-equivalent of the Rabi oscillations in the time domain—namely the AC Stark or Autler-Townes effect [39] in the frequency domain—serves as the measurement observable. In the ATAS scheme, intense femtosecond NIR laser pulses couple two-electron or inner-shell states of an atomic species. As a result of the Rabi strong-coupling phenomenon the corresponding spectral transition is found to be split into a doublet separated by the Rabi frequency Ω_{R} [42,43]. This scheme involves a broadband XUV-probe transition from a third (auxiliary) atomic level, which is scanned as a function of time delay with respect to the coupling field. The AC Stark effect is usually interpreted in the so-called dressed state picture which involves a mapping of the Rabi problem onto a frame rotating with the laser frequency, where new states are formed which shift in energy with increasing field strength. The dressed atom approach is covered in many standard textbooks such as [44,45]

As a last remark, for the analytical derivation of the considered strong-coupling problem the RWA was an integral assumption. Even though in the presented experiments effects beyond the RWA are expected to be relatively small, the numerical few-level model calculations do not neglect any phase terms for the simulation of strong coupling. How the numerical few-level treatment is realized will be described in section 2.3.

2.2.3 Ionization

In this section the most relevant aspects of ionization through light—matter interaction for the presented thesis will be introduced. For further details, the reader is referred to the textbook [46] and the review paper [47].

When the applied electric field strength is relatively weak compared to the inner-atomic Coulomb field ($< 10^{13}\,\mathrm{W/cm^2}$), the interaction can be described by perturbation theory (see section 2.2.1) considering a final free-electron (continuum) state. In this case, the amount of energy imparted by the (n) incident photon(s) is sufficient to bridge the ionization potential. According to the predictions of perturbation theory the electron is ejected instantaneously upon photo-absorption. A general power law for the non-resonant n-photon ionization yield can be directly derived from Eq. (2.22) of section 2.2.1 [48]

$$W^{(n)} \equiv \sigma_j^{(n)} \Phi^n, \tag{2.33}$$

where the leading-order contribution of the ionization rate, $W^{(n)}$, is proportional to the nth power of the incident photon flux

$$\Phi(t) = \frac{I(t)}{\hbar\omega_{\mathrm{C}}}, \tag{2.34}$$

i.e. the field intensity, $I(t)$, at a particular photon energy (in number of photons per second per unit area). The quantity $\sigma_j^{(n)}$ represents the intensity-independent, target-specific ionization cross section from an atomic/ionic charge-state configuration j to another higher charge-state configuration. A simple model to describe (multi-photon) ionization kinetics is based on differential rate equations employing the individual ionization steps. For example, the rate coefficient for a one-photon process from the neutral charge state of a quantum mechanical system is $\sigma_0 \Phi(t)$. Thus, the first rate equation for the neutral charge state population, $N_0(t)$, reads

$$\dot{N}_0(t) = -\sigma_0 \Phi(t) N_0(t). \tag{2.35}$$

Accordingly, the rate equations for higher charge states are of the form

$$\dot{N}_j(t) = \sigma_{j-1} \Phi(t) N_{j-1}(t) - \sigma_j \Phi(t) N_j(t) \tag{2.36}$$

where $N_j(t)$ is the time-dependent population yield for the jth ionic species. Here, the above equations only incorporate sequential one-photon channels. Direct multi-photon processes can be employed formally by the same scheme treating the associated multi-photon rate coefficients $\sigma_j^{(n)} \Phi^n(t)$, as for example examined in Ref. [49].

The probability of multi-photon ionization increases when intermediate resonance states are excited—a phenomenon called *resonance-enhanced multi-photon ionization* [50,51]. This case cannot be described with the above considerations alone, since additional system-specific parameters play a role. For instance the life time of the intermediate states need to be taken into account.

If the applied field strength is strong compared to the inner-atomic Coulomb field (typically for intensities of order $> 10^{14}\,\mathrm{W/cm^2}$) and it significantly deforms the binding potential and the field oscillations are slow compared to the bound-state electron motion (which is usually the case for optical wavelengths), then the electron can tunnel through the potential barrier into the continuum (*tunneling ionization*). Tunneling ionization is the underlying mechanism of high-harmonic generation (HHG), which will be discussed in chapter 3.3.

A common practice has been established to distinguish between the multi-photon ionization and the tunneling ionization regimes by means of the so-called Keldysh-parameter [52]

$$\gamma = \sqrt{\frac{I_\mathrm{P}}{2U_\mathrm{p}}}. \tag{2.37}$$

The quantity I_P is the ionization potential and U_p is the ponderomotive potential of the field. For $\gamma \ll 1$, the inner-atomic fields are strongly influenced by the external field and the electron can escape via tunneling ionization. The case $\gamma > 1$ indicates a small perturbation by the external field to the binding potential. Hence, in this case multi-photon ionization is the dominant process.

2.3 Numerical few-level models

While full quantum mechanical *ab initio* simulations allow to accurately complement the outcome of a transient absorption experiment [53–55], the underlying fundamental light—matter interaction processes can be thoroughly studied with elementary few-level models (FLM). FLM treatments are in particular beneficial for identifying and characterizing the quantum mechanical pathways along which a target system is driven, that is controlled by multiple experimental parameters. This section provides the theoretical background and a basic description of the numerical method used to simulate the experiments performed within this thesis.

The few-level model (FLM) is formulated in the framework of Schrödinger's equation in atomic units (a.u.)

$$i\frac{\partial}{\partial t}|\Psi(t)\rangle = \hat{\mathbf{H}}(t)|\Psi(t)\rangle \tag{2.38}$$

where $\hat{\mathbf{H}}(t)$ is the total Hamiltonian

$$\hat{\mathbf{H}}(t) = \hat{\mathbf{H}}_0 + \hat{\mathbf{H}}_\mathrm{int}(t). \tag{2.39}$$

The unperturbed atomic Hamiltonian is denoted by $\hat{\mathbf{H}}_0$ and the interaction Hamiltonian is $\hat{\mathbf{H}}_\mathrm{int}(t) = \hat{\mathbf{d}} \cdot \mathbf{E}(t)$ with the dipole-moment operator $\hat{\mathbf{d}}$ and the electric field $\mathbf{E}(t)$ assuming dipole approximation. Invoking the superposition principle, the wave function representing the considered FLM system can be written as a linear combination of a finite number of orthogonal normalized eigenfunctions $\{|\phi_j\rangle\}$

$$|\Psi(t)\rangle = \sum_{j=0}^{n} c_j(t)\,|\phi_j\rangle. \tag{2.40}$$

The complex expansion coefficients $c_j(t) = \langle\phi_j|\Psi(t)\rangle$ weight each eigenfunction and add an initial phase to it. Expressed in the eigenbasis (on projecting $|\Psi(t)\rangle$ on $|\phi_j\rangle$)

Schrödinger's equation representing the FLM reads

$$\mathrm{i}\frac{\partial}{\partial t}\begin{bmatrix} c_0(t) \\ c_1(t) \\ \vdots \\ c_n(t) \end{bmatrix} = \begin{bmatrix} \langle 0|\hat{\mathbf{H}}(t)|0\rangle & \langle 0|\hat{\mathbf{H}}(t)|1\rangle & \cdots & \langle 0|\hat{\mathbf{H}}(t)|n\rangle \\ \langle 1|\hat{\mathbf{H}}(t)|0\rangle & & & \vdots \\ \vdots & & & \vdots \\ \langle n|\hat{\mathbf{H}}(t)|0\rangle & \cdots & \cdots & \langle n|\hat{\mathbf{H}}(t)|n\rangle \end{bmatrix} \begin{bmatrix} c_0(t) \\ c_1(t) \\ \vdots \\ c_n(t) \end{bmatrix}. \tag{2.41}$$

The matrix form of Schrödinger's equation represents the starting point for many numerical calculations. It is the origin of the terms "state vector", $[c_0(t), c_1(t), \cdots, c_n(t)]^{\mathrm{T}}$, and "matrix elements". The matrix elements on the diagonal are the energy eigenvalues of $\hat{\mathbf{H}}_0$, ω_j. The electric field enters the off-diagonal matrix entries constituting (optical) transition amplitudes between two configurations of the quantum system.

The formal solution of Eq. (2.41) is:

$$\begin{bmatrix} c_0(t) \\ c_1(t) \\ \vdots \\ c_n(t) \end{bmatrix} = \mathrm{e}^{-\mathrm{i}\hat{\mathbf{H}}(t)\cdot t} \begin{bmatrix} c_0(t=t_0) \\ c_1(t=t_0) \\ \cdots \\ c_n(t=t_0) \end{bmatrix}. \tag{2.42}$$

In this expression time ordering is omitted. Assuming fairly small time increments, Δt, for the numerical propagation scheme the discretization error from this approximation is negligible [56].

The intricacy hidden in Eq. (2.42) is that the propagator $\exp[-i\hat{\mathbf{H}}(t)\,t]$ cannot be evaluated as long as the Hamiltonian $\hat{\mathbf{H}}(t)$ is non-diagonal. Thus, the time propagation of the state vector includes a basis transformation into a vector space on which $\hat{\mathbf{H}}(t)$ is diagonal. This involves three steps for each iteration step of the time propagation: Firstly, $|\Psi(t)\rangle$ has to be complex rotated in Hilbert space by a unitary transformation T

$$\left|\Psi^{\mathrm{D}}(t)\right\rangle = T^{-1}\,|\Psi(t)\rangle. \tag{2.43}$$

The columns of the transformation matrix T are the eigenvectors of the Hamiltonian $\hat{\mathbf{H}}(t)$, such that

$$\hat{\mathbf{H}}^{\mathrm{D}}(t) = T^{-1}\,\hat{\mathbf{H}}(t)\,T, \tag{2.44}$$

where $\hat{\mathbf{H}}^{\mathrm{D}}(t)$ is the diagonalized Hamiltonian. After the unitary transformation the set of differential equations [cf. Eq. (2.41)] associated with the rotated wave function $\left|\Psi^{\mathrm{D}}(t)\right\rangle$ is decoupled. Now, in the second step, the system can be propagated forward in time by a simple multiplication with a complex phase term, $\exp(-\mathrm{i}\lambda_j\Delta t)$, with λ_j being the eigenvalues of the diagonal Hamiltonian. The last step is the back-transformation into the original Hilbert space

$$|\Psi(t)\rangle = T\,\left|\Psi^{\mathrm{D}}(t)\right\rangle. \tag{2.45}$$

Calculated for a specific time step, t_n, the vector $|\Psi(t)\rangle$ of Eq. (2.45) represents the starting point for the subsequent propagation step, $t_{n+1} = t_n + \Delta t$, according to this scheme which is implemented in an iteration loop and repeated for all propagation steps successively. To guarantee negligible discretization errors from this propagation scheme, the incremental time steps, Δt, have to be chosen sufficiently small such that the Hamiltonian $\hat{\mathbf{H}}(t)$ can be assumed as constant in time between two computation steps. In general, for XUV transient absorption calculations, time increments of $\Delta t = 1$ a.u., which is a typical time scale for natural electronic motion, have proven to produce confident results.

For each time step, the system's full time-dependent dipole moment between the ground state $|0\rangle$ and the excited states, $|j\rangle$ with $(j = 1...n)$, can be calculated by

$$D(t) \equiv \langle\Psi(t)|\,\hat{\mathbf{d}}\,|\Psi(t)\rangle = \sum_j c_0^*(t)c_j(t)\ \langle 0|\,\hat{\mathbf{d}}\,|j\rangle + \text{c.c} \tag{2.46}$$

where $\langle 0|\,\hat{\mathbf{d}}\,|j\rangle$ are the ground—excited dipole transition matrix elements and $\langle 0|\,\hat{\mathbf{d}}\,|0\rangle = 0$. A quantity that is directly proportional to the experimentally observed optical density (OD) can be obtained from the Fourier transformed dipole moment, $D(\omega)$, and the electric field in the spectral domain, $E(\omega)$, as derived in section 2.4.

Atomic parameters characterizing a bound state besides the resonance energy, ω_j, are the linewidth (i.e. the inverse decay lifetime), Γ_j, and the (non-Lorentzian) line profile associated with Fano's q-parameter if bound states with autoionizing nature are treated. How these parameters can be accounted for will be explained in the discussion of the simulation results further below.

This propagation scheme also supports the partitioning (factorization) of the exponential operator and the separate computation of the individual components of $\hat{\mathbf{H}}(t)$ in different eigenvector bases in which each of them is diagonal. This method is closely related to the Split-Step method [57, 58] and is applied to simulate the HHG-based four-wave-mixing experiments of this work presented in chapter 5.

2.4 Fundamentals of absorption

Thus far, the concepts and formalisms for the description of light—matter interaction were discussed in the language of quantum mechanics and the focus was placed on the internal transitions an atom can undergo in the presence of light along quantum mechanical phase-space coordinates. However, how an atom responds to an external electric field and how experimental observables look like, can, in good approximation, also be understood from a classical point of view.

The following discussion is mainly based on Refs. [28, 59, 60] and further details can be found therein.

According to the classical laws of electrodynamics, an applied electric field, $E(t) = \mathcal{E}_0\,\mathrm{e}^{\mathrm{i}\omega t}$, displaces the electric charge e of a single (one-electron) atom with respect to the opposite core charge. The charge separation is measured by means of the atomic dipole moment,

$$d = \mathrm{e}x, \tag{2.47}$$

where x is the displacement from the original position. Within this hypothetical model the displacement will immediately give rise to a (spring-like) force pulling it back towards its equilibrium position. The underlying equation of motion is that of a damped harmonic oscillator,

$$\ddot{P} + \gamma \dot{P} + \omega_\mathrm{r} P = \frac{\rho_\mathrm{N}\,\mathrm{e}^2}{m} \mathcal{E}_0 \cdot \mathrm{e}^{\mathrm{i}\omega t}, \tag{2.48}$$

with the mass m, the damping constant γ and the resonance frequency ω_r. In Eq. (2.48) the polarization P was treated instead of d. The polarization describes the dipole response of a macroscopic material medium consisting of ρ_N individual dipole moments (or atoms) per unit volume. It is

$$P = \rho_\mathrm{N} \cdot \mathrm{e}x. \tag{2.49}$$

Eq. (2.48) has the solution

$$\chi^{(1)}(\omega) = \frac{\rho_\mathrm{N}\,\mathrm{e}^2}{\varepsilon_0 m} \frac{1}{(\omega_\mathrm{r}^2 - \omega^2 + \mathrm{i}\gamma\omega)} \tag{2.50}$$

which is commonly known as the *linear* susceptibility of a medium. Hence, apart from the electric permittivity of free space, ε_0, the susceptibility relates an applied electric field E to the induced polarization P. Note that E and P are in principle real-valued quantities (the complex notation is for mathematical convenience). The susceptibility, $\chi^{(1)}(\omega)$, however, is treated as a complex quantity, i.e

$$\chi^{(1)}(\omega) = \chi'(\omega) + \mathrm{i}\chi''(\omega), \tag{2.51}$$

with a real part, $\chi'(\omega)$, which is in phase with the driving field and related to (linear) refraction properties and an imaginary part, $\chi''(\omega)$, which is $\pi/2$ out of phase with the driving field and relates to (linear) absorption.

When the driving field is sufficiently intense to "overdrive" the system (which could be the case when the field strength approaches the internal Coulombic field strength of the material) the response will also exhibit *non-linear* contributions which can be represented as a power series expansion of the total electric field E

$$P(\omega) = \varepsilon_0 \chi^{(1)}(\omega) E(\omega) + \frac{1}{2} \varepsilon_0 \chi^{(2)}(\omega) E^2(\omega) + \frac{1}{6} \varepsilon_0 \chi^{(3)}(\omega) E^3(\omega) + \cdots. \tag{2.52}$$

Here, $\chi^{(2)}(\omega)$ and $\chi^{(3)}(\omega)$ are the second- and third-order non-linear susceptibilities. In general, the susceptibilities $\chi^{(n)}(\omega)$ are tensor quantities representing both material properties such as the density and the symmetry in a medium and the wave-mixing nature of non-linear interaction. The second, quadratic term in Eq. (2.52) can only occur in non-centrosymmetric crystals and the third- and higher-order terms are usually weak compared to the first linear term.

What is absorption? The macroscopic polarization gives rise to emission of a signal field $E_\mathrm{sig}(t) = \mathrm{i}P(t)$ (free-induction decay) with the typical $\pi/2$ phase delay of a (resonantly) driven damped oscillator with respect to the driving field $E(t)$. Note, that the phase term $\mathrm{i} \equiv \exp(\mathrm{i}\pi/2)$ also appears in the description of driven quantum mechanical systems [compare Eq. (2.13) in section 2.2.1]. Accordingly, the absorption of light in a medium can be understood as a (destructive) interference phenomenon between $E_{\text{sig}}(t)$ and $E(t)$ on a detector. Hence, a measured signal spectrum can be approximated by [28]

$$\begin{aligned} I(\omega) &\propto \left| \int_0^\infty E(t) + E_{\text{sig}}(t)\,dt \right|^2 \\ &\propto I_0(\omega) + 2\,\text{Re}\left[\text{i}E(\omega)P(\omega)\right] + I_{\text{sig}}(\omega) \end{aligned} \tag{2.53}$$

where the Fourier transform was taken and the intensities denote the squared fields. Usually, the term $I_{\text{sig}}(\omega)$is negligibly small and the intensities $I(\omega)$ and $I_0(\omega)$ are the observables of typical absorption spectroscopy experiments such as those presented in this work. Commonly, the data is quantified via the so-called optical density (OD)

$$\begin{aligned} \text{OD}(\omega) &= -\log_{10}\left[\frac{I(\omega)}{I_0(\omega)}\right] \\ &\propto \text{Im}\left[\chi^{(1)}(\omega)\right]. \end{aligned} \tag{2.54}$$

For the above derivation, a crucial assumption is that $E_{\text{sig}}(t) \ll E(t)$, as it is the case for *dilute* gas-phase media where temporal reshaping effects of the propagated field through the medium do not play a role. Furthermore, it was assumed that non-linear contributions are small, $\chi^{(\text{n})}(\omega) \ll \chi^{(1)}(\omega)$. Eqs. (2.53) and (2.54) also include higher-order contributions of Eq. (2.52) if the intensity of the incoming beam is high.

Only in the low-intensity case $[\chi^{(\text{n})}(\omega) \ll \chi^{(1)}(\omega)]$, Eq. (2.54) represents the logarithmic form of Lambert-Beer's well-known law

$$I(\omega, z) = I_0(\omega)\text{e}^{-\alpha^{(1)}(\omega)z} \tag{2.55}$$

which describes the attenuation of an incident light intensity $I_0(\omega)$ at a position z in the medium depending on the absorption coefficient

$$\alpha^{(1)}(\omega) = \rho_{\text{N}}\,\sigma^{(1)}(\omega) \tag{2.56}$$

with the number density of irradiated atoms ρ_{N} and the *linear* (microscopic) cross section $\sigma^{(1)}(\omega)$. The linear absorption coefficient, $\alpha^{(1)}(\omega)$, can be precisely related to $\text{Im}[\chi^{(1)}(\omega)]$ [59] such that

$$\sigma^{(1)}(\omega) \approx \frac{1}{\rho_{\text{N}}}\frac{\omega}{c}\text{Im}\left[\chi^{(1)}(\omega)\right] \tag{2.57}$$

or with Eqs. (2.47) and (2.52)

$$\sigma^{(1)}(\omega) \approx \frac{\omega}{\varepsilon_0 c}\text{Im}\left[\frac{d(\omega)}{E(\omega)}\right]. \tag{2.58}$$

To account for non-linear absorption effects, Eq. (2.56), in principle, can be generalized according to

$$\alpha(\omega) = \sum_n \alpha^{(\text{n})}(\omega) I^n \tag{2.59}$$

where $\alpha^{(\text{n})}(\omega)$ are the n-photon absorption coefficients in units $[(\text{length}^{(2n-3)})/(\text{power}^{(2n-3)})]$ [61]. It is important to note that this description is of phenomenological origin and its validity is questionable in the limit of high-intensity incoming beams when non-perturbative strong-field effects become dominant.

2.5 The neon atom

The neon atom is a central target system for the experiments presented in this thesis. While first time-resolved experiments on correlated electron dynamics in our group have been performed targeting the prototypical two-electron helium atom [23, 54, 62, 63] with the focus on the excitation of both electrons at once, neon is a few-electron system ($Z = 10$) and provides additional correlated-electron excitation modes. Despite the higher level of complexity, fundamental correlated electron dynamics still can be experimentally resolved on tiniest time scales [64] and theoretically modeled [65, 66].

In the extreme-ultraviolet (XUV) spectral region between ∼40 and 50 eV photon energy above the ground state, which is relevant for this thesis, neutral neon exhibits both doubly-excited and 2s inner-shell (or core-hole) excited states. Both excitation modes lead to quasi-stationary quantum states above the first ionization threshold that rapidly decay with lifetimes of a few tens to hundreds of femtoseconds by the electron ejection and the rearrangement of the electronic configuration in the remaining ion. This process is commonly referred to as *autoionization*, triggered by the high degree of electron correlation and the strong interaction to the underlying single-(valence-)electron continuum.

The phenomenon of autoionization is comprehensively described in many textbooks such as [67, 68], which the reader is referred to for further reading. In general, autoionizing states are characterized by non-Lorentzian, asymmetric resonance lineshapes observed in photo-ionization yield or photo-absorption spectra. This can be explained by the interference between competing quantum transition amplitudes for the direct photo-ionization ($\mathrm{Ne} + \hbar\omega \rightarrow \mathrm{Ne}^+ + \mathrm{e}^-$) and autoionization. The relative phase between these amplitudes is a fingerprint characteristic of electron—electron correlation encoded in the profile of resonance lines, defined by the asymmetry parameter q. The concept and the theoretical formalism goes back to Ugo Fano's pioneering work [69] derived in the framework of a time-independent (energy-domain) scattering theory. A recent publication [23] introduced a time-domain representation of the q-parameter as a phase offset $\varphi(q)$ in the time-dependent dipole moment of the excited system. The time-dependent dipole moment reads in its most general form:

$$\tilde{d}(t) \propto c_q \delta(t) + \mathrm{e}^{-\frac{\Gamma}{2}t + \mathrm{i}\left[-\frac{E_\mathrm{r}}{\hbar}t + \varphi(q)\right]}. \tag{2.60}$$

The Dirac-delta term accounts for the continuum background with a magnitude scaling c_q. The oscillatory decay function describes the resonant dipole emission at a central photon energy E_r and with a decay rate Γ which gives rise to the well-known symmetric Lorentzian lineshape. The phase offset $\varphi(q)$ represents the amount by which the oscillation is out of phase with respect to the event of excitation (assumed to be infinitesimally short). Such a phase offset could be for example introduced ponderomotively, by the impulse (kick-like) laser-coupling of an highly-excited electron to the continuum. A mapping between this phase shift and the q-parameter can be found analytically:

$$\varphi(q) = 2 \cdot \arg(q - \mathrm{i}) \tag{2.61}$$

and in turn

$$q(\varphi) = -\cot\left(\frac{\varphi}{2}\right). \tag{2.62}$$

For further details and the mathematical derivation, the reader is referred to the original work [23].

The electronic configuration of the 2s inner-shell states the focus is placed on in this thesis is written as $1s^2 2s 2p^6\, nl\, (^{2S+1}L_J^\pi)$. The overall symmetry term relates to overall orbital L and spin S momenta and π denotes the parity (e: even, o: odd). If LS-coupling is satisfied, J denotes the total momentum. Where necessary, sub-symmetry designations relating to inner parts of the system are also given. For brevity, closed shells are commonly omitted.

The non-equilibrium dynamics of autoionizing states of neutral neon are studied with the help of short-pulsed XUV high-harmonic generation pulses in combination with intense femtosecond near-infrared laser pulses in chapter 5. For the studies presented in chapter 6, the target neon is subjected to intense free-electron laser (FEL) pulses at ~ 50.6 eV photon energy obtained from the process of self-amplified spontaneous emission (SASE). In the presence of intense XUV radiation neon can ionize multiple times and ionic bound-state resonances become available. The singly-charged system (Ne^+) exhibits no spectral resonances in the considered spectral range around 50 eV photon energy [70]. In doubly-charged neon, the promotion of a valence electron out of the $2p^4$ shell of ground-state Ne^{2+} into the $2p^3\,3d$ shell is possible. This results in several cumulating multiplet transitions. The Ne^{2+} ground-state has an experimentally resolvable ($10 - 100$ meV scale) fine-structure splitting among the triplet states classified by $^3P^e_{0,1,2}$. The considered excited states are also fine-structure-split (1 meV scale) and classified by $2p^3\,3d\,(^3D^o_{1,2,3})$. The resonance excitations radiatively decay with ns-scale lifetimes (corresponding to ultra-narrow µeV-scale lines), but appear homogeneously broadened on the detector due to power broadening and/or dissipation mechanisms as for example the ionization into the Ne IV (Ne^{3+}) continuum. In total three spectral (naturally Lorentzian) lines can be observed with the detector convolved with the instrumental resolution-response function assumed to be of Gaussian shape with a full width at half maximum of ~ 50 meV for the FEL experimental configuration.

2.6 Multi-dimensional spectroscopy

Besides gaining new insights into physical phenomena of light—matter interaction, this thesis also pursuits the technological aim of advancing non-linear spectroscopy techniques. These are non-linear coherent wave mixing techniques involving short-pulsed x-ray or extreme-ultraviolet (XUV) fields from high-harmonic generation or free-electron laser sources. A long-standing and so far unreached scientific dream is combining those light sources with the technique of coherent *multi-dimensional spectroscopy* (MDS) to map the dynamic quantum coupling between electronic states among different sites of a molecule [30, 31, 71]. Viewing the presented work as a corner stone for further future experiments on the way towards this goal, in this section the basic principles of MDS are briefly discussed. More extended further literature is given in many textbooks such as [28, 72]. In what follows, the main referencing was taken from [73, 74].

In contrast to conventional (linear) spectroscopy, which only probes the spectral structure of a sample system, coherent MDS techniques also provide the unequivocal information whether the observed resonances are quantum mechanically coupled to one another. If coupling is present, the excitation of one quantum mechanical mode by light influences (e.g. bleaches) the excitation of the other. Hence, the technically simplest way to realize an MDS experiment is based on a tunable narrowband laser which is frequency-scanned across the resonances (pump), while the change in absorption (or optical density) of a probe pulse is monitored [75]. Plotting the optical density as a function of both (pump and probe) excitation frequencies in a two- or multi-dimensional correlation map, allows to measure the coupling of excitation modes in form of off-diagonal spectral signatures. See Fig. 2.1(a).

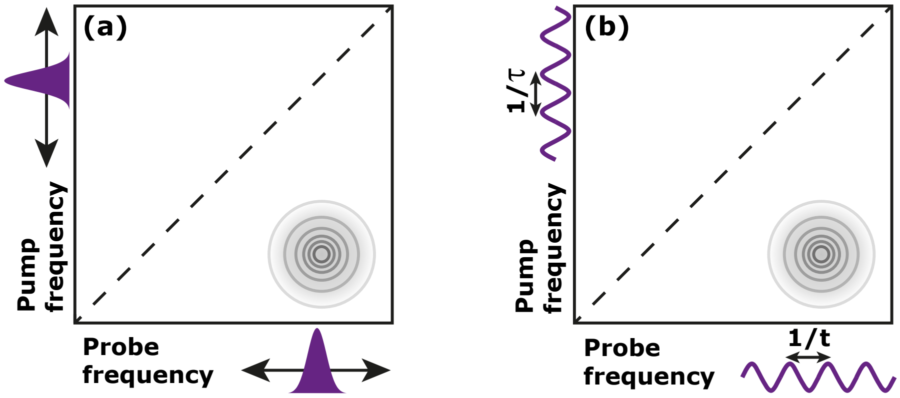

Figure 2.1: Cartoon representation of the principle of multi-dimensional spectroscopy (MDS). Pump and probe excitation frequencies are correlated in a two-dimensional spectral map. Spectral peaks in the off-diagonal region indicate coupling (gray circles), as explained further below in this section. Panel (a) depicts MDS with frequency-tunable narrowband lasers and (b) the equivalent method based on multiple ultrashort pulses.

In order to capture the dynamical evolution of the system, the narrowband laser fields are replaced by pairs of ultrashort pulses whose bandwidths cover all the considered resonances. In this case, the data is collected in the time domain as a function of the time delays τ (coherence time) between two pump pulses and t (detection time) between two probe pulses and represented in the spectral domain by taking the Fourier transform along those time-delay traces. To illustrate this time-domain approach, it is helpful to consider the spectrum of a pulse-pair as a sinusoidal function. Scanning the time delay is equivalent to scanning the sinusoidal periodicity of the pulse spectrum to sweep in and out of resonance with the system's excitation modes. The time interval between the pulse pairs is denoted by T (waiting time). In many setups only one probe pulse is utilized if the probe signal is measured by means of a frequency-dispersive spectrometer, which intrinsically converts the probe axis to the spectral domain. The result yields a 2d correlation map in the same manner as discussed above for the frequency-domain approach with frequency-tunable narrowband lasers. See Fig. 2.1(b).

A commonly used method to retrieve the phase of the emitted response is based on interfering the signal with a fully characterized (non-invasively weak) reference pulse—the so-called *local oscillator (LO)*—for heterodyne detection [28].

When the incoming fields are weak, MDS can be examined in the framework of perturbation theory calculating the non-linear n*th*-order polarization $P^{(n)}$ of a sample system [see Eq. (2.52) from section 2.4 for a frequency-domain description]. The third-order polarization in the time-domain due to the interaction with three driving fields is given by [72]:

$$\begin{aligned} P^{(3)}(x,t) = & \int \mathrm{d}t_3 \int \mathrm{d}t_2 \int \mathrm{d}t_1 \, S^{(3)}(t_3,t_2,t_1) \\ & \times E_3(x,t-t_3) E_2(x,t-t_3-t_2) E_1(x,t-t_3-t_2-t_1) \end{aligned} \tag{2.63}$$

where

$$E_i(x,t) = \mathcal{E}_i \left[\mathrm{e}^{\mathrm{i}\omega_\mathrm{C} t - \mathrm{i}k_i \cdot x} + \mathrm{e}^{-\mathrm{i}\omega_\mathrm{C} t + \mathrm{i}k_i \cdot x)} \right] \tag{2.64}$$

are the electric fields labeled by $i = 1 \cdots 3$ with amplitudes $\mathcal{E}_i$, central frequency ω_C and wave vectors k_i. The quantity $S^{(3)}(t_3,t_2,t_1)$ is the non-linear third-order response of the sample describing all the quantum mechanical interaction pathways the system is driven along at the interaction times t_1, t_2 and t_3 and during free evolution. While the temporal phases $\pm \mathrm{i}\omega_\mathrm{C}$ carried by the laser fields induce resonant transitions between quantum mechanical states of the sample, the spatial phase $\pm \mathrm{i}k_i \cdot x$ determines the phase difference of these transitions across the interaction volume in the sample. In a non-collinear (boxcar) geometry as illustrated in Fig 2.2, this gives rise to spatial phase gratings of excitations which interfere and lead to a whole set of wave-mixing signals with spatial frequencies for all permutations of $\pm k_1 \pm k_2 \pm k_3$, radiated into the corresponding spatial direction. By adjusting the wave vectors (i.e. the angles of incidence), a specific wave-mixing signal which satisfies a certain phase-matching condition (imposed by momentum conservation), e.g. for the combination $k_\mathrm{sig} = -k_1 + k_2 + k_3$, can be experimentally selected and measured without any background from the incident radiation. In this way, only a particular set of quantum transition pathways are extracted induced by the correspondingly ordered combination of frequencies $+\omega_1 - \omega_2 - \omega_3$ (energy conservation).

For a theoretical treatment, the above phase-matching conditions require to differentiate between the two conjugate components of the electric fields and consequently the expressions for the quantum mechanical transitions. For this reason, many theoretical derivations of MDS make use of the density-matrix operator $\rho(t)$ to describe a quantum state, defined by the outer product of the wave vector $|\Psi(t)\rangle$ [cf. Eq. (2.12)] and its conjugate [72]

$$\rho(t) \equiv |\Psi(t)\rangle \langle \Psi(t)| \, . \tag{2.65}$$

This choice is helpful, as the density-matrix operator allows to track all probabilities of occupying a state $|j\rangle$, $\rho_{jj} = c_j c_j^*$ (the so-called *populations*), in its diagonal matrix entries, the evolution of coherent superpositions of states $|j\rangle$ and $|k\rangle$, $\rho_{kj} = c_j c_k^* \mathrm{e}^{-\mathrm{i}\omega_{kj} t}$

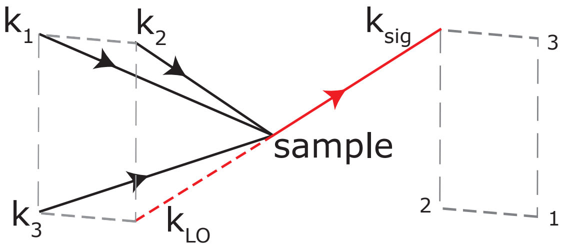

Figure 2.2: Boxcar phase-matching geometry of MDS experiments with incident beams along wave vectors k_i ($i = 1 \cdots 3$) indicated by the black lines. The generated wave-mixing processes in the sample can be interpreted as transient phase gratings of excitations induced by two incoming pulses (pump pulses), at which a third one (probe) is diffracted. For heterodyne detection methods a specular local oscillator (LO) field (red dashed line) can be utilized, which is collinear with the signal (red line) radiated along the phase-matched direction with k_{sig}.

(commonly referred to as *coherences*), in the off-diagonal entries, and their conjugates in a single (ensemble-averaged) entity [73].

How a series of interactions can be followed by the density-matrix picture is visualized diagrammatically in Fig. 2.3(a). Considered is a quantum three-level system of states $|0\rangle$, $|1\rangle$ and $|2\rangle$ that is initially prepared in the ground state, i.e. the matrix element of the projection operator $|0\rangle\langle 0|$ is $|c_0|^2 = 1$. Case 1 treats an ordered series of three light—matter interactions with frequencies $+\omega_{10} - \omega_{10} - \omega_{10}$ due to the pulses E_1, E_2, and E_3, respectively. Each applied frequency is in resonance with the 0-1 transition ($|\omega_{\text{C}}| = |\omega_{10}|$). The first interaction with a field of positive frequency acts on the bra side of the density matrix and causes excitation, i.e. the projector $|0\rangle\langle 1|$ yields the coherence $c_0 c_1^* \mathrm{e}^{\mathrm{i}\omega_{10}t}$. After the coherence time τ, the second interaction with a negative-frequency field excites the ket side and converts the coherence into a population state $|1\rangle\langle 1|$ with $|c_1|^2 \neq 0$. In contrast to the coherence state, the population is independent of any relative atomic phase induced by the excitation and "stores" the system on the excited state during T. Note, these first two interactions occur in conventional pump-probe experiments at once and can be associated with the pump-field intensity given by $E_{\text{pu}}E_{\text{pu}}^*$. The third interaction is again driven by a field of negative frequency and takes place after the time $\tau + T$. It acts on the bra side of the density matrix and causes de-excitation, which induces a second coherence $c_0^* c_1 \mathrm{e}^{-\mathrm{i}\omega_{10}t}$, which radiates a third-order signal at frequency ω_{10} in the phase-matched direction $k_{\text{sig}} = -k_1 + k_2 + k_3$. The final de-excitation brings the system back into the ground state $|0\rangle\langle 0|$. It is important to note, that the (initial) excitation and the emission frequencies are identical. Hence, this interaction pathway will result in a diagonal peak in the 2d spectral map. The second pathway depicted in Fig. 2.3 describes a series of interactions with driving frequencies $+\omega_{10} - \omega_{20} - \omega_{20}$ through the three fields E_1–E_3. With this configuration both excited states, $|1\rangle$ and $|2\rangle$, can be accessed from the common ground state $|0\rangle$ during the first two (pump) interactions. In case 2, the system evolves as a coherence along the full third-order interaction pathway. The key point is, that the third-order response signal is emitted with the frequency ω_{20}, but it was initially excited with ω_{10}. Hence, this pathway contributes to off-diagonal peaks in the 2d spectral map.

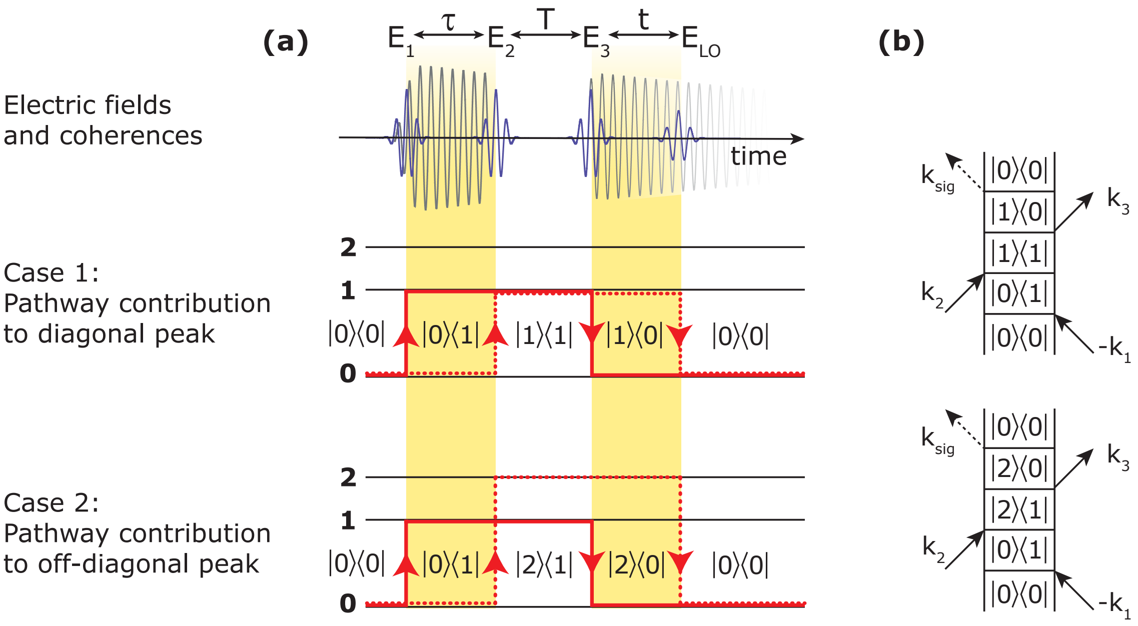

Figure 2.3: Pictorial representation of interaction pathways in MDS. In the top graphic of panel (a) the incoming fields E_1–E_3 (violet) at the times t_1–t_3 are shown separated by the time delays τ and T. The third-order signal field ($\propto \mathrm{i}P^{(3)}$) is emitted over time t and can be heterodyned with a reference field E_{LO}. Coherence oscillations are indicated by the gray sinusoidal lines. The ladder diagrams thereunder indicate interaction steps induced by the fields for two cases resulting in *diagonal* and *off-diagonal* peaks, as explained in the main text. Quantum states are black horizontal lines and the red solid (dashed) lines show the evolution of the bra (ket) sides of the density matrix. Note, the above drawn coherence oscillations (gray sinusoidal lines) correspond to the first described case (diagonal contribution). Diagram adapted from [73]. Panel (b) presents corresponding double-sided Feynman diagrams.

What was schematically visualized by the ladder-typ level diagram in Fig. 2.3(a) for the interaction of a quantum system with three fields, can also by represented by the popular technique of *double-sided Feynman diagrams* [72], as demonstrated in Fig. 2.3(b). In brief, vertical lines indicate the interaction time running from the bottom to the top. The right side propagates the bra and the left side the ket of the density matrix. Horizontal lines indicate interactions, whereas incoming arrows specify absorption and outgoing ones emission, which raises or lowers the density-matrix elements. The radiated third-order response signal is commonly drawn by dashed arrows.

The two possible interaction pathways discussed in Fig. 2.3 contribute to the third-order polarization $P^{(3)}(x,t)$ measured by MDS. Theoretical methods are available for the computation of the full third-order response $S^{(3)}(t_3,t_2,t_1)$, cf. for example the perturbative approach put forward by Shaul Mukamel [72].

Finally, Fig. 2.4 presents MDS-simulation results based on third-order perturbation theory (see section 2.4) applied to a simplified state-vector model associating the above described situation (cf. Fig. 2.3) with the 2s3p and 2s4p inner-shell excited states of neon at 45.55

and 47.12 eV photo-excitation energy [76]. The model includes three identical, assumed Gaussian laser fields, E_1–E_3, with a center photon energy of $\omega_C = 46$ eV and a temporal duration of 200 as. This choice opens resonant coherent transition channels between the ground and *both* higher states during the interaction with each pulse. The interactions are driven by a sequence of frequencies $+\omega_C - \omega_C + \omega_C$. The first and third interactions are described including the phase $-i\omega_{j0}\Delta t - \Gamma/2\,\Delta t$ (with the label j for the two excited states) accounting for coherence oscillation with a common decay rate $\Gamma = 0.1$ eV, while the second term does not include any relative atomic phase dependence. Scanned is the coherence time τ (i.e the delay of pulse E_2 with respect to E_1) with temporal steps $\Delta t =$ 0.024 fs over a time window of 30 fs. The third pulse, E_3, is fixed at a delay position of 48 fs with respect to E_1. Absorption spectra are obtained from the Fourier transformed dipole moment, $D(\omega)$, and the electric field in the spectral domain, $E(\omega)$, as derived in section 2.4. The simulation examines coupling mechanisms between transitions to the common ground state as discussed above in Fig. 2.3. The spectral position of the resulting cross peaks directly map to these couplings. See Fig. 2.4.

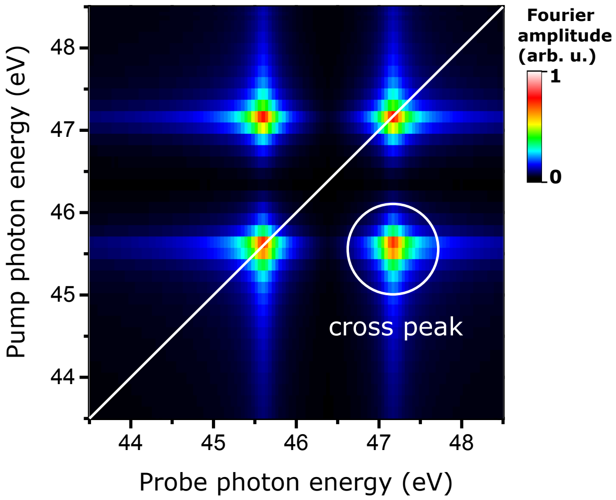

Figure 2.4: Simulated 2d spectral map for the 2s3p and 2s4p inner-shell excited states of neon at 45.55 and 47.12 eV photo-excitation energy. Only the diagonal peaks would be observed in the case where there is no coupling between the two transitions (cf. case 1 in Fig. 2.3). The (off-diagonal) cross peaks indicate coupling (cf. case 2 in Fig. 2.3).

Here, the MDS simulation only serves for illustration purposes. In many more advanced studies, amplitude and shape of the cross peaks are analyzed with varied waiting time T. This provides unambiguous information about energy transfer [77] and lineshape-broadening mechanisms [78] in complex systems.

Chapter 3

Light sources

3.1 Free-electron lasers

3.1.1 Synchrotron radiation and undulator principle

An accelerated particle of mass m_0 and charge e, such as an electron on a curved trajectory, emits electromagnetic radiation. The power emitted per solid angle Ω exhibits the characteristic toroidal radiation pattern of a Hertzian dipole with Θ, the angle between the acceleration and the direction of emission [79]:

$$\frac{\mathrm{d}P_{\mathrm{rad}}}{\mathrm{d}\Omega} = \frac{\mathrm{e}^2}{16\pi^2\varepsilon_0 m_0^2 c^3}\left(\frac{\mathrm{d}\mathbf{p}}{\mathrm{d}t}\right)^2 \sin^2\Theta. \tag{3.1}$$

This is known as Larmor's formula for a nonrelativistic accelerated charge. Here, **p** is the momentum, ε_0 the vacuum permittivity, and c the speed of light. At relativistic velocities the angular distribution of the emission is subject to the Lorentz contraction, which leads to a narrow conical forward peak of the radiation field in the direction of motion (tangent to the curve). With increasing velocity v the beam divergence angle ϑ decreases according to $\vartheta \simeq \gamma^{-1}$ with the Lorentz factor $\gamma \equiv (1 - v^2/c^2)^{-1/2}$. The resulting radiation spectrum depends on the bending radius R of the electron orbit and is commonly characterized by the so-called critical frequency ω_{crit}, which is that for which half of the radiated power is in higher-frequency photons and the other half in lower-frequency photons [80]

$$\omega_{crit} = \frac{3\gamma^3 c}{2R}. \tag{3.2}$$

Modern synchrotron machines or linear accelerators which are designed solely for the operation as a synchrotron-radiation source reach high efficiencies and high-flux radiation fields with the use of wigglers or undulators. Both wigglers and undulators are periodic magnetic arrangements with opposing north-south orientation to force the injected

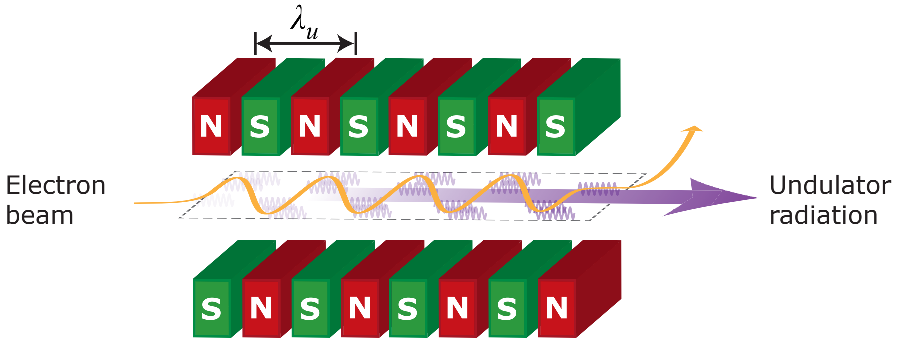

Figure 3.1: Principle of an undulator. A periodic magnetic field along the electron-beam axis, created by an arrangement of bending magnets with alternating polarity, generates the typical sinusoidal undulator trajectory (yellow) with a period λ_U. The undulator magnet is constructed such that the synchrotron radiation spontaneously emitted in each undulation cycle (violet wavy lines) overlaps in forward direction, which leads to a narrow and bright radiation cone (with, at this stage, yet a low degree of coherence). A typical undulator consists of ~ 100 bending magnets with period lengths of a few centimeters.

electrons on a sinusoidal trajectory due to the Lorentz force (see Fig. 3.1). The main technical difference between wigglers and undulators is the bending radius of the electron trajectories. A wiggler provides a more arched trajectory leading to a spatially broad radiation pattern (sweeping searchlight effect). In an undulator, the excursion is chosen sufficiently small to maintain overlap of the electron trajectory with the emitted radiation cone. Depending on the magnetic-field strength B and the undulation period λ_U, a deflection parameter K is defined by the ratio between the maximum electronic deflection angle α and the natural beam divergence angle ϑ, as

$$K \equiv \frac{\alpha}{\vartheta} = \frac{eB\lambda_U}{2\pi m_0 c}. \tag{3.3}$$

Only if $K \leq 1$ (undulator condition) there will be sufficient overlap between the electron trajectory and the radiation field such that radiation emitted in different undulator periods can interfere constructively. To an observer in a fixed laboratory reference frame, the undulator-radiation frequency is further increased by the relativistic Doppler effect. Taking this into account the resonance condition for undulator radiation in the laboratory frame can be expressed as [80]

$$\lambda = \frac{\lambda_u}{2\gamma^2 n}\left(1 + \frac{K^2}{2} + (\vartheta\gamma)^2\right) \tag{3.4}$$

where λ is the undulator output wavelength. For this expression the fundamental ($n = 1$) as well as high-order harmonic wavelengths (where $n = 2, 3, 4\cdots$) are resonant. In fact, due to destructive interferences, only the fundamental wavelength and odd harmonics have strong emission on-axis [17].

Apparently, the output wavelength λ can be tuned by three machine parameters: the electron-beam energy (via the Lorentz factor γ), the undulator gap (i.e. λ_U), and the deflection parameter K (via the B-field). The XUV/soft x-ray free-electron laser in Hamburg (FLASH) is equipped with a fixed-gap undulator (FLASH1 beamline), at which a change of the wavelength is obtained by changing the electron energy (cf. the FLASH parameters in Tab. 3.1). However, once established in the SASE lasing mode, a quick change of the wavelength is challenging. In the year 2016 a new variable-gap undulator (FLASH2 beamline) started user operation at FLASH. Keeping the electron energy fix and adjusting λ_U, FLASH2 allows a quick wavelength tuning over a broad spectral range [81]. The Linac Coherent Light Source (LCLS) is an example for an undulator, in which the whole undulator segment can be translated laterally to tune the wavelength via the K parameter (at least to a certain extent) [82].

So far, the influence of the generated electromagnetic field back on the electrons has been neglected. It plays a crucial role for the description of free-electron lasers.

3.1.2 Free-electron laser principle

The undulator radiation as described so far results from the superposition of spontaneous synchrotron radiation emitted by multi-electron bunches (of order 10^9 electrons per bunch). Considering the various electrons as being uncorrelated (randomly distributed in phase space), the radiated undulator power is proportional to the number of emitting electrons N_e.

A free-electron laser (FEL) is an undulator where the electrons within a bunch emit in phase. As in a quantum mechanical laser, the fixed phase relationship between the individual emitters is the key ingredient to achieve large amplification. In this case, the emitted field amplitudes add up constructively, and not the intensities, as it is the case for random, uncorrelated fields. As a consequence, the FEL power scales with the square of the electron number N_e^2. The field synchronization is obtained by the formation of a sinusoidal substructure in the velocity distribution of the electron bunches—a process commonly referred to as *microbunching*. Microbunching is a self-arrangement mechanism due to the ponderomotive back action of the electromagnetic field on the electrons. It is driven by the coupling of the transverse electron velocity component v_x to the transverse light field E_x, causing a net (undulator-cycle averaged) energy exchange

$$\frac{\mathrm{d}E_\mathrm{e}}{\mathrm{d}t} = -\mathrm{e}v_x E_x. \tag{3.5}$$

Depending on the relative position of the electrons with respect to the phase of the light field, the electron will gain kinetic energy and thus will be accelerated, this is the case for $\mathrm{d}E_\mathrm{e}/\mathrm{d}t > 0$, or it will loose kinetic energy, if $\mathrm{d}E_e/\mathrm{d}t < 0$, and hence will be slowed down. This process causes the development of microbunches at the radiation wavelength. The microbunching has a positive feedback on the radiation power, which consequently further amplifies the bunching (self-consistent feedback loop). As soon as all electrons are bunched in phase no further amplification is possible and the FEL process is saturated. At this point, the at first almost incoherent spontaneous undulator radiation has been converted into high-intensity partially coherent (laser-like) radiation. The microbunching concept is illustrated in Fig. (3.2).

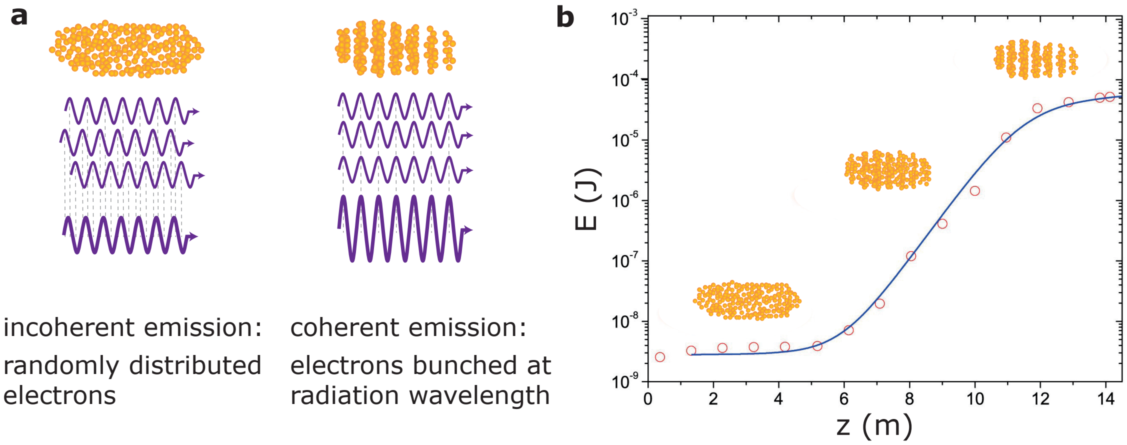

Figure 3.2: Operation principle of an FEL. (a) Electrons entering the undulator are randomly distributed and emit almost incoherent radiation at the wavelength λ (left figure). Initiated by shot noise and coherence fluctuations the ponderomotive back-action from the field on the electrons leads to microbunching causing strongly enhanced coherence and intensity (right figure). Graphic adapted from [17]. (b) The FEL microbunching mechanism drives amplification as a positive feedback process. The growth of the FEL pulse energy E scales exponentially with the undulator length z and saturates when all electrons are bunched in phase (plateau region). Data (red circles) and theoretical prediction (blue curve) obtained at the first stage of the FEL at DESY with 245 MeV electron energy. The microbunching process is indicated schematically. Graphic taken from [83].

The initialization of FEL lasing at extremely short (x-ray) wavelengths cannot be achieved using an external seed source due to the lack of light sources and optical elements in this spectral range. However, as in a conventional quantum laser, FEL lasing can also startup from noise. In this case, the always existing stochastic density fluctuations in the electron beam randomly excite (close to) resonant modulations, which, if strong enough, then act as an internal seed source for the FEL amplifier. Because this process is self-excited and it causes gain, (in analogy to the stimulated emission based quantum laser) it was termed *Self-Amplified Spontaneous Emission (SASE)* [84–86]. Due to the stochastic nature of SASE, the FEL radiation pulse is made up of many statistically independent coherent spikes.

3.1.3 The free-electron laser in Hamburg (FLASH)

The Free-electron LASer in Hamburg (FLASH) at DESY is a user facility for light-matter interaction experiments with extremely intense and ultrashort-pulsed XUV and soft x-ray radiation. Since 2016 FLASH operates two parallel SASE (self-amplified spontaneous emission) beamlines, FLASH1 and FLASH2, that share the same electron pulses [87]. In contrast to FLASH1, FLASH2 is based on a modern variable-gap undulator, which allows a quick change in wavelength (independent of FLASH1) if needed during an experimental run. The experiments presented in this work were conducted at the FLASH1 beamline. A schematic view of the FLASH facility is presented in Fig. 3.3.

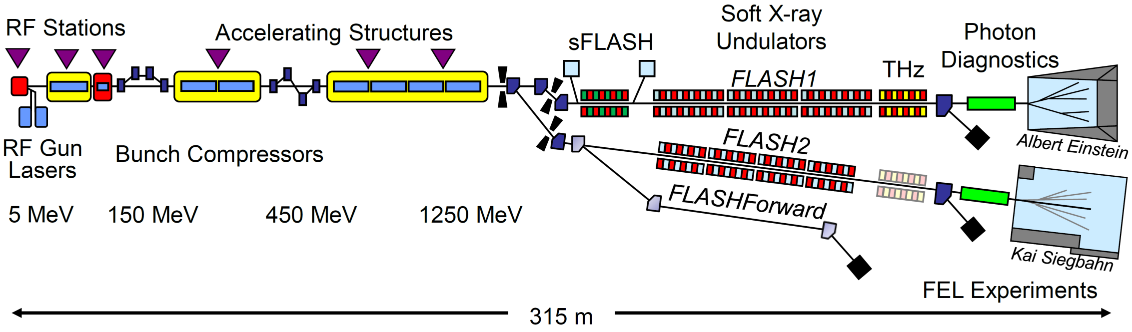

Figure 3.3: Schematic layout of the FLASH facility, current status. See the main text for description. The graphic also includes the injection beamline sFLASH for FEL-seeding experiments with high-harmonic generated XUV radiation, the beamline for FEL Terahertz (THz) radiation, and the future project FLASHForward for plasma-driven FEL experiments. Graphic adapted from [81].

FLASH1 reaches high gain (i.e. exponential radiation growth, cf. Fig. 3.2(b) by a single pass through a 27 m long undulator with a period of 27.3 mm, a peak B-field of 0.47 T, and thus, according to Eq. (3.3), a K-value of roughly 1. Upstream of the undulator section the electron bunches with nC-scale bunch charges are produced by a laser-driven radio frequency (RF) photocathode electron gun and then accelerated up to the GeV kinetic energy regime by superconducting RF-cavity based linear accelerator modules [88]. The superconducting accelerator technology allows the operation in a so-called *burst mode*, where 800μs long bunch trains with repetition rates of up to 1 MHz can be accelerated every tenth of a second. As each electron bunch produces one photon pulse, FLASH is able to generate in total 8000 photon pulses per second. In between the accelerator structures temporal bunch compression is introduced by magnetic chicanes. Both the bunch charge as well as the bunch duration are the typical control parameters for the 100-fs scale FEL-photon pulse durations of FLASH. In Tab. 3.1, the FLASH SASE photon beam parameters are summarized.

Downstream of the undulator section the electrons are separated from the photons and directed into a beam dump. The photon beam is transported under ultra-high vacuum conditions to the experimental hall where the beam is distributed into five user end stations (beamlines BL 1-3 and plane grating PG beamlines 1 and 2) which differ in their focusing optics and the permanent experimental equipment. The experiments reported in this work were conducted at the focused BL2 endstation incorporating the XUV-XUV split-and-delay interferometer setup [90]. Several electron beam and photon beam diagnostic units can be operated parasitically at FLASH. The most important ones for this work are a pair of gas-monitor detectors (GMDs) [91], almost transparent devices for

Table 3.1: FLASH parameters

Parameters at FLASH1	Typical values according to [81, 89]	Parameters of presented experiments
Wavelength range (fund.)	4.2 - 51 nm	24.5 nm
Average single pulse energy	1 - 500 μJ	$\sim 45\mu$J
Pulse duration (FWHM)	<30 - 200 fs	$\sim$100 fs
Spectral width (FWHM)	0.7 - 2 %	$\sim$1.5%
Angular divergence (FWHM)	90 ± 10 μrad	-
Pulses per second	10 - 5000	10
Photons per pulse	$10^{11} - 10^{14}$	$\sim 10^{13}$

pulse-energy measurements based on the photoionization of a gas and the grating-based reference photo spectrometer [92]. Further technical information on machine parameters and the diagnostic instruments of FLASH is given in [89].

3.2 The femtosecond laser system

For the here presented experiments we used a commercially available Ti:Sapphire multipass amplifier, the Femtolasers Compact Pro system [93], to generate ultra-short, sub-30 fs laser pulses with high pulse energies on the mJ level delivered at a 4 kHz repetition rate. The technical details of this laser system can be found in several foregoing PhD theses such as [94–96]. For this reason and because the laser system has been replaced by a follow-up system in the meanwhile, here only a brief overview of the laser system will be given. Details of the techniques by which ultra-short laser pulses are generated, such as mode locking, chirped-pulse amplification, self-phase modulation, etc., can be found in many textbooks such as [34].

The system consists of a laser oscillator which delivers sub-10 fs pulses at 80 MHz repetition rates and low pulse energies on the nJ level. These pulses are subsequently amplified up to pulse energies of roughly 0.7 mJ. To this end, the pulses are propagated multiple times (9 times in this setup) through an amplifying gain medium in a butterfly-like geometry. The gain medium is strongly pumped by a $\sim$30 W pump laser. To prevent any damage of optical elements inside the amplifier, the pulses are temporally stretched using a slab of glass (chirped-pulse amplification). Furthermore, a Pockels cell is integrated in order to gate only every 20000th oscillator pulse for amplification. This reduces the pulse repetition rate from 80 MHz down to 4 kHz. Finally, the amplified pulses are recompressed almost down to the bandwidth limit of roughly 30 fs pulse durations (having suffered from spectral gain-narrowing inside the amplifier crystal).

These pulses are further shortened in a hollow-core glass fiber filled with neon at 2–3 bar internal pressure in combination with a set of chirped mirrors. The non-linear interaction of the intense pulses with the gas medium causes an intensity-dependent phase change which leads to spectral broadening (self-phase modulation). The chirped mirrors (multi-layer coated for the reflection of different frequencies at different depths) are designed to compensate for higher-order dispersion accompanying the process of self-phase modulation and hence again temporally compress the pulses.

Finally, sub-7 fs, 1 mJ range laser pulses with a spectral bandwidth of about 0.7 eV centered around $\omega_{\mathrm{NIR}} = 1.6$ eV (wavelength $\lambda = 760$ nm) are available. Tightly focusing (f = 500 mm) these pulses down to a spot size of close to ~50 μm yields peak intensities up to the $10^{14}\,\mathrm{W/cm^2}$ regime. These intensities are needed for the generation of higher-harmonic radiation (HHG).

3.3 High-order harmonic generation

3.3.1 Principle of high-order harmonic generation

High-order harmonic generation (HHG) is a highly nonlinear frequency-conversion process beyond the conventional perturbative nonlinear formalism [see Eq. (2.52)], which becomes apparent when the electric field strength approaches values comparable to the binding energy of an electron Coulomb potential.

An intuitive understanding of HHG and other related processes under strong laser fields is provided by a semi-classical three-step model [97–99] illustrated in Fig.3.4. According to this model an assumed slowly varying, linearly polarized electric field strongly suppresses the atomic Coulomb potential along the axis of polarization. If the effective instantaneous Coulomb energy barrier is narrow enough an electronic wavefunction can (partially) tunnel through it (step 1). In the continuum the ionized wave packet is (classically) accelerated by the laser field and gains kinetic energy E_{kin} (step 2). The influence of the Coulomb force from the remaining ion core is in this step negligibly small. Finally, as the field reverses its direction, the wave packet is driven back to the vicinity of the ion core. It may then recollide with the parent ion and release its excess energy as coherent dipole radiation (step 3). If the wave packet recombines back to the ground state, the emitted photon energy is given by

$$\hbar\omega_{\mathrm{HHG}} = I_{\mathrm{p}} + E_{\mathrm{kin}} \tag{3.6}$$

where I_{p} is the ionization potential, i.e. the energy required to free a bound electron.

This simplistic model as described so far already suggest the natural attosecond time scale of HHG as radiative recollision only happens during a short, sub-driving-laser cycle time window when the electron wave packet is back in close vicinity of the ion core. However, because a multitude of different electron recollision trajectories, leading to different kinetic energies and recollision times, are possible and interfere the HHG radiation is emitted continuously over roughly half an optical cycle of the fundamental field. The produced HHG spectrum covers a broadband photon-energy range characterized by the

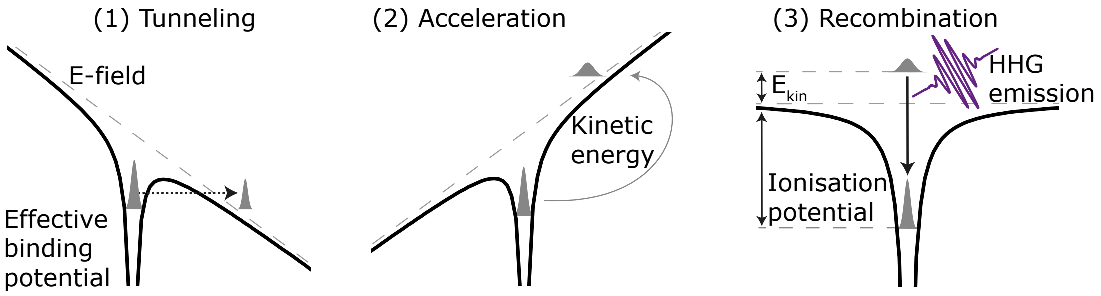

Figure 3.4: Schematic illustration of the three-step model for high-order harmonic generation. The black curve represents the effective binding potential in the presence of a slow, quasi-electrostatic field for an electron wavefunction (grey shaded). Illustrated are the tunneling, acceleration, and radiative recollision processes occurring at three different instants of time during an optical field driving cycle. See the main text for further description.

harmonic *cutoff* corresponding to the maximum kinetic return energy, which can be classically derived as [97]

$$\hbar\omega_{\mathrm{HHG,co}} = 3.17U_{\mathrm{p}} + I_{\mathrm{p}}. \tag{3.7}$$

Here, $U_{\mathrm{p}} = \mathcal{E}_0^2/4\omega_{\mathrm{L}}^2$ represents the ponderomotive potential, i.e., the average quivering energy of a free electron in an oscillating laser field with peak field strength $\mathcal{E}_0$ and the fundamental laser frequency ω_{L}. Below the cutoff there exist two different trajectories the electron can follow leading to the same photon energy that contribute to the emission. Along the so-called *short* trajectory the electron travels for approximately $1/2$ of the laser-cycle duration, and along the *long* trajectory the propagation time is up to a full cycle duration of the laser field. The quantum path interference of these degenerate trajectories strongly influences the spectral and temporal structure in HHG [100]. Gating techniques to optimize for clean and short attosecond pulses are available [101, 102]. For the experiments presented in the scope of this work the control of the detailed spectral and temporal structure in HHG is not of relevance. As it will be discussed in chapter 5, the ultra-broad XUV spectral bandwidth and the intrinsic synchronization to the fundamental near-infrared (NIR) driver laser are the crucial characteristics of HHG radiation to the presented experimental scheme.

The three combined processes (tunneling, acceleration, radiative recollision) are repeated periodically each half cycle of the laser field. Hence, in a multi- or few-cycle driving field all the generated XUV fields interfere giving rise to a $2\omega_{\mathrm{L}}$-spaced frequency-comb in the spectral domain. This can be illustrated using a simplified model [103, 104] by writing the n harmonic fields as a coherent superposition,

$$E(t) = \sum_{n=n_i}^{n=n_{\mathrm{co}}} A_n(t)\mathrm{e}^{-i\Psi_n(t)}, \tag{3.8}$$

where $A_n(t)$ and $\Psi_n(t)$ are (an assumed Gaussian) amplitude and the phase of the nth harmonic with n_i, the first considered harmonic and n_{co} the last one (cutoff). The phase $\Psi_n(t)$ includes the harmonic frequency, a carrier-envelope offset phase (CEP), a possible frequency chirp, as well as contributions originating from the generation process itself and the propagation through the medium (see Ref. [103] for more details). Due to the inversion symmetry in the recollision process, which is the case under typical experimental conditions using rare-gas generation media and single-color driver fields, the HHG spectrum contains only the odd harmonic components. A typical (Fourier-transform-limited) HHG attosecond pulse train constructed according to Eq. (3.8) is presented in Fig. 3.5. The duration of each interference peak further decreases with an increased number of harmonics in the sum which, according to Fourier's principle, leads to broad and continuous HHG spectra in the frequency domain.

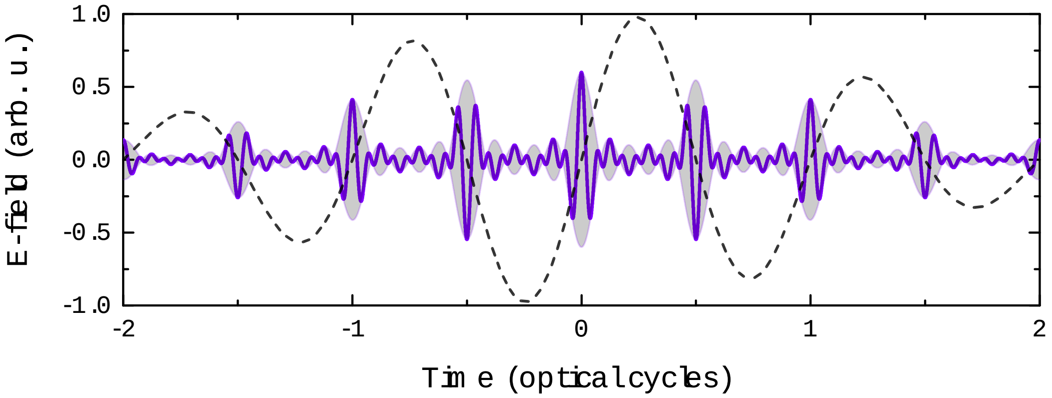

Figure 3.5: Simple model of an HHG attosecond pulse train in the time domain corresponding to a flat-top (plateau-like) frequency-comb (not shown) as observed in many experiments (compare Fig. 5.9 of chapter 5.5 or Ref. [105]). High-order harmonic electric-field modes assuming a Gaussian envelop are summed coherently over the odd harmonics $n_i = 7$ to $n_{\mathrm{co}} = 17$. This gives rise to temporal peaks (shaded violet) as short as a small fraction of the fundamental harmonic period of the driving laser (black dashed curve). The pulses are mutually phase-locked and emitted at each fundamental optical half cycle. As only odd integer harmonic components are considered, the sign of the pulses reverses between consecutive pulses (violet curve). In reality, the harmonic bursts emerge near the zero points of the fundamental field. For illustration purposes, this was included by a $\pi/2$ NIR CE-phase offset.

HHG can also be described in a fully quantum mechanical framework. In the quantum mechanical treatment also interference effects between continuum and bound wave packets are taken into account, which will not be discussed in this work. For this, the reader is referred to the original work [106] and to the review article [107] and references therein.

3.3.2 Phase matching

So far, only the microscopic, single-atom aspects of HHG have been discussed. In a bright HHG source the whole medium in the fundamental laser focus radiates collectively such that many of the generated individual fields for a given harmonic component interfere constructively in forward direction. For this to be achieved, the wave-vector difference, Δk, (traditionally denoted as phase mismatch), between the fundamental driver field and the harmonics has to be balanced. A general dephasing mechanism is the dispersion of NIR driver laser frequencies and XUV harmonic frequencies in the neutral medium (Δk_{disp}). The counterbalancing effect arises from the plasma dispersion in the medium (Δk_{e^-}). A significant additional phase term is of microscopic nature and due to the above mentioned different electron pathways of harmonic components, in this context sometimes termed dipole phase (Δk_{dip}). Finally, the Gouy phase of the Gaussian fundamental laser beam across the focus volume has to be considered (Δk_{Gouy}). The total phase mismatch is given by

$$\Delta k = \Delta k_{\mathrm{disp}} + \Delta k_{e^-} + \Delta k_{\mathrm{dip}} + \Delta k_{\mathrm{Gouy}}. \tag{3.9}$$

For minimized Δk (phase-matching condition), the harmonic intensity grows with the square of the number of participating atoms in a well-collimated beam with typical photon numbers per pulse of the order 10^6. In practice, achieving phase matching is challenging as several parameters, such as the gas medium, the gas density, the gas-cell position with respect to the focus, the beam-focusing properties, have to be optimized.

Chapter 4

Apparatus for multi-dimensional spectroscopy with XUV pulses

The advent of short-pulsed extreme ultraviolet (XUV) light sources for the investigation of ultrafast dynamical processes in matter triggered the development of novel time-resolved spectroscopy schemes and experimental apparatus.

Most time-resolved XUV spectroscopy schemes rely on a split-and-delay unit (SDU) to tailor at least two temporally correlated pulses to a specific system under study. An interferometric mirror setup for XUV light is technically highly demanding. The challenge is to combine an extremely high (up to sub-XUV-wavelength) interferometric resolution and stability with sufficient XUV transmission to preserve the pulse properties of the light source. A widely used geometry for pump-probe experiments with XUV high harmonic generation (HHG) and the fundamental near-infrared (NIR) laser field is based on a Mach-Zehnder-type setup. Here, holey mirrors (usually Ag coated mirrors containing a centric few-mm-diameter hole) are used to decouple and/or recombine the fields. In collinear [108–112], non-collinear [33], or non-concentric parallel [113] pulse propagation geometry, this scheme has proven to be a versatile tool for experiments on temporal and spatial aspects of the light-matter interaction with XUV and NIR fields. However, due to mechanical vibrations and fluctuations in the environmental conditions of the interferometer arms, these setups often suffer from considerable interferometric instabilities, which needs to be compensated for by an active-stabilization scheme [110–112, 114, 115]. Another, successfully implemented scheme comprises an inline two-component XUV-NIR split-mirror geometry based on a holey Ag mirror, which is equipped with an inner, dynamical (motorized), mirror coated for XUV radiation (quasi-monolithic design) [23, 54, 116–119]. The great benefit of the quasi-monolithic geometries is their compactness and their intrinsic high passive interferometric stability. It is important to note that, in general, an SDU for HHG-NIR two-color experiments needs to be combined with a suitable spatial bandpass filter.

So far, SDUs for single-color XUV-XUV pump-probe experiments with free-electron laser (FEL) or high-flux HHG light have been based on the geometrical splitting of the wavefront of an incoming beam into two time delayed replica pulses. At the free-electron laser facility in Hamburg, FLASH, grazing-incidence Mach-Zehnder-type SDUs (consisting of 8 mirrors) are available for user experiments [90, 120]. Other approaches use a compact half-mirror design with plane [121, 122], or back-reflecting spherical mirrors [123–125]. XUV-XUV SDUs are often equipped with an additional dynamical tilt-degree-of-freedom to keep the beam pointing exactly at the target position while tuning the optical path length and thus the time delay [126]. Recently, a novel collinear SDU design based on two interleaved gratings has been successfully demonstrated at FLASH [127]. A review about the present SDUs in operation for time-resolved experiments with FEL XUV, soft x-ray, and hard x-ray radiation is presented in [128].

Besides the split-and-delay unit, the spectrometer system is the second integral part of an XUV time-resolved spectroscopy beamline. Basically two detection approaches are possible and have been established today. The first one is based on the detection of charged particles and fragments and the measurement of their time-of-flight (TOF) [129] and the 2D [130] or 3D [19–21] momentum-distributions. This method aims to record ionization and dissociation pathways initiated by intense (ionizing) pulses, and, in principle, allows the reconstruction of the system's quantum state before light—matter interaction. Numerous experiments have successfully applied this detection technique in both strong-field XUV-XUV and XUV-NIR pump-probe schemes. The second spectroscopy approach is based on the detection of the XUV-photon beam itself after transmission through a target medium. Photo-absorption spectroscopy provides the information about the studied quantum system from spectral fingerprint structures. The method has been recently established in HHG-based pump-probe experiments, which use moderately strong (non-ionizing) NIR pulses to probe bound—bound transitions of the *intact* (laser-dressed) target system in the XUV photo-absorption spectrum [23, 131, 132]. However, this method has not yet been combined with strong-field XUV-XUV time-resolved experiments.

In the course of this work, a whole new beamline for time-resolved XUV spectroscopy experiments was constructed, built up, and commissioned. The aim was to realize a versatile hybrid system for first XUV multi-dimensional spectroscopy experiments operable at two different types of XUV light sources: the laser-driven broadband attosecond HHG-source at the Max-Planck Institute for nuclear physics (MPIK) in Heidelberg, and the strong-field SASE free-electron laser in Hamburg (FLASH) at DESY. Thus, the setup ought to combine a broad XUV photon-energy coverage ($\sim$20 eV to 110 eV), high variability in the pulse configurations (XUV-only and XUV-NIR multi-pulse schemes), sub-XUV-wavelength interferometric stability, and compactness and transportability. The detection scheme relies on measuring the XUV photo-absorption spectrum, which has been successfully implemented at the MPIK in Heidelberg in recent HHG experiments [23, 54]. The integration of a commercial TOF spectrometer for electrons, ions, or charged fragments is considered in the mechanical beamline design as an add-on instrument. This chapter describes the technical aspects and challenges of the XUV multi-dimensional spectroscopy beamline developed in this work.

4.1 Instrumental setup for HHG experiments

For time-resolved four-wave-mixing experiments with extreme-ultraviolet (XUV) high-harmonic generation (HHG) and intense near-infrared (NIR) laser fields sub-7-femtosecond, 1 mJ range laser pulses are available at a 4 kHz repetition rate. See chapter 3.2 for further technical information on the laser system. When focused down to a spot size of $\sim 50\,\mu\text{m}$ ($f = 500\,\text{mm}$), these pulses reach peak intensities in the $10^{14}\,\text{W/cm}^2$ regime.

For the XUV high-harmonic generation, the femtosecond NIR beam is focused into a gaseous conversion medium. A theoretical introduction and general aspects of phase matching in HHG can be found in chapter 3.3.2. Usually, rare gases are the favorable HHG generation media because of their high ionization potentials. As rare gas atoms are resistant against anything but the highest field intensities, the freed electrons (step 1, ionization) gain on average the highest possible amount of kinetic energy while being accelerated by the laser field in the continuum (step 2). Hence, high cutoff photon energies are reached in the emitted XUV light upon recombination (step 3). However, the cross-section for recombination decreases with the size of the atom. This imposes a trade-off between XUV photon energy and photon flux. While argon, krypton, and xenon—the large rare-gas atoms with a smaller ionization potential—are the most efficient HHG media, neon and helium allow the generation of the highest photon energies. For the presented experiments argon and neon was used at backing pressures of 30 to 80 mbar (atom density $\sim 10^{17}\,\text{cm}^{-3}$) in a cylindrical 2 mm inner diameter cell with 100 µm diameter entrance and exit pinholes for the focused laser beam. To optimize for HHG phase matching, the cell can be 3d manipulated using motorized XYZ micrometer stages.

To avoid re-absorption and scattering of XUV radiation in ambient air, the whole experimental setup is mounted under vacuum conditions with base pressures below 10^{-3} mbar in the vicinity of the HHG and target gas inlets and below 10^{-6} mbar in the remaining part of the beamline. The vacuum housing consists of three large chambers (based on 250 mm diameter stainless steel tubes) and several smaller cross chambers that, being connected to each other by small extension tubes, serve as differential pumping stages. All chambers of this setup are evacuated by turbomolecular pumps. Typical gas loads during HHG are 0.1 mbar l/s.

Fig. 4.1 presents an overview of the experimental apparatus as employed in the "HHG mode" for many experiments [23, 54, 55, 62, 63]. For the presented four-wave-mixing experiment only slight modifications in the two-color bandpass filter were made. In the following only a brief description of the HHG-NIR experimental geometry will be given which adheres to the original dissertation [94] and Refs. [55, 133]. The technical modifications for the "FEL mode" including a different split-mirror geometry, further differential pumping sections to maintain base pressures below 10^{-8} mbar when connected to the ultra-high vacuum beamline at the FLASH facility, and several beam steering and diagnostic instruments, will be explained further below in section 4.2.

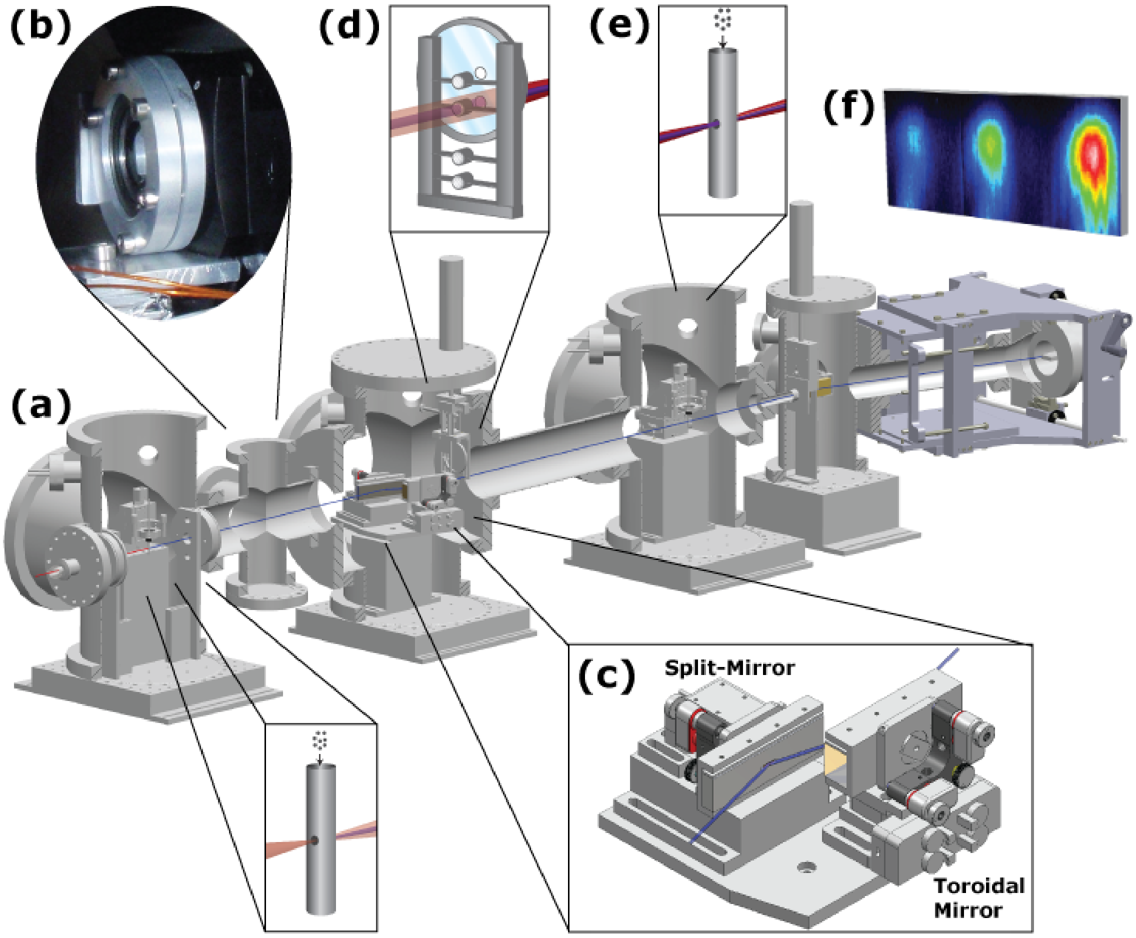

Figure 4.1: Overview of the experimental apparatus as assembled for HHG experiments. The first chamber (a) contains the gas cell for HHG. Further downstream the NIR beam intensity can be controlled using a piezo-driven iris aperture (b). The second large chamber is the central "mirror chamber" including the holey-mirror SDU (c) in combination with a toroidal (re-)focusing mirror, as well as a two-component filter geometry (d) (see description in the main text). The target cell for the two-color light—matter interaction is located in the third large chamber (e). The beamline endstation is a high-resolution VLS-grating-based spectrometer with an XUV-sensitive CCD camera (f). Reprinted from [133].

The HHG-NIR experimental geometry relies inherently on the different angular divergence of XUV ($\sim 1\,\mathrm{mrad}$) and NIR radiation ($\sim 15\,\mathrm{mrad}$). Having passed through the first large vacuum chamber (the HHG chamber), a remote-controlled, piezo-driven iris diaphragm is employed to adjust the NIR-photon flux without affecting the sub-2 mm diameter, almost collimated HHG beam. The instrument is based on a high-repeatability (0.002 degree) rotation stage using a home-built mounting adapter for commercial iris diaphragms. The assignment of iris steps to NIR intensities is done for each experiment individually, in retrospect, on the basis of detected intensity-dependent spectral features such as the Autler-Townes splitting [39].

The second large vacuum chamber, the so-called mirror chamber, contains the SDU and

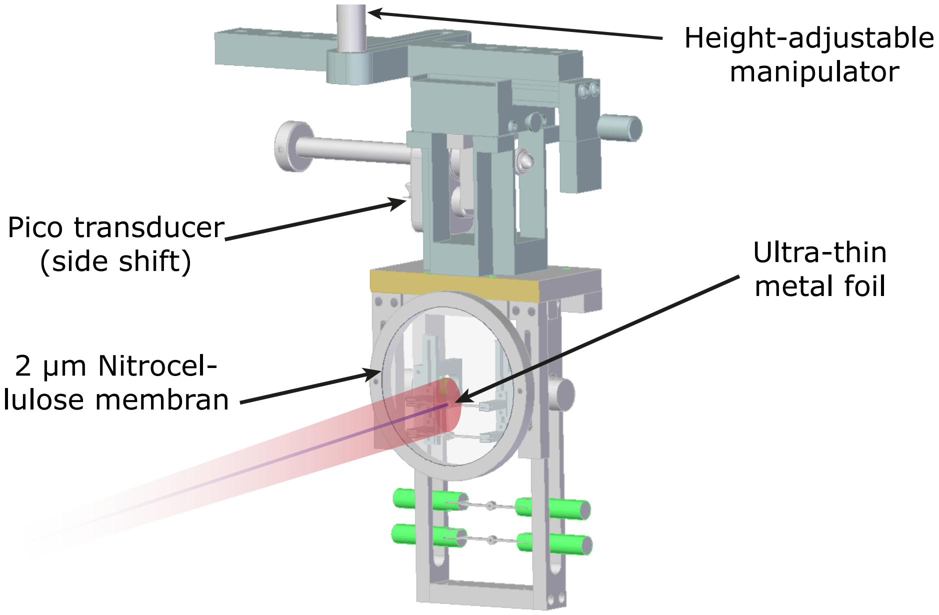

Figure 4.2: 3d model drawing of the two-color filter assembly. The device combines a perforated nitrocellulose membrane spanned on a 2-inch diameter ring with an ultra-thin Al foil placed in the central pinhole. This geometry allows to spatially separate an XUV-NIR light beam with differently diverging beam components. The filter assembly is mounted in the vicinity of the toroidal mirror and can be retracted.

a re-focusing 15-degree grazing incidence, Au-coated toroidal mirror for the 2f-2f image formation of the NIR focus and the HHG source from the first large chamber onto the target atoms in the third large chamber. The toroidal mirror provides ∼50% reflectivity for XUV radiation between 20 and 110 eV and almost fully preserves the incident NIR pulse spectrum. The SDU comprises an annular holey-mirror based two-part split mirror also hit under a 15-degree grazing angle of incidence with an inner, dynamical Au-coated mirror and an outer Ag mirror optimized for intense optical and NIR pulsed-laser radiation. An interferometric stability of about 10 as was determined with this setup by two-beam interference of a focused wavelength-stable helium-neon laser beam reflected from both the outer and the scanned inner mirror.

In order to fully separate the reflected HHG and NIR beam components spatially, a two-part spectral bandpass filter is employed of which the outer annular part consists of a 2-µm thin nitrocellulose membrane (1.2 mm centric hole) to further purify the NIR light. The inner part is a 0.2-µm-thin aluminum foil (1.2 mm diameter) that transmits about 50% of the XUV photons between 20 to 70 eV [134]. The filter assembly is mounted such that the inner Al foil overshadows the inner XUV mirror of the SDU. In order to maintain four-wave mixing, it is crucial that the central Al foil transmits a residual NIR-photon intensity on the order of 1 to 10%, which can be considered as a perturbative NIR-replica pulse that remains locked in temporal overlap with the XUV. The NIR transmission is due to small holes or other imperfections in the extremely fragile foil (e.g. created during the manufacturing process and/or mechanical strain while assembling the custom-made filter arrangement). The experimental control of the perturbative NIR-light flux is not possible with this setup. Only by comparing the experimental results with corresponding theoretical calculations the applied NIR-light flux can be inferred, in retrospect. For near-future experiments with a novel multi-pulse SDU design (see section 4.3), both time-delay and intensity control of a third experimental pulse will be possible.

In the third large vacuum chamber, the refocused beam by the toroidal mirror passes through the target cell, where the two-color light—matter interaction takes place. In order to fully separate the XUV optical response of the target atoms from NIR stray light, additional metal filters are placed into the travel path right before the XUV spectrometer. The latter is the endstation of the beamline and consists of a variable-line spacing (VLS) grating in combination with an XUV-sensitive CCD chip. The spectral resolution at around 50 eV photon energy is about 50 meV. See section 4.2 and the original dissertation [94] for further technical information on the spectrometer system.

4.2 Instrumental setup for SASE-FEL experiments

For the operation with XUV SASE-FEL radiation at FLASH, the beamline setup is equipped with additional instruments as shown in the overview in Fig. A.1 of appendix A. First FLASH experiments were performed at the user port beamline 2 (BL2) in 2016 integrating the ellipsoidal focusing mirror ($f = 2\,\mathrm{m}$) and the in-house SDU [90] into the setup. The apparatus includes an own dual-mirror SDU and a beam re-focusing mirror, but builds on the FLASH in-house SDU as an instrumental fallback.

In the “FEL mode” the beamline includes a vacuum interlock system based on pneumatic valves to protect the FEL from accidental venting. Furthermore, to maintain ultra-high-vacuum (UHV) base pressures (below $10^{-8}\,\mathrm{mbar}$) during the experiments, an efficient two-stage differential pumping system is integrated between the experimental target chamber and the vacuum interface with the FEL machine. On a total length of 392 mm the differential pumping system achieved differential pressures of almost 5 orders of magnitude in the HV-UHV pressure regime even under highest gas loads of $\sim$1 mbar l/s in the experimental target chamber. Typical experimental gas loads are on the order of 0.1 mbar l/s. The molecular conductance between the pumping sections is limited by 100-mm long tubes with diameters of 5 and 10 mm to match the beam size of the focused and thus converging FEL beam. Each chamber is connected with turbomolecular pumps (2000 l/s and 300 l/s pumping speed class).

The target-gas cell itself is a 2-mm inner-diameter tube made of stainless steal or MACOR® with two 100 µm entrance and exit pinholes for the focused beam. It is mounted on a motorized closed-loop XYZ positioner with sub-µm repeatability. For the positioning of the cell exactly into the beam focus, the fluorescence image of a phosphor screen attached to the cell is recorded using a microscope camera. The cell also comprises a heating jacket for experiments on targets with small vapor pressures under room temperature, such as halogenated hydrocarbon molecules. The heating prevents the cell

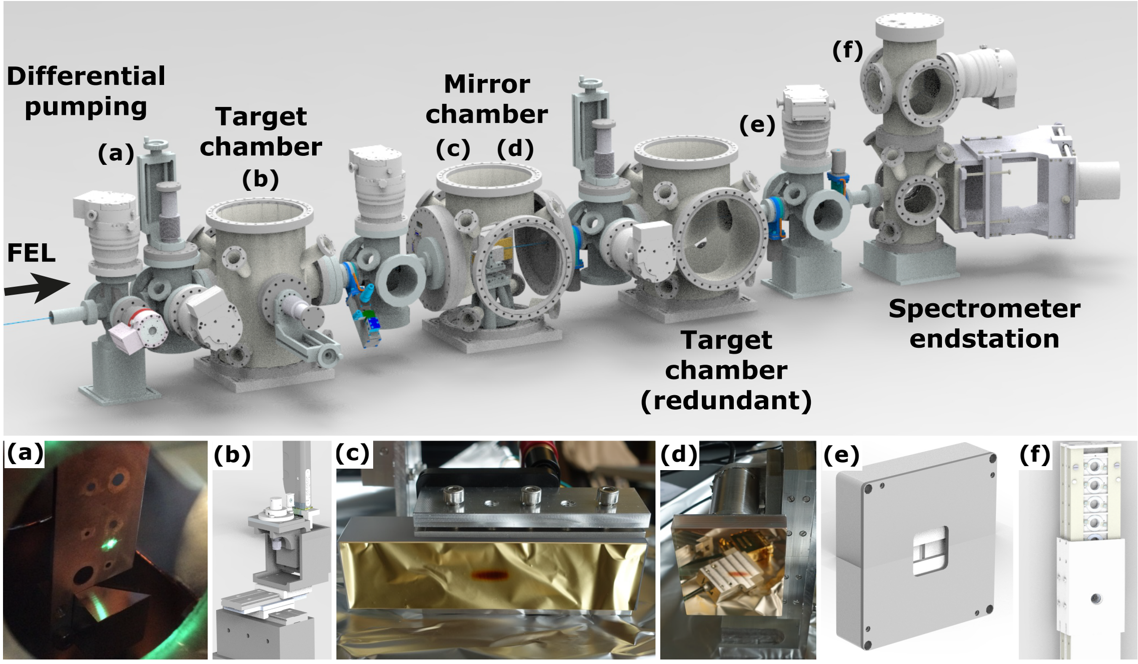

Figure 4.3: Overview of the experimental vacuum apparatus. The FEL beam is focused into the first large chamber (target chamber) downstream of a short differential pumping section and a panel of apertures for diagnostic purposes coated with a greenish shining phosphor when irradiated (a). The 3d model design of the target cell and the mounting unit is presented in (b). In Figs. (c) and (d) the toroidal re-focusing mirror and the dual-mirror split-and-delay unit are shown. Clearly visible is a brownish carbon layer on the Au mirror surfaces deposited during high-intensity XUV exposition and leading to decreasing mirror performances. The novel spectrometer endstation incorporates a 2d motorized entrance slit (e) and a highly-flexible assembly for many different beam attenuators (f).

from clogging in the pinholes. A 3d model drawing of the novel cell design is presented in Fig. 4.3(b).

The experimental vacuum chamber also is designed for the operation of a commercial ion time-of-flight (TOF) spectrometer [135] with a small-bore gas-inlet capillary as an option to the target cell. For upcoming experiments at FLASH, it is planned to measure the produced ion yield by the (non-linear) interaction of two or more FEL pulses with a target gas for a more efficient and accurate determination of the focus and the spatial pulse overlap position. The ion yield reaches a sharp maximum in the pulse overlap. Moreover, by scanning the temporal pulse delay, temporal information on the FEL pulse characteristics can be probed [124]. The TOF spectrometer will be mounted on an XYZ manipulator with precision spindle drive and can be completely retracted.

As in the "HHG mode" (see Fig. 4.1), the beamline comprises three large main vacuum chambers. The FEL beam is focused into the first large chamber with a focal spot size of approximately 25 µm. The central chamber of the setup, the mirror chamber, includes a 15-degree grazing incidence dual-mirror SDU with tilt degrees of freedom for the correction of the geometrical beam walk-off when tuning the delay and the toroidal mirror for the 2f–2f imaging of the FEL focus into the third large chamber. The dual-mirror system is one mirror pair of the four-quadrant split mirror designed for multi-dimensional spectroscopy, as described in section 4.3 of this chapter. Both the first large chamber, as well as the third large chamber can, in principle, be used as experimental target chambers incorporating a gas cell. Aside from the dual-mirror SDU and the bandpass filter, this refocusing geometry resembles exactly the configuration as applied in many experiments with our focused NIR fundamental laser and the HHG source in the first large chamber and the target sample in the third one (see section 4.1). However, due to vacuum contamination by hydrocarbons in the mirror chamber and/or because of limitations in the surface characteristics of the Au-coated toroidal mirror (surface flatness: $\lambda/10$, surface roughness: 0.5 nm rms), a proper focus-to-focus imaging obtaining sufficiently high throughput for FEL-pump—FEL-probe experiments turned out to be *not* possible. Our contingency strategy builds on employing the FLASH in-house SDU (see section 4.2.1) for the preparation of pump and time-delayed probe pulses upstream of the beamline setup and using the first large chamber as an experimental target chamber. The task of the dual-mirror SDU and the toroidal mirror in this configuration is simply the beam transportation of the FEL—target response signal along the optical setup towards the spectrometer endstation. The corresponding optics scheme is described in detail in section 4.2.2. Photographic pictures of the dual-mirror SDU and the toroidal mirror taken after the experiments are presented in Figs. 4.3(c,d) showing considerable radiation damage on the mirror surfaces.

The spectrometer endstation is based on a dispersive grating [136] with a variable line spacing (VLS) for the imaging of the XUV/soft x-ray spectral region between ~20 and 110 eV onto a flat spectral plane. An XUV-sensitive CCD camera [137] with 1340 spectral pixels ($20 \times 20\,\mu\mathrm{m}^2$) is mounted on a mechanical translation stage which allows to shift the 26.8 mm sized camera chip along the spectral plane of ~ 110 mm length. The design is adapted from a previous setup and described in detail in the dissertation [94]. The original design was optimized for the detection of weak-field HHG radiation, where an efficient light collection is crucial. Hence, in this case, the opening of the target cell itself is used as a spectrometer entrance slit. For the spectroscopy of high-flux FEL radiation the setup is equipped with a two-dimensional (2d) slit system [138] consisting of 4 piezo-driven (sub-µm resolution and repeatability) blades with a maximum opening of $20 \times 20\,\mathrm{mm}^2$. The 2d slit allows to form a rectangular aperture in any size down to $\sim 1\,\mu$m in x- and y-direction at any position in the transverse plane of the beam. A 3d model drawing of the slit is presented in Fig. 4.3(e). For the presented experiments the benefit of the 2d slit is the control over the incident light flux, the spectral resolving power ($\lambda/\Delta\lambda \approx 940$ determined from the measurement and characterization of the He 2s2p Fano lineshape during the experimental campaign [139]) and the spatial coverage of the beam profile. This is in particular instrumental when two or more radiation sources are imaged by the spectrometer at once, as for example pump and probe beams. Further beam attenuation is accomplished by a mechanical home-built filter assembly that allows to insert many different attenuation foils (see Fig. 4.3f).

For diagnostic purposes a panel of differently sized circular apertures with a phosphor coating around the cutting edges can be inserted into the beam at several sections of the beamline. As demonstrated in the photographic picture in Fig. 4.3(a) the greenish fluorescence light allows to monitor FEL beam position and shape.

4.2.1 The in-house split-and-delay unit at FLASH

The in-house split-and-delay-unit (SDU) at FLASH is integrated into BL2 and can be inserted into the FEL beam path by heavy-duty translation stages. The optical layout consists of eight grazing incidence C-coated plane mirrors optimized for high reflectivity in a broadband XUV/soft x-ray spectral range and arranged in a Mach-Zehnder-type interferometric configuration. Two interferometer arms are created by geometrically splitting the wavefront of an incoming beam into two partial beams at the rear edge of a mirror that is partly placed into the beam. The optical length of one of those arms can be varied by a stepper-motor driven delay stage before recombining the beams again. Technically, the parallelogrammatic optics arrangement avoids a lateral walk-off of the beam pointing during the delay manipulation. However, the delay mirrors parasitically tilt during displacement. To compensate for this walk-off the mirrors are equipped with additional (re-)tilt actuators. A sketch of the optics design inside the SDU is given in Fig. 4.4.

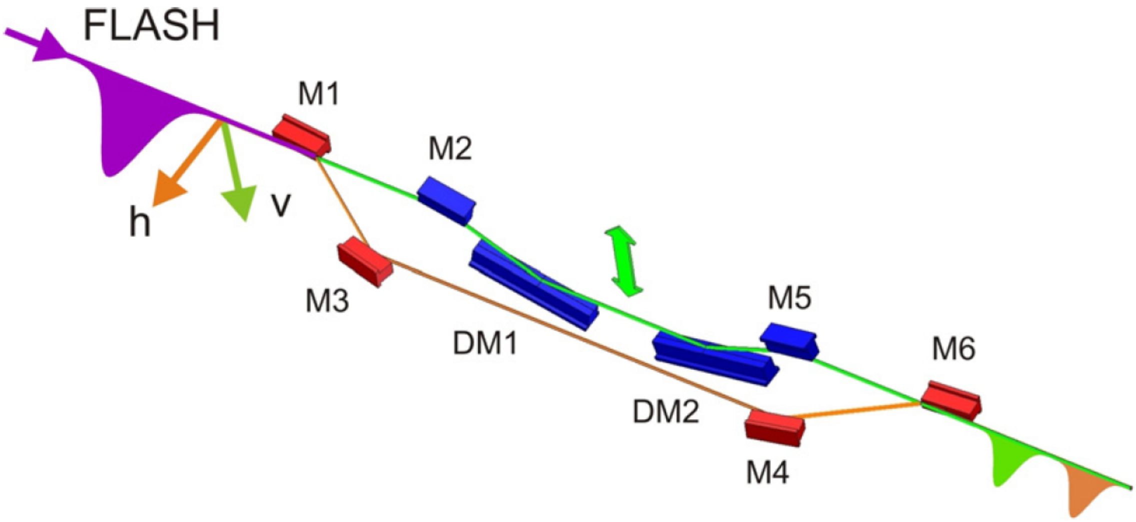

Figure 4.4: Optical layout of the in-house SDU integrated into BL2 at FLASH. The mirrors depicted in blue belong to the variable interferometer arm and the red mirrors to the fixed arm. The first mirror (M1) and the last mirror (M6) split and recombine the beam. The mirrors DM1 and DM2 are part of the variable delay line. These mirrors can be shifted upwards and downwards, respectively, to set the time delay. Reprinted from [90].

The setup provides an entire delay range of 18 picoseconds that can be scanned with subfemtosecond temporal resolution. The interferometric stability, i.e. the delay jitter due to ground vibrations in the interferometer arms, amounts to 0.28 fs [90]. Further technical details can be found in Refs. [90, 128, 140].

Normally, a closed-loop encoder system provides accurate time-delay feedback and the option to move to a specific delay position with a $\leq 1\,\mathrm{fs}$ repeatability [90]. During our experimental campaign in June 2016 the encoder was out of order. By feeding the actuator unit for the stepper motor with 5 V direct current signals for each step via our own analog-to-digital converter and a self-developed LabVIEW routine, an open-loop operation was possible, however, without having the information of the interferometric pulse-overlap position. The pulse overlap was inferred in retrospect based on a “coherence spike” observed and reproduced in the recorded absorption data (see chapter 6). A relative delay of 40 fs corresponds to 1000 motor steps [141].

4.2.2 The optical layout

As discussed in the foregoing sections, the preparation of pump and time-delayed probe pulses is accomplished using the FLASH in-house SDU at BL2. A snapshot of the split and delayed partial beams taken from a phosphor screen behind the SDU is shown in Fig. 4.5.

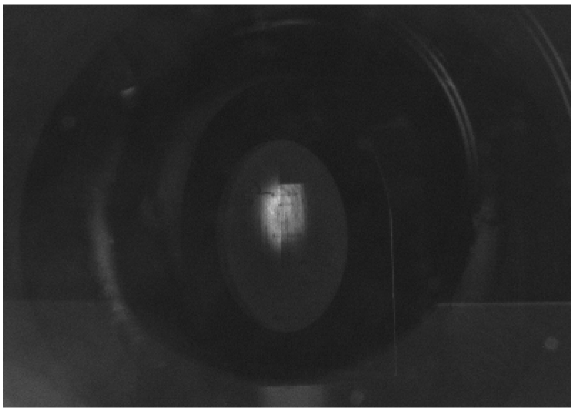

Figure 4.5: Fluorescence image of pump (right) and time-delayed probe (left) partial beams taken from a retractable phosphor screen behind the FLASH in-house SDU right before the ellipsoidal focusing mirror. The FWHM beam diameter is on the order of 10 mm.

Having passed the SDU, pump and probe partial beams are focused into the experiment by a grazing-incidence C-coated ellipsoidal mirror ($f = 2\,\mathrm{m}$). The two beam components enter the target cell side-by-side split along the vertical dimension (see Fig. 4.5). However, for the spectroscopy of both pump and probe, separately, on the same grating (vertical grooves) the beam has to be converted into up-down orientation behind the target. This can be accomplished by an additional spatial wavefront splitting along the horizontal dimension using our dual-mirror SDU (see further technical information in section 4.3). The beam is now divided into 4 partial beams, in total. By rotating the two mirror segments in opposite directions, the transmitted pump and probe signals can be steered onto the spectrometer slit, separately, on top of each other. Fig. 4.6 shows a sketch of the optical beam path inside the experimental apparatus and the optical instruments.

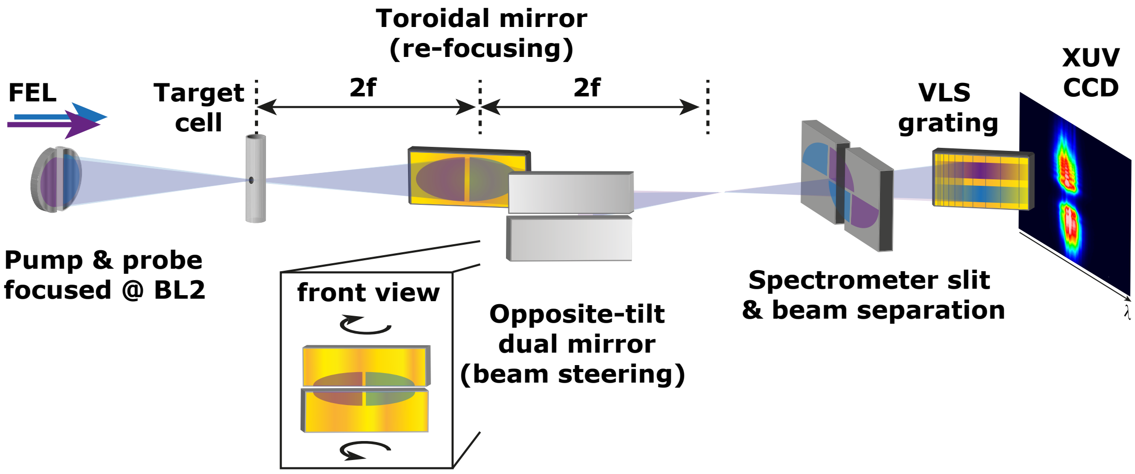

Figure 4.6: Optical layout of the experimental setup as employed for the FLASH beamtime 2016. The FLASH in-house SDU (symbolically represented by the mirror halfs on the left hand side) and the ellipsoidal focusing mirror (not shown) are implemented into the setup to create pump (blue beam, variable mirror) and probe (violet beam, fixed mirror) pulse pairs. FEL—target interaction takes place in the target cell in the first focus. A toroidal 2f–2f imaging mirror and a plane dual mirror guides the signal beam through the setup onto the spectrometer entrance (2d) slit. The two have-mirrors are tilted in opposite directions such that pump and probe beam components form two spatially (along the vertical dimension) separated sources on the spectrometer slit. This allows to record the dispersed signal of both pump and probe simultaneously, with the XUV grating and CCD-camera-based spectrometer system.

4.3 A novel XUV multi-pulse split-and-delay unit

For first near-future multi-dimensional spectroscopy experiments in the extreme-ultraviolet (XUV) spectral region, a novel split-and-delay unit (SDU) was developed. Together with the spectrometer scheme, the SDU can be considered as the heart of the beamline. The SDU setup ought to be well transportable and flexible for both radiation sources intense XUV free-electron lasers (FELs) and combined high-harmonic generation (HHG) plus intense near-infrared (NIR) lasers. Also due to the high technical demands on the interferometric design regarding the temporal resolution and the XUV transmission, such experiments have not yet been realized.

The mirror setup consists of four quadratic plane mirrors arranged in a passively phase stable, quasi-monolithic structure [142]. For XUV radiation, only mirrors optimized for a grazing angle of incidence provide sufficiently high reflectivity over a broad spectral range. A good compromise between a reasonable $\sim 50\%$ reflectivity for photon energies between $\sim$20 and 110 eV [134] and a compact design is provided by 15-degree grazing-incidence mirrors with a 30 nm Au-coating (roughness $< 0.2\,$nm rms) and a surface size of $50 \times 30\,\text{mm}^2$. To keep the loss of photons through the $\sim 200\,\mu$m gap between the mirrors when arranged to a four-quadrant geometry (see Fig. 4.7a) as low as possible, the usual protection bevels are avoided. Each substrate is attached on a piezo-driven multi-axis tip-and-tilt actuator unit. This device builds on a piezo-driven tripod platform [143] for tilting movements around a pivot point in two dimensions (angles Θ_X, Θ_Y) with a 0.1 µrad closed-loop resolution that is stacked on a piezo-driven translation stage [144] with a 250 µm travel range and 0.7 nm closed-loop resolution (Z direction). These two instruments in combination for three of the four mirror quadrants allow to introduce sequences of four replica pulses with a maximum relative delay of $\sim$ 850 fs. Fig. 4.7 presents a 3d model drawing of the assembled four-quadrant SDU as installed in the mirror chamber and the dynamical multi-axis mirror mount. When focused, the pulses are arranged in a non-collinear "boxcar" geometry as known from multi-dimensional spectroscopy experiments with visible and IR light [28], where one of the four pulses serves as a local oscillator (reference) field for heterodyne signal detection (see chapter 2.6).

The major challenge accompanying this kind of interferometer system is to preserve the beam quality behind the setup. Normally, in large-scale devices as the ones permanently installed at free-electron lasers [128], therefor thick and massive mirror substrates are used for better surface flatness and resistance against mechanical strain. The optical delay in those setups is usually achieved with high-load stepper motors providing a temporal limit of $\sim$1 fs in the interferometric delay resolution. For multi-dimensional spectroscopy experiments on XUV-dipole transitions, a temporal resolution on the order of 10 attoseconds is needed, which can only be realized with piezoelectric transducers. To not overload our piezo actuators, a lightweighted (100 g order of magnitude) design for mirrors and mirror holders was required. The mirrors are permanently glued to an Al-adapter plate that connects to the cylindrical tripod head. To prevent the substrates from mechanical strain and to preserve the high surface flatness ($\lambda/20$ at 633 nm), locally, in the irradiated mirror region (see Fig. 4.7b), three adhesive contact points in the "in-active", non-irradiated corner points on the mirror's rear face were chosen.

The piezo actuators mounted below a mirror quadrant operate in a coupled mode. During the displacement of the mirror in Z-direction by the (one-axis) translation stage alone the partial beam loses spatial overlap with the target and the other partial beams in the focus. This walk-off is compensated for by the movement of the tilt actuators. The pointing information is provided by a feed-forward spreadsheet which must be prepared manually before each experiment. The spreadsheet contains the actuator positions for beam overlap (observed e.g. with a phosphor screen) at minimum and maximum delay. The correction values for the beam miss pointing during the delay scan are determined by linear interpolation. A detailed description of the programmatic implementation is presented in the master's thesis in Ref. [139].

The whole mirror assembly is mounted on a hexapod alignment platform [145] which can be commanded to perform fine-resolved closed-loop translation and tilt movements around arbitrary pivot points along the full three-dimensional workspace. The platform is used for beam steering purposes and to change the splitting ratio and hence the relative intensities of the four reflected partial beams. During the experiment the hexapod is inactive to avoid additional ground noise.

The interferometric (i.e. phase-noise) stability is experimentally determined to be below 20 attoseconds rms-noise during operation of all vacuum pumps in our home laboratory

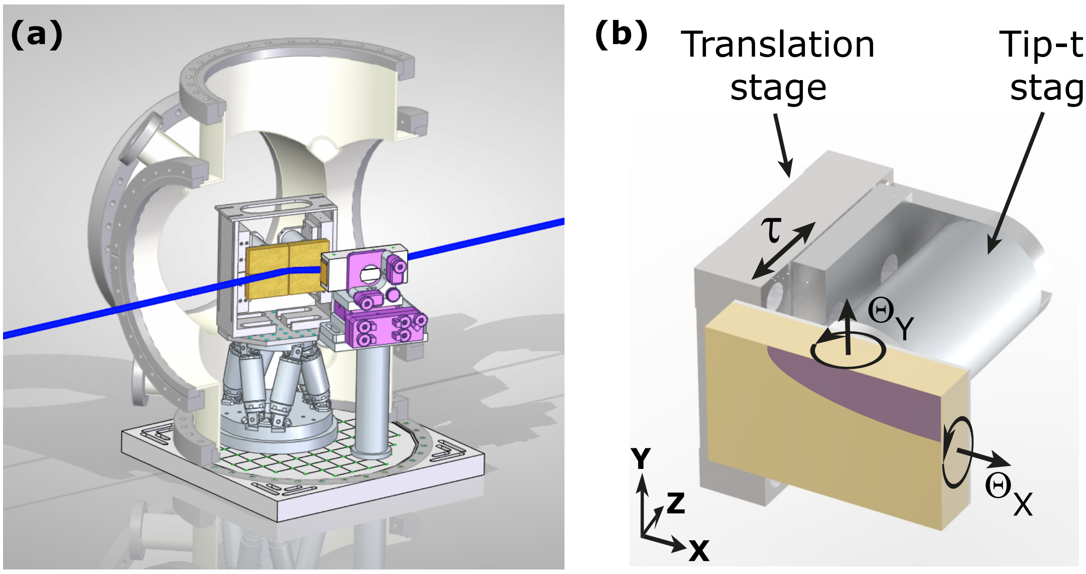

Figure 4.7: 3d model drawing of the split-and-delay unit for four-pulse sequences. Panel (a) shows the mirror chamber including the SDU mounted on a hexapod alignment platform and a toroidal re-focusing mirror. Three of the four mirror quadrants are motorized by a multi-axis tip-and-tilt piezo actuator system [panel (b)].

in Heidelberg. The measurement procedure is similar as for the annular two-split mirror (see the previous section 4.1). A helium-neon laser beam reflected from two mirror quadrants was superposed on the same focal point by means of the toroidal mirror. Changing the delay position continuously, an interferometric (sinusoidal) intensity pattern was detected on the common focus. The root-mean-square error of the phase of this intensity modulation corresponds to the interferometric stability. The interferometric stability sets a temporal limit to the observation of coherent coupling dynamics for near-future XUV multi-dimensional spectroscopy experiments. The time interval of 20 as corresponds to a quarter of the temporal period of an optical cycle at 50-eV photon energy, which promises the capability for time-resolved measurements of coherent ground—excited coupling signatures due to 2s-inner shell and two-electron transitions, e.g. in neon, as discussed in chapter 2.6.

The beamline is also designed for the operation of a second, parasitic spectrometer system for the simultaneous detection of reference spectra *before* the laser—target interaction. To this end, one of the four mirror quadrants (the one for the low-intensity local oscillator field) can be replaced by an Au-coated plane grating. In this concept, the zero*th* diffraction order enters the target cell without any change in the experimental trajectory and only minor changes in its pulse characteristics, while the first order is diffracted into a second spectrometer arm. Ray-tracing calculations were performed to construct the setup and to determine the spectrometer resolution to be sub-1 eV (employing a common constant-spacing grating) [146], which renders it suitable for applications with quasi-continuous HHG radiation. The application at the FEL however is impeded, on the one hand, by the dominant spectral chirp as observed during the presented experiments and, on the other, by the sharply-spiked nature of FEL spectra that will not be resolved employing a conventional contant-spacing grating. The setup is currently being commissioned. A 3d drawing is shown in Fig. 4.8.

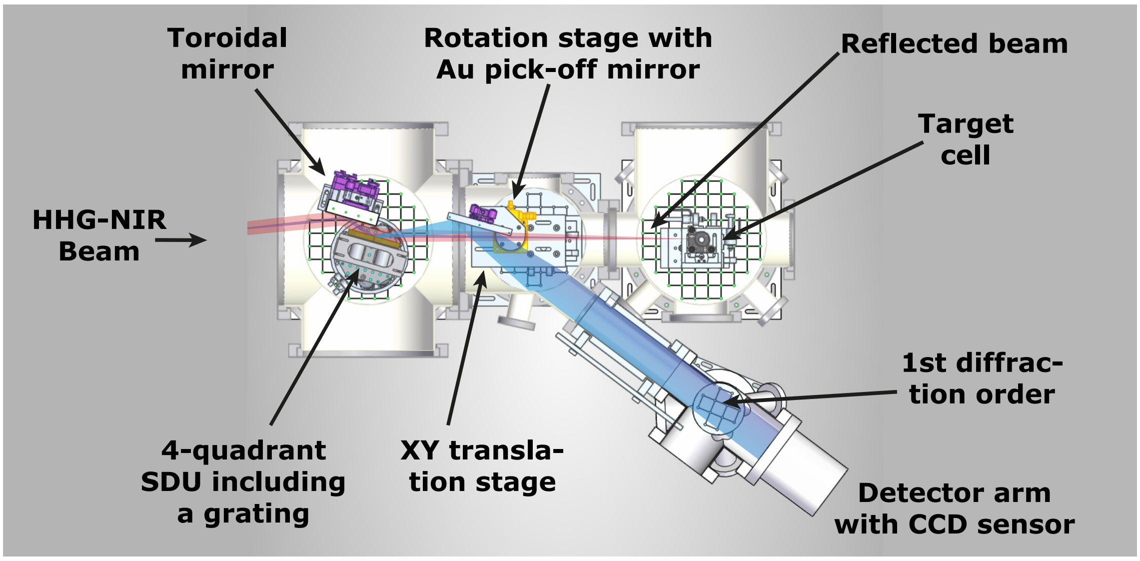

Figure 4.8: Top-view of a novel parasitic spectrometer system for the online measurement of reference spectra before the beam transmits through the target medium for future experiments. One of the SDUs mirror quadrants is a grating whose first diffraction order is guided to an XUV CCD-sensor via a pick-off mirror, while the zero*th* order is reflected into the target cell together with the other replica pulses. The parallel detection scheme allows for a more accurate and clean determination of the optical density according to Beer's law avoiding spectral modifications due to pulse-to-pulse fluctuations.

Chapter 5

Attosecond transient absorption with multiple laser fields

This chapter is devoted to the 1-fs-scale dynamics of correlated electronic wave packets formed through superposition of inner-shell states. An inner-shell state is a non-stationary quantum state created when an electron from an inner sub-shell is propelled to an outer one leaving a hole behind in the inner electronic distribution around the nucleus. The presence of the sub-valence vacancy (or the hole) causes modifications in the excited orbital due to the changed effective core attraction due to different shielding by the remaining electrons. The subsequent non-equilibrium dynamics involve a high degree of correlation between the relaxing electron and the sub-valence hole (seen as a quasi particle) in particular when a large quantum mechanical overlap between the hole and the excited orbital is given. This is for example the case when 2s inner-shell electrons are excited to higher-lying states (principle quantum number $n \geq 3$) with s-angular momentum in the valence shell. However, due to the conservation of angular momentum and parity during absorption of a photon, the preparation and the probing of such states is not directly possible by conventional spectroscopy approaches based on *one-photon* transitions.

Apart from the scientific potential for fundamental studies on (multi-)electron correlation dynamics, the observation, the quantum mechanical control by lasers, and the understanding of inner-shell-to-valence excited systems are central goals in the field of ultrafast science. The controlled preparation of such states is the key ingredient for novel (near-future) multi-dimensional spectroscopy approaches [30, 31] probing *site-selective* information when applied to (larger) molecules.

A coherent inner-shell wave packet made of excited states of different orbital quantum numbers, $l = \mathrm{s}, \mathrm{p}, \mathrm{d}$, can only be launched in the presence of multiple laser fields (due to dipole selection rules). Exactly this was achieved by well-controlled high-harmonic extreme-ultraviolet (XUV) and near-infrared (NIR) laser pulses as a result of non-linear (four-wave mixing) light—matter interaction in the experiments presented in this chapter.

The purpose of this chapter is to convey the concept and the scientific findings of the developed four-wave-mixing scheme that creates and measures s, p, d-orbital inner-shell wave packets. The chapter is based on an already published work [55] targeting neon as a first (proof-of-principle) model system where the basic principle and the key results are described. Beforehand, a brief overview about wave-packet interferometry, recent related studies in helium and the general aspects of the spectroscopy technique will be presented.

5.1 Quantum wave-packet interferometry

A wave packet in general is a coherent superposition of at least two excited states of a quantum system, $\Psi_i(t) = |i\rangle \exp(-i\omega_i t)$ and $\Psi_j(t) = |j\rangle \exp(-i\omega_j t)$ with $\omega_{i,j} = E_{i,j}/\hbar$. Since each state has a different energy, the constructive and destructive interference among the states leads to periodic wave-packet dynamics between the turning points of the binding potential giving rise to a beating in the signal-intensity trace

$$\begin{aligned} I_{\mathrm{sig}}(t) &\propto |a_i(t)\Psi_i(t) + a_j(t)\Psi_j(t)|^2 \\ &\propto a_i^2 + a_j^2 + 2a_i a_j \cos[(E_j - E_i)t/\hbar]. \end{aligned} \tag{5.1}$$

Therein the coefficients $a_i(t)$ and $a_j(t)$ describe the exponential decay of the transient with a lifetime time corresponding to the inverse decay rates $\tau_{i,j} = 2\hbar/\Gamma_{i,j}$ (provided there is no further loss of coherence e.g. due to interactions with the environment or ionization). The time period of this motion is determined by the energy difference between the states $T = h/\left|E_j - E_i\right|$. Fig. 5.1 visualizes this motion associated with the coherent superposition of eigenstates of a Hydrogen-like ($1\mathrm{e}^-$) Coulomb potential.

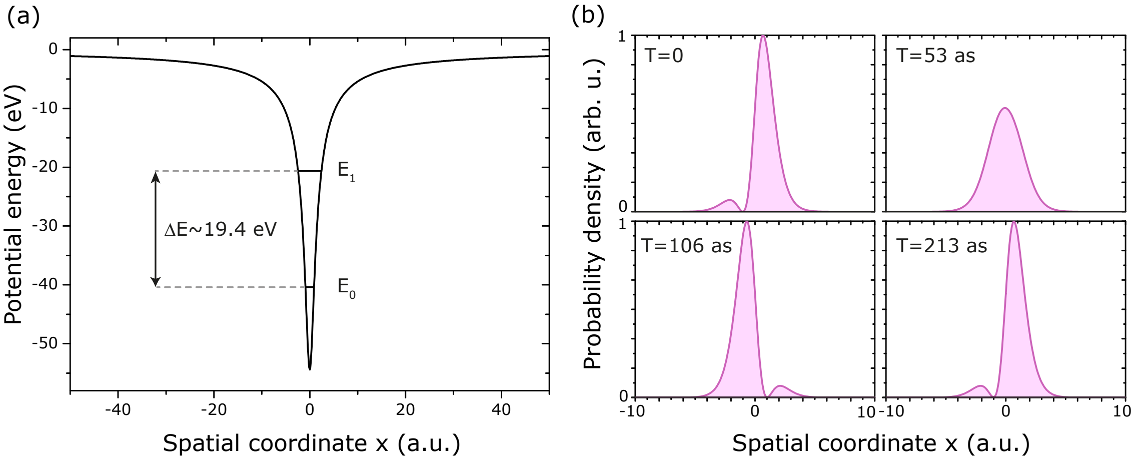

Figure 5.1: Temporal evolution of a coherent wave packet involving the two lowest eigenstates of a soft-core Coulomb potential [147, 148], $V(x) = -2/\sqrt{x^2+1}$, propagated in time numerically via the time-dependent Schrödinger equation. Both the soft-core potential as well as the numerical framework for related time-dependent quantum dynamics simulations will be introduced in section 5.2 in the context of the helium atom. The energy-level difference of $\sim$19 eV corresponds to the spatially localized oscillation with a period (roundtrip time) of about 200 as in the probability-density distribution, see the snapshots presented in panel (b).

The key ingredient to launch a coherent wave packet are ultra-short laser pulses with a spectral bandwidth broadband enough to coherently excite several quantum states by photons with the same phase and with a pulse duration much shorter than the lifetime time $\tau_{\mathrm{i,j}}$. First time-resolved observations of wave packets of nuclear vibrational and rotational character in molecules were made with the advent of picosecond and femtosecond laser pulses applied in pump-probe configuration (see [149–151], and references therein).

While these first observations in the early 1990s were made in rather slow I_2 molecules mapping dynamics on the ~ 300 fs time scale, the rapid progress in ultra-short pulse laser technology over the last decades allowed the visualization of nuclear wave packets even of the fastest molecules, that are for instance H_2^+, D_2^+, and D_2 on the 10-fs time scale [152–155].

The availability of strong-field free-electron laser (FEL) pulses in the extreme-ultraviolet (XUV) and soft x-ray spectral region made it possible to perform pump-probe schemes based on the ionization of one or several electrons at each light—matter interaction step. This allowed the research on electronic transitions both initiating and probing nuclear motion [156–158] and the mapping of wave-packet dynamics along the entire quantum mechanical pathway of chemical reactions [159].

A pioneering experiment based on high-harmonic generation (HHG) for the development of interferometric pump-probe techniques on *bound* attosecond electron wave packets is reported in [160]. This method measures the photoelectron spectrum of continuum electrons created via two different excitation/ionization pathways: directly by the absorption of one XUV photon, and indirectly by a time-delay controlled two-step [XUV+fundamental near-infrared (NIR)] absorption process. In the continuum the electrons are energetically degenerate and interfere (which-way interference). The delay-dependent spectral direct—indirect interference pattern allowed the extraction of the temporal evolution of the bound wave-packet composed of autoionizing helium states by referencing to the direct continuum channel.

A related approach based on HHG and the fundamental NIR driver pulses is the technique of attosecond transient absorption spectroscopy (ATAS) which measures the optical response of the bound-state (non-ionized) target system directly, as first presented in [131, 132, 161]. ATAS provides both a high temporal and spectral resolution which allows for the detection of sharp fingerprint spectral signatures (resonance lineshapes) that encode amplitude and phase information about the studied quantum system in the presence of the delay-controlled XUV and VIR/IR fields. In the meanwhile, a multitude of ATAS investigations both in theory [162] and experiment [163] have been carried out on atomic, molecular [164, 165], and solid-state [166] samples, as exemplified for instance by the development of a universal laser-driven phase-control scheme tuning spectral resonances between Fano and Lorentzian lineshapes [23], the observation of the time-dependent lineshape build-up of a Fano resonance [63], and the laser-induced polarization of the electronic core in the Xe atom [167]. Even though the focus is placed on different kind of physical phenomena, all these ATAS schemes share the same interferometric approach based on the direct mapping of the temporal evolution of coherent electronic quantum dynamics similar to [160]. Electron wave-packet dynamics are usually probed by the delay-controlled laser-induced coupling either to the continuum [23] or resonantly to neighboring bound states [168], which will be described in the following on the example of the paradigmatic He atom.

The purpose of the following sections 5.2 and 5.3 is to convey a principle understanding about the spectroscopic observables of ATAS-based wave-packet interferometry relevant for this work that are general, *regardless* of the specific target system. Sections 5.2 and 5.3

reflect the theoretical and experimental prototypical work on the helium atom carried out by our group with contribution within the scope of this thesis.

5.2 Related work in helium

The two-electron helium atom represents a benchmark system for atomic physics in particular for investigations on the correlated interaction of bound electrons with light. This is because the underlying quantum three-body problem is highly tractable from a theoretical point of view and thus precise comparison of experimental observables and theoretical predictions is possible. In He both electrons can be excited cooperatively by a single XUV photon. This leads to discrete doubly-excited bound states above the first ionization threshold with quantum interference between the autoionization pathway and the pathway for direct photo-ionization. The relative phase between these pathways is a fingerprint characteristic of electron—electron correlation that is encoded in the profile of resonance lines (defined by the asymmetry-parameter q [69], as introduced in Eq. (2.61) of section 2.5), which are observed in photo-ionization yields or photo-absorption spectra.

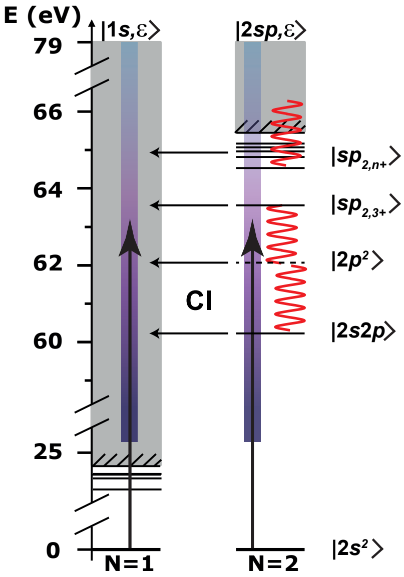

Figure 5.2: Illustration of Fano's natural quantum interferometer [69] and our pump-probe approach to control the involved transition pathways in the energy domain. Broadband XUV-excitation is indicated in violet and VIS/IR strong-field bound—bound and bound—continuum couplings by red wavy lines. See the main text for further information and chapter 2.5 for theoretical background on autoionization.

Fig. 5.2 illustrates the developed multiple-pathway interferometric spectroscopy scheme on He in the energy domain. A general time-domain description being instrumental for the physical interpretation of time-dependent spectra will be introduced in section 5.3.

The crucial idea is to employ broadband high-harmonic generated XUV pulses to coherently excite the doubly-excited states initiating wave-packet dynamics. The system's free evolution is accompanied by XUV-dipole emission due to polarization decay. The XUV pulses are followed by moderately strong (10^{12} W/cm^2 intensity range) few-cycle ($\sim$5 fs) NIR laser pulses that transiently interact with the excited system well-before it has decayed due to autoionization after about 10 to 100 fs. Either the NIR laser induces strongly coupled bound—bound transitions between excited states in case of resonance, and/or it induces bound—continuum transitions, both indicated in Fig. 5.2 by the red wavy lines. Both NIR interaction processes leave their characteristic traces behind in the measured XUV-spectral response as a function of time delay thus probing the wave-packet evolution (see Fig. 5.3).

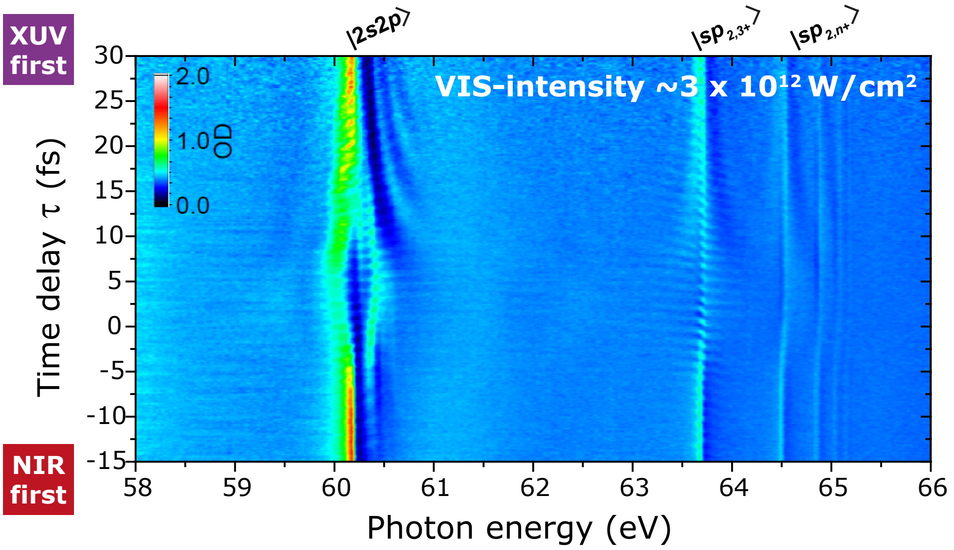

Figure 5.3: Attosecond transient absorption spectroscopy on autoionizing He states employing attosecond HHG-pulses and time-delayed fundamental strong NIR pulses. The spectrogram shows the measured optical density (color scale) as a function of time delay τ. At negative delays when the NIR field hits the target first almost undisturbed resonance lines can be observed. In contrast, strong spectral changes (i.e. τ-dependent periodic structures at low-energy 2s2p and sp$_{2,3+}$ states and line-shape inversion at sp$_{2,n+}$ Rydberg states) across the lines emerge in particular in the pulse overlap and at positive time delays where the transient NIR interaction shortly after XUV excitation modifies the fast spectral XUV-dipole response. This allows to probe phase and amplitude information of the underlying quantum dynamics.

The detailed physical description of the presented data in Fig. 5.3 is not in the scope of this thesis. In brief, the time-delay dependent modulations across the 2s2p and sp$_{2,3+}$ lines are associated with correlated two-electron wave-packet dynamics probed by strong NIR coupling. Both phase and amplitude information of the quantum states [54, 169], as well as detailed quantum mechanical information about the two-photon coupling mechanism itself [62] can be extracted from these signatures. Tuning the laser intensity up to higher values ($\sim 10^{13}$ W/cm^2) where ionization becomes more likely, even the time-dependent asymmetric lineshape build-up can be observed [63]. The higher-lying Rydberg lines $\mathrm{sp}_{2,n+}$ are ideal targets to study ponderomotive continuum effects like the laser-controlled lineshape inversion [23].

From the theoretical side, several (low-budget) methods are available to gain profound understanding of the underlying physical processes. In order to emulate the above experimental scenario so-called "computer experiments" based on an *ab initio* non-perturbative two-electron toy model [170, 171] are employed. The model is constructed based on the time-dependent Schrödinger equation (TDSE) in one dimension (1d) that accounts for the full electron—electron correlation and all the linear and non-linear light—matter interaction pathways, intrinsically. Assuming dipole approximation the non-relativistic Hamiltonian in the velocity gauge reads

$$\hat{\mathrm{H}} = \sum_{i=1}^{2} \frac{[\hat{\mathbf{p}} + \mathbf{A}(t)]^2}{2} - \frac{2}{\sqrt{\hat{\mathbf{x}}_i^2 + 1}} + \frac{1}{\sqrt{(\hat{\mathbf{x}}_1 - \hat{\mathbf{x}}_2)^2 + 1}}. \tag{5.2}$$

Both the electron—core attraction and the electron—electron repulsion are defined by soft-core Coulomb potentials [147, 148] as plotted in Fig. 5.1(a). This way, the singularity of the natural Coulomb potential is circumvented, which allows the electrons to enter their full 1d phase space. The vector potential $\mathbf{A}(t)$ represents the superimposed XUV and NIR external laser-fields that can be shifted (time delayed) with respect to each other being defined in accordance with the described experimental configuration. The two-electron wavefunction $\Psi(\hat{\mathbf{x}}_1, \hat{\mathbf{x}}_2, t)$ is numerically propagated forward in time by means of the Split-Step Fourier method [57, 58], that partitions the Hamiltonian into real space ("$\hat{\mathbf{x}}$") and imaginary space ("$\hat{\mathbf{p}}$"). Evaluating each space domain separately, i.e. the position operator in position space and the momentum operator in momentum space, before reconnecting them via Fourier transform has the computational advantage that differential operators can be avoided in the time-evolution propagator $\exp(-\mathrm{i}\hat{\mathrm{H}}_{\mathrm{x,p}}\Delta t)$. The initial ground-state wavefunction is obtained by the field-free propagation in imaginary time steps ($\Delta t \to -\mathrm{i}\Delta t$) of a completely random wavefunction. In this case the time propagator represents the superposition of exponentially decaying functions with decay rates corresponding to the respective eigenenergies of the potential. Employing an appropriate renormalization at each propagation step leads to the lowest energy (ground) state in the limit of infinite imaginary time. In order to mimic the effect of an electron continuum imaginary boundaries are defined near the edges of the numerical grid that "absorb" the ionized wave packet. Writing the total wave function in the spatially symmetric form, $\Psi^{\mathrm{s}}(\hat{\mathbf{x}}_1, \hat{\mathbf{x}}_2) = \Psi(\hat{\mathbf{x}}_1, \hat{\mathbf{x}}_2) + \Psi(\hat{\mathbf{x}}_2, \hat{\mathbf{x}}_1)$, restricts it to spin-singlet states according to Pauli's principle, which accounts for spin correlation even though spin-orbitals are not explicitly defined. As a consequence, the allowed radiation transitions obey the common opposite-parity selection rules in the electric-dipole approximation.

The simulated results are presented in Fig. 5.4 and confirm the experiment qualitatively. As in the experiment, prominent NIR-laser induced spectral modifications can be observed near the doubly-excited two-electron states termed by $|2,n\rangle$ with $n = 3, 5, 7, \cdots$. Also refer to a more detailed theoretical study [170] based on this approach elucidating these signatures for different NIR-wavelengths.

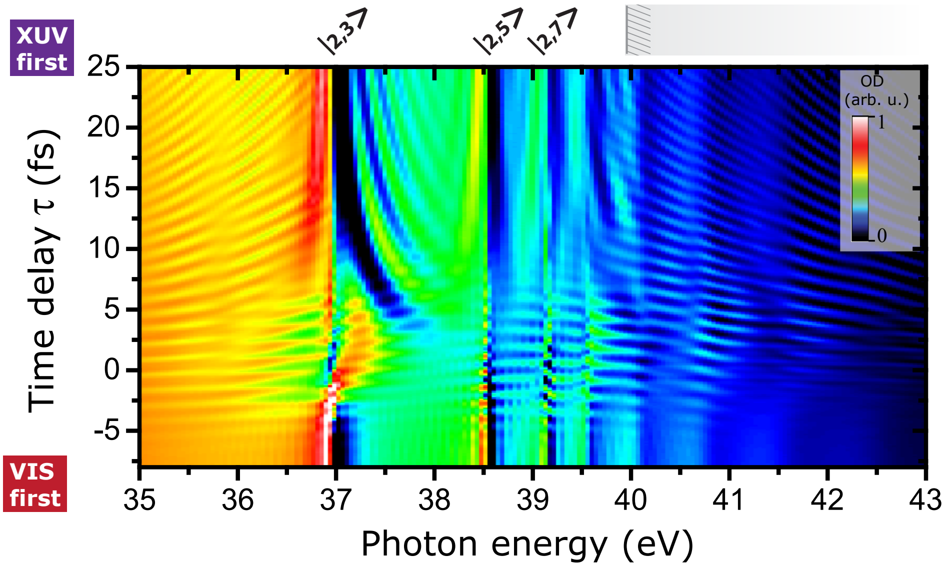

Figure 5.4: Numerically calculated (1d-2e$^-$-TDSE) attosecond transient absorption spectroscopy on doubly-excited states in a two-electron model as described in the main text with a 200 as coherent XUV-excitation pulse and a time-delayed 5 fs NIR pulse at $\sim$1.6 eV central photon energy and 8×10^{12} W/cm^2 peak intensity. The spectrogram resembles the experimental data shown in Fig. 5.3 qualitatively even though the artificial model system is restricted to only one dimension in space constructed of 256 grid points (numerical spacing $\Delta x = 0.5$ a.u.). The imaginary absorbing barrier comprises 45 grid points leaving the system composed of both bound and continuum states enough phase space to evolve in time (40.000 propagation steps with temporal spacing $\Delta t = 0.1$ a.u.).

The 2e$^-$ toy model is an ideal tool to study the role of the electron correlation at work in the interaction of doubly-excited targets with light in particular in the cross-over field-strength regime from weak (perturbative) to strong (non-perturbative) light—matter interaction. The effect of electron correlation seem to crucially influence the ionization dynamics of doubly-excited He at a certain critical NIR intensity—an effect that is currently being investigated in our group [172]. However, the drawback of such *ab initio* simulations is that a basic physical description of the involved light—matter interaction mechanisms cannot be directly inferred. To study all the individual underlying quantum transition pathways, few-level TDSE-like model simulations are employed. Section 5.6 of this chapter is dedicated to few-level model (FLM) calculations. In the following section an analytical time-domain formalism will be introduced capable of reconstructing the main spectral coupling features of ATAS in general.

5.3 The dipole control model

For the spectral interpretation of time-dependent absorption near laser-coupled resonances a general analytical description in the time-domain has been developed, termed dipole-control model (DCM). This section provides a brief description of the basic ideas of the

DCM. A detailed analysis can be found in the published work [173].

The excitation of an atom is accompanied by an oscillating and exponentially-damped polarization, which is responsible for the electromagnetic dipole radiation. In analogy to observed induced oscillating current signals in the field of nuclear magnetic resonance (NMR) spectroscopy in the 1950s [174–176], this is called (optical) *free-induction decay* (FID) [177–180] and in general described by

$$d(t) \propto -\mathrm{i}e^{\mathrm{i}[\omega_\mathrm{r} t+\varphi(q)]-\frac{\Gamma}{2}t} \tag{5.3}$$

with a resonance frequency ω_r and a relaxation rate Γ. Depending on the natural dipole phase $\varphi(q)$ [23], the oscillation gives rise to symmetric (Lorentzian) or asymmetric (Fano) resonance lines in the frequency domain. When subject to an abrupt perturbation during the dipole oscillation, the dipole spectrum exhibits strong coherent modifications, as illustrated in Fig. 5.5. This phenomenon has been named *perturbed free-induction decay* [178–180], or recently in the context of HHG spectroscopy *controlled free-induction decay* [181], respectively. The prerequisite for the experimental realization are impulsively short (δ-function-like) excitation and control pulses compared to the system's coherence time. This condition is fulfilled in practically all reported ATAS experiments targeting the XUV-response of transiently laser-coupled autoionizing states.

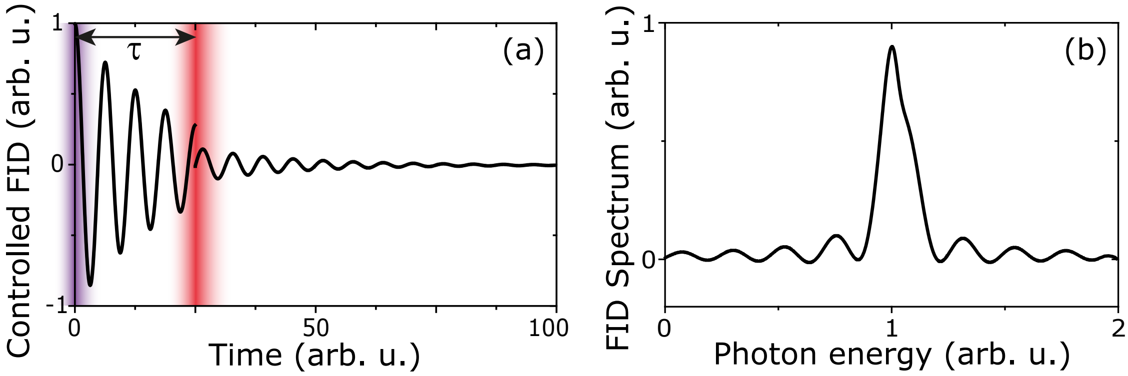

Figure 5.5: Illustration of the dipole control model (DCM) in the time domain, panel (a), and frequency domain, panel (b). In panel (a), the assumed impulsive XUV-excitation at a time $t = 0$ is indicated by the violet shaded area. The time-delayed assumed impulsive perturbation by the NIR-control pulse at a time $t = \tau$, indicated by the red shaded area, induces both a phase jump and a change in amplitude in the dipole oscillation. As a result of the perturbation, the spectral response, i.e. the Fourier transformed controlled FID, $\tilde{d}(\omega)$, exhibits spectral artifactual signatures such as modulations shown in panel (b) and observed in many experiments.

The external control of the dipole phase $\varphi(q)$ in order to tune resonance lineshapes between Fano and Lorentzian profiles has been demonstrated by applying the control-laser field instantaneously with the XUV-excitation at $t \approx 0$ [23]. The key idea of the DCM is to extend this framework to the control at arbitrary time-delay τ between the excitation XUV and the perturbation NIR laser pulse. Therefore Eq. (5.3) is treated piecewise for the two temporal regions before the NIR perturbation, $t < \tau$ (natural free-induction decay), and after it, $t > \tau$ (perturbed/controlled free-induction decay). The NIR interaction is assumed δ-function-like, which is justified when the duration T_{NIR} of the laser pulses is negligible compared with the lifetime $2\hbar/\Gamma$ of the system. Consequently, the NIR interaction can in general be accounted for by an abrupt change in amplitude and phase of $d(t)$ at $t = \tau$ described by an artificial complex-valued factor $A(\tau)$. Parametrized by the time delay τ a 2d spectral representation can be obtained by evaluating $\mathrm{Im}\left[\tilde{d}(\omega,\tau)\right]$—the observable quantity for absorption spectroscopy (see chapter 2.4 for the theoretical background)—with the Fourier transformed dipole response

$$\tilde{d}(\omega,\tau) \propto -\mathrm{i}\frac{1-\mathrm{e}^{\mathrm{i}(\omega_{\mathrm{r}}-\omega)\tau-\frac{\Gamma}{2}\tau}(1-A(\tau))}{\mathrm{i}(\omega_{\mathrm{r}}-\omega)-\frac{\Gamma}{2}}. \tag{5.4}$$

In general, two fundamental NIR interaction processes are possible and can be tailored by $A(\tau)$:

- The first one is of *non-resonant* character like e.g. the effect of tunneling ionization and can be described by a static amplitude and phase factor $A(\tau) = a_1\mathrm{e}^{\mathrm{i}\phi_1}$. This term produces spectral modulations whose period is inversely proportional to the time delay τ. Thus, scanning the time delay characteristic hyperbolic lines associated with constant time delay—photon energy ($\tau \times \omega$) values emerge in the 2d time-domain spectrum, $S(\tau,\omega)$, as shown in Fig. 5.6(a). The origin of these modulations is spectral interference between the FID and the perturbation. In the Fourier transformed ($\tau \to \Omega$) 2d spectral representation, $S(\Omega,\omega)$, this corresponds to a peak centered at zero Fourier energy [Fig. 5.6(b)]. This phenomenon is closely related to so-called *coherent artifacts* reported in the field of femtosecond spectroscopy [182–184].

- The second fundamental interaction is *resonant* and induced by the coherent coupling to another quantum state. In this case, the free evolution of a quantum wave-packet and the thus differently accumulated quantum mechanical phases of the coupled states during the time window $t < \tau$ plays a major role. Accounting for the wave-packet evolution the factor function is written in the form $A(\tau) = (1 + a_2\mathrm{e}^{\mathrm{i}\Delta E\tau+\mathrm{i}\phi_2})$ with the energy difference of the coupled states ΔE. Consequently, the 2d time-domain spectrum, $S(\tau,\omega)$, is characterized by a τ-dependent beat modulation with a period $h/\Delta E$ as observed in Fig. 5.6(c). In the 2d spectrum $S(\Omega,\omega)$ in Fig. 5.6(d) this yields a diagonal peak at a non-zero Fourier energy corresponding to the resonance energy ΔE. This diagonal feature is generally of slope 1. It's orientation dictated by the sign of the phase $\Delta E \times \tau$ allows to infer the coupling partner by the extrapolation of the diagonal towards the photon energy (ω) axis. Hence, this coupling feature allows for the probe of unambiguous spectroscopic information about the underlying quantum mechanical dynamics.

Both, the non-resonant and the resonant coupling features represent the basic building blocks of the DCM for the reconstruction of a typical time-resolved ATA spectrum. This method is in particular instrumental for the interpretation and the disentanglement of complex and congested ATA spectra.

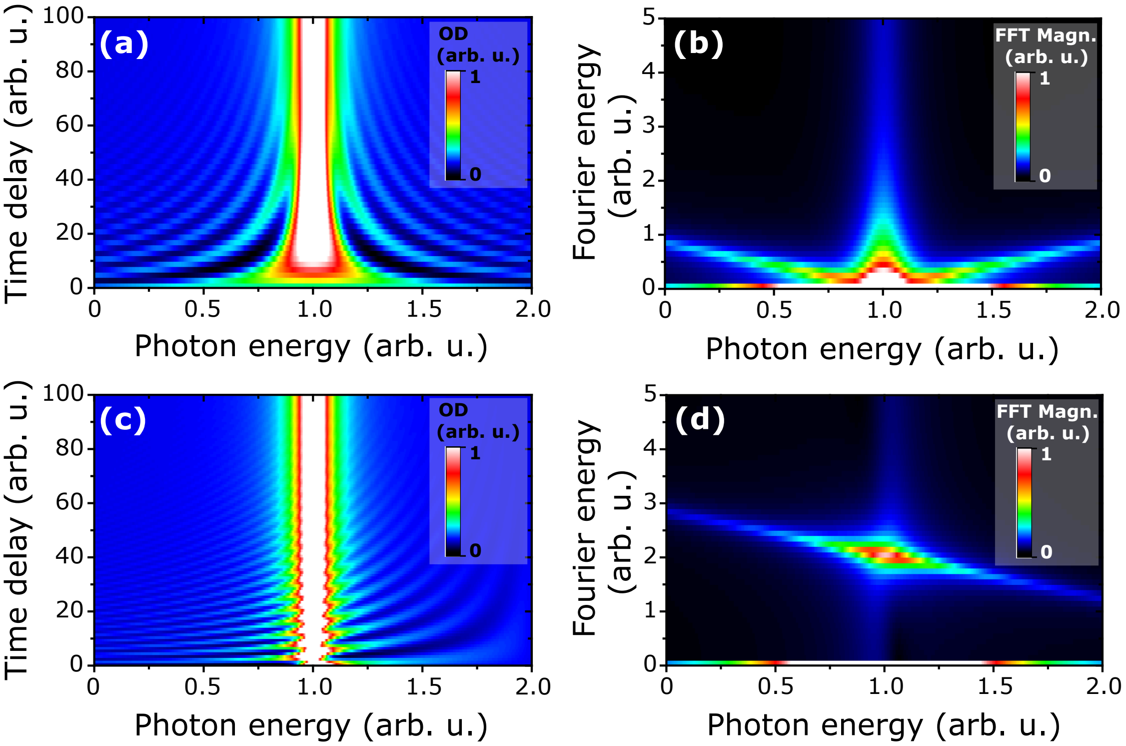

Figure 5.6: Transient absorption spectroscopy both in 2d time-domain, $S(\tau,\omega)$, and spectral domain, $S(\Omega,\omega)$, representation on the controlled free-induction decay (FID) modeled for an arbitrary XUV-NIR pump-probe scenario according to the DCM formalism (Eq. 5.4). Panels (a) and (b) are modeled for the case of a *non-resonant* time dependent laser-control for instance induced by ionization in the trivial case $a_1 = 0$. In this case, slow hyperbolic modulations arise in the 2d time-domain spectrum as a result of spectral interference [see panel (a)] corresponding to a fork-like peak at zero Fourier energy in the spectral domain [panel (b)]. In panels (c) and (d) the situation for the case of *resonant* time dependent laser-control due to strong coupling is presented (with parameters $a_2 = 0.5$, $\Delta E = 8\pi$, and $\phi_2 = 0$). Here, fast “ripples” as a function of τ [see panel (c)] give rise to diagonal peaks in the spectral representation in panel (d). These peaks show up at a certain (non-zero) Fourier energy corresponding to the energetic level-spacing between the coupled states and are directed towards the energy position of the “coupling partner” on the photon energy (ω) axis.

5.4 The experimental concept

Fig. 5.7 illustrates the experimental geometry. The technical details about the experimental setup are described in chapter 4. The key components are a split-and-delay mirror setup to prepare time-delay controlled XUV-NIR pulse sequences, and an iris aperture, which allows for NIR pulse-intensity tuning, simultaneously. Hence, the experimental control parameters are (*i*) the pump-probe time delay τ, and (*ii*) the laser intensity I. In principle, also the target-gas density serves as a control parameter [162, 185, 186] which

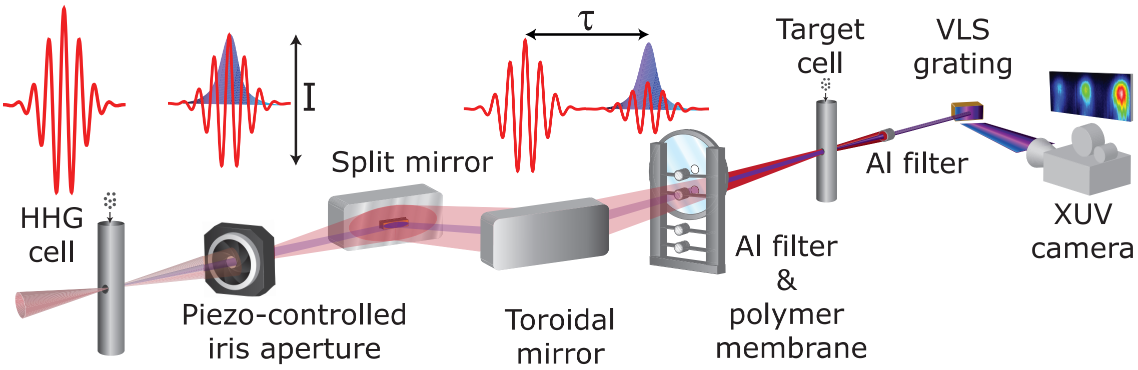

Figure 5.7: Schematic view of the experimental ATAS scheme for four-wave-mixing experiments on neon. In a gas-filled cell attosecond XUV pulses (violet) are produced by HHG close to the focus of the NIR fundamental field (red). A continuous NIR intensity tuning is possible by varying the size of the piezo-controlled iris diaphragm. Temporal separation of the collinearly propagating XUV and NIR pulses is possible by controlling a split-and-delay mirror module, where the inner XUV-reflective gold-coated mirror is displaceable with respect to the stationary silver-coated outer one. In combination with a spectral two-component (ultra-thin aluminum and polymer) bandpass-filter this allows to prepare weak XUV and NIR two-color fields and a time-delayed strong NIR control field. A toroidal mirror refocuses the intensity and time-delay controlled beam into the target-gas cell. The coherent dipole response emitted by the target medium interferes with the transmitted XUV field and carries information about the two-color light-matter interaction encoded in the spectral structure—the observable of this setup. A variable line-space (VLS) flat-field grating in combination with an XUV-sensitive camera serves as the detector. See section 4.1 for further technical details concerning the experimental setup. Adapted from [55].

can be accurately adjusted via the pressure. However, in the presented case the target-gas density was kept constant throughout the experimental run at a dilute density below $10^{18}\,\mathrm{cm}^{-3}$ where effects due to the propagation through the sample only play a minor role.

The prototypical ATAS experiments on helium as introduced in section 5.2 were performed utilizing a similar setup, however, in a collinear *two*-pulse (XUV-NIR) single-delay configuration. This configuration is inappropriate for the study of time-resolved multi-wave-mixing effects because higher-order photon transitions induced by the strong NIR field originate from the same (control) pulse and cannot be separated. To control non-linear third- or higher-order polarization it is useful to have a way of distinguishing the individual interaction steps. Therefore, the setup was extended into a collinear *three*-pulse (XUV-NIR-NIR) configuration with a single delay. As described in detail in chapter 4.1, a two-component bandpass-filter geometry is employed such that a second non-invasively weak NIR pulse can be applied traveling on top of the broadband XUV HHG field. This allows for perturbative two-color, two-photon transitions at time zero of the experiment coherently exciting the target system into final excited states that cannot be reached with a single XUV photon from the ground state due to dipole selection rules. The key idea is to probe and control the induced dynamics by the time delayed NIR field which strongly couples the excited states. Thus, in contrast to conventional ATAS schemes, here the NIR interaction with the target is temporally split and recorded for different delays.

Various 2s inner-shell excited states of s, p, and d orbital character can be reached by the two-color excitation step from the s-symmetry (even-parity) ground state. Here, only the three-level sub-system comprising the lowest autoionizing inner-shell states will be considered. The experimental scheme as applied to the autoionizing (2s inner-shell excited) neon atom is illustrated in Fig. 5.8.

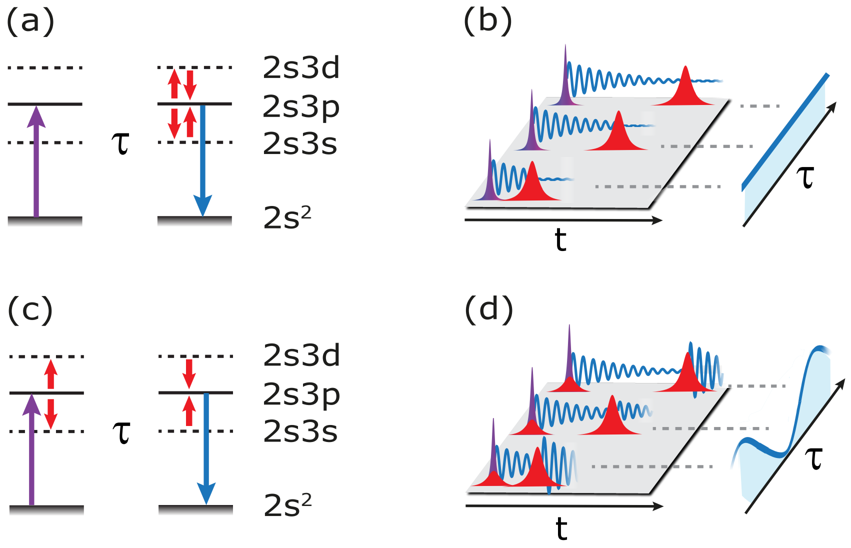

Figure 5.8: Schematic illustration of the possible four-wave-mixing quantum pathways in the time-resolved spectroscopy on neon inner-shell (sub-valence) wave-packets. The top panels illustrate the non-linear polarization as measured by the "conventional" ATA spectroscopy both in the energy domain, panel (a), and time domain, panel (b). In this case the XUV pulse excites a 2s electron (violet arrow) creating a coherent superposition of the ground state and the 2s3p state, while XUV transitions into final states 2s3s and 2s3d are dipole-forbidden [panel (a)]. In panel (b) the superposition leads to coherent dipole emission (blue wavy lines). After the time delay τ, the NIR pulse induces transient coupling (red arrows) of the 2s3p state and the 2s3s and 2s3d states. Amplitude and phase modifications lead to the characteristic spectral coherence signatures near zero Fourier energy in the 2d Fourier spectrum, $S(\Omega, \omega)$, as described in section 5.3 and shown in Fig. 5.6. The key ingredient to probe 2s3s and 2s3d wave-packet dynamics is the initial two-photon (XUV-NIR) excitation into a coherent superposition of 2s3p, 2s3s, and 2s3d states as depicted in panel (c). After free-induction decay until the time delay τ, the interaction with the third (NIR) pulse mediates a coupling between these states, which leads to constructive or destructive dipole emission of the 2s3p state, periodic in time delay with the full NIR optical cycle [panel (d)]. In the 2d Fourier spectrum, this creates the diagonal features near a Fourier energy corresponding to the NIR-photon energy (cf. Fig. 5.6). Adapted from [55].

The lifetime of the XUV-NIR excited wave packet due to autoionization is on the order of a few tens of femtoseconds, thus long-lived enough compared to the ~5-fs-pulsed laser to let the system freely evolve (free-induction decay) before strong coupling by the time delayed laser transiently perturbs/probes this decay (controlled free-induction decay) by a third light—atom interaction step. The resulting changes of the correlated dynamics inside the laser-dressed atoms manifest in the spectral structure of the emitted dipole radiation (the fourth light—atom interaction step). The coupling strength can be varied from weak to strong couplings via NIR intensity tuning. Moderately strong couplings are achieved with intensities on the order of 10^{12} $\mathrm{W/cm^2}$.

Further details on the experimental procedure and relevant experimental parameters will be described in the following section.

5.5 Transient absorption measurements and data analysis

The high-harmonic generation (HHG) based attosecond transient absorption spectroscopy experiments were conducted using the setup as described in chapter 4.1 and schematically illustrated in Fig. 5.7. Near-infrared (central wavelength ~ 760 nm) laser pulses at about 0.4 mJ pulse energy and compressed down to temporal durations below 7 fs were tightly focused into a gas-filled stainless steel cell to generate high harmonics with a 4 kHz repetition rate. Technical details concerning the combined NIR-laser and HHG-light source can be found in chapter 3. It is important to note that the HHG pulse sub-structure both in the time domain and spectral domain, as well as effects due to the pulse-to-pulse carrier-envelope phase (CEP) variation do *not* influence the experimental observations significantly, as discussed in the supplement of Ref. [54]. CEP fluctuation effects are avoided by averaging over numerous HHG spectra with statistical CEP. The only necessary requirements are (*i*) quasi-continuous XUV pulses broadband enough to cover the full spectral region of interest, (*ii*) short pulse durations with respect to the coherence time of the target system, and (*iii*) a well-defined relative spectral coherence of the XUV and NIR pulses.

A typical measured HHG spectrum propagated through vacuum is shown in Fig. 5.9 (black curve). The spectrum covers the XUV energy region of the neon 2s inner-shell states starting from ~ 45 eV with a spectrometer resolution of 20 meV Gaussian standard deviation near 45 eV (note, as explained in chapter 4.2, with the slightly different spectrometer geometry of the FLASH experiment, only a resolution of ~ 50 meV was achieved in this spectral range). The spectrum exhibits a broadband quasi-continuous interference structure with ~ 4 eV (twice the fundamental laser photon energy) peak-to-peak energy separation. Such a broad frequency-comb pattern is typical for short attosecond pulse trains of only a few pulses (also refer to chapter 3.3.1 for background information on HHG-pulse trains).

In order to enhance the signal-to-noise ratio, the HHG signal is binned over a certain region along the spatial coordinate of the 400 × 1340 CCD-pixel array of the detector.

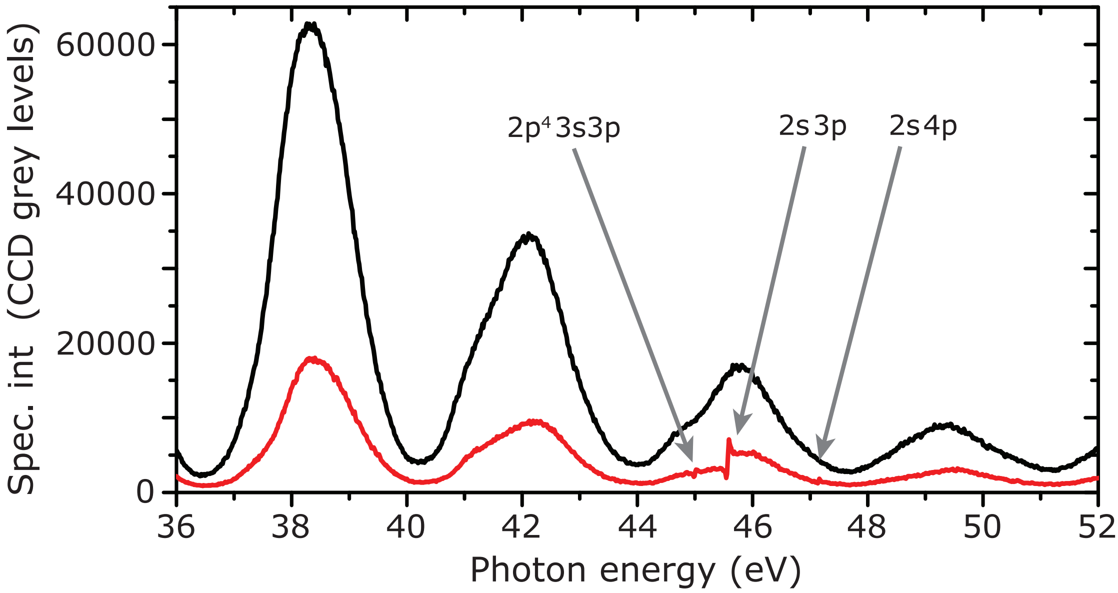

Figure 5.9: Measured HHG reference spectrum, $I_0(\omega)$, (black) and transmission spectrum, $I(\omega)$, (red) through a gaseous ~ 35 mbar neon sample. The NIR fundamental field was fully filtered out before the neon sample. Typical spectral modulations (~ 4 eV) corresponding to the half laser cycle temporal spacing between two attosecond XUV fields are apparent in both cases. The transmission spectrum is characterized by broad continuum absorption and autoionizing Fano-type resonance lines. Both spectra were obtained successively by averaging over 400 single laser shots. The fluctuations observed between averaged HHG spectra are on the order of 15% and explained by the extreme non-linearity of the underlying HHG process. Statistical noise is marginally visible.

This process is performed in the on-chip circuitry of the CCD and thus reduces the pixel-readout noise and increases the frame rate. Typical CCD exposure times are 100 ms integrating over 400 single shots.

The spectrometer calibration, i.e. the relationship between CCD-pixel number and photon energy, is achieved by comparing the measured spectral features with accurately known benchmark data from synchrotron measurements [76, 187]. As the grating equation can be approximated by a quadratic equation, the calibration routine involves a quadratic fit to the spectrum which produces high accuracy (mean standard error $< 10^{-5}$) when at least three spectral lines exist in the coverage region.

Fig. 5.9 presents the raw (except for the energy-axis calibration) HHG-power spectra measured successively *with* and *without* the sample medium, denoted by $I(\omega)$ (transmitted signal) and $I_0(\omega)$ (reference signal through vacuum), respectively. According to Lambert Beer's law [compare Eq. (2.55) from section 2.4] classical absorption spectra are determined by the optical density (OD)

$$\mathrm{OD}(\omega) = \log_{10}\left(\frac{I_0(\omega)}{I(\omega)}\right) = \frac{\sigma(\omega)}{\ln 10} \cdot \rho \cdot l \tag{5.5}$$

of a given medium of thickness l containing an average gas concentration ρ. The quantity $\sigma(\omega)$ is the absorption cross section for ionization as a function of the photon energy and specific for any absorbing species. An extensive data collection for rare-gas cross sections is given in [188].

The basic technique according to Eq. (5.5) relies on a high spectral stability of the experimental light source which is usually the case in classical (static) absorption experiments with standard monochromatic radiation sources. However, the pulse-to-pulse spectral power variation of HHG is typically on the order of ~15%, which is significant even if the spectra are integrated over many single shots. The reason for these high fluctuations is rooted in the extreme non-linearity of the HHG process which amplifies slight instabilities and drifts of the fundamental driver pulses. Hence, applying Eq. (5.5) to the successively measured signals $I(\omega)$ and $I_0(\omega)$ of Fig. 5.9 creates photo-absorption spectra with non-physical periodic artifacts imprinted on the OD (see Fig. 5.10). For the data analysis of time-resolved absorption spectra those artifacts are particularly problematic as they might interfere with spectral coherence signatures arising from the transient NIR-laser interaction with the sample—the observables of the presented experiments. To circumvent the lack of reproducibility of independently generated HHG spectra, in principle, the signals $I(\omega)$ and $I_0(\omega)$ have to be measured simultaneously, which is not possible with the setup used for these experiments. This will be possible with the next-generation beamline as discussed in chapter 4. Optionally, "artificial" reference signals $I_0^{\mathrm{rec}}(\omega)$ can be reconstructed based on the residual HHG interference pattern of the transmission signals $I(\omega)$. The following brief description of the data processing adheres to a previous work [133].

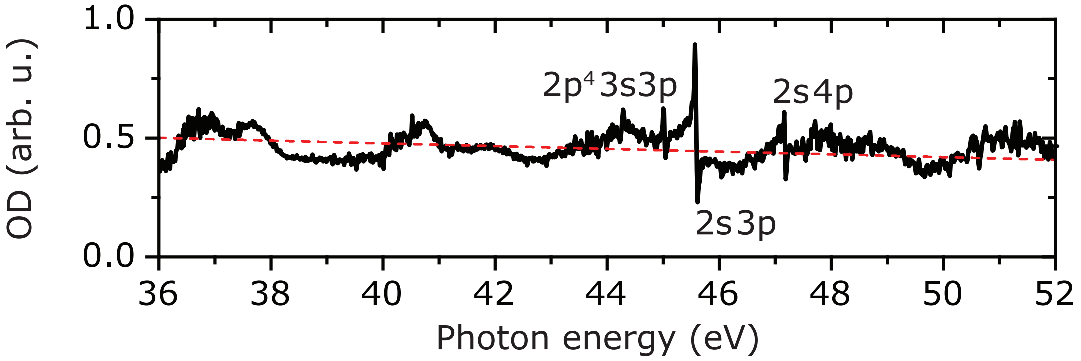

Figure 5.10: Optical density obtained by Lambert Beer's law [see Eq. (5.5)] considering the measured spectra $I_0(\omega)$ and $I(\omega)$ of Fig. 5.9. The red dashed line displays the linear dependence of the OD on the non-resonant continuum cross section $\sigma(\omega)$ [188], as well as the path length-density product, $\rho \cdot l = (0.14 \pm 0.02) \cdot 10^{18}\,\mathrm{cm}^{-2}$. A residual spectral ~ 4 eV modulation due to the ~15% pulse-to-pulse harmonic variation is clearly visible. A few dominant spectral lines can be identified (assigned based on [76, 187]) and discriminated from the statistical-noise level which is on the order of ~0.04 units in OD.

The data processing for the reconstruction of reference spectra, $I_0^{\mathrm{rec}}(\omega)$, from measured transmission spectra, $I(\omega)$, as they would be detected in the absence of any absorbing medium, includes two steps: Firstly, the sharp absorption resonances are removed from the long-term harmonic modulation pattern of a measured transmission signal $I(\omega)$ by means of a Fourier low-pass filter. The transmission spectrum after having been Fourier filtered is henceforth denoted by $I^{\mathrm{f}}(\omega)$. The attenuation with respect to a measured reference spectrum is due to the non-resonant absorption of photons leading to ionization of the target atoms. This effect is accounted for in a second step that re-scales the signal $I^{\mathrm{f}}(\omega)$ according to the right-hand side of Eq. (5.5). The right-hand side of Eq. (5.5) describes the linear dependence of the OD on the non-resonant photo-ionization cross section $\sigma(\omega)$ and the instrument parameters l (path length the light travels through the sample medium in the gas cell) and ρ (gas density adjustable by the backing pressure inside the gas cell). Hence, a reconstructed reference signal $I_0^{\mathrm{rec}}(\omega)$ is obtained by

$$I_0^{\mathrm{rec}}(\omega) = I^{\mathrm{f}}(\omega) \cdot \mathrm{e}^{\sigma(\omega)\cdot\rho\cdot l}. \tag{5.6}$$

The non-resonant cross section $\sigma(\omega)$ is accurately known from literature [188], while the so-called path length-density product, $\rho \cdot l$, can be fitted by relating the low-pass filtered transmission spectra to directly measured reference spectra as

$$\rho \cdot l = (0.14 \pm 0.02) \cdot 10^{18}\,\mathrm{cm}^{-2}.$$

The error corresponds to the 15% pulse-to-pulse HHG fluctuations. The reconstructed OD determined by the ratio $I_0^{\mathrm{rec}}(\omega)/I(\omega)$ is presented in Fig. 5.11. Compared to the successively measured OD (see Fig. 5.10), the periodic artifacts due to HHG fluctuations are almost non-existent. Minimal residues from harmonic modulations are nevertheless apparent, which, however, are uncritical for the data analysis and can be explained by a worse CCD signal-to-noise performance in the signal minima of $I(\omega)$.

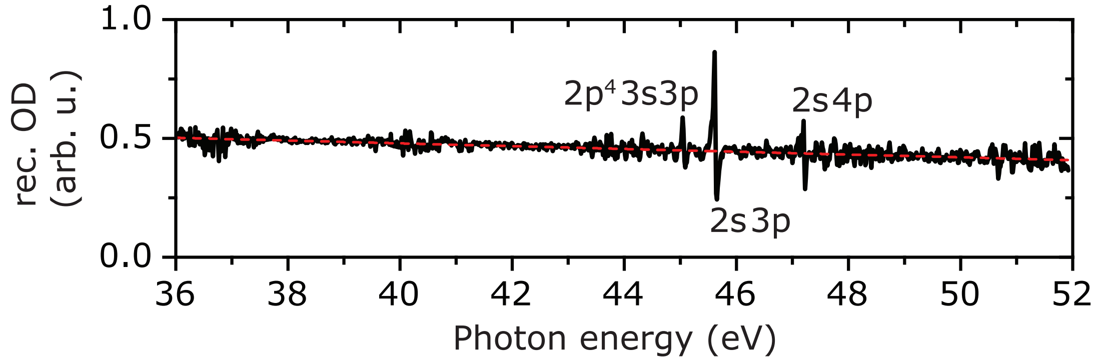

Figure 5.11: Reconstructed optical density determined from the directly measured transmission spectrum, $I(\omega)$, as displayed in Fig. 5.9 and a reconstructed reference spectrum, $I_0^{rec}(\omega)$. The reconstruction method is described in the main text. The red dashed line corresponds to the right-hand side of Eq. (5.5) with $\sigma(\omega)$ taken from [188] and $\rho \cdot l = (0.14 \pm 0.02) \cdot 10^{18}\,\mathrm{cm}^{-2}$.

The experimental transient absorption spectra presented in this work and denoted by $S(\tau,\omega)$ were all evaluated based on the above described reconstruction method. Time-resolved transient absorption spectra are created by concatenating single OD spectra as a function of the XUV-NIR pump-probe delay. Typical scanned split-mirror time-delay steps are ∼ 170 as. The interferometric pump-probe timing stability (or temporal resolution) achieved with the split-and-delay unit is on the order of 10 as, which is a fraction of the NIR optical laser cycle (∼ 2.4 fs). Refer to section 4.1 for technical details on the split mirror.

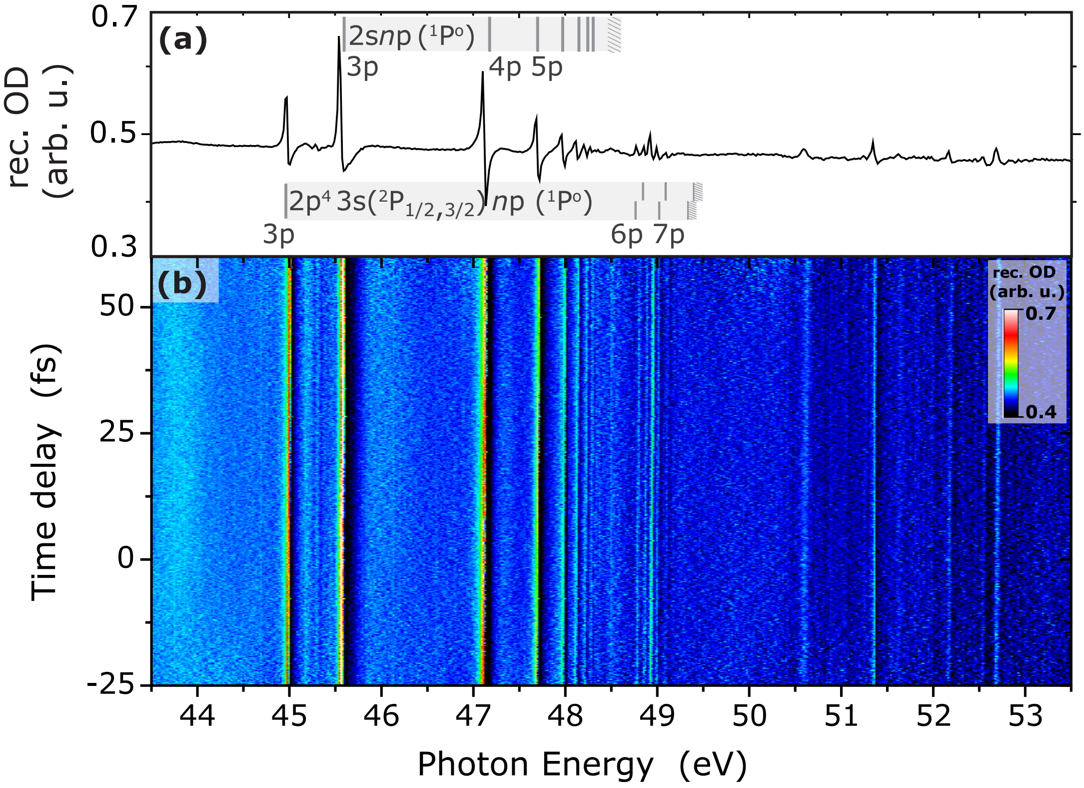

Figure 5.12: Panel (a) shows the averaged photo-absorption spectrum of neon from the $^1S^e$ ground state measured by broadband XUV radiation in the absence of the strong NIR laser. With a spectral resolution of about 20 meV near 45 eV the natural (unperturbed) resonance signatures from discrete autoionizing (2s inner-shell and doubly-excited) states can be accurately observed comparable to benchmark synchrotron [76, 187] and electron-spectroscopy [189] measurements. Various lines are apparent starting at ∼ 45 eV. A comprehensive theoretical discussion on all observed features is given in [76]. For this work, the lowest lying 2snp ($n = 3, 4, 5, ...$) inner-shell states are of relevance. Panel (b) shows the static spectrum as a function of split-mirror time-delay steps in the absence of the strong NIR control field. OD spectra were *in-situ* reconstructed by the method described in the main text.

A *static* transient absorption spectrum without the presence of any NIR control field is shown in Fig. 5.12(a). This measurement allows to observe various discrete resonance signatures above ∼45 eV corresponding to dipole transitions between excited short-lived autoionizing neon states of odd parity and the even-parity ground state mediated by a *single* XUV photon. Spectral signatures of even-parity higher states, which are also present in this spectral region [190], cannot be observed due to dipole selection rules. This would require the extended four-wave-mixing spectroscopy scheme based on more than one photon (see section 5.4). The time-delay axis in Fig. 5.12(b) reflects the relative interferometric path-length difference between the dynamical, inner (XUV) and the outer (NIR) mirror components converted by the speed of light c. Positive delays are introduced when the inner mirror protrudes from the surface of the outer one and XUV pulses thus hit the target first (reduced total optical path length through the setup). Panel (b) of Fig. 5.12 contains the same spectroscopic information as panel (a). It ought to illustrate the time-resolved measurement scheme in the absence of the strong NIR control field.

For *dynamical* transient absorption spectra *non-zero* NIR-laser intensities in the field-strength regime ($> 10^{12}\,\mathrm{W/cm^2}$) are adjusted. In this case, prominent spectral changes arise across the natural resonance landscape of neon in particular at positive delays and near the pulse overlap at zero delay, which can be observed in Fig. 5.13. Spectral modulations at negative delays (the NIR control-laser precedes the XUV) are due to weak but significant NIR-satellite pulses leading to a broad temporal pedestal that cannot be completely avoided in chirped-mirror compression based laser systems [191].

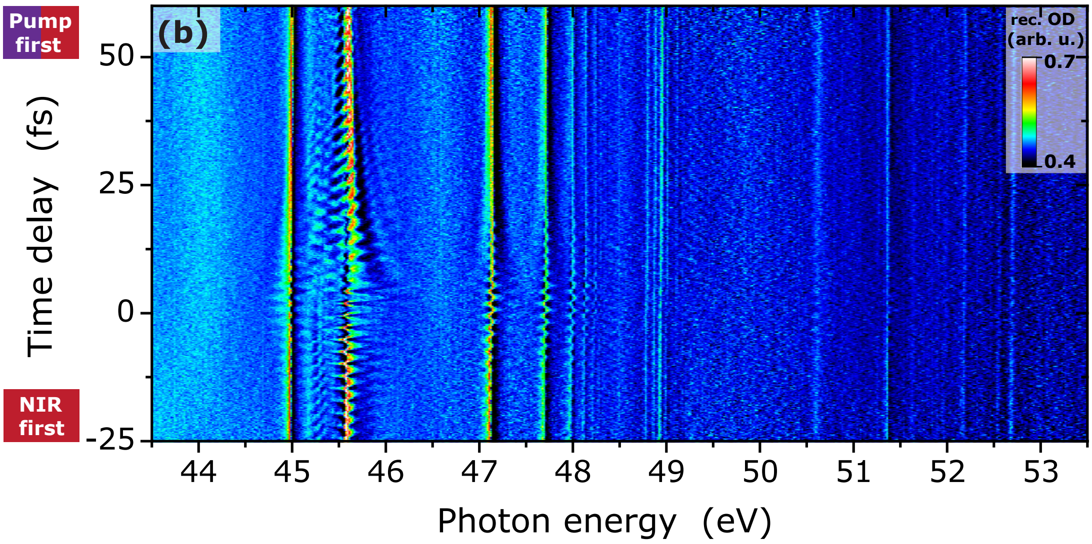

Figure 5.13: Pump-probe time-delay resolved attosecond transient absorption spectroscopy (ATAS) on neon with weak two-color XUV-NIR-excitation pulses (pump) and strong NIR-control pulses (probe). The color scale represents the reconstructed optical density (OD). Compared to the case without the NIR-control field (see Fig. 5.12), here, dominant delay-dependent spectral coherence signature are evident across the discrete lines. These signatures are the result of resonant and non-resonant quantum transitions as discussed in section 5.3 and serve as a probe for the underlying wave-packet dynamics. The physical interpretation of these features will be discussed in the remainder of this chapter. The NIR intensity is $\sim 2\times 10^{12}\,\mathrm{W/cm^2}$.

The calibration of the peak NIR-laser intensity is usually achieved by $in-situ$ measurements of strong-field induced light—matter interaction processes that are naturally sensitive to the applied laser intensity. The spectral behavior of the doubly-excited helium atom when subject to a transient femtosecond NIR dressing field is well-understood and serves as a suitable measure for the intensity (see section 5.2). For this purpose, the peak separation of the prominent 2s2p Autler-Townes doublet [39] can be analyzed. The 2s2p Autler-Townes splitting is most pronounced at a split-and-delay mirror setting of time-delay: +5 fs. The idea is to analyze the laser-driven red-shifting (to lower energies) of the 2s2p peak starting exactly at 60.15 eV as a function of the iris opening. As a direct mapping of the peak-laser intensity vs. the spectral shift is possible by fitting the experimental data to numerical calculations, the piezo-drive for the iris aperture can be calibrated in terms of intensities in retrospect [54, 169]. Another, related $in-situ$ calibration method measures non-resonant ponderomotive shifts of the doubly-excited sp_{2n+} helium states as a function of the time delay. Thereby, full information about the pulse profile can be reconstructed by fitting the measurement to the dipole control model (DCM) [192] (see section 5.3). The traditional *ex-situ* way of calculating the peak intensity of a focused laser pulse from observables such as the pulse energy, the temporal pulse duration, and the spatial beam profile cannot be performed exactly on-site where light—matter interaction takes place inside the vacuum setup and is thus less reliable. Furthermore, *ex-situ* measurements are subject to many individual errors that can quickly add up to 50% uncertainty in the intensity [193, 194].

As a final remark, the peak intensity of the NIR-excitation pulse acting together with the XUV to excite single-photon dipole-forbidden states, is perturbatively weak and thus cannot be measured with the described technique. However, indirect estimates on the applied NIR-excitation intensity are possible by comparing the experiment to numerical calculations as described in the following section.

5.6 Numerical calculations

The few-level model (FLM) system consists of three autoionizing bound states of the neon atom. These states are exited by the promotion of a 2s inner-shell electron from the $2s^2\,(^1S^e)$ ground state to the outer shell rearranging the system to electronic configurations $2s3s\,(^1S^e)$, $2s3p\,(^1P^o)$ and $2s3d\,(^1D^e)$. For the sake of simplicity states will be henceforth denoted by $|1\rangle$, $|2\rangle$ and $|3\rangle$, respectively. The corresponding resonance excitation energies are $\omega_1 = 43.67\,\mathrm{eV}$, $\omega_2 = 45.55\,\mathrm{eV}$ and $\omega_3 = 46.97\,\mathrm{eV}$ with respect to the ground-state energy assumed as $\omega_0 = 0\,\mathrm{eV}$. The level scheme is depicted in Fig. 5.14.

Electric dipole transitions that are allowed by parity (i.e. $^1S^e, ^1D^e \leftrightarrow ^1P^o$) are added to the level scheme in Fig. 5.14 and expressed by real-valued matrix elements $d_{ij} = d^*_{ij}$. According to Eq. (2.41) of chapter 2.3, the corresponding Schrödinger equation with the complex expansion coefficients $c_j(t)$ reads

$$\mathrm{i}\frac{\partial}{\partial t}\begin{bmatrix} c_0(t) \\ c_1(t) \\ c_2(t) \\ c_3(t) \end{bmatrix} = \begin{bmatrix} \omega_0 & 0 & 0 & 0 \\ 0 & \omega_1 & d_{12}E_{\mathrm{NIR}}(t) & 0 \\ d^*_{20}E^*_{\mathrm{XUV}}(t) & d^*_{12}E_{\mathrm{NIR}}(t) & \omega_2 & d_{32}E_{\mathrm{NIR}}(t) \\ 0 & 0 & d^*_{32}E_{\mathrm{NIR}}(t) & \omega_3 \end{bmatrix} \begin{bmatrix} c_0(t) \\ c_1(t) \\ c_2(t) \\ c_3(t) \end{bmatrix}. \tag{5.7}$$

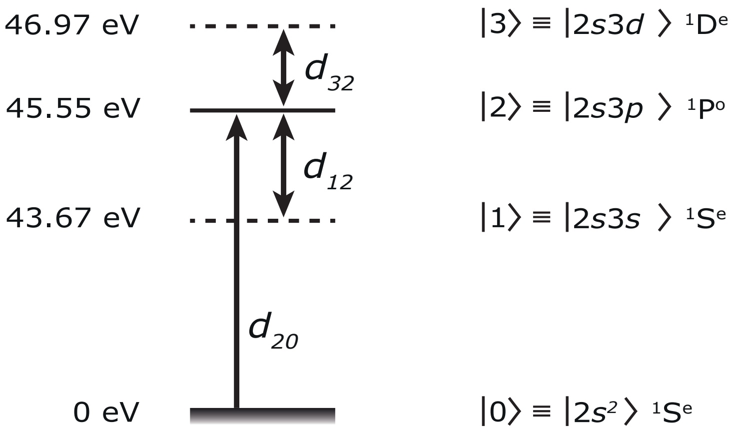

Figure 5.14: Level scheme of the simulated sub-system, including the neon $|0\rangle \equiv |2s^2\rangle$ ground state, the XUV dipole-allowed $|2\rangle \equiv |2\mathrm{s}3\mathrm{p}\rangle$, and the forbidden $|1\rangle \equiv |2\mathrm{s}3\mathrm{s}\rangle$ and $|3\rangle \equiv |2\mathrm{s}3\mathrm{d}\rangle$ states according to the opposite-parity selection rule. The $|2\mathrm{s}3\mathrm{s}\rangle$ and $|2\mathrm{s}3\mathrm{d}\rangle$ states can be accessed by a second, NIR, photon via the 2s3p intermediate state. The considered bound states are of autoionizing nature with a vacancy in the 2s inner shell. Transition pathways and corresponding dipole-matrix elements, d_{ij}, are depicted.

The strategy to numerically integrate this set of coupled differential equations involves the partitioning of the Hamiltonian matrix into three sub-systems, which are treated separately at a time step Δt in different eigenbases in which the associated sub-systems are diagonal. The sub-systems are (*i*) the unperturbed $\hat{\mathbf{H}}_0$-system which is diagonal in the initial base. (*ii*) The XUV light—matter interaction, henceforth denoted by $\hat{\mathbf{H}}_{\mathrm{XUV}}(t)$ and described by the first column (and the first row) of the Hamiltonian matrix in Eq. (5.7). And, (*iii*) the NIR light—matter interaction, denoted by $\hat{\mathbf{H}}_{\mathrm{NIR}}(t)$, being the remaining (off-diagonal) part of the Hamiltonian matrix. This approach is adopted from the well-known split-step Fourier method [57,58]. Here, however, the change of basis is mediated by an appropriate transformation matrix T [see Eqs. (2.43) to (2.45)] which is specific for the defined problem. The split-step method presents a considerable numerical simplification, as the time-dependence due to the NIR electric field can be factored out of the corresponding Hamiltonian sub-matrix

$$\hat{\mathbf{H}}_{\mathrm{NIR}}(t) = E_{\mathrm{NIR}}(t) \cdot \begin{bmatrix} 0 & d_{12} & 0 \\ d_{12}^* & 0 & d_{32} \\ 0 & d_{32}^* & 0 \end{bmatrix} . \tag{5.8}$$

Thus the diagonalization must *not* be performed at every propagation step. As each computation step only considers the diagonal part of the Hamiltonian, while neglecting the off-diagonal one, a discretization error of order Δt^2 is introduced [195].

The different steps of the simulation within one propagation time increment, Δt, are the following:

Step 1: Initial XUV excitation, $|0\rangle \rightarrow |2\rangle$, described in the weak-field limit by means of perturbation theory (see chapter 2.2.1) so that only a small fraction of the ground-state population is excited. The first-order expansion coefficient is numerically evaluated according to Eq. (2.20):

$$c_2(t+\Delta t) = c_2(t) - \mathrm{i}\, d_{20}^{*} \cdot E_{\mathrm{XUV}}^{*} \mathrm{e}^{\mathrm{i}\omega_{\mathrm{XUV}} t}\, \Delta t. \tag{5.9}$$

The XUV electric field, $E_{\mathrm{XUV}}(t) = \mathcal{E}_{\mathrm{XUV}}(t)\mathrm{e}^{-\mathrm{i}\omega_{\mathrm{XUV}} t}$, with a pulse envelope $\mathcal{E}_{\mathrm{XUV}}(t)$ and the central frequency ω_{XUV}, is assumed as complex-valued. This choice allows to use the rotating wave approximation (RWA).

Step 2: Both the rather weak NIR-excitation step (coinciding with the XUV excitation of step 1) as well as the time delayed NIR-laser coupling between the three excited states are treated in the strong-field limit (see chapter 2.2.2). This means that a periodic exchange of population between a lower level, $|i\rangle$, and an upper level, $|j\rangle$—known as Rabi oscillations [38]—is accounted for including the transition amplitudes for *both* processes the absorption and the (re-)emission of a NIR photon, described by $d_{ij} E_{\mathrm{NIR}}(t)$ and $d_{ji} E_{\mathrm{NIR}}(t)$, respectively. To include effects beyond the RWA, the NIR-electric field, $E_{\mathrm{NIR}}(t)$, is assumed as real-valued. Based on the method explained in chapter 2.3 the NIR-laser coupling is evaluated after unitary basis transformation by the multiplication with a complex phase factor, $\exp(-\mathrm{i}\lambda_j \Delta t)$, with λ_j being the eigenvalues of the Hamiltonian $\hat{\mathbf{H}}_{\mathrm{NIR}}(t)$ [see Eq. (5.8)].

Step 3: The field-free evolution of the excited states with energies ω_j and autoionization-decay rates Γ_j $(j = 1,2,3)$ is governed in the back-transformed original basis by multiplying the state amplitudes, $c_j(t)$, with a phase factor $\exp(-\mathrm{i}\omega_j \Delta t - \frac{\Gamma_j}{2}\Delta t)$. The simulation does not include the autoionization decay to the $N = 1$ continuum as described by Fano's theory. The asymmetry-effect on natural resonance line profiles when subject to autoionization is accounted for by a phase offset of the dipole response in the time domain according to the relation $\varphi(q) = 2\arg(q-\mathrm{i})$, which links the dipole phase, $\varphi(q)$, to Fano's q-parameter [23]. The related theoretical background can be found in chapter 2.5.

The three steps are repeated iteratively. For each iteration, the time-dependent dipole moment between the ground state $|0\rangle$ and the (single-photon allowed) excited state $|2\rangle$ is calculated by Eq. (2.46):

$$D(t) = d_{02}\, c_0^{*}(t) c_2(t). \tag{5.10}$$

Absorption spectra, $S(\tau,\omega)$, that are proportional to the experimentally observed optical density (OD) spectra are obtained by

$$S(\tau,\omega) = -\mathrm{Im}\left[\frac{D(\tau,\omega)}{E_{XUV}(\omega)}\right] \tag{5.11}$$

with the Fourier transformed dipole moment, $D(\tau,\omega)$, for a specific delay setting τ and the XUV electric field in the spectral domain, $E_{\mathrm{XUV}}(\omega)$. Also refer to section 2.4 for deeper information on the theory of absorption.

In the following, the numerical parameters used for the simulation will be discussed.

The propagation time increments are $\Delta t = 1$ a.u. (0.0242 fs) and the total propagation time is 32.000 a.u. (774 fs). This choice guarantees a proper sampling of the XUV-dipole response oscillating at periods of ~0.1 fs until the system has been fully decayed after ≥100 fs. It also constitutes a good compromise between negligibly small discretization errors and low computational costs.

The spectral resonance parameters characterizing the three excited bound states are listed in Tab. 5.1 consulting benchmark data from synchrotron- and electron-impact spectroscopy measurements. Benchmark data for the coupling matrix elements d_{ji} between the considered states is not available. Those were estimated based on the single-orbital assumption of hydrogenic wavefunctions expanded in the angular momentum basis, $\Psi_{n,l,m_l} = R_{n,l}(r) \cdot Y_l^{m_l}(\theta,\phi)$, and a linearly polarized laser field calling $\hat{\mathbf{e}}_z$ the polarization axis

Table 5.1: Spectral resonance parameters of the 2s inner-shell excited state as considered for the simulation. The Γ-value for the 3d-state is not available. This value was assumed as 0.01 eV. Errors quoted are estimated uncertainties. Values taken from Refs. [187,190].

j	Configuration	ω_r (eV)	Γ (eV)	q
1	$2s^13s\,(^1S^e)$	43.669 (±0.015)	0.091 (±0.006)	3.825 (±0.107)
2	$2s^13p\,(^1P^o)$	45.546 (±0.008)	0.013 (±0.002)	-1.6 (±0.2)
3	$2s^13d\,(^1D^e)$	46.971 (±0.031)	-	-3.239 $\binom{+1.146}{-1.668}$

$$d_{ji} = \left\langle \Psi^i_{n,l,m} \middle| \hat{\mathbf{r}} \cdot \hat{\mathbf{e}}_z \middle| \Psi^j_{n,l,m} \right\rangle. \tag{5.12}$$

Hence, the spatial degrees of freedom of a one-electron displacement vector $\hat{\mathbf{r}}$ are reduced to only one effective dimension and therefore only transitions with $m_l = 0$ (the system is initially assumed in the $1s$ ground state) and $\Delta m_l = 0$ are necessary. With this simplification and expressed in spherical-polar coordinates the dipole moment expectation values were calculated via

$$d_{ji} = \int_{-\infty}^{+\infty} \Psi^{i*}_{n,l,m_l}(r,\theta,\phi) \cdot r^3 \cdot \Psi^j_{n,l,m_l}(r,\theta,\phi)\, \mathrm{d}r \sin\theta \cos\theta \,\mathrm{d}\theta \,\mathrm{d}\phi. \tag{5.13}$$

obtaining $d_{12} = -3.58\,\text{a.u.}$ and $d_{32} = -2.53\,\text{a.u.}$. The shielding effect of the neon ($Z = 10$) Coulomb potential due to the inner electrons close to the nucleus is accounted for by an effective nuclear charge of $Z_{eff} = 2.05$ in the wave functions $\Psi^{i,j}_{n,l,m}(r,\theta,\phi)$. Z_{eff} was estimated using a semi-empirical method [196]. The ground—excited matrix element $d_{02} = 1\,\text{a.u.}$ is chosen arbitrarily. A quantitative values is not necessary for this simulation.

The electric field parameters where chosen in accordance with the experimental pulse configuration. This means, in total three Gaussian pulses are considered. See chapter 1 for a general description of short laser pulses. The XUV field is assumed as a Gaussian 250 as pulse with a central photon energy of $\omega_{\text{XUV}} = 45$ eV and a (fix) intensity of 10^{-5} a.u.. Coinciding with the XUV field, a NIR (excitation) pulse with a central photon energy $\omega_{\text{NIR}} = 1.6$ eV and a Gaussian duration of 5 fs is implemented. This pre-pulse is an intensity-scaled replica field of the time-delayed strong-field NIR coupling pulse. On an empirical basis, the peak intensity of the NIR pre-pulse is chosen to be 10 % of the peak NIR-coupling field intensity.

5.7 Sub-valence wave-packet dynamics probed by four-wave mixing

The general aspects of correlated electronic wave-packet dynamics probed by attosecond transient absorption spectroscopy (ATAS) in the usual HHG-pump—NIR-probe configuration were introduced in section 5.2 targeting the paradigmatic Helium atom. In these prototypical studies fast $\sim 1.2\,\mathrm{fs}$ modulations as a function of the NIR-pulse delay (corresponding to half an optical cycle of the 730 nm NIR wavelength) were observed and understood as *two*-NIR-photon coupling signatures between XUV-excited states. Recent related experimental studies also report about $\sim 0.6\,\mathrm{fs}$ modulations due to the coupling by four NIR photons [168]. It is important to note that spectroscopically allowed states due to the absorption of one XUV photon share the same parity which must be the opposite of the ground-state parity. Hence, only an even-integer number of NIR photons can mediate the coupling between those XUV-excited (identical-parity) states. Accordingly, the interference structures observed so far by ATAS in the 2d Fourier spectra, $S(\Omega,\omega)$, consisted of maxima at zero and/or *even*-integer multiples of the NIR-photon energy.

The time-delay dependent spectral modulations measured in the inner-shell excited neon atom (see Fig. 5.13 in section 5.5) evidences that also in these experiments coherent electronic wave-packets were created. However, here, the probed temporal periodicity of the NIR-coupling signatures is about 2.4 fs, i.e. the time duration of one full optical cycle of the NIR field. This suggests that additional channels that are spectroscopically hidden for the conventional pulse configuration of ATAS (an XUV-pump and a *single* time-delayed NIR-probe pulse) are accessed and probed by *one*-NIR-photon coupling.

In the following part of this section, the interfering quantum pathways the neon target system is driven along during the interaction with three distinct short-pulsed laser fields (XUV-NIR-NIR) applied in ATAS geometry will be analyzed in detail. For the sake of simplicity and in order to showcase the methodology, only the atomic sub-system of the energetically lowest lying 2s inner-shell states of neon will be considered, i.e. the XUV dipole-allowed state $2s3p\,(^1P^o) \equiv |3p\rangle$, and the XUV dipole-forbidden states $2s3s\,(^1S^e) \equiv |3s\rangle$ and $2s3d\,(^1D^e) \equiv |3d\rangle$ at 45.55 eV, 43.67 eV and 46.97 eV photo-excitation energy, respectively.

As described in section 5.4, the non-linear dipole response is stimulated from coinciding non-invasively weak XUV- and NIR-pump pulses together with a strong time-delayed NIR-probe pulse. The interaction of the neon target system with the first two pulses (XUV and NIR) creates a polarization, i.e., the coherent superposition of ground and both odd- ($|3p\rangle$) and even-parity ($|3s\rangle$ and $|3d\rangle$) excited states. This means, this two-color pump step extends the coherent excitation onto states, the transition into which would be forbidden by a single XUV photon from the ground state. After the time delay τ, during which the coherent superposition has freely evolved in time (free-induction decay), the interaction with the third pulse—the strong NIR-probe pulse—mediates the coupling between these states (controlled free-induction decay). The ladder-diagram-type illustration in Fig. 5.8(c) visualizes this four-wave-mixing (FWM) mechanism. The created non-linear response signal manifests itself as constructive and destructive interferences as a function of time delay with a period of the optical cycle of the NIR field imprinted on the atomic XUV dipole response [cf. Fig. 5.8(d)].

The resulting interference signals as observed in the time-resolved 2d absorption spectra, $S(\tau,\omega)$, encode the quantum-pathway information of the underlying coherent dynamics. Fourier decomposition is employed along the time-delay axis of $S(\tau,\omega)$ to unfold the beat pattern onto a 2d spectral map, $S(\Omega,\omega)$, for each resonance, which exhibits diagonal regions with distinct point-like and/or line-like peaks. Both 2d spectral representations, $S(\tau,\omega)$ and $S(\Omega,\omega)$, respectively, are shown in Fig. 5.15. The experimental data is complemented with *ab initio* time-dependent R-matrix simulations [65] accounting for the full electronic correlation of neon and the full (3d) dimensionality. The simulation was carried out by our collaboration partners A. Brown and H. Van Der Hart, Queen's University Belfast (see Ref [55] for further information) and is found to be in good agreement with the experiment.

The basic structures seen in the ATAS signals in Fig. 5.15 are general and can be understood referring the dipole-control model (DCM) (see section 5.3). The slow τ-dependent hyperbolic modulation close to the $|3p\rangle$ resonance line in the time-domain signal, $S(\tau,\omega)$, correspond to a (fork-like) peak at zero Fourier energy in the 2d Fourier signal, $S(\Omega,\omega)$, and are associated with the depletion of the quantum-state amplitude and thus are of *non-resonant* character. Due to their non-specificity those features are not of substantial spectroscopic relevance. In contrary, the fast τ-dependent rippling-like modulations stem from the *resonant* coupling, i.e. the back and forth transfer of population, between coherently excited states. These features are linked to the diagonal line-like Fourier peaks of slope ± 1 emerging at non-zero Fourier energies in the 2d Fourier signal, $S(\Omega,\omega)$. Fourier-peak position, its shape, and its orientation provide unambiguous information about the quantum transitions the system has undergone driven by light—matter interaction.

Looking closely at the 2d Fourier spectra presented in Figs. 5.15(c,d), two dominant line-like peaks can be observed near the XUV dipole-allowed $|3\mathrm{p}\rangle$ state (45.55 eV photon energy) at $\sim$1.42 eV and $\sim$1.88 eV Fourier energy. These peaks evidence the coupling by *one* NIR photon between *opposite*-parity states (referring to the opposite-parity selection rules of electric dipole transitions). The longitudinal width of these peaks reflect the $\sim$0.5 eV FWHM spectral bandwidth of the $\sim$5 fs NIR pulse with a central photon energy of $\sim$1.6 eV. The spectroscopically hidden even-parity "coupling partners" of the $|3\mathrm{p}\rangle$ state must be located in its resonant one-NIR-photon spectral vicinity. Their exact spectral positions can be retrieved by the extrapolation of the diagonal Fourier peaks towards the photon-energy axis (zero Fourier energy). By referring to benchmark electron-impact spectroscopy data [190] the even-parity $|3\mathrm{s}\rangle$ and $|3\mathrm{d}\rangle$ states at 43.67 eV and 46.97 eV photon energy can be identified as the coupled states. Note, that the energy gap between the coupled states and the $|3\mathrm{p}\rangle$ state is in both cases not accurately in resonance with the NIR photon energy which is the reason why the observed diagonal Fourier peaks do not appear exactly at 1.6 eV Fourier energy. Figs. 5.15(c,d) also exhibit a vertical (non-diagonal) peak close to 3.5 eV Fourier energy. This peak can be explained by the two-NIR-photon coupling to virtual light-induced states [197].

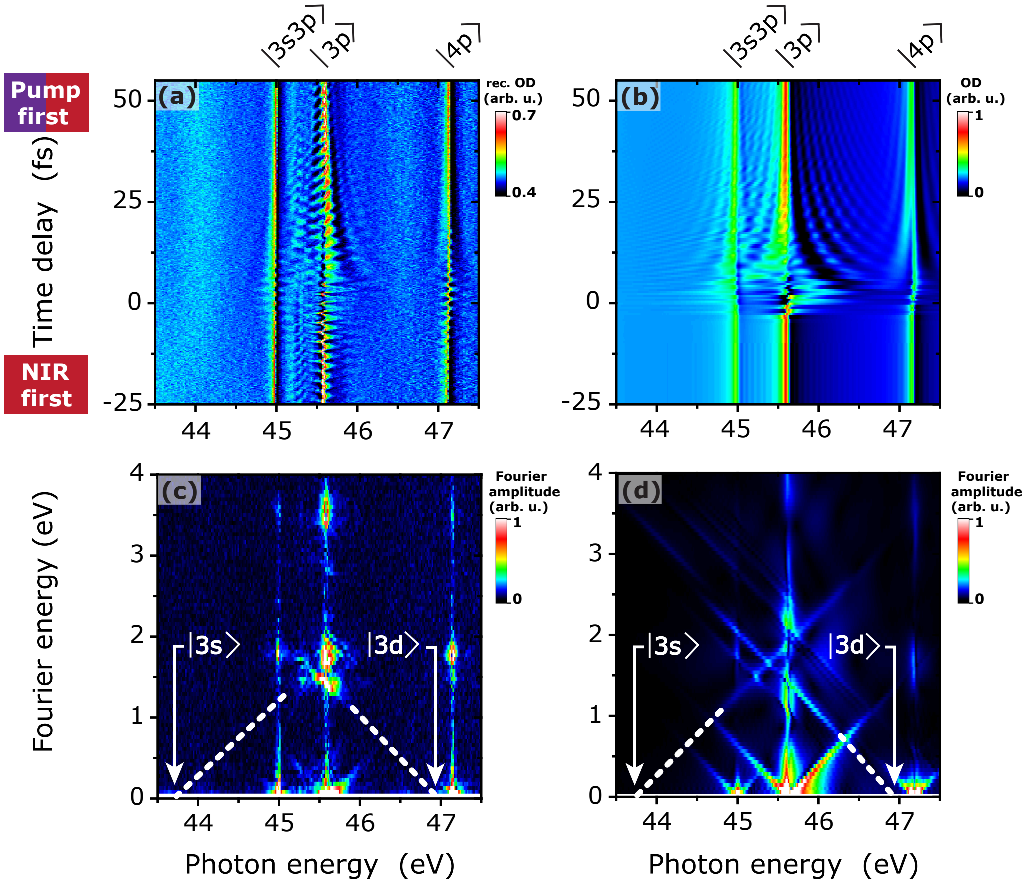

Figure 5.15: Time-resolved transient absorption spectra, $S(\omega,\tau)$, at $\sim 2.2\cdot 10^{12}\,\mathrm{W/cm^2}$ NIR-laser intensity obtained from (a) the experiment and (b) from complementary *ab initio* simulations based on the R-matrix with time dependence approach (A. Brown and H. V. D. Hart, Queen's University Belfast). Fast time-dependent $\sim 2.4\,\mathrm{fs}$ modulations near the $|3\mathrm{p}\rangle$ resonance line appear as a result of *one*-NIR-photon couplings to states of *opposite* parity. In the 2d Fourier spectra, $S(\tau\rightarrow\Omega,\omega)$ [see panels (c) and (d)], these coupling signatures correspond to distinct peaks of diagonal shape. The extrapolation of the diagonals (white dashed line) allows the identification of the transition energies of the XUV dipole-forbidden states $|3\mathrm{s}\rangle$ at ~43.67 eV and $|3\mathrm{d}\rangle$ at ~46.97 eV photon energy. Assignment based on [190]. Discrepancies between experiment and simulation are likely due to uncertainties in the exact experimental pulse shapes. Figure adapted from [55,198].

To further confirm this understanding and to extract quantitative information on the underlying individual quantum transitions, few-level model (FLM) simulations were carried out as described in section 5.6 [see Fig. 5.16(c-f)]. By comparison of the FLM simulations with the experiment the intensity ratio of about 1-to-10 between the weak NIR-pump and the strong NIR-probe field was approximated. The good agreement between FLM simulation and the experiment as well as the *ab initio* simulation also verifies the confidence of the assumed (approximated) dipole-matrix elements. In principle, this method allows to determine absolute values for the dipole-matrix elements, as soon as the experimental field strength and the pulse shape are more accurately known.

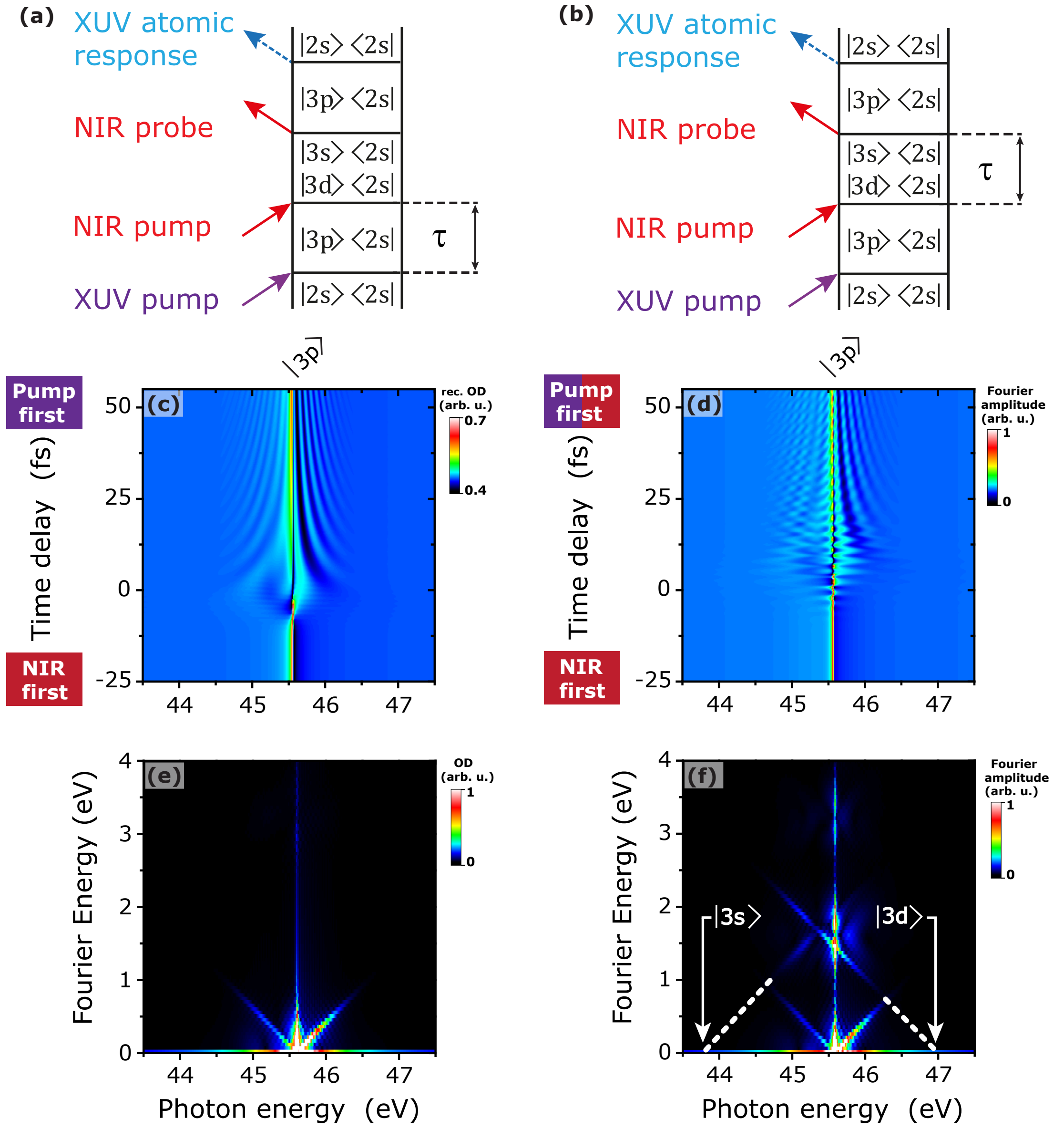

Figure 5.16: Double-sided Feynman diagrams [panels (a) and (b)] of the studied four-wave-mixing process, time-resolved transient absorption spectra, $S(\tau,\omega)$, and 2d Fourier spectra, $S(\Omega,\omega)$, obtained from few-level model simulations considering the $|3\mathrm{p}\rangle$, $|3\mathrm{s}\rangle$, and $|3\mathrm{d}\rangle$ excited states. Panels (a), (c), (e), describe the "conventional" ATA spectroscopy where the XUV- and NIR-field interactions are temporally separated by the time delay τ. In this case, only the non-specific (non-resonant) spectral signatures due to depletion effects of the $|3\mathrm{p}\rangle$ state are apparent, i.e. hyperbolic τ-dependent modulations in the spectrum $S(\tau,\omega)$ [panel (c)] corresponding to a zero Fourier-energy peak in $S(\Omega,\omega)$ [panel (e)]. In the scenario described by panels (b), (d) and (f) the NIR interaction is temporally separated by the time delay τ into a weak NIR pump (coinciding with the XUV pump) and an intense NIR probe. Here, the spectrum $S(\tau,\omega)$ [panel (d)] exhibits fast rippling-like modulations on top of the hyperbolas, which correspond to diagonal features at 1.6 eV Fourier energy in the spectrum $S(\Omega,\omega)$. This is a result of NIR-driven quantum state interferences between the coherently XUV-NIR-excited states $|3\mathrm{p}\rangle$, $|3\mathrm{s}\rangle$, and $|3\mathrm{d}\rangle$. The diagonal peaks point towards the $|3\mathrm{s}\rangle$ and $|3\mathrm{d}\rangle$ transition energies at 43.7 eV and 47.0 eV, respectively. Withe dashed lines are guides to the eye. Figure adapted from [55, 198].

Fig. 5.16(a,b) show time-ordered double-sided Feynman diagrams as introduced in chapter 2.6 which traces the evolution of the quantum system in time during non-linear optical interaction. These diagrams are usually used to analyze multi-wave mixing processes and, in contrast to ladder-diagrams, allow to distinguish between population and coherence dynamics. Here, the diagrams are used to point out the temporal splitting of the NIR field such that excitation and probing by an NIR-laser pulse occurs at *two* different times as the key mechanism for the observation of time-resolved four-wave-mixing (FWM) effects by ATAS.

5.8 Conclusion and outlook on the results from the HHG experiments

In this chapter, the well-known technique of attosecond transient absorption spectroscopy (ATAS) was extended to a novel multi-pulse four-wave-mixing scheme. In conventional (two-pulse) ATAS experiments, an attosecond extreme-ultraviolet (XUV) pulse (train) obtained from high-harmonic generation (HHG) is employed as an initial coherent excitation step to a target system, followed by a time-delayed near-infrared (NIR) intense pulse acting as a probe. In these conventional geometries, the intense NIR pulse can interact twice with the sample (i.e. with the partial fields E_{NIR} and E^*_{NIR}, as known from traditional pump-probe geometries [199]) at the same time. The individual non-linear interaction pathways however cannot be disentangled.

In the here developed method, the NIR interaction is temporally split and the excitation and probing by the NIR pulse occurs at different times. This enables on the one hand to directly access excitation and coupling channels that are otherwise spectroscopically prohibited (due to dipole-selection rules) and on the other it allows to extract the corresponding non-linear interaction-pathway information. The probed coherent dynamics are traced by controlling this time delay with a sub-cycle ($\sim$10 as) temporal precision. In analogy to two-dimensional spectroscopy [28], the data processing involves the Fourier transform of the collected interferogram in the time domain [$S(\tau,\omega) \to S(\Omega,\omega)$] to differentiate the individual coupling modes.

In this work, the method was demonstrated targeting the XUV spectral region of the neon atom. Neon exhibits inner-shell (core-hole) states of XUV-dipole-allowed p and -forbidden s and d orbital character that are spectrally separated by approximately the amount of energy of one NIR photon ($\hbar\omega_{\mathrm{NIR}} \approx 1.6$ eV)—the ideal test ground for this method. The corresponding four-wave-mixing coupling dynamics between those states could be unambiguously measured and disentangled in the form of directed, diagonal Fourier peaks in the 2d map $S(\Omega,\omega)$.

Supported by home-made numerical few-level model simulations, the quantum-pathway analysis allowed to reconstruct the system's entire coherence evolution and the propagation through the retrieved XUV-only allowed/forbidden quantum states with respect to the ground state. Although the numerical model is a simplified approximation fed with dipole moments estimated based on hydrogen wavefunctions and an effective nuclear shielding, the results resemble the experiment and complementary *ab initio* calculations. The numerical treatment with more realistic electric fields [192] suggest an even closer agreement with the experiment and in principle allows to obtain absolute values of the dipole-matrix elements.

In the meanwhile, the methodology has been extended by an additional time-delay degree-of-freedom with the near-future goal of performing full multi-dimensional spectroscopy [72] in a non-collinear boxcar geometry with combined wave-vector specific HHG and NIR fields. First test measurements are being made, again on the target neon, and are currently under analysis. Near-future measurements could for instance involve molecular targets probing electronic population and coherence dynamics which include vibrational and rotational contributions [200, 201]. Furthermore, the site-specific probing of molecular electron dynamics and excitation transfer is planned for the future.

Chapter 6

XUV-pump—XUV-probe strong-field transient absorption at FLASH

The previous chapter introduced the experimental transient-absorption spectroscopy scheme with HHG and strong-field NIR laser pulses elaborated in our group during the last few years and conducted in many experiments [23, 54, 55, 62, 63, 173]. In this thesis, emphasis was put on multi-pulse measurements probing four-wave mixing due to coupling between inner-shell states of (neutral) neon. In (near-)future experiments with the novel four-split-mirror design, as introduced in chapter 4.3, follow-up experiments as a function of multiple time delays will be possible to extract the full temporal information about the studied coupling dynamics.

This chapter describes first applications of our transient-absorption scheme with XUV-pump and XUV-probe pulses delivered by the free-electron laser in Hamburg (FLASH). Here, the aim is to carry out dynamical studies on light—matter interaction with self-amplified spontaneous emission (SASE) pulses during temporal coherence spikes as a function of the pump-probe delay and the FEL intensity. In contrast to "conventional" pump-probe experiments at FLASH, where usually the fragmented charged particles are collected upon destructive (ionizing) light—matter interaction, our scheme accesses bound—bound transition of the atomic/ionic target system. Our beamtime campaign at FLASH in June 2016 included several experiments as for example on FEL-intensity-dependent lineshape effects of the He 2s2p line, on dissociation dynamics of methyl iodide and diiodomethane (the analysis of which is not in the focus of this thesis), and on (partially-)coherent coupling effects in doubly-charged neon.

It will be demonstrated in this chapter that performing strong-field transient absorption experiments on neon—a prototype system of atomic physics—allows not only to test common theoretical understanding of fundamental (intense) light—matter interactions, but also expands our knowledge on FEL statistics, its pulse structure and coherence properties. Furthermore, neon presents an ideal test ground to study (non-resonant) ionization kinematics and at the same time (resonant) XUV bound—bound transitions, which serve as benchmark measurements for (near-future) XUV multi-dimensional spectroscopy experiments with three or four SASE-FEL pulses.

6.1 The experimental concept

The experimental XUV-pump—XUV-probe geometry with two SASE-FEL replica pulses as employed for this work is shown in Fig. 6.1 in a simplified illustration. All the optical and opto-mechanical instruments for the pulse-pair preparation, the beam focusing into the target, and the beam transportation through the beamline towards the spectrometer endstation are omitted in Fig. 6.1. Technical details on the instrumentation can be found in chapter 4.2.

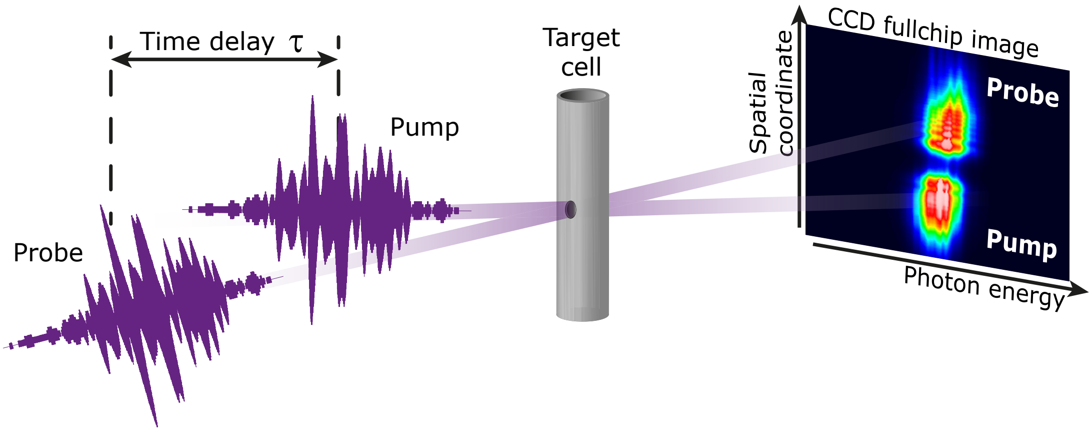

Figure 6.1: Simplified illustration of the experimental geometry. XUV-pump and XUV-probe pulses with (almost) identical SASE-noise pattern in the temporal and spectral distribution of the radiation fields can be time-delayed with respect to each other. The pulses are focused into a dilute neon gas-phase target following the trajectories of a non-collinear interferometric mirror setup. In the far-field downstream of the target cell, a dispersive grating (not shown) in combination with a CCD-sensor array detects the transmission response signals of both pump and probe, simultaneously. A complete technical scheme of the setup including all optical instruments is presented in section 4.2.

The experimental procedure relies on two (almost) identical, but differently intense SASE-pulse copies—denoted as pump and probe pulses—focused into a neon target medium in a *non-collinear* scheme. In contrast to the collinear two-color geometry of the HHG experiment presented in chapter 5, this geometry allows to measure the XUV transmission response of both pump and probe pulses, simultaneously, spatially separated on the same spectrometer. The XUV transmission signal gives direct access to the internal quantum mechanical processes of the *bound-state* atomic/ionic system as response to two cooperatively interacting intense fields. So far, most previous related XUV-pump—XUV-probe experiments aimed at the measurement of the ion-electron momentum distributions and the kinetic energy released in the interaction process [158, 202].

In contrast to the pump—probe experiments of the previous chapter 5 with HHG radiation as a weak (perturbative) excitation-transition step in the intact (neutral) neon atom, here, the pump pulse multiply ionizes the neon atom in sequential steps. The initial ionization strongly changes the opacity/transparency of the target medium for the succeeding probe pulse. In addition to those spectral changes due to ionization, resonant transition signatures from the created Ne^{2+} can be probed as a function of the time delay. The considered ionization and transition pathways in neon for intense (10^{13} W/cm^2-scale intensity) XUV radiation close to 50.6 eV photon energy are illustrated in Fig. 6.2.

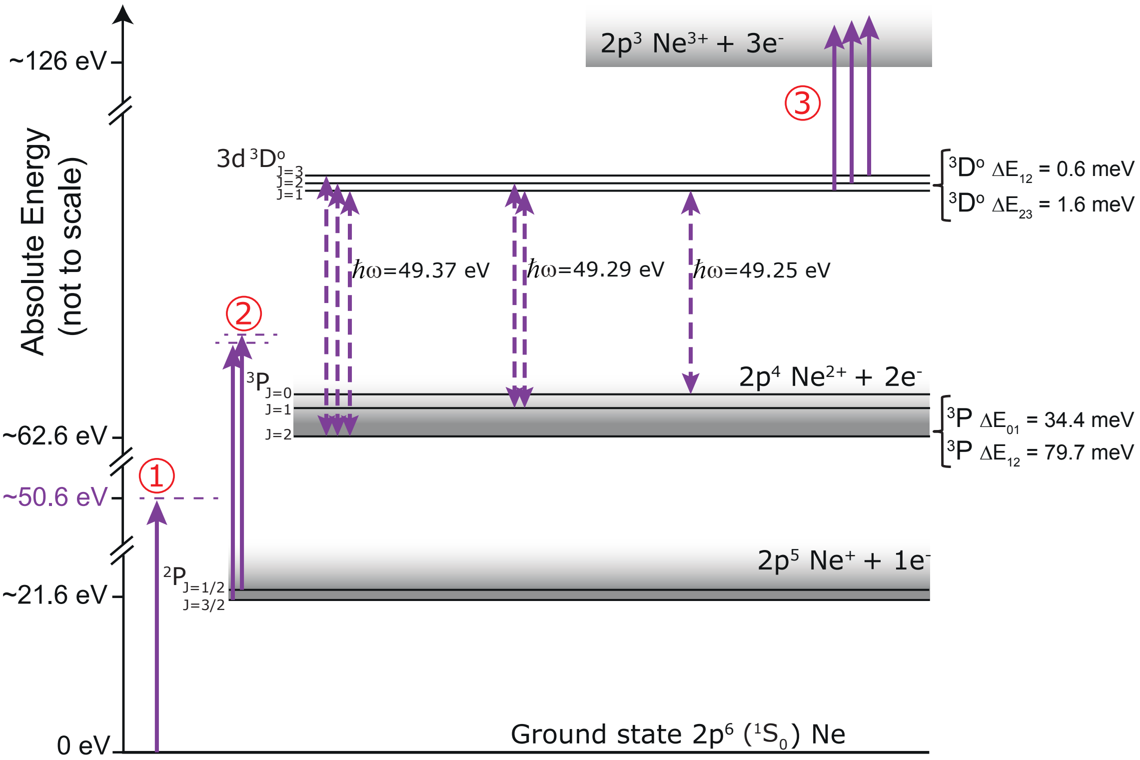

Figure 6.2: Schematic illustration of the sequential ionization and transition pathways the neon target can undergo in the presence of the applied strong-field radiation at ~50.6 eV photon energy (violet arrows). Three sequential ionization steps from ground-state neutral Ne to Ne^{3+} are indicated by the red numbers (time-ordering from left to right). The axis of ordinates indicates the absolute (photon) energy absorbed by the system with respect to the neon ground state. Ionization edges are shaded in gray. A first interaction step ionizes Ne (1st continuum threshold: ~21.6 eV) creating Ne^+ with the spin-orbit ground state ${}^2P_{\frac{1}{2},\frac{3}{2}}$. The subsequent second ionization step leads to Ne^{2+} of spin-orbit triplet ground-state configuration ${}^3P_{0,1,2}$ (2nd continuum threshold: ~62.6 eV). In Ne^{2+} several (de-)excitation quantum transitions termed by ${}^3P_{0,1,2}$–$3d\,{}^3D_{1,2,3}$ are possible, indicated by the dashed violet arrows. The subsequent generation of Ne^{3+} via the absorption of an additional photon and the transition above the 3rd continuum threshold at ~126 eV is comparatively weak, however, it might play a role for observed spectral broadening effects. Note, that due to a limited spectrometer resolution of ~ 50 meV only three spectral bound—bound transition lines can be observed near ~49.37 eV, ~49.29 eV and ~49.25 eV photon energy. Drawn according to [203].

Three sequential ionization steps are possible and indicated by the red numbers (time-ordering from left to right). In the doubly-charged neon ion (Ne^{2+}), a valence electron can be promoted out of the $2p^4$ ground state into the 3d shell upon absorption of an additional photon. This leads to several bound—bound multiplet transitions of Ne^{2+} classified by $^3P_{0,1,2}$–$^3D_{1,2,3}$ and marked by the dashed violet arrows in Fig. 6.2. Due to limitations in the spectrometer resolution, the 1-meV-spaced 3d multiplets cannot be resolved and only the ground-state ($^3P_{0,1,2}$) fine-structure splitting is observed in the experiment as a triplet spectral resonance structure with peaks near ∼49.37 eV, ∼49.29 eV and ∼49.25 eV photon energy. Benchmark measurements based on discharge spectroscopy are available [204].

6.2 Statistical properties of SASE pulses

In this section, the statistical properties of SASE (self-amplified spontaneous emission) radiation as emitted by free-electron lasers (FELs) will be discussed. As described in section 3.1.2 of chapter 3, the FEL lasing process originates from shot noise, which grows with the undulator length. Consequently, the emitted SASE-FEL pulses exhibit the properties of chaotic linearly polarized light. How SASE-FEL pulses can be characterized and simulated with a simple model [18] will be explained in what follows. The model is a computationally inexpensive (reduced) alternative to fairly complete SASE-FEL theory [86].

The FEL start-up is typically provided by a white noise spectrum that has spectral components within the FEL bandwidth range, which will be amplified. As a starting point for the modeling, the frequency-domain electric field can be written as

$$E_0(\omega) = \widetilde{\mathcal{E}}_0(\omega)\exp[\mathrm{i}\widetilde{\varphi}_0(\omega)], \tag{6.1}$$

with a discrete spectral amplitude function $\widetilde{\mathcal{E}}_0(\omega) = \sqrt{\widetilde{I}(\omega)}$ that is initially defined in accordance with an experimentally measured average FEL spectrum $\widetilde{I}(\omega)$ of width $\Delta\omega_{\mathrm{FWHM}}$. Usually, a Gaussian profile is a good first approximation for $\widetilde{\mathcal{E}}_0(\omega)$. The spectral phase function $\widetilde{\varphi}_0(\omega)$ is given by independent random numbers between $-\pi$ and π at all frequencies. The SASE phase relation is fixed within each pulse, but it fluctuates from pulse to pulse.

The time-domain representation of Eq. (6.1) can be obtained by means of the Fourier transform

$$E_0(t) = \frac{1}{\sqrt{2\pi}}\int E_0(\omega)\,\mathrm{e}^{\mathrm{i}\omega t}\,\mathrm{d}\omega, \tag{6.2}$$

which leads to an infinite-duration temporal signal (corresponding to the infinite number of electron arrival times in the undulator) consisting of stochastic spikes. Now, the field $E_0(t)$ is multiplied by a Gaussian (or any other realistic profile) temporal-amplitude filtering function

$$F_{\mathrm{G}}(t) = \mathcal{E}_0\,\mathrm{e}^{-(t/t_{\mathrm{G}})^2} \tag{6.3}$$

with its width $t_\mathrm{G} = t_\mathrm{FWHM}/\sqrt{2\ln 2}$ corresponding to the known (average) FEL pulse intensity duration t_FWHM. The eventually tailored SASE-FEL pulse is given by

$$E_\mathrm{f}(t) = F_\mathrm{G}(t) \cdot E_0(t) = \frac{\mathcal{E}_0\, \mathrm{e}^{-(t/t_\mathrm{G})^2}}{\sqrt{2\pi}} \int E_0(\omega)\, \mathrm{e}^{\mathrm{i}\omega t}\, \mathrm{d}\omega. \tag{6.4}$$

With the temporal boundaries of $F_\mathrm{G}(t)$, the SASE phase relation is not fully random anymore and the pulses are said to be *partially coherent*. Fourier transforming back into the frequency domain yields the spectral properties of the final SASE-FEL pulse

$$\widetilde{E}_\mathrm{f}(\omega) = \mathcal{F}[E_\mathrm{f}(t)] \equiv \widetilde{\mathcal{E}}_\mathrm{f}(\omega) \exp[\mathrm{i}\widetilde{\varphi}_\mathrm{f}(\omega)], \tag{6.5}$$

with a partially coherent phase $\widetilde{\varphi}_\mathrm{f}(\omega)$ and a spectral amplitude $\widetilde{\mathcal{E}}_\mathrm{f}(\omega)$ now exhibiting narrow peaks similar to realistic FEL spectra as known from many experiments and FEL theory [86].

In general, the averaged FEL spectral bandwidth, $\Delta\omega_\mathrm{FWHM}$, can be related to the SASE coherence time τ_coh according to the definition [205]

$$\tau_\mathrm{coh} \equiv \int_{-\infty}^{\infty} [C(\tau)]^2\, \mathrm{d}\tau = \frac{2\sqrt{2\ln 2\pi}}{\Delta\omega_\mathrm{FWHM}} \tag{6.6}$$

with the first-order temporal correlation function

$$C(\tau) \equiv \frac{\langle \int E(t) E^*(t+\tau)\, \mathrm{d}t \rangle}{\langle \int |E(t)|^2\, \mathrm{d}t \rangle}, \tag{6.7}$$

under the realistic assumption that the overall FEL pulse duration t_G is much longer than τ_coh. The angle brackets in Eq. (6.7) denote the (assumed Gaussian) statistical average over many single-shot SASE pulses. The coherence time is a measure for the mean time interval between two phase fluctuations. Hence, when applied to a target system, τ_coh dictates the time scale on which coherent quantum-dynamical effects (compare section 2.2.2 of chapter 2.1) due to FEL light—matter interaction play a role.

One way to verify Eqs. (6.7) and (6.6) by experimental means is the measurement of interferometric autocorrelation traces [18], which exhibit characteristic peaks of temporal width corresponding to the coherence time τ_coh [206, 207]. Note, that most experimental techniques only have access to the second-order "intensity" correlation function, which can be related to Eq. (6.7) [208]. The first-order "field" correlation can only be measured in fully collinear [127], or non-collinear boxcar geometries employing a collinear local oscillator field.

Because the electron density distribution is not only stochastic in time but also in space when entering the undulator, the phase of the wavefront at different points transverse to the propagation direction of the SASE-FEL beam also fluctuates. In the beam focus region all the transverse SASE radiation modes overlap and interact with the target. In analogy to Eq. (6.7) also the spatial (transverse) coherence behavior of the FEL can be analyzed [209]. Typical transverse coherence lengths at FLASH are on the order of

300 µm [210]. Also fluctuations in the beam size and the beam pointing originate from the randomness in the spatial beam properties.

Finally, Fig. 6.3 presents a set of measured SASE-FEL spectra, $\widetilde{I}(\omega)$, recorded during the experimental campaign at FLASH, and is compared with corresponding simulations. While each single-shot spectrum has its individual spectral shape composed of randomly distributed peaks (or undulator modes), on average, the SASE-FEL spectrum converges towards a continuous Gaussian-like profile function with the FEL bandwidth $\Delta\omega_{\mathrm{FWHM}}$.

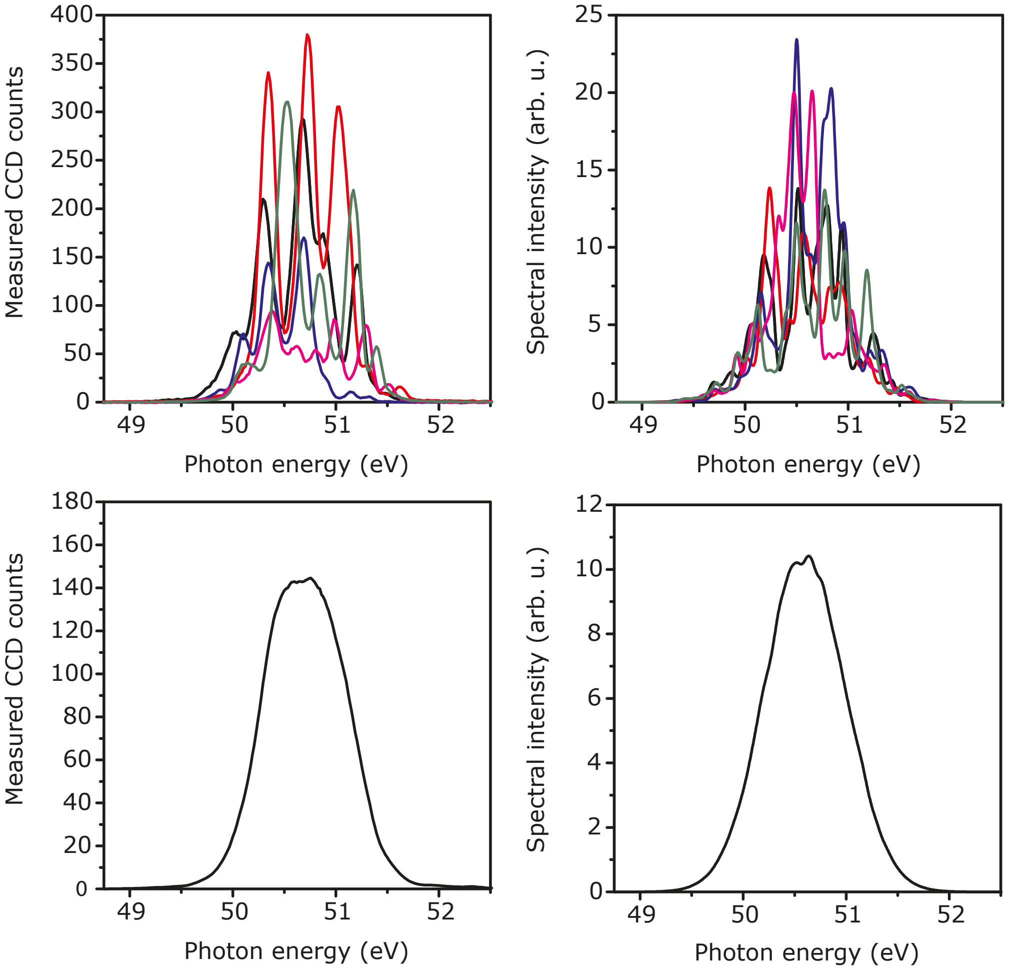

Figure 6.3: Measured SASE-FEL pulse spectra vs. simulations according to Eq. (6.4). Panel (a) shows 5 subsequent FLASH light pulse spectra at ~50.6 eV central photon energy measured with the online VLS reference spectrometer [92]. Averaged over 1000 single shots, the SASE spectrum converges towards a Gaussian-type profile with a fitted bandwidth $\omega_{\mathrm{FWHM}} \approx 0.78$ eV (panel c). Panels (b) and (d) present corresponding simulation data assuming an overall pulse duration $t_{\mathrm{FWHM}} = 100$ fs and convoluted with an assumed 80 meV FWHM Gaussian spectrometer response function.

6.3 Instrumentation and data acquisition at FLASH

The presented XUV-pump—XUV-probe experiments were carried out at the free-electron laser FLASH (DESY, Hamburg) where the experimental apparatus was setup at the user port "beamline 2" (BL2) with a primary focus of focal spot size $\sim 25\,\mu$m full width at half maximum (FWHM). Background information on FEL theory and general FLASH machine parameters are given in chapter 3. Technical details of the own experimental setup and the in-house split-and-delay unit (SDU) used for the preparation of time-delayed FEL pulse pairs can be found in chapter 4 of this thesis.

All experiments presented here were conducted in the so-called single-bunch (or single-shot) mode at a repetition rate of 10 Hz. In the single-bunch mode, various FEL pulse parameters are measured by the FLASH diagnostic system, such as the pulse energy, the beam position, or the spectral distribution, on a non-invasive shot-to-shot basis. The FLASH diagnostic system runs in parallel with user experiments and assigns each FEL pulse (train) with a time stamp, the so-called bunch ID. In order to synchronize our own "experimental clock" to the FLASH timing, we readout our XUV CCD (charge-coupled device) spectrometer camera per trigger signal supplied by the FLASH operation system for each single shot. The acquired data was saved together with the actual bunch ID for this very moment. In the post-analysis, the measured spectra were sorted according to pulse energy monitored by the in-house photon diagnostics.

The spiky nature and the considerable shot-to-shot fluctuations of the spectral intensity distribution in the SASE-radiation field were demonstrated in Fig. 6.3 of section 6.2. These spectra represent the typical SASE-pulse characteristics during the presented experiments. The spectral intensity fluctuates around a center FEL photon energy of $\sim$50.6 eV (wavelength $\lambda = 24.5$ nm) with an average spectral bandwidth of $\Delta\omega_{\mathrm{FWHM}} \approx 0.78\,\mathrm{eV}$ FWHM.

For all measurements, an average temporal pulse duration of $\sim$100 fs was deduced from electron bunch length measurements in the accelerator section (so-called LOLA measurement, named after the authors of Ref. [211]). This is only an estimated upper limit since the FEL lasing process can vary along the longitudinal electron distribution and the generated temporal photon pulse duration hence can differ from the electron bunch length. The precise measurement of the photon pulse duration is usually achieved with photo-electron streaking or two-beam cross-correlation experiments, which cannot be performed in parallel to other FEL experiments.

The averaged pulse energy measured for all shots with a gas monitor detector (GMD) [89, 91] upstream of the experiment was 47.5 µJ with shot-to-shot rms deviations of $\sim 28\%$, as shown in Fig. 6.4 for 1000 consecutive shots. These pulse energies correspond to XUV intensities on the order of up to $10^{14}\,\mathrm{W/cm^2}$. Since the beam passes several optical components, such as mirrors and the grating of the parasitic reference spectrometer [92] along the FEL-beam distribution line before it enters the experimental setup, the intensity in the FEL—target interaction region is expected to be considerably lower.

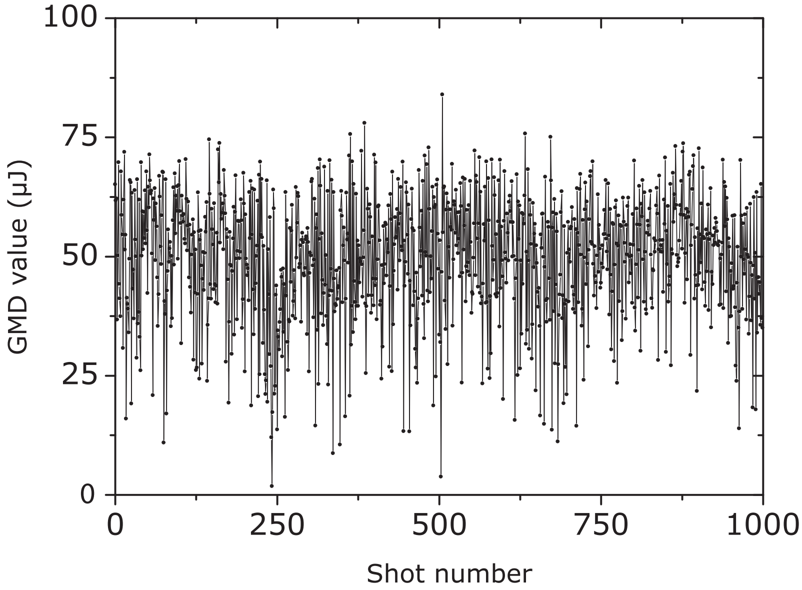

Figure 6.4: Shot-to-shot FEL pulse energy of 1000 consecutive pulses measured by the online gas-monitor detector (GMD) in the beam distribution area (BDA) at FLASH for the presented Ne pump—probe experiment. The expected stochastic variations due to the SASE process, as well as slight systematic drifts, are evident. The systematic drifts might be attributed to the control circuit of the electron accelerator section.

As described in chapter 4, the split-and-delayed FEL-beam components by the in-house SDU hit the same spectrometer grating and CCD sensor, but slightly separated vertically (one above the other) so that both spectra could be readout simultaneously. In order to capture spatio-spectral information of the transverse FEL beam profile (along the vertical beam axis) for diagnostic purposes and to obtain a faster CCD frame rate, the 1340×400 CCD pixel array was partitioned into six regions-of-interest (ROIs). The six ROIs were readout in the vertical binning mode, which is done internally in the hardware of the chip. The two spectral beam signatures recorded with the CCD camera and the selected ROI readout pattern are shown in Fig. 6.5.

The part of the FEL beam that passed the variable mirror delay line (the lower beam in Fig. 6.5) of the SDU has on average a $\sim$35% higher signal count rate on the detector than the other partial beam, which was reflected by the second, fixed mirror. In analogy to traditional pump—probe time-resolved experiments [13], where usually a strong pump pulse is used to initiate quantum mechanical motion and a time-delayed, often much weaker probe pulse, the "variable" beam is henceforth denoted as "pump" and the "fixed" beam is denoted as "probe". However, it is important to point out, that here both detected beam parts may play the role of a "traditional pump" and a "traditional probe" depending on the time-delay configuration, since their pulse properties are almost identical and both pulses can drive the same quantum mechanical ionization/excitation channels in the target system.

The slight shift in the photon energy between pump and probe beams in Fig. 6.5 already

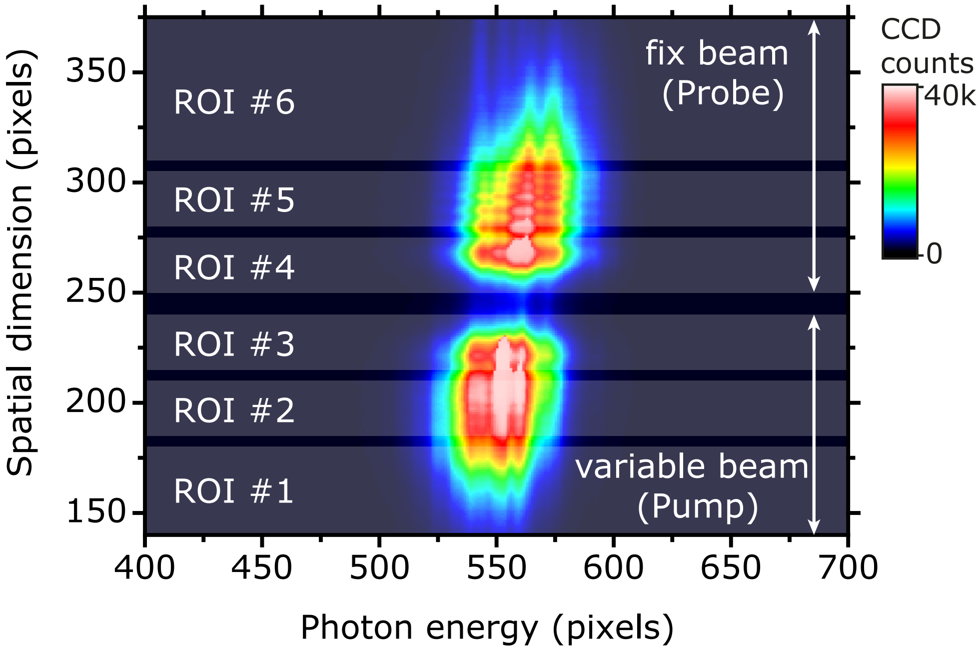

Figure 6.5: CCD fullchip image of both FEL pump (lower beam component) and probe (upper beam component) measured within 5 s of exposure time and 3.5 µm of Al attenuation material before the sensor. The pump beam was reflected over the dynamical, variable mirror of the SDU. The mirror for the probe was locked to a fixed position. Under experimental conditions, the spectral information was binned over six certain regions-of-interest (ROIs) as indicated by the shaded areas (pump: ROIs #1–3; probe: ROIs #4–6). The horizontal stripes observed on top of the spectral beam signatures are likely due to Fraunhofer diffraction at the horizontal blades of the 2d spectrometer slit. Note, that the vertical axis contains spatial information and the horizontal one only spectral information (yet in uncalibrated CCD pixel units).

suggests the presence of a systematic spatial chirp, i.e. an inhomogeneous frequency distribution along the transverse spatial dimension of the FEL beam profile. This is further substantiated in Fig. 6.6, where the binned detector signal processed for the six CCD ROIs individually is plotted as a function of the FEL photon energy. The signal peak of the three pump spectra is found to be centered around $\sim$ 50.1 eV photon energy. The three probe spectra are observed close to 50.6 eV photon energy, as specified for the experimental campaign, each exhibiting a weak side peak near $\sim$ 50.1 eV photon energy.

For the calibration of the CCD sensor to photon energy units, the pixel-to-energy relation from the previous experiment with HHG radiation was recycled (cf. chapter 5.5). The pixel-to-energy assignment was matched with respect to the known photo-excitation energy value of the $2p^4(^1D)3s(^2D)4p$ line of Ne close to 50.6 eV [76] observed in both experiments. Effectively, the reassignment of calibrated pixels corresponds to a mechanical shift of the camera along the spectral flat-field plane (or a rotation of the grating) towards the original camera position of the HHG experiment and the flat-field energy range originally subtended by the camera chip. The geometrical instrument parameters of the spectrometer system, i.e. the grating orientation and its distance from the slit, were

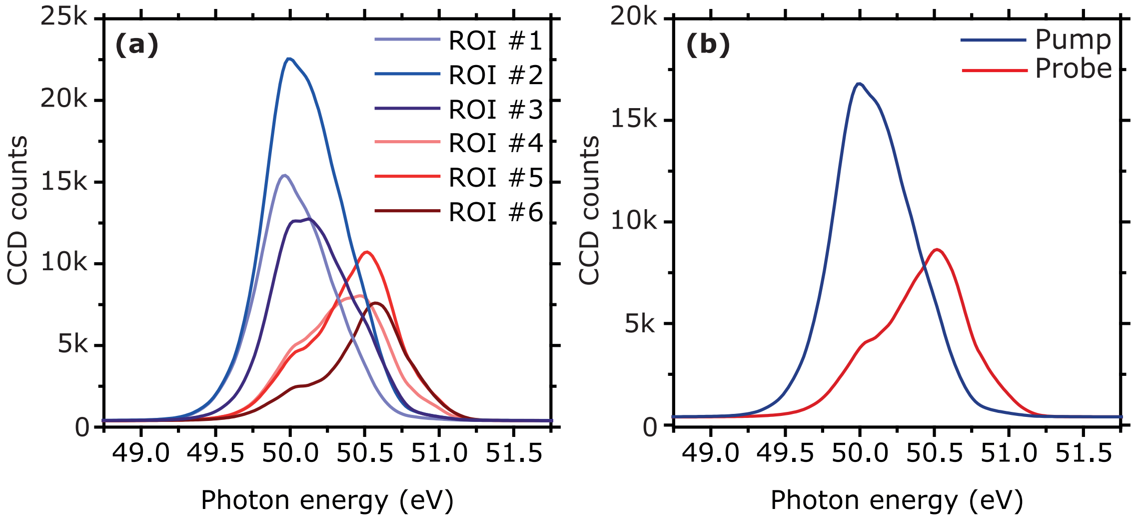

Figure 6.6: SASE-FEL pump and probe pulse spectra measured with our own XUV spectrometer endstation and binned over six different ROIs on the CCD sensor array as indicated in Fig 6.5. In panel (a), only slight spectral differences can be observed for signals taken for the same half-pulse but in different ROIs (pump: ROIs #1–3, and probe ROIs #4–6). Clear differences however are detected in the spectral composition between pump and probe pulses. The averaged spectra over the ROIs #1–3 for the pump and ROIs #4–6 for the probe serve as reference signals, $I_0(\omega_{\mathrm{FEL}})$, for the data analysis (panel b). Data is averaged over 3300 single FEL shots.

not changed between the experimental campaigns. Only the point of incidence of the beam on the grating cannot be exactly reproduced for each experiment. However, this does not change the spectrometer response significantly. In both experiments, the spectral resolution is approximately 50 meV at energies close to 50 eV.

6.4 Post analysis

The post analysis of data taken at FLASH relies on a correct assignment of measured spectral signals or other experimental parameters to the bunch ID supplied by the FLASH data acquisition (DAQ). Confidence of the timestamp-based synchronization between the FLASH DAQ and our self-developed, LabVIEW-based experimental control and DAQ software can be proven by correlating the respective data sets to each other.

Plotted in Fig. 6.7 is the CCD-signal strength—pulse-energy relationship for 3.300 reference signals, $I_0(\omega)$. The data set reveals a high degree of almost linear point-by-point correlation and fits well with a linear regression line (linear regression coefficient $\mathrm{R}^2 \approx 0.8$). Slight deviations from the linear slope are attributed to non-linearities in the measurement performance of the CCD camera and/or the gas-monitor detector (GMD). Only a few point pairs can be identified as outliers.

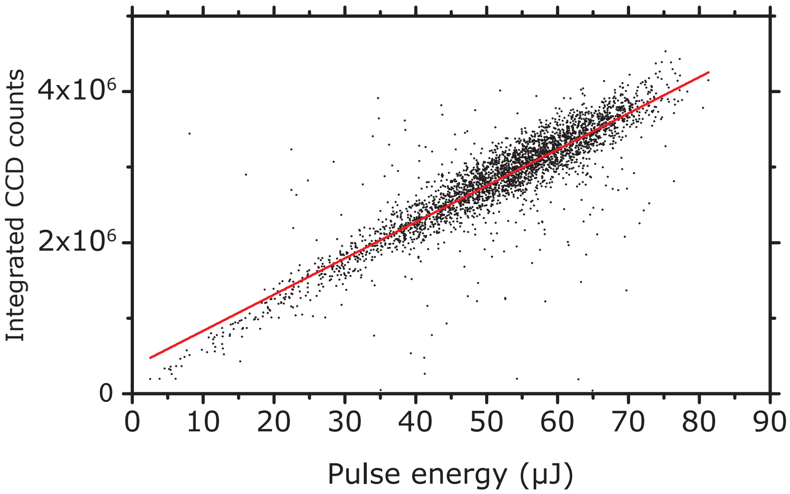

Figure 6.7: Correlation map of integrated reference signals detected by the CCD camera vs. pulse energy measurements by the GMD (black dots). The data set was fitted with a linear regression line ($R^2 \approx 0.8$). The measured pulse energy is on average $\sim 52\,\mu J$ with a $\sim$24% rms shot-to-shot deviation.

For comparison, Fig. 6.8 presents the correlation analysis of the CCD-signal strength after transmission through the neon target, $I(\omega)$, vs. the corresponding pulse energy detected by the GMD. This data set consists of 24.800 events. As expected, the point-by-point relationship is clearly non-linearly correlated, in particular at higher pulse energies and CCD signals, respectively, which is a result of FEL—matter interaction in the target (i.e. transparency due to excitation/ionization processes, as investigated in section 6.5 of this thesis). Except for different aluminum attenuation foils before the CCD sensor, both data sets were taken successively under the same experimental conditions and the specified FLASH machine parameters.

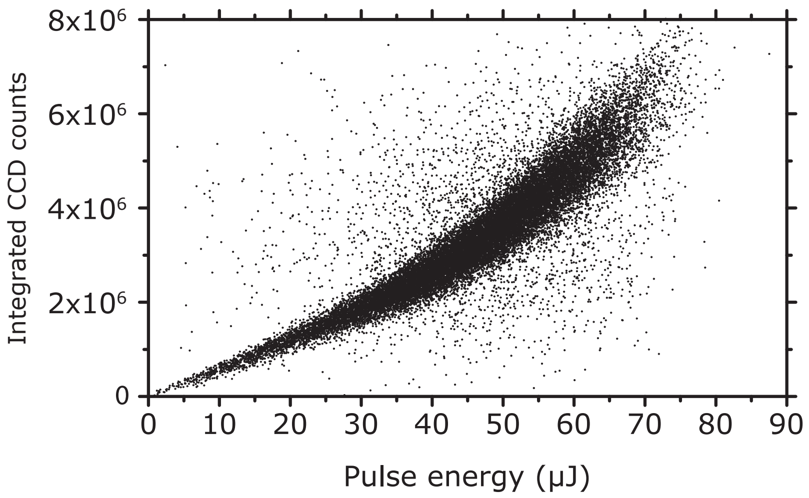

Figure 6.8: Correlation map of integrated CCD transmission signals through dilute neon vs. GMD pulse energy measurement. A clear non-linear dependence can be observed due to light—matter interaction and the resulting enhancement of transparency (cf. section 6.5). The measured pulse energy is on average ∼ 47 μJ with ∼28% rms deviation.

6.5 Ionization control by XUV strong-field absorption in neon

The irradiation of a sample medium with an intense XUV pulse causes photo-ionization and, depending on the produced ion species and its concentration, variations of the refractive index of the medium. As the density distribution of the ionized medium depends directly on the instantaneous photon flux,

$$\Phi(t,z) = \frac{I(t,z)}{\hbar\omega_{\mathrm{FEL}}}, \tag{6.8}$$

assuming a constant photo-absorption cross section σ over the radiation bandwidth and a detuning far from any resonance [212], the ultra-fast variation of the opacity (or the transmission) of the medium for a second, delayed (assumed non-invasive probe) light pulse follows the temporal intensity profile of the ionizing (pump) pulse. The coordinate z is the propagation distance through the (assumed dilute) medium of density ρ according to the time-domain representation of Beer's law [also cf. Eq. (2.55)]

$$I(t,z) = I_0(t)\, e^{-\sigma\rho z}. \tag{6.9}$$

The z-dependence will be henceforth omitted as the evolution of the intensity signal at different positions z inside the medium itself will not be treated here. Only the signal before, $I_0(t)$, and behind the sample, $I(t)$, will be considered.

In this section, the relationship between the *temporal* FEL intensity profile and the induced transient transmission changes of a neon sample will be investigated. The non-collinear pulse geometry (see Fig. 6.1) allows for the probing of spatio-temporal information of transmission signals from both pulses (pump and probe) simultaneously on a single-shot basis.

So far, only FEL reference spectra *without* the sample-gas medium in the interaction cell, $I_0(\omega_{\text{FEL}})$, were presented. Shown in Fig. 6.9 are transmission signal spectra, $I(\tau,\omega_{\text{FEL}})$, propagated through a neon-gas medium at a backing pressure of ~50 mbar. Both pump and probe pulse spectra are plotted as a function of the relative pump—probe delay τ, complemented with corresponding averaged pulse energy (GMD) values. The presented data have been compiled from the results of three time-delay scans repeated consecutively under the same experimental conditions. In total 600 single shots were integrated at each time-delay position. The data set for the three scans individually is presented in appendix B. During all measurements, the data was binned over the three CCD ROIs for pump and probe as depicted in Fig. 6.5.

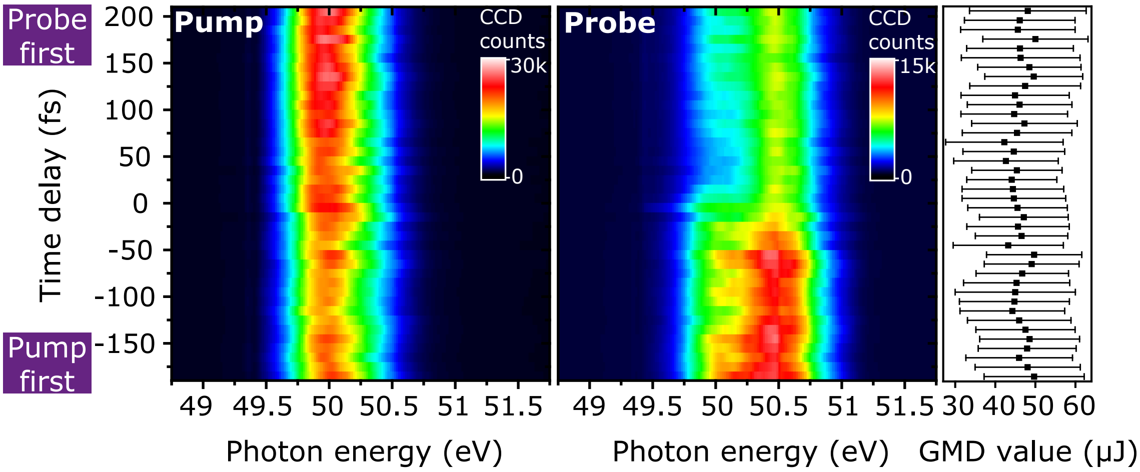

Figure 6.9: Pump and probe pulse transmission spectra through gaseous Ne as a function of the relative time delay τ scanned with 10-fs steps. The color scale indicates the spectral intensity measured on the CCD chip. At positive delays, the probe precedes the pump (probe—pump configuration), and vice versa for negative delays (pump—probe configuration). Spectral artifacts imprinted on the transmission signal of both pump and probe along the delay axis can be directly correlated to the pulse energy measurement performed by the gas-monitor detector (GMD) in conjunction with the experiment. The mean pulse energy determined by the GMD is 47.5 μJ with a relative shot-to-shot standard deviation of ~28%. GMD standard error of the mean value over 600 shots is ~ 0.02 μJ.

An enhanced transparency can be observed in both spectra depending on the time delay as soon as one pulse, the pump or the probe, respectively, precedes and interacts earlier with the target. The transmission signal observed in the pump spectrum is increased at positive delays (probe—pump configuration), while it appears to be decreased in the probe spectrum at the same time-delay setting, and vice versa (pump—probe configuration).

Because the incident pump and probe pulses are not exact identical copies of each other, both in the their spectral distribution as well as their pulse energy (as investigated in the previous section 6.3), the recorded transmission signals for pump and probe are not perfectly symmetric with respect to τ.

The integration over the full measured spectral intensity envelope,

$$S(\tau) = \int I(\tau, \omega_{\mathrm{FEL}},)\, \mathrm{d}\omega_{\mathrm{FEL}}, \tag{6.10}$$

provides the total transmission signal for each τ-setting (assuming a constant CCD performance for each pixel and subtracting the background). The signal $S(\tau)$ represents the delay-dependent cross-correlation of the probe pulse intensity $I_0^{\mathrm{probe}}(t)$ with the instantaneous transmission function $T\left[I_0^{\mathrm{pump}}(t)\right] \equiv T(t)$:

$$S(\tau) = \int_{-\infty}^{\infty} I_0^{\mathrm{probe}}(t-\tau) \cdot T(t)\, \mathrm{d}t. \tag{6.11}$$

The instantaneous transmission function can be obtained from Beer's law

$$T(t) := \frac{I^{\mathrm{pump}}}{I_0^{\mathrm{pump}}}(t) = \exp\big(-\sum_j \sigma_j N_j(t)\, \rho\, z\big), \tag{6.12}$$

with $N_j(t)$ representing the relative population of neon in the charge state j ($j = 0, 1, 2$; neutral, singly and doubly ionized) and corresponding (single-photon) ionization cross sections σ_j. The pathlength–density ($\rho\, z$) product is known in good approximation from the HHG experiment presented in chapter 5.5. The involved processes mentioned above are described by a set of coupled rate equations [213] for the population of the different ionic species of Ne, as described in chapter 2.2.3:

$$\begin{aligned} \dot{N}_0(t) &= -\sigma_0\, \Phi(t)\, N_0(t) \\ \dot{N}_1(t) &= \sigma_0\, \Phi(t)\, N_0(t) - \sigma_1\, \Phi(t)\, N_1(t) \\ \dot{N}_2(t) &= \sigma_1\, \Phi(t)\, N_1(t) - \sigma_2\, \Phi(t)\, N_2(t). \end{aligned} \tag{6.13}$$

Since the needed cross sections for a full description according to the level scheme in Fig. (6.2) are only partly known, Eqs. (6.13) only account for the dominant single-photon processes Ne → Ne^+ with $\sigma_0 = 9.32$ Mb [214], $\mathrm{Ne}^+ \rightarrow \mathrm{Ne}^{2+}$ with $\sigma_1 = 9.36$ Mb [214], and for an assumed small loss channel $\mathrm{Ne}^{2+} \rightarrow \mathrm{Ne}^{3+}$ via resonance-enhanced two-photon transitions with a cross section of $\sigma_2 = 0.01$ Mb chosen to best fit by eye.

Eqs. (6.11) and (6.12) in principle also hold for the description of the inverse case, in which the pump signal is modified by the preceding probe (probe—pump configuration). The crucial assumption however is the non-invasive (non-ionizing) "probe character" of the succeeding pulse.

Fig. (6.10) presents measured cross-correlation signals $S(\tau)$ determined according to Eq. (6.10) for three different pulse-energy regimes as selected by the GMD statistics. Dots are measured data and the solid lines are least-square fits by the Gaussian error function.

In order to investigate relative transmission changes, the data are at first normalized by the division through the fitted high-error-plateau value of the curve. Afterward the low-error baseline was set to 0. Consequently, when no Ne ions are present $S^{\text{pump}}(\tau \ll 0) = 0$ and $S^{\text{probe}}(\tau \gg 0) = 0$. In the opposite extreme case, i.e. for $S^{\text{pump}}(\tau \gg 0)$ and $S^{\text{probe}}(\tau \ll 0)$, an enhancement of the relative transmission can be observed in all cross-correlation signals with the highest values for the highest applied pulse energies. A smooth transition in the signal can be observed when both pulses overlap, $S(\tau \approx 0)$. Given values for the time-delay position and the width are derived from the first derivative of the fitted error function. The derivative has the shape of a Gaussian and reflects the temporal profile of the cross-correlation and the intensity response. The width taken at the FWHM of the derivative Gaussian distribution determines the difference between the $\sim 12\%$ and $\sim 88\%$ values of the normalized error function. The measured rise time of the probe intensity-response signal is between 50–60 fs for pulse energies above 35 µJ (panels b and c). The error function appears to be shifted towards negative time-delays with respect to the pulse overlap ($\tau = 0$) by roughly 18 fs. It is important to note that only for the probe-pulse signals in panels (b) and (c) of Fig. 6.10 fits with a high degree of confidence have been achieved. While the data in panel (a) suffer from a large statistical RMS error, the fits for the pump spectra are impeded by a dominant "coherence artifact" emerging exactly in the pulse overlap ($\tau = 0$) and coinciding with the rising edge of the signal. Nevertheless, these data fits indicate a slight temporal shift of the pump-transmission signal in the opposite way as observed for the probe [panels (b) and (c)], and for lower probe-pulse energies an increased $\sim$100-fs signal rise time (panel a).

For the analysis of the transient behavior in the pulse-overlap region the measurements are complemented with a model calculation based on the above theoretical description. A Gaussian intensity envelope is assumed representing the average over many FEL pulses. Fig. (6.11) compares cross-correlation signals, $S(\tau)$, calculated for 100-fs and 50-fs pulse durations at peak intensities of 1×10^{13} W/cm^2, 2×10^{13} W/cm^2 and 7×10^{13} W/cm^2. Assuming an experimental focal spot size of 25 µm, the lower 10^{13} W/cm^2-scale intensities correspond to 1-µJ-level pulse energies, while values in the higher 10^{13} W/cm^2-intensity region correspond to pulse energies of a few tens of µJ, as obtained from the GMD measurement. Comparing the calculations with the measurements suggests the presence of $\sim$ 50-fs duration FEL pulses (on average) with $\sim 10^{13}$ W/cm^2 peak intensities (cf. the blue curve in Fig. 6.11b). The numerical results also demonstrate the behavior of the transmission response when the involved ionization processes already start saturating in the leading edge of the pump pulse at 7×10^{13} W/cm^2 peak intensity for 100-fs pulse durations (cf. the green curve in Fig. 6.11a). In this case, the signal shifts towards positive delays exhibiting a decreased rise time. This behavior is not observed in the experimental data, which gives reason to presume that saturation is not reached in the experiment.

Based on the online measurement of the electron beam properties (LOLA-measurement [211]), a pulse duration of $\sim$ 100 fs was determined for all presented experiments. However, the measurement technique only provides an upper limit for the pulse duration. The FEL photon-pulse duration for pulse energies of a few 10 µJ usually deviates by a factor of $\sim$1.2 (for the largest available wavelengths) to $\sim$2.5 (for the smallest wavelengths) from the LOLA-measurement [215]. A precise online monitoring of the FEL-pulse duration is still not available.

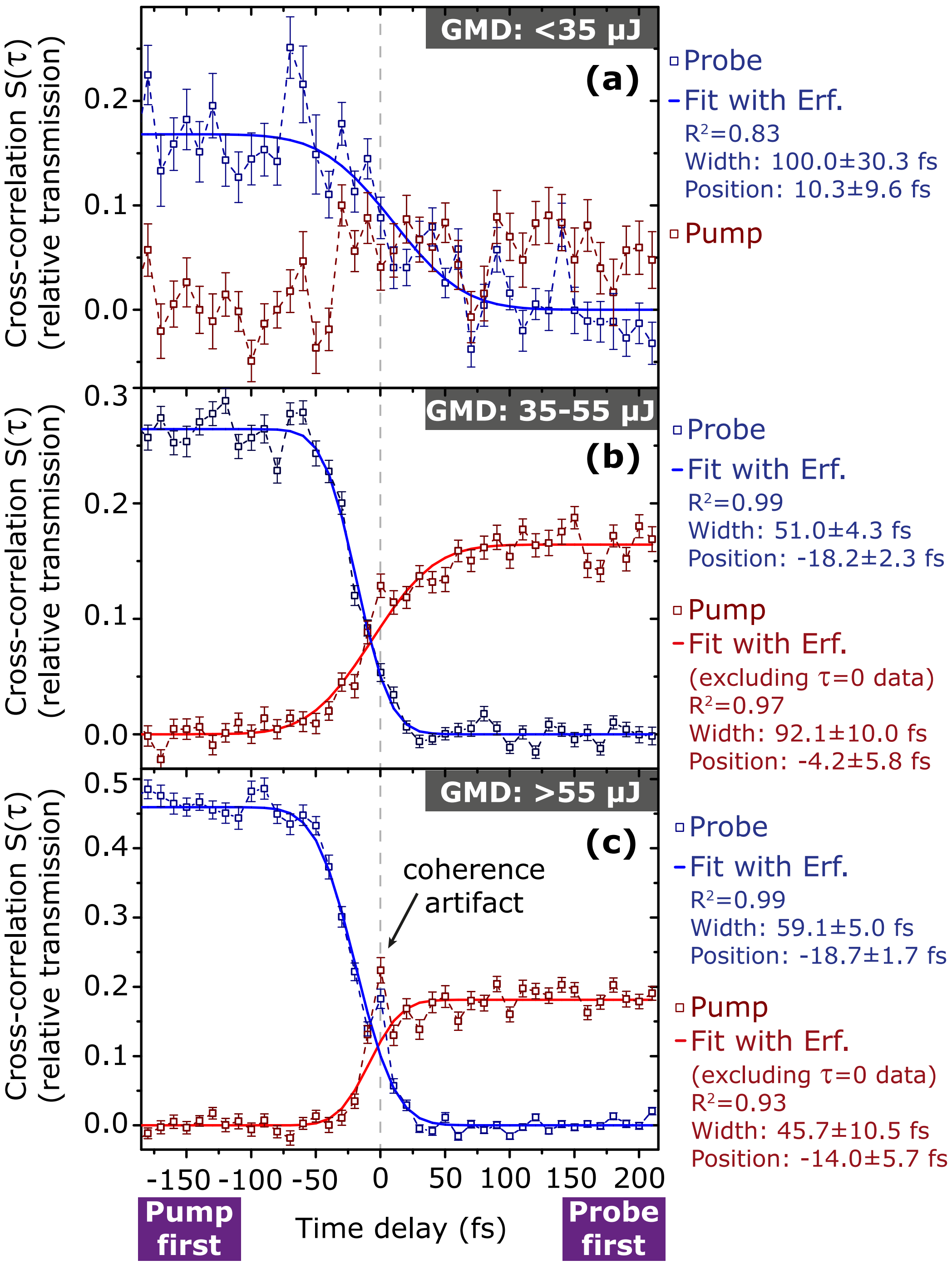

Figure 6.10: Cross-correlation measurements of the transmitted pump and probe intensity for different pulse energies. Given error bars specify the standard error of the mean, σ_n, i.e. the standard deviation of the single results divided by $\sqrt{n}$, where n denotes the total number of measurements. Fits are weighted by $1/\sigma_n^2$. Fit errors indicate uncertainties in the predictor data. In particular for the highest pulse energies (GMD $>$ 55 μJ), an artifactual spike emerges in the signal at $\tau = 0$, which is due to coherence enhancement. This phenomenon will be analyzed in the following section.

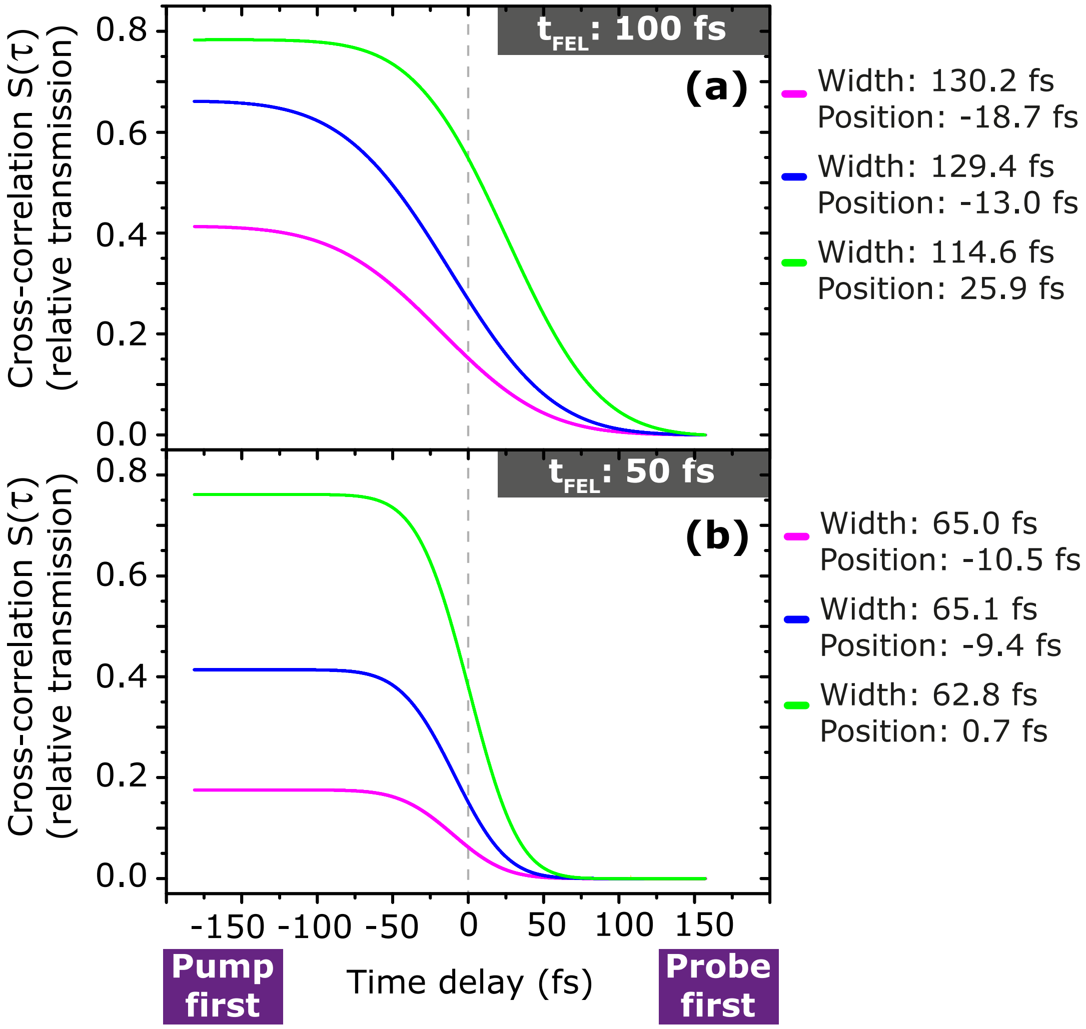

Figure 6.11: Cross-correlation calculations based on Eqs. (6.11) and (6.12) for three different peak intensities: $1 \times 10^{13}\,\mathrm{W/cm^2}$ (magenta curves), $2 \times 10^{13}\,\mathrm{W/cm^2}$ (blue curves) and $7 \times 10^{13}\,\mathrm{W/cm^2}$ (green curves). Panel (a) presents calculation results for 100-fs pulse durations and (b) for 50-fs pulse durations. See the discussion in the main text.

The good agreement between the numerical model and the experiment and the capability of measuring both spectral and temporal information renders the presented methodology a promising experimental tool to monitor FEL-pulse characteristics with the potential to detect irregularities such as spatial chirp and pulse-front tilt [124]. Furthermore, it allows to time-resolve and control multiple sequential ionization processes in a medium by controlling the time delay and the intensity. What remains to be implemented for further improvement of the model is a more realistic, ionizing probe pulse.

As a final remark, The experiment presented here complements a recent study based on an XUV/optical cross-correlation scheme targeting a solid-state sample [216]. The authors report the measurement of the averaged FEL pulse duration with their method. With the here presented method in the gas phase, in addition, information on the FEL coherence time can be extracted, which will be discussed in the following section.

6.6 Coherence enhancement

Several techniques are available for the *direct* measurement of the XUV pulse duration at FLASH, such as auto- or cross-correlation methods, terahertz streaking methods, and methods based on reflectivity or opacity changes of a solid-state sample. A comprehensive overview of the individual methods is given in Ref. [217].

Intensity auto- or cross-correlation in a gas-phase sample has been established as one of the most versatile methods, as information of the overall pulse structure (e.g. Gaussian), the temporal duration and the (partial) coherence properties can be probed. Usually, the cross-correlation signal is created by multiple ionization of the sample through the replica pulses measuring the charged-state-resolved ion yield with an ion detector [218]. The drawback is that cross-correlation measurements usually cannot be implemented as easily as a parasitic pulse diagnostic monitor for user experiments.

In this work, a novel cross-correlation scheme is presented based on the technique of transient absorption. In addition to the temporal FEL-pulse characteristics, this technique provides information on the spectral distribution of the half-pulses *in-situ*. In parallel, the resonant transient bound-state response of the sample system can be probed as function of the delay. How information on the overall averaged FEL pulse duration can be extracted from the data, was discussed in the previous section 6.5. This sections describes the characterization of a temporal SASE-coherence signal measured in the spectral domain, which is the "absorption counterpart" of well-known sharp enhancement features in the ion yield of traditional (ion-detector based) cross-correlation measurements [18,218]. Coherent enhancement of an intensity-dependent signal yield occurs when the replica pulses overlap temporally and the "spiky" SASE-intensity structure interferes constructively. Note, that the electric-field-cycle interference is only possible in collinear geometries, or in non-collinear boxcar geometries including a local oscillator field in collinear alignment with the non-linear light—matter response signal. Furthermore, a sub-field-cycle interferometric stability is necessary (on the order of 10 as for XUV-fields) to avoid cycle-averaging and thus the signal wash-out.

Photo-absorption spectra are obtained in the same way as for the HHG experiments by calculating the optical density (OD) (also cf. chapter 5.5):

$$\mathrm{OD}(\omega_{\mathrm{FEL}}) = \log_{10}\left[\frac{I_0(\omega_{\mathrm{FEL}})}{I(\tau,\omega_{\mathrm{FEL}})}\right]. \tag{6.14}$$

The intensity $I(\tau,\omega_{\mathrm{FEL}})$ is the transmitted signal and $I_0(\omega_{\mathrm{FEL}})$ is the reference signal without the gas target. Both signals were measured successively under the same experimental conditions. The signal $I_0(\omega_{\mathrm{FEL}})$ is presented in Fig.6.6(b) of section 6.3. It was determined from the average over 3300 single shots accounting for an additional 1.5 µm thick Al beam attenuator by re-scaling the signal amplitude (see [134] for the characteristic XUV transmission curve). It is important to point out that no effect of beam clipping at the target cell was evident for any time-delay setting and single reference spectra are not by any means dependent on delay. By averaging over 200 single spectra at each time-delay

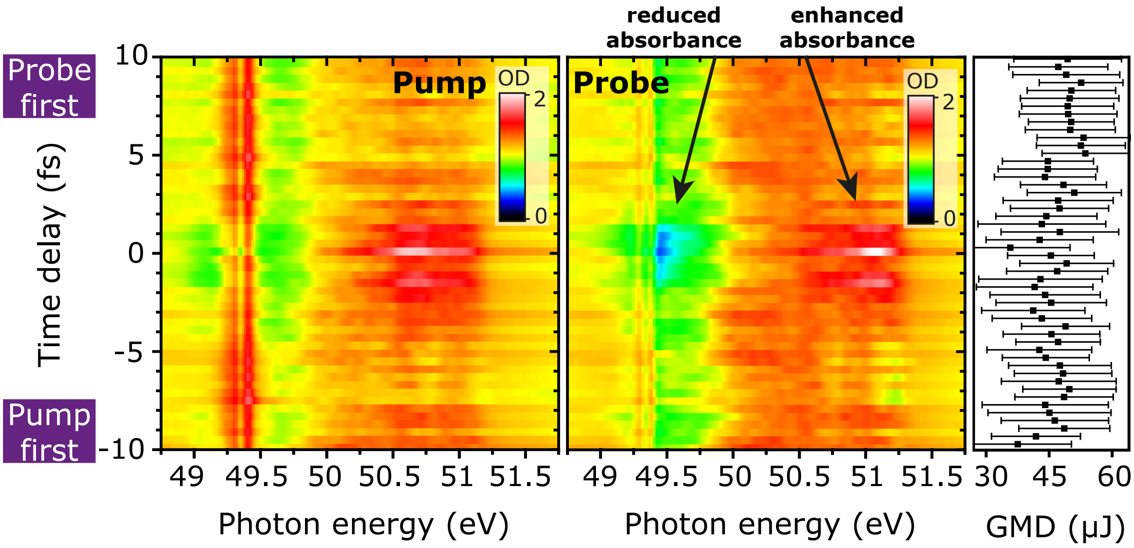

Figure 6.12: XUV-XUV time-resolved absorption spectroscopy on neon with intense SASE-FEL fields measured for pump (left panel) and probe (central panel) signals. Data are complemented with the pulse-energy (GMD) measurements (right panel). Error bars specify rms deviations from the mean over 200 shots per delay setting.

setting for $I(\tau, \omega_{\text{FEL}})$, spectral irregularities imprinted on the OD due to the $\sim 28\%$ rms shot-by-shot fluctuations can be minimized, however, it cannot be fully avoided. Fig. 6.12 presents the obtained time-delay dependent absorption spectra for both pump and probe partial beams again on the target neon. Experimental conditions were the same as those in the previous section 6.5. Only the interferometric incremental step size was reduced to $\Delta\tau = 0.4\,\text{fs}$, where the 20-fs limited observation range hides the general monotonic trend as seen before, thus both traces appear more symmetric.

The spectra shown in Fig. 6.12 exhibit dominant resonance signatures from cumulating multiplet transitions, $^3\text{P}_0 -^3\text{D}_1\,3\text{d}$, $^3\text{P}_1 -^3\text{D}_{1,2}\,3\text{d}$ and $^3\text{P}_2 -^3\text{D}_{1,2,3}\,3\text{d}$ in bound-state Ne^{2+} located at around 49.25 eV, 49.3 eV, and 49.4 eV (assigned according to [203,204]). These observations and other spectral structures resolved in this experiment will be examined in detail in the following section. Here, the focus is exclusively placed on the absorption changes observed around time delay $\tau = 0$, i.e. a bleaching effect of the resonances and the non-resonant background in their close spectral vicinity. As the most prominent feature, a time-dependent dip in the OD shows up in the probe spectrum at ~ 49.5 eV photon energy accompanied by an enhanced OD in the spectral region of the center FEL photon energy around 50.6 eV. Fig. 6.13 shows the averaged data over the spectral range between 49.4 and 49.6 eV photon energy taken from the probe-OD data set (center panel of Fig. 6.12). The dip clearly follows a Gaussian shape with a full width at half maximum (FWHM) temporal duration of $\tau_{\text{coh}} = 2.2 \pm 0.4\,\text{fs}$ fitted using the least squares method. The quantity τ_{coh} reflects the temporal duration of the cross-correlation signal of coherent intensity spikes present in the noisy temporal SASE profile of the replica pulses, or in other words the time scale of the SASE-field fluctuations. For this reason, τ_{coh} is often referred to as the FEL coherence time.

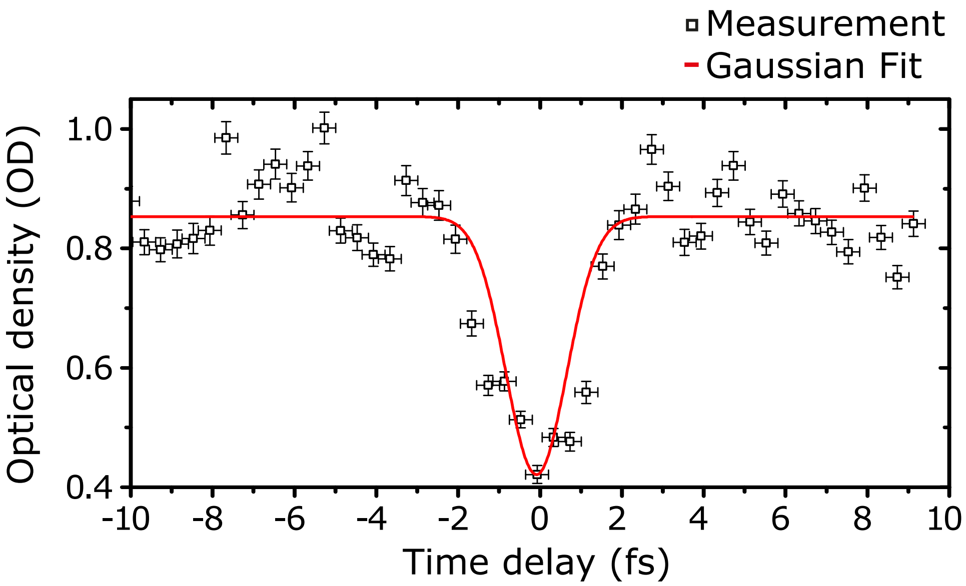

Figure 6.13: Averaged lineout for the range between 49.4 and 49.6 eV photon energy of the absorbance dip observed in the probe data of Fig. 6.12. Error bars specify the standard error of the mean value for each result and the temporal stability of 0.28 fs of the SDU [90]. Fits are weighted in x- and y-coordinates achieving an R^2-value of 0.89.

Referring to the time–bandwidth relation of Fourier-limited Gaussian pulses [see Eq. (2.7)], the related spectral bandwidth is $\Delta\omega_{\text{FEL}} = 0.8 \pm 0.2\,\text{eV}$, in accordance with the direct, grating-spectrometer-based measurement for the full (un-split) beam (see for example Fig. 6.3 of section 6.2). Note, that this is a first, preliminary analysis in order to demonstrate consistency. Further analysis will include the mathematical evaluation of the second-order (intensity) autocorrelation function in order to derive a (more accurate) expression for the coherence time–bandwidth product in analogy to Eq. (6.6), adequate for our non-collinear experimental geometry. While the feature studied in Fig. 6.13 refers to the reduction of the probe absorbance signal, also the time-dependent enhancement of the absorbance on the same time scale can be observed around the 50.6 eV center photon energy. The spectral dependence of the observed coherence "spike" is not yet fully understood. The bleaching effect close to the resonances at $\sim$49.5 eV photon energy can be understood as the result of strong coupling of a quasi-resonantly driven excited quantum state. This interpretation is based on corresponding non-perturbative model calculations, which will be discussed in section 6.8. The enhancement effect at 50.6 eV photon energy might be a first hint for the presence of additional non-linear absorption channels in the very pulse overlap that contribute to the detected absorbance signal according to Eq. (2.59) of section 2.4. However, the time-delay setting $\tau = 0$ coincides with slightly lower FEL overall pulse energies of $\sim 37\,\mu\text{J}$ (scanned mean value $47\,\mu\text{J}$) as indicated in the GMD-value histogram in the right panel of Fig. 6.12. As discussed in the previous section 6.5, a lower incoming pulse energy is associated with a higher absorbance in the medium. Note, the observed effects appear in both pump and probe spectra, but are more pronounced in the probe spectrum. These anomalies are rooted in the different intensities and spectral compositions of pump and probe pulses [also cf. Fig.6.6(b) of section 6.3] as discussed in section 6.5.

The results from the analysis of the Gaussian coherence "spike" in Fig. 6.13 sets the definition of the interferometric time-delay zero setting of the SDU. Time zero corresponds to the internal stepper motor position $p_0 = -25247.65$ steps.

6.7 Resonance excitation in Ne^{2+} by intense XUV fields

So far, the focus was placed on time-dependent refractive-index changes in the sample medium examined under the conditions of far off-resonant fields. Depending on the timing of pump and probe fields a net increase (or decrease) of transmission signal was found on the detector. Those changes are induced by the *instantaneous* destruction (ionization) of the sample atoms during the interaction with XUV photons (e.g. $\mathrm{Ne} + \hbar\omega_{\mathrm{FEL}} \rightarrow \mathrm{Ne}^{+} + \mathrm{e}^{-}$). Hence, the resulting time-dependence can be well explained by the underlying ionization kinematics. The situation is different when the sample system is polarized by the interaction with a resonant photon (free-induction decay). Under these conditions, the system's response is *non-instantaneous*, emitted with a $\pi/2$-phase lag and during a specific lifetime due to relaxation or other dephasing mechanisms. This phenomenon is often referred to as *transient* and has been extensively studied in our group using perturbative HHG and NIR time-resolved spectroscopy techniques, as for example described in chapter 5 of this work.

The following section is dedicated to resonant absorption signatures observed in XUV SASE-FEL spectra. These resonances originate from bound—bound transitions in the doubly charged neon ion. Its spectral characteristics are examined for different pump-probe pulse-delay configurations and from low to high field strengths.

Fig. 6.14 shows the time-resolved absorption spectra obtained via Eq. (6.14) from the transmission signal, $I(\tau, \omega_{\mathrm{FEL}})$, as shown and described in Fig 6.9 of section 6.5. The reference signal, $I_0(\omega_{\mathrm{FEL}})$, was determined from the average over 3300 single shots measured under the same experimental conditions and presented in Fig.6.6(b) of section 6.3. Note that the reference spectrum $I_0(\omega_{\mathrm{FEL}})$ is common for all $I(\tau, \omega_{\mathrm{FEL}})$. Apart from a strongly reduced OD at the delay setting $\tau = 0$ due to coherence enhancement (see section 6.6) and the non-resonant, continuous 50-fs time scale changes of the (global) OD in the pulse overlap region (discussed in section 6.5), the data also exhibits ionic resonance signatures. The spectral lines are due to the promotion of a valence electron out of the $2p^4$ shell of ground-state Ne^{2+} into the 3d shell. The most dominant resonance lines at ~ 49.25 eV, ~ 49.3 eV and ~ 49.4 eV photon energy emerge as the result of several cumulating multiplet transitions, $^3P_0 - ^3D_1\,3d$, $^3P_1 - ^3D_{1,2}\,3d$ and $^3P_2 - ^3D_{1,2,3}\,3d$ (assigned according to [203,204]), as illustrated in the level scheme of Fig. 6.2 in section 6.1. Note, that slight deviations in the spectral position of the measured resonances on the order of 30 meV with respect to the NIST benchmark values are likely due to inaccuracies in the spectrometer calibration, which is based on a recycled calibration curve, cf. section 6.3. It is interesting to note, that those lines are surrounded by a ~ 1 eV broad spectral region of reduced OD which changes its appearance depending on the pulse-delay configuration. The reduced background OD might originate from doubly-excited state $3s(^2P_{\frac{3}{2},\frac{1}{2}})np$

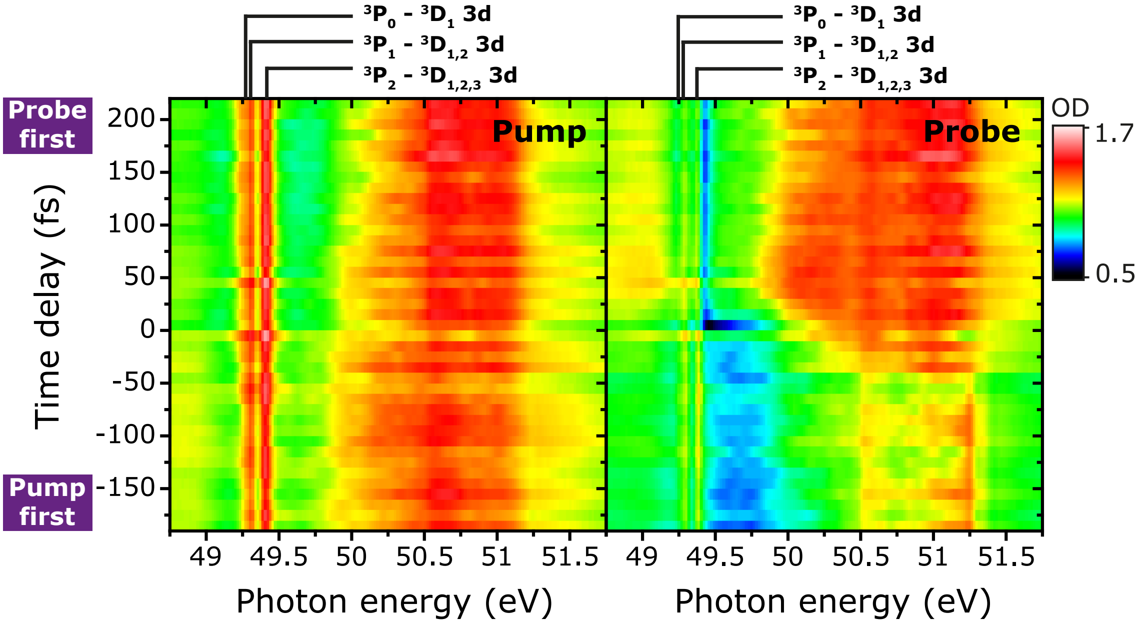

Figure 6.14: XUV-XUV strong-field time-resolved absorption spectroscopy on neon measuring pump and probe signals as a function of pump-probe delay. Optical density (OD) values are obtained via Eq. (6.14) and given by the color scale. The transmission signal spectra, $I(\omega_{\mathrm{FEL}})$, correspond to the data presented and described in Fig. 6.9 of section 6.5. Data is averaged over 600 measurements for each single delay setting taken with a mean FEL pulse energy of $\sim 47\,\mu$J and 28% rms deviation. Further information on the pulse-energy statistics can be found in Fig. 6.8 of section 6.4. Lines were assigned according to [203, 204].

ionization edges of neutral neon that fall within this energy range [76]. Furthermore, in particular at positive delays in the probe spectrum (probe first) a sharp dip in the OD is apparent at around 49.5 eV photon energy in close vicinity to the resonances. The origin of this effect is yet unknown. It might be a spectral artifact due to the impulsive (during a short period of time with respect to the excited-state evolution) Stark shift as examined in the bachelor's thesis [219] on the example of the 2s2p Fano resonance in He. Note, as already discussed in section 6.5, the magnitude of absorption decreases drastically for the probe, but only slightly (and seemingly in the wrong direction in the spectral region between 50.5 and 51 eV photon energy) for the pump, which is due to the different intensities and spectral compositions of pump and probe pulses (cf. section 6.3). Those anomalies are also a hint for the presence of other, yet unknown mechanisms beyond the depletion of ground-state Ne and the induced transparency, that again reduce the transparency and play a different role at different photon energies and intensities. Because the probe pulse is *not* perturbatively weak ($\sim 1:0.65$ pump-probe pulse energy splitting ratio), it not only projects the pump-induced ultrafast absorption changes, but also (destructively) manipulates the sample itself. This is the reason, why the ionic resonance structures observed in Fig. 6.14 at $\sim$ 49.25 eV, $\sim$ 49.3 eV and $\sim$ 49.4 eV photon energy do not disappear in the probe spectrum for a preceding probe pulse at positive delays.

In order to extract the spectral differences occurring across these resonances during the temporal transition from the pump-probe ($\tau < 0$) to the probe-pump ($\tau > 0$) pulse ordering, the data shown in Fig. 6.14 is averaged for these two temporal periods excluding the pulse overlap at $\tau = 0$. Furthermore, the data is sorted for pulse-energy (GMD) values that are available in a broad range between a few µJ and almost 100 µJ within the random SASE shot-to-shot fluctuation, cf. Fig. 6.8 of section 6.4. The cumulative resonance signature fits with a triple Gaussian model function relating the signal with the photon energy $\hbar\omega_{\mathrm{FEL}}$

$$F(\hbar\omega_{\mathrm{FEL}}) = \sum_{i=1}^{3} a_i \,\mathrm{e}^{-\frac{1}{2}\left(\frac{b_i-\hbar\omega_{\mathrm{FEL}}}{c_i}\right)^2} + d\cdot\hbar\omega_{\mathrm{FEL}} + \mathrm{const.} \qquad (6.15)$$

The fit parameters are the (positive) amplitudes a_i, peak positions b_i, peak widths c_i, and a common baseline of slope d. Spectra and their fit are presented in Fig. 6.15. Dots are measured OD values and the solid lines are the fitted predictor data for probe-first (black) and pump-first (red) configurations. Looking closely at the features observed in the pump spectrum [top panels (a) to (e) with increasing pulse energy], a clear increase in the resonance amplitude as a function of the pulse energy can be observed. As expected, the amplitude is lower when the pump precedes ($\tau > 0$) and the probe has not yet interacted with the sample. While this behavior is particular evident in the limit of low pulse energies (GMD values ≤ 25 µJ, panel a), for the highest pulse energies (GMD values > 55 µJ in panel e), the line amplitudes seem to be almost identical converging towards a peak OD of ~ 1.5. The relative ratio between the amplitudes however remained constant (note the different non-resonant background absorption). This will be clarified further below in the remainder of this section. The resonance amplitude correlates with the number of Ne^{2+} ions available in the presence of the high-flux radiation as estimated for the cross-correlation analysis in section 6.5. This effect, however, competes with a loss channel into the Ne^{3+} continuum via the absorption of a second photon and with excited-state depopulation mechanisms due to strong coupling. Under strong-coupling conditions, also the electronic level structure changes, which gives rise to spectral modifications such as Stark shifting. The clear spectral broadening of the cumulative resonance structure with increasing pulse energies and its decomposition into three distinct peaks, as in particular visible in the probe-first signal in panel (e), is attributed to this effect. The diagrammatic level scheme in Fig. 6.2 indicates the involved transition pathways. The spectra of the less intense probe half-pulse shown in the bottom panels (f) to (j) do not exhibit such clear strong-field coupling signatures. Here, the build-up of the resonance signal can be followed from bottom up. While in the probe-first signal in panel (f) for the lowest pulse energies almost no resonance line is apparent, it grows with increasing pulse energies and seems to reach the pump-first signal amplitude in panel (j) for the highest pulse energies. The absence of clear strong-field signatures in the probe spectrum is accounted for the bichromatic pump-probe geometry. In contrast to the probe, the pump pulse is slightly red-shifted by about 0.5 eV photon energy towards the spectral region of the considered resonances (cf. Fig. 6.5 of section 6.3). The spectral composition of pump and probe pulses have very little effect on the Ne^{2+} generation processes itself. The ion yield is merely influenced by the photon flux. The transition rate between two coupled states however directly depends on the on-resonance spectral photon density which is higher in the pump spectrum. The Gaussian fit function in Eq. (6.15) does not converge for

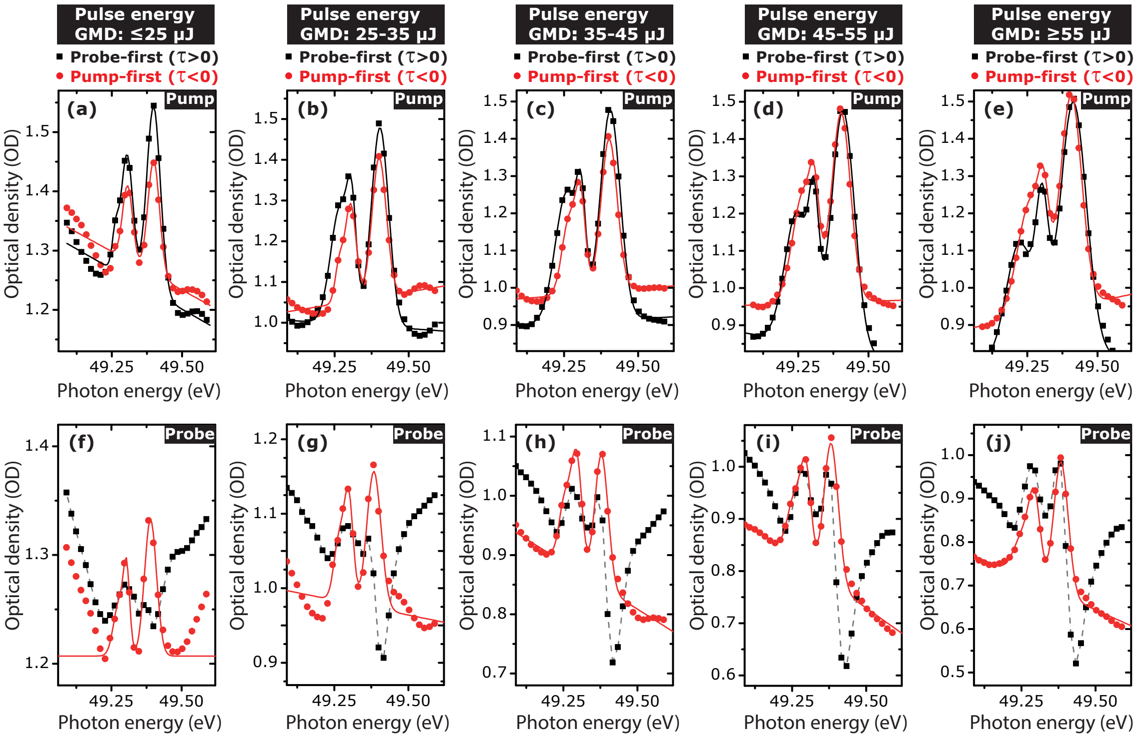

Figure 6.15: XUV-pump—XUV-probe absorption spectra of Ne^{2+} resonances averaged over negative delays (pump-first) in red and positive delays (probe-first) in black. Dots are measured optical density (OD) values, solid lines are least-square fits and the gray dashed lines connect measurement results and are guide to the eyes. Top panels (a) to (e) are recorded pump spectra and bottom panels (f) to (j) are probe spectra obtained by decomposing the data presented in Fig. 6.14 according to pulse energy (GMD) values. Three cumulating spectral absorption lines due to the transitions ${}^3P_0 - {}^3D_1$ 3d at $\sim$ 49.25 eV, ${}^3\mathrm{P}_1 - {}^3\mathrm{D}_{1,2}$ 3d at $\sim$ 49.3 eV, and ${}^3\mathrm{P}_2 - {}^3\mathrm{D}_{1,2,3}$ 3d at 49.4 eV photon energy can be identified within the FWHM Gaussian spectrometer resolution of $\sim$ 50 meV. Except for the probe-pump signals in the bottom panels (black dots), fits achieved high R^2-values on the order 0.99.

the recorded probe spectra in the probe-first configuration shown in panels (f) to (j) of Fig. 6.15. The reason for this are dominant spectral structures in the non-resonant background in close vicinity to the studied resonances, such as the above mentioned dip in the OD-signal at around 49.5 eV photon energy.

The main results of the above analysis are visualized and further quantified in Figs. 6.16 and 6.17. In Fig. 6.16 the fitted peak position of the three lines observed under probe-pump conditions in the pump-transmission spectrum is plotted as a function of the pulse energy. The uncertainties of the fitted data is on the order of 2 meV (fit without error weight). A clear spectral shift of the ${}^3\mathrm{P}_0 - {}^3\mathrm{D}_1$ 3d absorption line can be seen which substantiates the presence of strong coupling.

Fig. 6.17 shows the fitted amplitude of the ${}^3\mathrm{P}_2 - {}^3\mathrm{D}_{1,2,3}$ 3d triplet line at 49.4 eV photon energy as a function of the pulse energy measured in the pump and the probe signal (note, that probe-first data taken from the probe signal could not be fitted reliably). The uncertainties of the fitted data is on the order of 2% (fit without error weight). Under strong-field conditions for the highest pulse energies, the amplitude growth observed in the pump-signal seems to start saturating and/or balancing with loss channels (dashed curves), while the amplitude measured in the weaker probe signal further increases linearly.

As a final remark, the studied resonance lines correspond to long-lived (non-autoionizing) excitations with a ns-scale radiative decay lifetime. The natural μeV-scale linewidth of those transitions cannot be resolved with our spectrometer. Such a Dirac-delta-like signal appears as a Gaussian-shaped peak (convolved with the Gaussian spectrometer-response function) on the detector. In the case considered here, the system is permanently dressed by a high photon flux during the temporal duration of the FEL pulses, which parasitically manipulates the atomic/ionic coherences and hence leads to (homogeneous) line broadening. This effect is supported by dissipation channels via the ionization to Ne^{3+} upon absorption of a second photon (see Fig. 6.2). These broadening mechanisms play an important role for the detection of such ultra-narrow resonances with our spectrometer (resolving power $E/\Delta E \approx 940$).

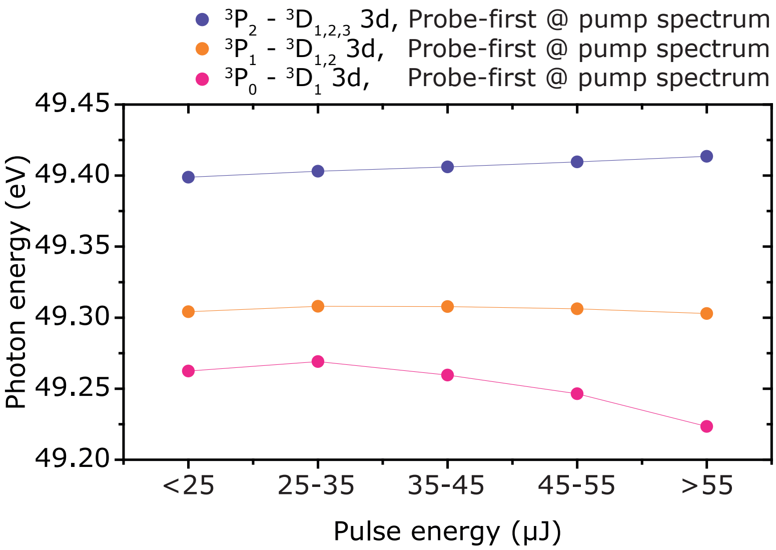

Figure 6.16: Fitted peak positions of the studied multiplet absorption signatures of Ne^{2+} plotted as a function of the FEL pulse energy.

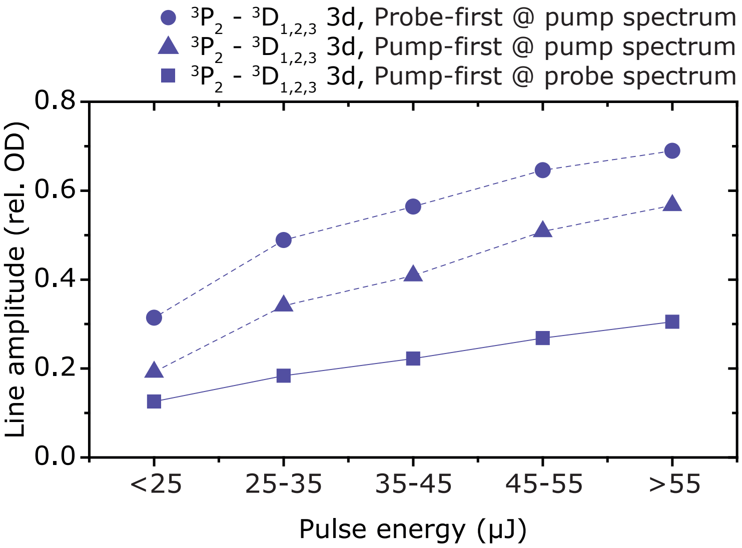

Figure 6.17: Fitted spectral-line amplitude of the $^3\mathrm{P}_2 - ^3\mathrm{D}_{1,2,3}\,3\mathrm{d}$ triplet of Ne^{2+} plotted as a function of the FEL pulse energy taken from the pump spectrum (dashed lines) and the probe spectrum (solid line).

6.8 Numerical calculation

A series of experimental findings has been described so far studying the interaction of neon with strong SASE-FEL fields in the XUV spectral region. Treating the target under off-resonant conditions, where it directly ionizes upon XUV photo-absorption, macroscopic observations such as the medium's time-dependent transparency changes could be explained in section 6.5 based on perturbative ionization-rate calculations. In the doubly-ionized charge state, the target can interact resonantly with the FEL as discussed based on the experimental observation of Stark shifting of Ne^{2+} bound—bound transition lines in section 6.7. Furthermore, a time-dependent bleaching effect of those lines was discussed in section 6.6 due to enhanced FEL brightness in the time-delay region closely around the exact temporal pulse overlap during a time-delay window of $\sim 2.2 \pm 0.4$ fs—the SASE-coherence time.

This section is dedicated to the theoretical modeling of those resonance observations. The underlying framework is based on the Schrödinger-type approach as introduced in chapter 5.6 and supports the interaction of a quantum few-level system with radiation *beyond* perturbation theory. The doubly-charged neon ion, Ne^{2+}, is approximated by a coupled six-level sub-system encountering the excited-state triplet $2\mathrm{p}^3 3\mathrm{d}\,(^3\mathrm{D}^\mathrm{o}_J)$ with total angular momentum $J = 1 \cdots 3$ and the ground-state triplet $2\mathrm{p}^4\,(^3\mathrm{P}_J)$ with $J = 0 \cdots 2$, as drawn in the level scheme in Fig. (5.8). Those states are henceforth denoted by $|\mathrm{g}\rangle$ with $\mathrm{g} = 0 \cdots 2$ indicating the three ground states and $|\mathrm{e}\rangle$ with $\mathrm{e} = 3 \cdots 5$ indicating excited states. Also see Tab. C.1 of appendix C. The coupling is mediated by (real-valued) ground—excited dipole transition matrix elements, d_{eg}, obtained from Hartree-Fock calculations [214], listed in Tab. C.2. The six transitions lead to cumulating spectral resonance lines observed as a triple peak in the experiment, see for example Fig. 6.15 in section 6.7. The underlying (incoherent) ionization processes for the generation of the Ne^{2+} system itself and other off-resonant interaction channels are not considered here.

The underlying Schrödinger equation is written in matrix form with a coupling matrix

$$\hat{\mathbf{H}} = \begin{bmatrix} \omega_0 & 0 & 0 & d_{30}E_\mathrm{FEL}(t) & d_{40}E_\mathrm{FEL}(t) & d_{50}E_\mathrm{FEL}(t) \\ 0 & \omega_1 & 0 & d_{31}E_\mathrm{FEL}(t) & d_{41}E_\mathrm{FEL}(t) & 0 \\ 0 & 0 & \omega_2 & d_{32}E_\mathrm{FEL}(t) & 0 & 0 \\ d^*_{30}E_\mathrm{FEL}(t) & d^*_{31}E_\mathrm{FEL}(t) & d^*_{32}E_\mathrm{FEL}(t) & \omega_3 & 0 & 0 \\ d^*_{40}E_\mathrm{FEL}(t) & d^*_{41}E_\mathrm{FEL}(t) & 0 & 0 & \omega_4 & 0 \\ d^*_{50}E_\mathrm{FEL}(t) & 0 & 0 & 0 & 0 & \omega_5 \end{bmatrix}.$$

The numerical solution is accomplished by the diagonalization of the Hamiltonian matrix for each propagation step forward in time. The propagation scheme is comprehensively described in chapter 5.6.

Electric free-electron laser (FEL) fields, $E_\mathrm{FEL}(t)$, are treated in terms of real-valued functions to allow for strong-field effects beyond the rotating-wave approximation. The field functions $E_\mathrm{FEL}(t)$ are defined in the framework of the partial-coherence method [18] according to Eq. (6.4) of section 6.2. A temporal duration of $t_\mathrm{G} = 50\,\mathrm{fs}$ for the overall intensity envelope and a SASE-coherence time of $\tau_\mathrm{coh} = 2.2\,\mathrm{fs}$ corresponding to a spectral FWHM bandwidth of $\Delta\omega_\mathrm{FEL} \approx 0.8$ eV was assumed. On average, in the limit of many pulses, the noisy temporal SASE-intensity pattern converges towards a Gaussian envelope profile. A (Gaussian) peak intensity of $2 \times 10^{13}\,\mathrm{W/cm^2}$ corresponds to a pulse energy of the order $10\,\mu\mathrm{J}$ assuming a focal spot size of $25\,\mu\mathrm{m}$ in diameter. The pump-probe intensity splitting ratio of 1 : 0.65 is considered for the time-delay scans. Apart from that, pump and probe pulses are treated as *identical* copies of each other with the same random phase characteristics.

The propagation time increments are $\Delta t = 0.1$ a.u. (2.4 as) and the total propagation time is 32.000 a.u. (774 fs). This choice guarantees a proper sampling of the temporal spiky XUV pulse-characteristics (mean time scale between phase fluctuations: ~ 2.2 fs) and the XUV-dipole response oscillating at periods of $\sim$0.1 fs. A small radiative decay rate of $\Gamma = 5$ meV was assumed commonly for the three excited states to model the long-lived, quasi-infinitesimal natural excited-state decay time.

The interaction of the system with a single pulse (pump or probe) creates a time-dependent polarization, i.e., the coherent superposition of ground ($|g\rangle \equiv |0\cdots 2\rangle$) and excited ($|e\rangle \equiv |3\cdots 5\rangle$) states described in terms of the complex expansion coefficients

$$c_{\mathrm{g}}(t) \cdot c_{\mathrm{e}}^{*}(t) \propto \mathrm{e}^{-i\omega_{\mathrm{eg}}t - \frac{\Gamma}{2}t}. \tag{6.16}$$

After free temporal evolution, Eq. (6.16) leads to (Lorentzian) spectral lines centered at the resonance frequencies ω_{eg} with linewidths Γ. When the system interacts with a second (replica) pulse at a time delay τ after the first excitation and during the polarization decay, amplitude and phase changes lead to characteristic spectral fringes across the resonance signatures as a function of τ, as for example described in chapter 5.3 in the context of the dipole-control model. These fringes are typical of collinear pump-probe experiments. In non-collinear geometries however, the two crossing beams form a grating-type wavefront pattern in the focal interaction region. Depending on the wavelength, the focal spot size and the crossing angle, atoms at different transverse positions in the sample volume may experience a slightly different time delay between pump and probe pulses and those fast oscillations average out, as depicted in Fig. 6.18. In order to account for this effect in the simulation, the time-dependent coherence (or dipole) response induced by the pump is averaged out, by averaging over the coherence signals calculated with and without an assumed $\pi-$phase change for the pump pulse. The pump-induced population changes, described by $c_{\mathrm{e}}(t) \cdot c_{\mathrm{e}}^{*}(t)$, remain present. This method leads to similar results as the spectral filtering approach applied in [220].

The time-dependent dipole moment $D(t)$ is finally calculated via Eq. (2.46). Its Fourier transform, $D(\omega)$, is related to the probe-pulse spectrum $E_{\mathrm{pr}}(\omega)$ via

$$\mathrm{OD}(\omega) \propto \mathrm{Im}\left[\frac{D(\omega)}{E_{\mathrm{pr}}(\omega)}\right] \tag{6.17}$$

yielding a quantity that is proportional to the experimentally obtained optical density (OD) of the probe spectrum.

Initially, upon ionization ($\mathrm{Ne} \rightarrow \mathrm{Ne}^{+} \rightarrow \mathrm{Ne}^{2+}$), the Ne^{2+}-system's ground-state triplet $2\mathrm{p}^4\,(^3\mathrm{P}_J)$ (i.e. states $|0\rangle \cdots |2\rangle$) is assumed incoherently populated (neglecting any non-vanishing coherences and alignment effects [221]). The initial population ratio is not yet known. For the calculations presented here an ensemble of equally populated ground

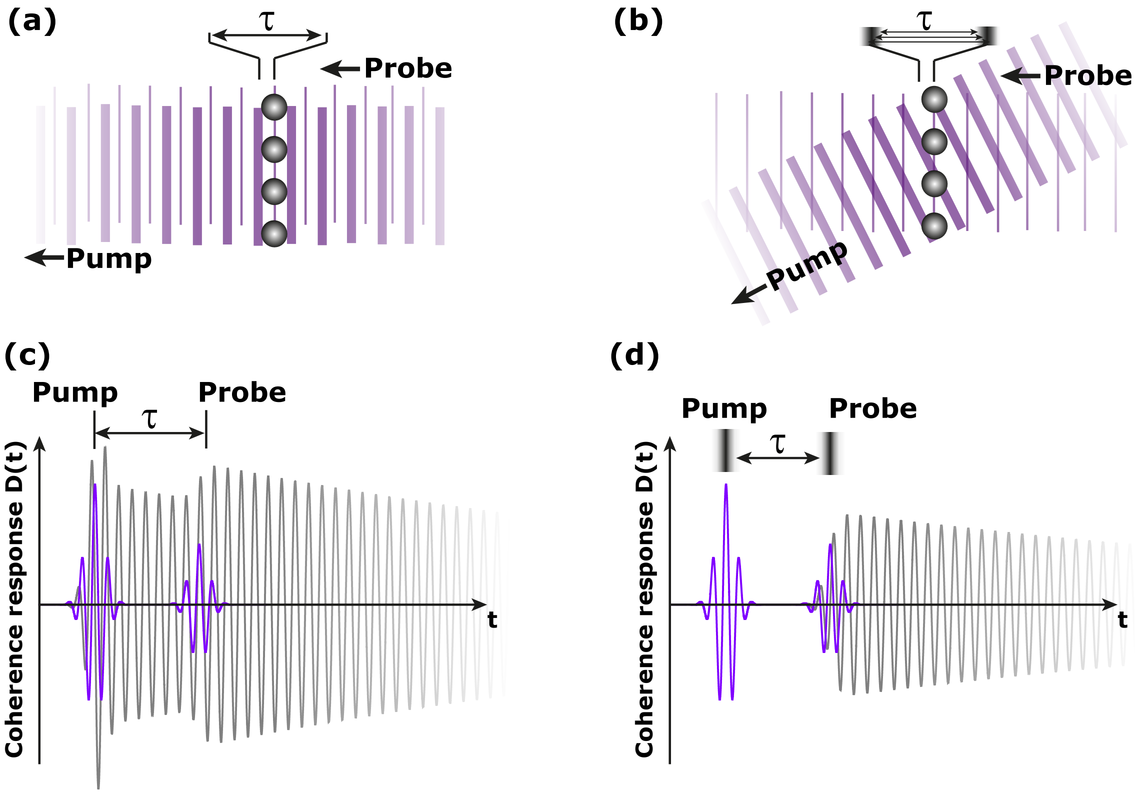

Figure 6.18: Illustration of the collinear (panel a) and non-collinear (panel b) pump-probe geometry (pulse-propagation from right to left). Pump and probe pulse-fronts are indicated by bold and thin lines, respectively. In the collinear geometry, all target atoms (gray) experience the same pump-probe delay τ. (panel c) The resulting time-dependent coherence (dipole) response (gray wavy line) exhibits characteristic oscillations induced by both pulses (violet wavy lines) and hence is explicitly depending on τ. If the pump pulse-front is tilted (panel b), the pump pulse hits the atoms at different times τ with respect to the probe, depending on the transverse (vertical) target position. Consequently, the pump-induced coherence oscillations average out and only the probe-induced coherence remains (panel d).

states is assumed. The initial mixed-state condition is accounted for by averaging over calculated OD spectra with initial state amplitudes $[c_0(0), c_1(0), c_2(0)]^T = (1,0,0)^T$, $[c_0(0), c_1(0), c_2(0)]^T = (0,1,0)^T$ and $[c_0(0), c_1(0), c_2(0)]^T = (0,0,1)^T$ (assuming all excited states fully unpopulated at time zero).

First simulation results are presented in Fig. 6.19, where the interaction of the system with a *single* SASE pulse is examined as a function of the peak intensity in the range between $10^{12}\,\mathrm{W/cm^2}$ and $10^{14}\,\mathrm{W/cm^2}$. Here, the assumed FEL center photon energy is 50.1 eV commensurate to the measured pump spectrum. Panel (a) shows the “raw” calculated optical-density spectra and for panel (b) the narrow spectral line (assumed linewidths $\Gamma = 5\,\mathrm{meV}$) is convolved with the assumed Gaussian spectrometer-response function of 50 meV full width at half maximum (FWHM) to mimic the experiment. The data demonstrate a clear Stark-shifting of all lines towards lower photo-excitation energies. This

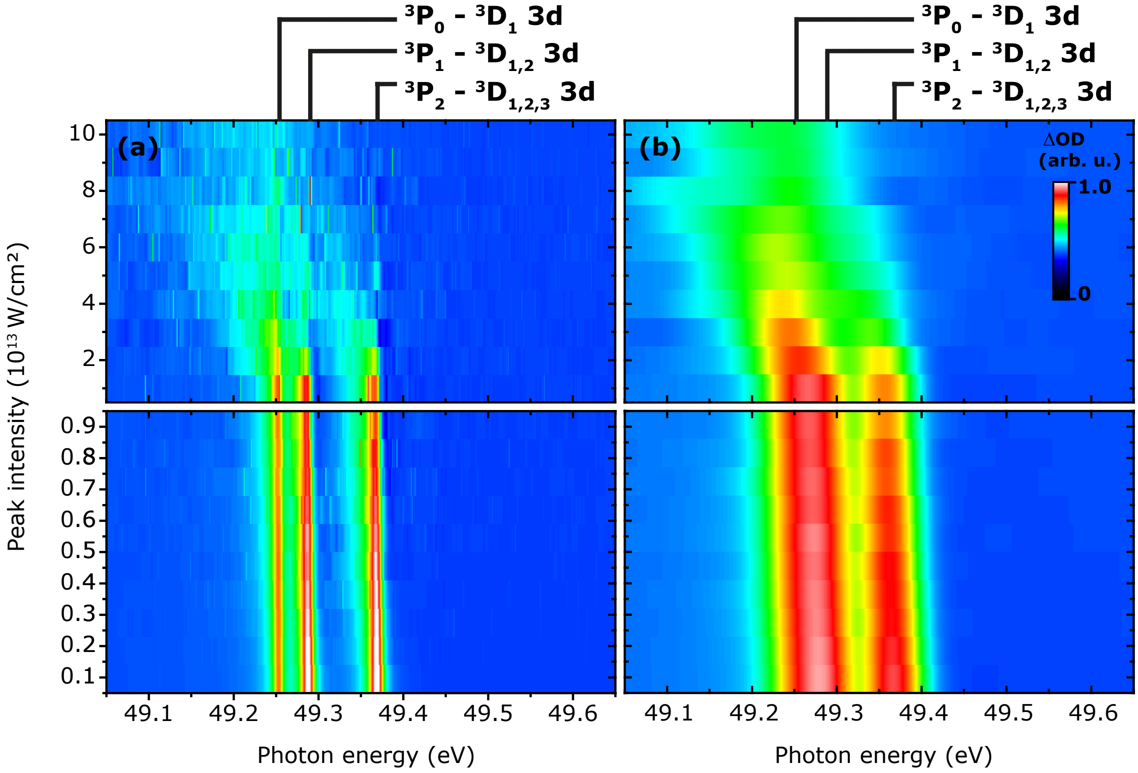

Figure 6.19: Simulated intensity scan for the considered few-level quantum model in interaction with a single SASE-FEL pulse with 50.1 eV center photon energy (as the experimental pump). For the upper panels, the data is scanned over the range of peak intensities between 10^{13} W/cm^2 and 10^{14} W/cm^2, while for the lower panels the peak-intensity range between 1×10^{12} W/cm^2 and 9×10^{12} W/cm^2 is scanned. Panels (a) show the "raw" numerical data and for panels (b) the data is convolved with the Gaussian spectrometer response function of 50 meV FWHM accounting for the experimental spectral resolution. Data is averaged over in total 300 single spectra for each intensity setting.

trend is intuitively expected and in accordance with the observed spectral line shift of the $^3P_0$–$^3D^o_1$ transition in the experiment, as shown in Fig. 6.15 of section 6.7. In the lower 10^{13} W/cm^2-regime [cf. the upper panels in (a) and (b) of Fig. 6.19] the effect of power broadening becomes apparent accompanied by a decrease in the amplitude until the lines fully vanish for the highest peak intensities around 10^{14} W/cm^2. In the highest-intensity regime the temporal oscillatory coherence evolution is massively disturbed by strong coupling and the formation of a spectral resonance line is suppressed. The seemingly (at first glance surprising) exclusive shift of the $^3P_0$–$^3D^o_1$ spectral line, as seen in the experiment, can also be suggested to appear in the calculated data, at least to some extent, in the intensity range between 2×10^{13} and 4×10^{13} W/cm^2, where the $^3P_1$–$^3D^o_{1,2}$ and $^3P_2$–$^3D^o_{1,2,3}$ lines start vanishing. It is important to emphasize that the Stark shift effect itself only depends on the coupling strength given by the field strength and the dipole matrix elements of Tab. C.2. However, the appearance of this effect in the presented data might also be influenced by the (yet unknown) initial ground-state population ratio of the model system as well as other coupling or ionization channels that have been neglected in this first attempt to reproduce the trend observed in the experimental data.

The time-dependent pump-probe scenario is examined under the condition of an ideal *monochromatic* geometry with identical pulses neglecting any deviations in the spectral composition of pump and probe. The assumed (common) central photon energy is 50.6 eV, as experimentally determined for the probe. The only difference between pump and probe (besides the temporal delay) is the peak intensity assuming $1 \times 10^{13}\,\mathrm{W/cm^2}$ for the pump and $0.65 \times 10^{13}\,\mathrm{W/cm^2}$ for the probe. The optical density for the probe pulse is calculated according to Eq. (6.17) (note, that for the intensity scan in Fig. 6.19, the pump spectrum was calculated). The pump pulse is centered at the time coordinate $t = 0$, such that it precedes the probe pulse for negative delays ($\tau < 0$), and vice versa.

The numerical results for XUV-pump—XUV-probe time-dependent absorption spectra are presented in Fig. 6.20, where the Ne^{2+} triplet transition, $^3\mathrm{P}_2$–$3\mathrm{d}\,^3\mathrm{D}_{1,2,3}$, observed in the experiment close to 49.4 eV photo-excitation energy is modeled. Note, as already discussed in sections 6.7 and 6.3, slight discrepancies (of the order of 30 meV) of the measured spectral peak position with the benchmark data as used for the simulation [203] are likely due to inaccuracies in the spectrometer calibration, which is based on a reused calibration curve from the HHG experiment.

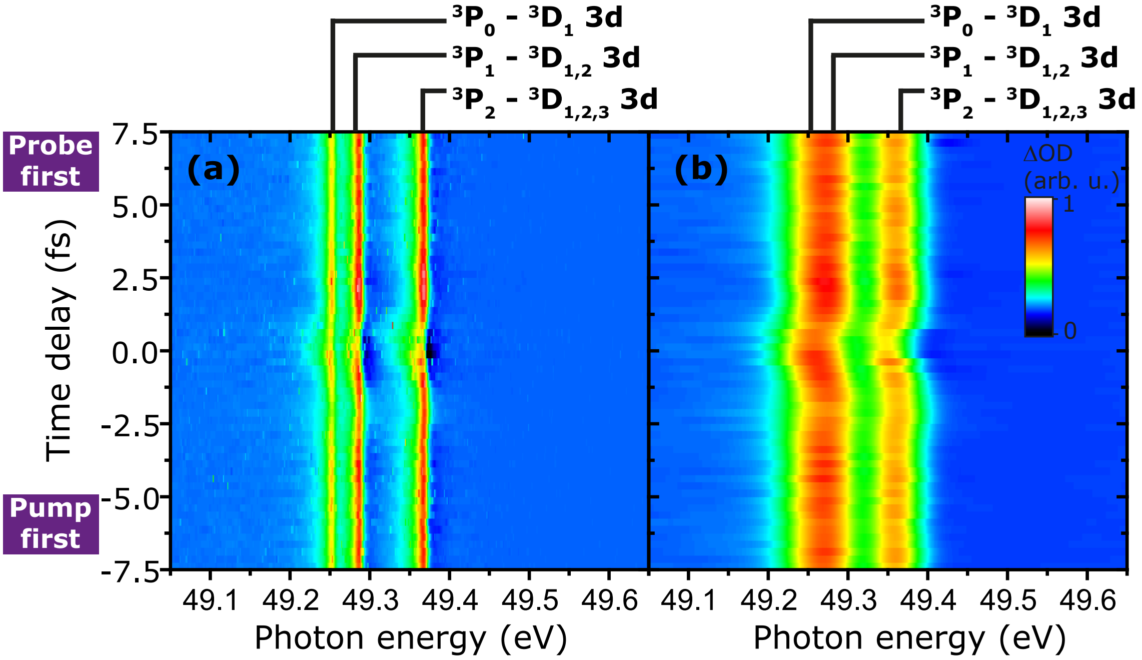

Figure 6.20: Simulated XUV-pump—XUV-probe time-delay scan of the examined $^3\mathrm{P}_{0,1,2}$–$3\mathrm{d}\,^3\mathrm{D}_{1,2,3}$ transitions in Ne^{2+} averaged over 300 single spectra. “Raw” data are presented in panel (a) and panel (b) presents those spectra convolved with the assumed Gaussian 50 meV FWHM spectrometer-response function.

Even though the simulation is based on a simplified model neglecting details such as deviations in the experimental FEL pump-probe spectral compositions, as well as the underlying ionization channels for both the formation and the dissipation of the target (via ionization to Ne^{3+}), the main spectral features observed in the experiment can be reproduced qualitatively. The simulated spectra exhibits an, albeit faint, bleaching of the spectral lines around the temporal pulse overlap ($\tau = 0$) on the time scale of the coherence time. During this period of time, the overall FEL intensity is significantly increased leading to enhanced field—atom coupling and hence to the suppression of the lines, as observed in the intensity scan (see Fig. 6.19). Similar to the experiment, the ionic spectral lines feature a dip of reduced OD in their high-photon energy (blue-wavelength) wing of the spectral lineshape [below 49.4 eV in the simulation (Fig. 6.20) and at ~49.45 eV in the experiment (Fig. 6.12)], or in other words, a slight lineshape change from Lorentzian to Fano is present at all delays. This feature can be explained by the impulsive (kick-like, for a short instant of time) Stark-shift due to sharp temporal intensity spikes, which abruptly change the dipole phase [23]. Its dependence on the FEL-detuning out of resonance is not yet fully understood. First numerical studies based on the presented simulation scheme and applied for the He 2s2p Fano resonance have been made [219] (also see section 6.9.1). The discussed effect becomes more dominant in the pulse-overlap region, where temporal SASE-intensity spikes add-up and thus enhance the FEL brightness. In the experimental data, this signature is much more pronounced and appears spectrally broadened in an energy range between 49.4 and 49.6 eV. As already discussed in section 6.7, this spectral region coincides with ionization thresholds of doubly-excited $3\mathrm{s}(^2\mathrm{P}_{\frac{3}{2},\frac{1}{2}})n\mathrm{p}$ states in neutral neon [76], which may affect the absorption/transmission characteristics of the target medium in this specific spectral region and which is not accounted for in the simulation.

6.9 Related experiments

In this section, related experiments conducted during the experimental beamtime campaign at FLASH in June 2016 under the same experimental conditions (except for a few parameters such as for instance the FEL wavelength) are briefly discussed, the analysis of which is not in the focus of this thesis.

6.9.1 Strong-field excitation of doubly-excited helium

The doubly-excited helium atom represents a paradigmatic system for the science on electron-correlation dynamics. How it responds to intense *near-infrared* laser pulses was studied in detail in several recent experiments, as discussed in chapter 5.2. Here, the scheme was extended subjecting the helium atom to intense XUV pulses delivered by the SASE-FEL FLASH with photon energies around 60.15 eV to match the transition energy between the ground and the 2s2p doubly-excited state. The aim is to study the impact of this radiation on Fano interference and electron-electron correlation—information that can be extracted from the spectral resonance profile in terms of the q-parameter [69]. A very recent theoretical work, where corresponding photo-electron spectra are calculated, suggests the observation of lineshape changes as a function of the intensity [222].

Fig. 6.21 presents optical-density (OD) spectra obtained according to Eq. (2.54) measured as a function of the FEL fluence $\Phi(\omega_{\text{FEL}})$ [related to the intensity via the pulse duration τ_{FWHM} by $\Phi(\omega_{\text{FEL}}) = I(\omega_{\text{FEL}}) \cdot \tau_{\text{FWHM}}$] of a single incoming pulse (static spectroscopy). The measurement exhibit a change in the lineshape from the (natural) asymmetric Fano-lineshape to an almost symmetric Lorentzian lineshape with increasing fluence. These observations are substantiated by two-level model calculations employing the model as described in chapters 2.3 and 6.8. Wave packet dispersion in the N = 1 continuum is modeled assuming a band of (almost) degenerate states with an imaginary energy part (i.e. a “damping” term).

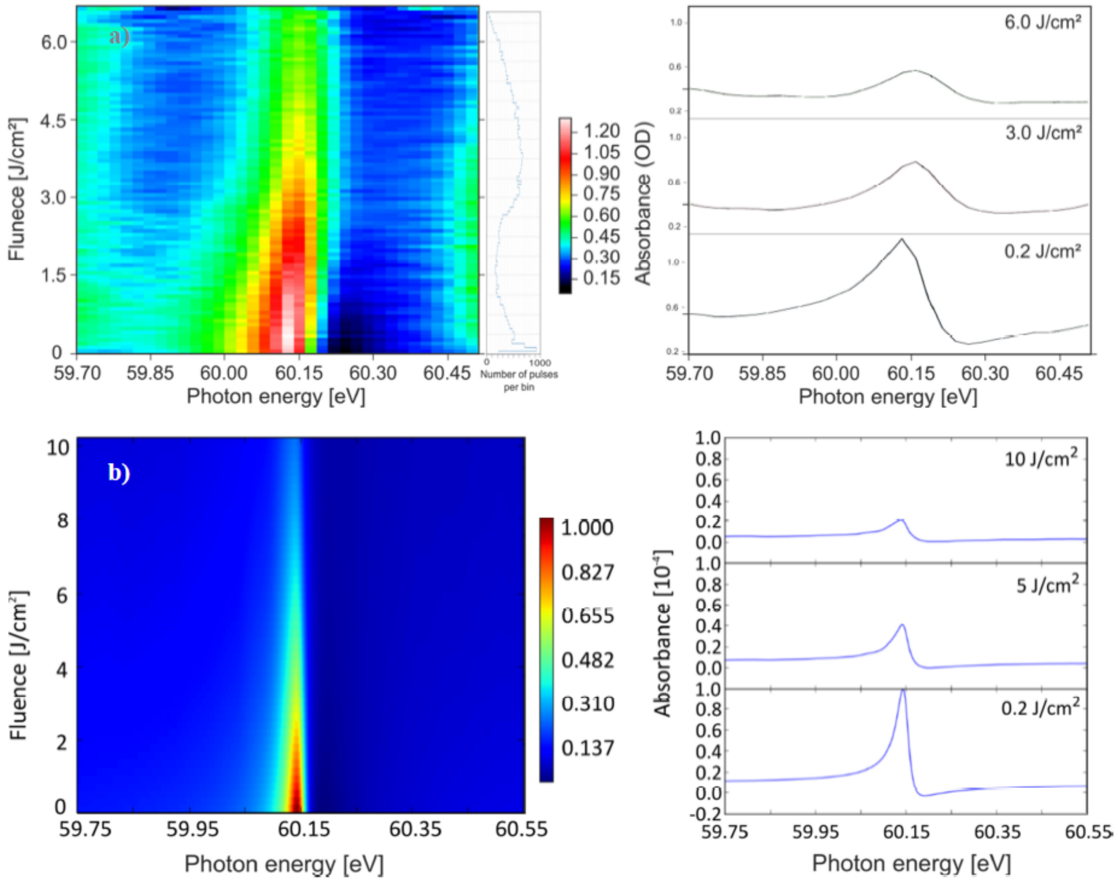

Figure 6.21: Static (single pulse) photo-absorption spectroscopy near the He 2s2p doubly-excited-state Fano resonance measuring the absorption of FEL light transmitted through a dilute gaseous sample. The changes of absorption are displayed by the color map in terms of the optical density (OD) and by lineouts taken at different fluences. Panel (a) presents measurement data averaged over ~500 shots. In panel (b), corresponding non-perturbative two-level simulation results are shown assuming partially-coherent pulses, as described in sections 6.2. Pulse energies were tuned from weak to strong fields with averaged pulse duration of 75 fs FWHM and a SASE spectral width of 1 eV FWHM.

The observations are currently being analyzed and the underlying mechanisms are not yet fully understood. An explanation for the observations could be the phenomenon of the so-called impulsive (i.e. on a short period of time with respect to the dipole evolution) Stark-shift due to coherence intensity spikes. The SASE coherence time has been measured to be around ∼2.2 fs in section 6.6 of this chapter, which can be considered short compared to the ∼17-fs 2s2p autoionization lifetime. The experimental details can be found in the Master's thesis of Ref. [139]. The theoretical treatment is described in the bachelor's thesis of Ref. [219].

6.9.2 XUV-pump—XUV-probe transient absorption experiments in small halogenated hydrocarbons

In this section, first XUV-pump—XUV-probe transient absorption spectroscopy measurements on molecular targets are presented with the aim to study charge-rearrangement effects during dissociation. Methyl iodide (CH_3I), including one iodine atom, and diiodomethane (CH_2I_2), with two iodine atoms serve as targets. The experimental pump-probe scheme relies on resonantly exciting the $4d \rightarrow \sigma^*(I)$ transition with the first XUV pulse, which triggers C–I bond breaking and thus dissociation, and probing the dissociation dynamics with the time-delayed probe pulse by driving exactly the same transition. The goal is to extract signatures due to transient modifications in the electronic environment during the dissociation from the absorption (optical density) spectra.

First preliminary measurement results are presented in Fig. 6.22, where the pump-probe cross-correlation signal is compared for the two targets. The measurement scheme is similar as described in section 6.5 for the target neon. Note, in contrast to the before discussed neon measurements, here the absorbance is given in terms of *difference spectra*, meaning the difference of absorption between measurements with the pump-pulse switched on minus the pump-pulse switched off [28]. The temporal profile of the cross-correlation signal measured for CH_2I_2 has a duration of 116 ± 23 fs, while the corresponding values for the CH_3I measurement is significantly shorter with 57 ± 19 fs. Intuitively, associating the signal rise time with the molecular fragmentation time, these differences can be explained by the particularly heavier and thus slowly moving fragments in the case of CH_2I_2. The impact of redistribution dynamics of the electronic structure is currently being investigated in collaboration with the group of Alexander Kuleff (Theoretical Chemistry Group, Heidelberg University).

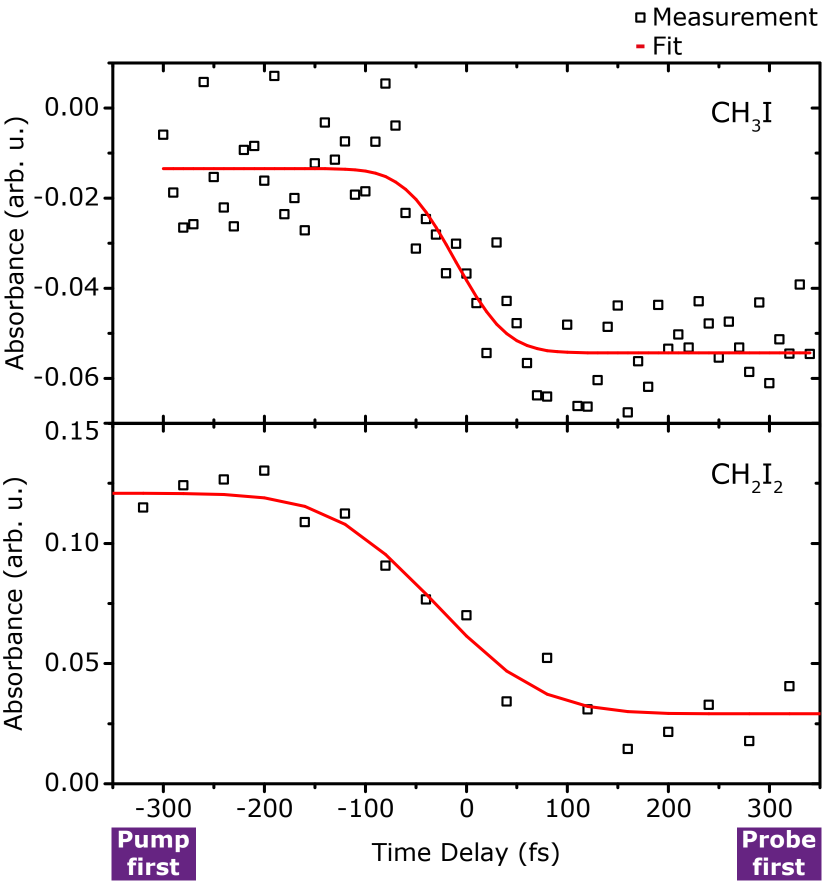

Figure 6.22: Preliminary results presenting XUV-pump—XUV-probe transient absorption spectroscopy measurements on CH_3I shown in the upper panel and CH_2I_2 in the bottom panel.

6.10 Conclusion and outlook on the results from the FEL experiments

This chapter reports on the first all-optical transient absorption spectroscopy experiments with a *high-intensity* extreme-ultraviolet (XUV) light source—FLASH (free-electron Laser at DESY). The basic experimental geometry has become a matter of routine in the field of attosecond science employing XUV high-harmonic light pulses in the *weak-field limit* (see Refs. [23, 54, 63, 131, 132, 161, 167] to mention a few). In all these schemes, a high-intensity (near-)infrared field is used—either as a pump [161], or as a probe [63]—to drive strong-field interaction. Being exclusively sensitive to the XUV spectral region, so far, strongly-driven light—matter interaction dynamics could only be accessed *indirectly*, via XUV-transition to an "auxiliary" quantum state. This led for instance to the observation of an Autler-Townes doublet [54] or electromagnetically induced transparency [223] in the paradigmatic doubly-excited helium system.

The here presented extension of this technique into the XUV *strong-field* regime promises a *direct* view into the underlying quantum dynamics of strongly driven two-level systems for near-future experiments. Especially the impact of intense fields on correlated two-electron transitions and Fano interference with competing direct-ionization vs. autoionization channels is of paramount scientific interest [224]. The experimental access to such information is given by the spectral resonance profile parameter q [23, 69]. First static (with a single strong-field XUV-SASE pulse) absorption experiments exploring the helium 2s2p resonance profile as a function of the field strength are presented in section 6.9.1. The results are yet preliminary, but suggest a change in the measured lineshape from a (natural) Fano to Lorentzian profile during the passage from the 10^{12} to the $10^{14}\,\mathrm{W/cm^2}$ intensity regime and hence a manipulation of the natural Fano interferometer. In how far the cooperative interaction of the two correlated electrons with the incoming photon plays a role, is not yet fully understood. In proposed experiments for a follow-up beamtime at FLASH employing two time-delayed (with $\sim$20 as temporal resolution) XUV-SASE pulses, the fundamental Rabi dynamics when cooperatively driving two bound electrons at the same time, are planned to be explored. Rabi oscillations in such systems are subject to additional decoherence and dephasing channels leading to spectral changes (depletion) to which this spectroscopy method is sensitive. The question is: Does the interaction with a strong field promote the two electrons back to the ground state (Rabi oscillation), or will it breakup the electronic correlation and lead to the ionization of one or even both electrons?

In this thesis, the focus is placed on the analysis of XUV-pump—XUV-probe experiments on the target neon conducted during our first beamtime at FLASH in June 2016. Compared to the ionization cross sections of helium for XUV photons with energies in the 60-eV (doubly-excited state) region ($\sim$ 1.5 Mb), both neutral neon and its first ionized charge state exhibit large ionization cross sections for $\sim$ 50-eV photons (both on the order of 9 Mb [214]). The affinity to ionization and the therefore present transparency/opacity changes of the medium when subjected to strong-field radiation renders neon an ideal target system for first benchmark cross-correlation experiments in order to gain *in-situ* information on the SASE-FEL pulse statistics and the spectro-temporal pulse structure. At the same time, coherence effects from resonantly driven bound—bound transitions in the atomic (or generated ionic) Ne system can be directly probed. The measured spectroscopic data sets include two control parameters: (i) The pump-probe time delay, and (ii) the FEL-photon energy measured parasitically with a gas-monitor detector (GMD) for each single pulse and retrieved after the measure for the post analysis. Thanks to the non-collinear beam geometry, the method allows to detect both the XUV-pump and XUV-probe half-beam spectra, simultaneously.

An XUV—XUV cross-correlation study allowed to control the transparency/opacity of the gaseous neon target by controlling the ionization yield as a function of both the pulse delay and the FEL intensity. The off-resonant spectral changes can be understood following the underlying (perturbative) ionization kinematics for $\mathrm{Ne} \to \mathrm{Ne}^{+} \to \mathrm{Ne}^{2+} \to \mathrm{Ne}^{3+}$. The rise time of the sigmoidal cross-correlation curve, as well as its temporal center position with respect to the exact pulse overlap depend on both the FEL intensity and the pulse duration. Although the accompanying model calculation builds on the simplifying assumption of a non-invasive (non-ionizing) probe pulse, it resembles the experimental results suggesting FEL-pulse intensities in the lower $10^{13}\,\mathrm{W/cm^2}$ range and pulse durations of 50–60 fs. Indeed, these values disagree with corresponding measurement results from the FLASH online diagnostic tools, which suggest $10^{14}\,\mathrm{W/cm^2}$-scale peak intensities and $\sim$100-fs pulse durations. However, those online measurements only provide upper limits as they are taken *ex-situ*, upstream of the experiment and/or are based on indirect electron-bunch measurement techniques.

Intensity cross-correlation measurements scanned with a fine, sub-fs temporal resolution yielded clear signatures of enhancement due to coherence spikes in the form of bleaching of spectral resonance lines and absorption changes in their close spectral vicinity. Such signatures have not yet been observed in measured spectra from all-optical absorption techniques so far and their physical origin is not yet fully understood. However, the comparison with unisonous calculation results obtained from a home-made non-perturbative model simulation suggest that the *impulsive* Stark-shift plays a major role.

In the doubly ionized neon system (Ne^{2+}), a number of coupled bound—bound transitions, $^3\mathrm{P}_{0,1,2}$–$3\mathrm{d}\,^3\mathrm{D}_{1,2,3}$, can be excited and probed by the combined fields. The resonance line strength (amplitude) and the spectral position are found to be varied as a function of the FEL-pulse energy (or intensity). The changes in the resonance amplitude are attributed to the pulse-energy dependence of the Ne^{2+} ion yield itself (mixed with loss channels due to power broadening and further ionization). The spectral shifts can be explained by the (ordinary, non-impulsive) Stark-shift as a result of strong (partially-)coherent coupling. The experimental findings are in good (albeit qualitative) agreement with accompanying non-perturbative model simulations.

The third class of experiments carried out during the beamtime campaign 2016 involve the molecular targets $\mathrm{CH_3I}$ and $\mathrm{CH_2I_2}$ studying charge-rearrangement effects in dissociation phenomena. In this case, both XUV-replica pulses are tuned in resonance with a $4\mathrm{d} \rightarrow \sigma^*(\mathrm{I})$ transition to initially break a C–I bonding (pump), while probing this transition as a function of time delay. The taken data demonstrates the real time probing of the dissociation times of the two targets. The impact of electronic redistribution dynamics is currently being investigated.

For the future, multi-dimensional spectroscopy experiments based on a non-collinear box-car beam geometry are planned employing three FEL pulses (and optionally a fourth one as a local oscillator field) as a function of two (or three) delays. The aim is to probe electronic coupling dynamics across a molecule with site- or element-specific information [30, 31]—a long-standing goal in the field of ultra-fast science. A first target candidate could be $\mathrm{CH_2IBr}$, which can be excited through two individual element-specific core-to-valence transitions originating from the 4d and 3d core orbitals of I and Br atoms, yielding spectrally separated resonances in the 50 eV and 70 eV photo-excitation energy range [225]. While for the pump-step two intense and time-delay controlled FEL-pulses are needed (resonant with one of those transitions), the probe-step can be realized either with a third FEL-pulse (resonant with the other transition), or with broadband, target-spectrum-spanning HHG pulses. Two-color FELs are already available [226] and the

FLASH facility is planned to be upgraded by an HHG-source for the combined application of FEL and HHG pulses in the course of the next years.

Chapter 7

Conclusion

The guiding theme of this thesis is the exploration of dynamical processes in quantum systems such as atoms and (small) molecules by non-linear methods. Measuring the dynamical evolution of such a target system not only requires short enough laser pulses, appropriate photon energies and field intensities, but also adequate two- or multi-pulse pump-probe schemes to launch and interrogate these dynamics. The key point of the presented experiments is to use ultra-short extreme-ultraviolet (XUV) pulses obtained from high-harmonic generation (HHG), or from self-amplified spontaneous emission (SASE) in a free-electron laser (FEL) to access electronic transitions.

In the course of this work a versatile setup for novel time-resolved multi-dimensional pump-probe techniques based on transient absorption with XUV pulses has been developed, buildup and experimentally tested. The setup can be operated with broadband HHG radiation combined with the near-infrared femtosecond driving pulses, or with intense SASE-FEL radiation and, in principle, it can combine both XUV-light sources as soon as HHG is available at FLASH for user experiments.

The presented experiments include the time-resolved four-wave-mixing spectroscopy based on attosecond transient absorption with multiple (XUV-NIR-NIR) fields targeting coupling mechanisms between inner-shell excitations in neon. Performing “conventional” time-resolved spectroscopy with an XUV and a single time-delayed NIR pulse only provides spectroscopic access to XUV-dipole-allowed states. Here, the target system was propagated through *coherent* (phase-dependent) superposition states between the ground- and XUV-dipole-allowed and -forbidden excited states via the individual XUV-NIR-NIR interactions. The corresponding coupling pathways were retrieved from the 2d spectral map correlating the Fourier-transformed time delay to the XUV-photo-excitation energy axis.

The second integral experimental part of this thesis reports about first XUV-pump—XUV-probe measurements with the novel setup conducted at FLASH. The here presented key results are the demonstration of the *incoherent* ionization-control in cross-correlation measurements characterizing the delay- and intensity-dependent refractive-index changes of the target medium neon. While these measurements allowed to reconstruct the (incoherent) ionization kinematics at work during FEL-matter interaction and to retrieve spectro-temporal information on the overall FEL-pulse duration and intensity, cross-correlation measurement with fine (sub-fs) time-delay steps over the very pulse overlap allowed to study the impact of coherent SASE-intensity spikes on the spectral structure. In particular in the spectral vicinity of bound—bound resonances in Ne^{2+}, ${}^3P_{0,1,2}$–$3d\,{}^3D_{1,2,3}$, bleaching-effects and lineshape changes are observed. These signatures appear on a time scale of 2.2 ± 0.4 fs, which we identify as the SASE-coherence time. Furthermore, Stark-shifting of those resonance lines evidencing strong coupling between ionic ground- and excited states due to the partially-coherent SASE-FEL pulses is observed.

All these experimental findings were scrutinized and understood with the help of home-made numerical model calculations based on perturbative and non-perturbative approaches. Although the experiments are highly complex and the pulse structures were not accurately known, experimental and numerical data are found to be in good agreement.

To sum up, the presented interferometric technique with ultra-short XUV pulses can be employed for the study of various aspects of quantum dynamics and light—matter interaction. This includes both coherent as well as incoherent non-linear (sequential) mechanisms. The experimental findings allow to test (and expand) existing theories. The presented results on the few-electron target system neon serve as benchmark for upcoming experiments with this setup employing *multiple* delay-controlled pulses both in our HHG home-laboratory in Heidelberg, as well as at the free-electron laser on more complex systems such as (small) molecules.

Appendix A

Experimental setup at FLASH

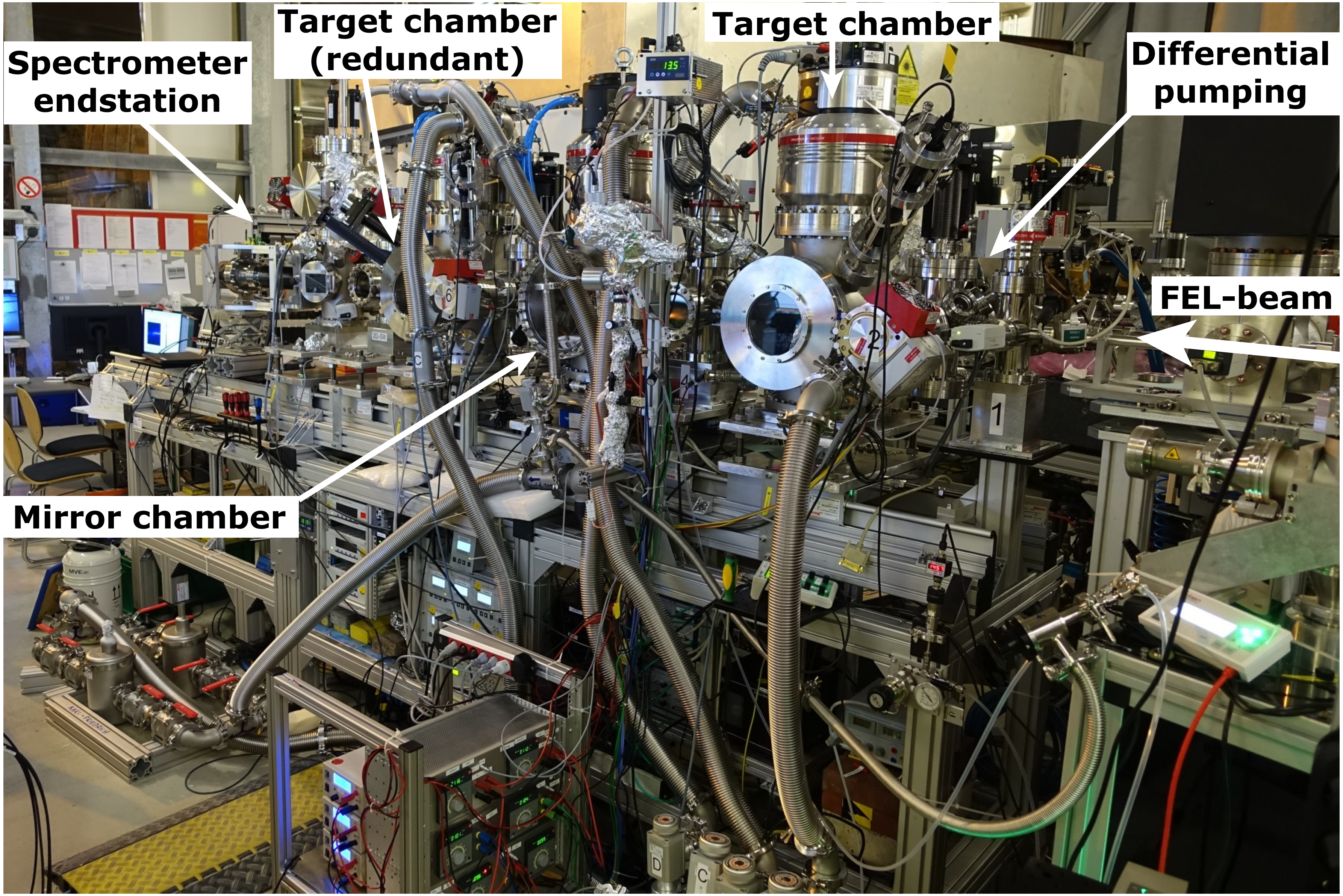

Figure A.1: Photographic picture of the experimental vacuum apparatus during the experimental campaign at FLASH 2016 as described in section 4.2. The setup is mounted on a massive 4-meter ITEM rack. The beam enters the two-stage differential pumping section on the right hand side and is focused into the sample target in the first large (target) chamber. The central large (mirror) chamber contains the dual-mirror SDU and the re-focusing toroidal mirror, here used for the beam transportation. The third large chamber contains the imaged focus and serves as a redundant target chamber. The beam is detected in the spectrometer endstation on the left hand side. The apparatus is equipped with many instruments e.g. for beam diagnostics, the vacuum control, the cell heating, or the piezo-driven optics setup.

Appendix B

Measured FEL transmission spectra through Ne

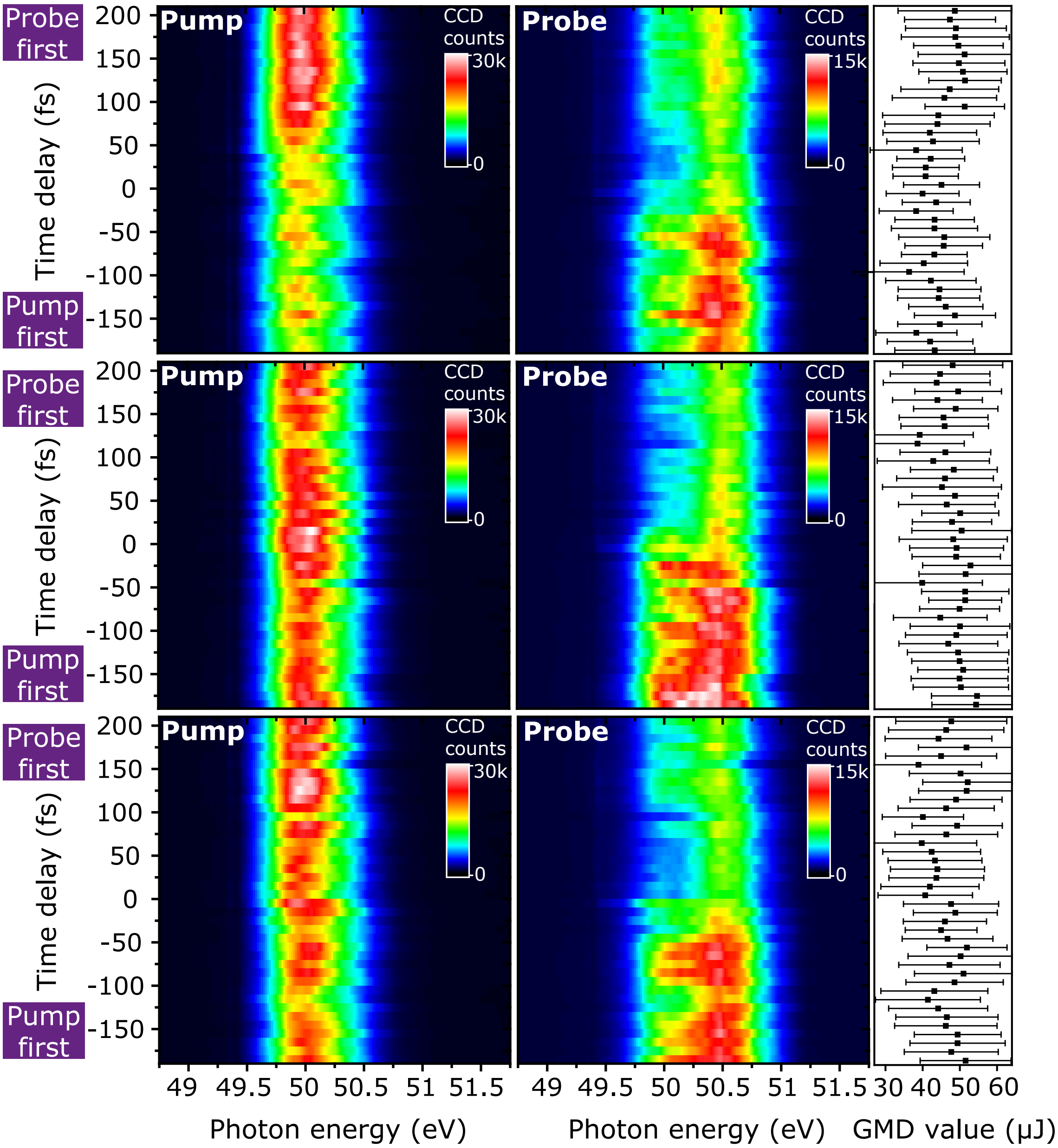

Figure B.1: Pump (left panels) and probe (right panels) pulse transmission spectra through Ne gas with a (constant) backing pressure of 50 mbar as a function of the pulse delay τ, scanned with 10-fs steps. Single spectra were averaged over 200 shots. Compared are the data taken from three measurements conducted consecutively under the same experimental conditions (top to bottom). Time-dependent transmission changes, i.e. an increase of the signal for the probe-first configuration observed in the pump spectrum and an increase of the signal for the pump-first configuration in the probe spectrum, can be reproduced in each scan. However, slight discrepancies arise due to statistical shot-to-shot fluctuations and slight systematic drifts of the FEL-pulse properties. Corresponding pulse-energy (GMD) values are given.

Appendix C

Numerical input parameters

Table C.1: Energy levels of the Ne^{2+} ground-state triplet $\mathrm{2p^4\,(^3P_{\mathit{J}})}$ ($J = 0\cdots2$) and excited-state triplet $\mathrm{2p^3 3d\,(^3D^o_{\mathit{J}})}$ ($J = 1\cdots3$) as drawn in Fig. (5.8) and considered for the simulation. Values according to NIST spectra database [203].

Short-hand notation	Configuration	$\hbar\omega_{e,g}$ (eV)
$\lvert 0\rangle$	$\mathrm{2p^4\,(^3P_2)}$	0
$\lvert 1\rangle$	$\mathrm{2p^4\,(^3P_1)}$	0.0797
$\lvert 2\rangle$	$\mathrm{2p^4\,(^3P_0)}$	0.1141
$\lvert 3\rangle$	$\mathrm{2p^3 3d\,(^3D^o_1)}$	49.3678
$\lvert 4\rangle$	$\mathrm{2p^3 3d\,(^3D^o_2)}$	49.3683
$\lvert 5\rangle$	$\mathrm{2p^3 3d\,(^3D^o_3)}$	49.3700

Table C.2: Electric dipole-matrix elements, d_{eg}, for ground—excited transitions of Ne^{2+} as implemented in the Simulation. Labels g$= 0\cdots2$ indicate ground-state levels and e$=$ $3\cdots5$ excited-state levels. Values obtained from Hartree-Fock calculations [214]

Transition	d_{eg} (a.u.)
$\mathrm{2p^4\,(^3P_0) - 2p^3 3d\,(^3D^o_1)}$	d_{32} =0.217290
$\mathrm{2p^4\,(^3P_1) - 2p^3 3d\,(^3D^o_1)}$	d_{31} =0.188594
$\mathrm{2p^4\,(^3P_1) - 2p^3 3d\,(^3D^o_2)}$	d_{41} =0.252870
$\mathrm{2p^4\,(^3P_2) - 2p^3 3d\,(^3D^o_1)}$	d_{30} =0.048988
$\mathrm{2p^4\,(^3P_2) - 2p^3 3d\,(^3D^o_2)}$	d_{40} =0.146885
$\mathrm{2p^4\,(^3P_2) - 2p^3 3d\,(^3D^o_3)}$	d_{50} =0.293236

Bibliography

[1] T. H. Maiman.
Stimulated Optical Radiation in Ruby.
Nature **187**, 493–494 (1960).
(Cited on p. 1)

[2] S. Chu, J. E. Bjorkholm, A. Ashkin, and A. Cable.
Experimental Observation of Optically Trapped Atoms.
Phys. Rev. Lett. **57**, 314–317 (1986).
(Cited on p. 1)

[3] S. Chu, L. Hollberg, J. E. Bjorkholm, A. Cable, and A. Ashkin.
Three-Dimensional Viscous Confinement and Cooling of Atoms by Resonance Radiation Pressure.
Phys. Rev. Lett. **55**, 48–51 (1985).
(Cited on p. 1)

[4] M. H. Anderson, J. R. Ensher, M. R. Matthews, C. E. Wieman, and E. A. Cornell.
Observation of Bose-Einstein Condensation in a Dilute Atomic Vapor.
Science **269**, 198–201 (1995).
(Cited on p. 1)

[5] K. B. Davis, M.-O. Mewes, M. R. Andrews, N. J. van Druten, D. S. Durfee, D. M. Kurn, and W. Ketterle.
Bose-Einstein Condensation in a Gas of Sodium Atoms.
Phys. Rev. Lett. **75**, 3969–3973 (1995).
(Cited on p. 1)

[6] L. B. Fletcher et al.
Ultrabright X-ray laser scattering for dynamic warm dense matter physics.
Nat Photon **9**, 274–279 (April 2015).
(Cited on p. 1)

[7] A. Bauch and H. R. Telle.
Frequency standards and frequency measurement.
Reports on Progress in Physics **65**, 789 (2002).
(Cited on p. 1)

[8] M. DiDomenico Jr.
Small-Signal Analysis of Internal (Coupling-Type) Modulation of Lasers.
Journal of Applied Physics **35**, 2870–2876 (1964).
(Cited on p. 1)

[9] L. E. Hargrove, R. L. Fork, and M. A. Pollack.
Locking of He-Ne Laser Modes induced by Synchronous Intracavity Modulation.
Applied Physics Letters **5**, 4–5 (1964).
(Cited on p. 1)

[10] A. Yariv.
Internal Modulation in Multimode Laser Oscillators.

Journal of Applied Physics **36**, 388–391 (1965).
(Cited on p. 1)

[11] J. N. Eckstein, A. I. Ferguson, and T. W. Hänsch.
High-Resolution Two-Photon Spectroscopy with Picosecond Light Pulses.
Phys. Rev. Lett. **40**, 847–850 (Mar 1978).
(Cited on p. 1)

[12] A. H. Zewail.
Femtochemistry.
J. Phys. Chem. **97**, 12427–12446 (1993).
(Cited on p. 1, 2)

[13] A. H. Zewail.
Femtochemistry: Atomic-Scale Dynamics of the Chemical Bond.
J. Phys. Chem. A **104**, 5660–5694 (2000).
(Cited on p. 1, 2, 91)

[14] A. McPherson, G. Gibson, H. Jara, U. Johann, T. S. Luk, I. A. McIntyre, K. Boyer, and C. K. Rhodes.
Studies of multiphoton production of vacuum-ultraviolet radiation in the rare gases.
J. Opt. Soc. Am. B **4**, 595–601 (1987).
(Cited on p. 2)

[15] X. F. Li, A. L'Huillier, M. Ferray, L. A. Lompré, and G. Mainfray.
Multiple-harmonic generation in rare gases at high laser intensity.
Phys. Rev. A **39**, 5751–5761 (1989).
(Cited on p. 2)

[16] A. L'Huillier, K. J. Schafer, and K. C. Kulander.
Theoretical aspects of intense field harmonic generation.
Journal of Physics B: Atomic, Molecular and Optical Physics **24**, 3315 (1991).
(Cited on p. 2)

[17] B. W. J. McNeil and N. R. Thompson.
X-ray free-electron lasers.
Nat Photon **4**, 814–821 (December 2010).
URL `http://dx.doi.org/10.1038/nphoton.2010.239`.
(Cited on p. 2, 28, 30)

[18] T. Pfeifer, Y. H. Jiang, S. Düsterer, R. Moshammer, and J. Ullrich.
Partial-coherence method to model experimental free-electron laser pulse statistics.
Opt. Lett. **35**, 3441–3443 (2010).
(Cited on p. 2, 7, 87, 88, 101, 110)

[19] J. Ullrich, R. Moshammer, R. Dörner, O. Jagutzki, V. Mergel, H. Schmidt-Böcking, and L. Spielberger.
Recoil-ion momentum spectroscopy.
Journal of Physics B: Atomic, Molecular and Optical Physics **30**, 2917 (1997).
(Cited on p. 2, 38)

[20] R. Dörner, V. Mergel, O. Jagutzki, L. Spielberger, J. Ullrich, R. Moshammer, and H. Schmidt-Böcking.
Cold Target Recoil Ion Momentum Spectroscopy: a "momentum microscope" to view atomic collision dynamics.
Physics Reports **330**, 95 – 192 (2000).
(Cited on p. 2, 38)

[21] J. Ullrich, R. Moshammer, A. Dorn, R. Dörner, L. P. H. Schmidt, and H. Schmidt-Böcking.
Recoil-ion and electron momentum spectroscopy: reaction-microscopes.
Reports on Progress in Physics **66**, 1463 (2003).
(Cited on p. 2, 38)

[22] J. Itatani, F. Quéré, G. L. Yudin, M. Y. Ivanov, F. Krausz, and P. B. Corkum.
Attosecond Streak Camera.
Phys. Rev. Lett. **88**, 173903 (2002).
(Cited on p. 2)

[23] C. Ott, A. Kaldun, P. Raith, K. Meyer, M. Laux, J. Evers, C. H. Keitel, C. H. Greene, and T. Pfeifer.
Lorentz Meets Fano in Spectral Line Shapes: A Universal Phase and Its Laser Control.
Science **340**, 716–720 (2013).
(Cited on p. 2, 20, 21, 37, 38, 40, 56, 59, 61, 74, 83, 115, 118, 119)

[24] A. H. Zewail.
The Nobel Prize in Chemistry 1999 URL
`http://www.nobelprize.org/nobel_prizes/chemistry/laureates/1999/`.
(Cited on p. 2)

[25] P. B. Corkum and F. Krausz.
Attosecond science.
Nat. Physics **3**, 381–387 (2007).
(Cited on p. 2)

[26] K. Schnorr, A. Senftleben, M. Kurka, A. Rudenko, G. Schmid, T. Pfeifer, K. Meyer, M. Kübel, M. F. Kling, Y. H. Jiang, R. Treusch, S. Düsterer, B. Siemer, M. Wöstmann, H. Zacharias, R. Mitzner, T. J. M. Zouros, J. Ullrich, C. D. Schröter, and R. Moshammer.
Electron Rearrangement Dynamics in Dissociating I_2^{n+} Molecules Accessed by Extreme Ultraviolet Pump-Probe Experiments.
Phys. Rev. Lett. **113**, 073001 (2014).
(Cited on p. 2)

[27] K. Schnorr, A. Senftleben, M. Kurka, A. Rudenko, L. Foucar, G. Schmid, A. Broska, T. Pfeifer, K. Meyer, D. Anielski, R. Boll, D. Rolles, M. Kübel, M. F. Kling, Y. H. Jiang, S. Mondal, T. Tachibana, K. Ueda, T. Marchenko, M. Simon, G. Brenner, R. Treusch, S. Scheit, V. Averbukh, J. Ullrich, C. D. Schröter, and R. Moshammer.
Time-Resolved Measurement of Interatomic Coulombic Decay in Ne_2.
Phys. Rev. Lett. **111**, 093402 (2013).
(Cited on p. 2)

[28] P. Hamm and M. Zanni.
Concepts and Methods of 2D Infrared Spectroscopy.
Cambridge University Press (2011).
(Cited on p. 2, 17, 19, 22, 23, 49, 80, 117)

[29] G. S. Engel, T. R. Calhoun, E. L. Read, T.-K. Ahn, T. Mancal, Y.-C. Cheng, R. E. Blankenship, and G. R. Fleming.
Evidence for wavelike energy transfer through quantum coherence in photosynthetic systems.
Nature **446**, 782–786 (2007).
(Cited on p. 2)

[30] I. V. Schweigert and S. Mukamel.
Coherent Ultrafast Core-Hole Correlation Spectroscopy: X-Ray Analogues of Multidimensional NMR.
Phys. Rev. Lett. **99**, 163001 (2007).
(Cited on p. 2, 21, 53, 120)

[31] I. V. Schweigert and S. Mukamel.
Probing valence electronic wave-packet dynamics by all x-ray stimulated Raman spectroscopy: A simulation study.
Phys. Rev. A **76**, 012504 (2007).
(Cited on p. 2, 21, 53, 120)

[32] F. Bencivenga, R. Cucini, F. Capotondi, A. Battistoni, R. Mincigrucci, E. Giangrisostomi, A. Gessini, M. Manfredda, I. P. Nikolov, E. Pedersoli, E. Principi, C. Svetina, P. Parisse, F. Casolari, M. B. Danailov, M. Kiskinova, and C. Masciovecchio.

Four-wave mixing experiments with extreme ultraviolet transient gratings.
Nature **520**, 205–208 (April 2015).
(Cited on p. 2)

[33] W. Cao, E. R. Warrick, A. Fidler, D. M. Neumark, and S. R. Leone.
Noncollinear wave mixing of attosecond XUV and few-cycle optical laser pulses in gas-phase atoms: Toward multidimensional spectroscopy involving XUV excitations.
Phys. Rev. A **94**, 053846 (2016).
(Cited on p. 2, 37)

[34] J.-C. Diels and W. Rudolph.
Ultrashort Laser Pulse Phenomena.
Second Edition. Academic Press (2006).
(Cited on p. 6, 7, 32)

[35] A. E. Siegman.
Lasers.
University Science Books (1986).
(Cited on p. 7)

[36] M. Weissbluth.
CHAPTER 14 - APPROXIMATIONS.
In M. Weissbluth (Ed.), *Atoms and Molecules*, pp. 290 – 312. Academic Press (1978).
(Cited on p. 10, 11)

[37] L. Ballentine.
Quantum Mechanics: A Modern Development.
World Scientific (1998).
(Cited on p. 11)

[38] I. I. Rabi.
Space Quantization in a Gyrating Magnetic Field.
Phys. Rev. **51**, 652–654 (1937).
(Cited on p. 11, 12, 74)

[39] S. H. Autler and C. H. Townes.
Stark Effect in Rapidly Varying Fields.
Phys. Rev. **100**, 703–722 (1955).
(Cited on p. 11, 13, 41, 72)

[40] E. P. Kanter, B. Krässig, Y. Li, A. M. March, P. Ho, N. Rohringer, R. Santra, S. H. Southworth, L. F. DiMauro, G. Doumy, C. A. Roedig, N. Berrah, L. Fang, M. Hoener, P. H. Bucksbaum, S. Ghimire, D. A. Reis, J. D. Bozek, C. Bostedt, M. Messerschmidt, and L. Young.
Unveiling and Driving Hidden Resonances with High-Fluence, High-Intensity X-Ray Pulses.
Phys. Rev. Lett. **107**, 233001 (Nov 2011).
(Cited on p. 13)

[41] N. Rohringer and R. Santra.
Strongly driven resonant Auger effect treated by an open-quantum-system approach.
Phys. Rev. A **86**, 043434 (Oct 2012).
(Cited on p. 13)

[42] A. N. Pfeiffer and S. R. Leone.
Transmission of an isolated attosecond pulse in a strong-field dressed atom.
Phys. Rev. A **85**, 053422 (May 2012).
(Cited on p. 13)

[43] M. Wu, S. Chen, M. B. Gaarde, and K. J. Schafer.
Time-domain perspective on Autler-Townes splitting in attosecond transient absorption of laser-dressed helium atoms.
Phys. Rev. A **88**, 043416 (Oct 2013).
(Cited on p. 13)

[44] C. Cohen-Tannoudji, J. Dupont-Roc, and G. Grynberg.
Atom-Photon Interactions: Basic Processes and Applications.
A Wiley-Interscience publication. Wiley (1998).
(Cited on p. 13)

[45] P. Berman and V. Malinovsky.
Principles of Laser Spectroscopy and Quantum Optics.
Princeton University Press (2010).
(Cited on p. 13)

[46] N. B. Delone and V. P. Krainov.
Multiphoton Processes in Atoms.
Springer Berlin Heidelberg, Berlin, Heidelberg (1994).
(Cited on p. 13)

[47] M. Protopapas, C. H. Keitel, and P. L. Knight.
Atomic physics with super-high intensity lasers.
Reports on Progress in Physics **60**, 389 (1997).
URL `http://stacks.iop.org/0034-4885/60/i=4/a=001`.
(Cited on p. 13)

[48] F. H. M. Faisal.
The Perturbation Theory, pp. 29–51.
Springer US, Boston, MA (1987).
(Cited on p. 14)

[49] P. Lambropoulos and G. M. Nikolopoulos.
Multiple ionization under strong XUV to X-ray radiation.
The European Physical Journal Special Topics **222**, 2067–2084 (Oct 2013).
(Cited on p. 14)

[50] M. Goeppert-Mayer.
Über Elementarakte mit zwei Quantensprüngen.
J. A. Barth (1931).
(Cited on p. 14)

[51] G. S. Voronov and N. B. Delone.
Ionization of the xenon atom by the electric field of ruby laser emission.
JETP Letters **1**, 66 (1965).
(Cited on p. 14)

[52] L. V. Keldysh.
Ionization in the field of a strong electromagnetic wave.
Soviet Physics JETP **20**, 1307 (1965).
URL `http://www.jetp.ac.ru/cgi-bin/e/index/e/20/5/p1307?a=list`.
(Cited on p. 15)

[53] L. Argenti, C. Ott, T. Pfeifer, and F. Martín.
Attosecond Transient Absorption Spectroscopy of doubly-excited states in helium.
ArXiv e-prints (2012).
(Cited on p. 15)

[54] C. Ott, A. Kaldun, L. Argenti, P. Raith, K. Meyer, M. Laux, Y. Zhang, A. Blattermann, S. Hagstotz, T. Ding, R. Heck, J. Madronero, F. Martin, and T. Pfeifer.
Reconstruction and control of a time-dependent two-electron wave packet.
Nature **516**, 374–378 (December 2014).
(Cited on p. 15, 20, 37, 38, 40, 58, 66, 72, 83, 118)

[55] T. Ding, C. Ott, A. Kaldun, A. Blättermann, K. Meyer, V. Stooss, M. Rebholz, P. Birk, M. Hartmann, A. Brown, H. V. D. Hart, and T. Pfeifer.
Time-resolved four-wave-mixing spectroscopy for inner-valence transitions.
Opt. Lett. **41**, 709–712 (Feb 2016).

(Cited on p. 15, 40, 54, 64, 65, 77, 78, 79, 83)

[56] A. D. Bandrauk and H. Shen.
Exponential split operator methods for solving coupled time-dependent Schrödinger equations.
The Journal of Chemical Physics **99**, 1185–1193 (1993).
(Cited on p. 16)

[57] J. Fleck, J.A., J. Morris, and M. Feit.
Time-dependent propagation of high energy laser beams through the atmosphere.
Applied physics **10**, 129–160 (1976).
(Cited on p. 17, 59, 73)

[58] M. Feit, J. F. Jr., and A. Steiger.
Solution of the Schrödinger equation by a spectral method.
Journal of Computational Physics **47**, 412 – 433 (1982).
(Cited on p. 17, 59, 73)

[59] B. E. A. Saleh and M. C. Teich.
Fundamentals of Photonics.
Second Edition. Wiley (2007).
(Cited on p. 17, 19)

[60] P. Milonni and J. Eberly.
Lasers.
Wiley Series in Pure and Applied Optics. Wiley (1988).
(Cited on p. 17)

[61] A. Feldman, U. S. N. B. of Standards, and O. S. of America.
Basic Optical Properties of Materials: Summaries of Papers Presented at the Topical Conference on Basic Optical Properties of Materials, Held at the National Bureau of Standards, Gaithersburg, Maryland, May 5-7, 1980.
Bd. 13. U.S. Department of Commerce, National Bureau of Standards (1980).
(Cited on p. 19)

[62] A. Kaldun, C. Ott, A. Blättermann, M. Laux, K. Meyer, T. Ding, A. Fischer, and T. Pfeifer.
Extracting Phase and Amplitude Modifications of Laser-Coupled Fano Resonances.
Phys. Rev. Lett. **112**, 103001 (Mar 2014).
(Cited on p. 20, 40, 58, 83)

[63] A. Kaldun, A. Blättermann, V. Stooß, S. Donsa, H. Wei, R. Pazourek, S. Nagele, C. Ott, C. D. Lin, J. Burgdörfer, and T. Pfeifer.
Observing the ultrafast buildup of a Fano resonance in the time domain.
Science **354**, 738–741 (2016).
(Cited on p. 20, 40, 56, 59, 83, 118)

[64] M. Schultze, M. Fiess, N. Karpowicz, J. Gagnon, M. Korbman, M. Hofstetter, S. Neppl, A. L. Cavalieri, Y. Komninos, T. Mercouris, C. A. Nicolaides, R. Pazourek, S. Nagele, J. Feist, J. Burgdorfer, A. M. Azzeer, R. Ernstorfer, R. Kienberger, U. Kleineberg, E. Goulielmakis, F. Krausz, and V. S. Yakovlev.
Delay in Photoemission.
Science **328**, 1658–1662 (2010).
(Cited on p. 20)

[65] L. Moore, M. Lysaght, L. Nikolopoulos, J. Parker, H. van der Hart, and K. Taylor.
The RMT method for many-electron atomic systems in intense short-pulse laser light.
Journal of Modern Optics **58**, 1132–1140 (2011).
(Cited on p. 20, 77)

[66] L. R. Moore, M. A. Lysaght, J. S. Parker, H. W. van der Hart, and K. T. Taylor.
Time delay between photoemission from the $2p$ and $2s$ subshells of neon.
Phys. Rev. A **84**, 061404 (Dec 2011).
(Cited on p. 20)

[67] J.-P. Connerade.
Highly Excited Atoms.
Cambridge University Press (1998).
(Cited on p. 20)

[68] A. Temkin and A. K. Bhatia.
Autoionization: Recent Developments and Applications.
Springer US, Boston, MA (1985).
(Cited on p. 20)

[69] U. Fano.
Effects of Configuration Interaction on Intensities and Phase Shifts.
Phys. Rev. **124**, 1866–1878 (1961).
(Cited on p. 20, 57, 115, 119)

[70] A. M. Covington, A. Aguilar, I. R. Covington, M. F. Gharaibeh, G. Hinojosa, C. A. Shirley, R. A. Phaneuf, I. Álvarez, C. Cisneros, I. Dominguez-Lopez, M. M. Sant'Anna, A. S. Schlachter, B. M. McLaughlin, and A. Dalgarno.
Photoionization of Ne^+ *using synchrotron radiation*.
Phys. Rev. A **66**, 062710 (Dec 2002).
(Cited on p. 21)

[71] K. Bennett, Y. Zhang, M. Kowalewski, W. Hua, and S. Mukamel.
Multidimensional resonant nonlinear spectroscopy with coherent broadband x-ray pulses.
Physica Scripta **2016**, 014002 (2016).
(Cited on p. 21)

[72] S. Mukamel.
Principles of Nonlinear Optical Spectroscopy.
Oxford, New York (1995).
(Cited on p. 22, 23, 25, 81)

[73] G. S. Schlau-Cohen, J. M. Dawlaty, and G. R. Fleming.
Ultrafast Multidimensional Spectroscopy: Principles and Applications to Photosynthetic Systems.
IEEE Journal of Selected Topics in Quantum Electronics **18**, 283–295 (Jan 2012).
(Cited on p. 22, 24, 25)

[74] M. Zanni, C. Middleton, M. Arrigoni, and J. Henrich.
ULTRAFAST TUNABLE LASERS: 2D infrared spectroscopy moves toward mainstream use (2013).
URL `http://www.laserfocusworld.com/articles/print/volume-49/issue-07/features/ultrafast-tunable-lasers-2d-infrared-spectroscopy-moves-toward-mainstream-use` `html`.
(Cited on p. 22)

[75] P. Hamm, M. Lim, and R. M. Hochstrasser.
Structure of the Amide I Band of Peptides Measured by Femtosecond Nonlinear-Infrared Spectroscopy.
The Journal of Physical Chemistry B **102**, 6123–6138 (1998).
(Cited on p. 22)

[76] K. Schulz, M. Domke, R. Püttner, A. Gutiérrez, G. Kaindl, G. Miecznik, and C. H. Greene.
High-resolution experimental and theoretical study of singly and doubly excited resonances in ground-state photoionization of neon.
Phys. Rev. A **54**, 3095–3112 (1996).
(Cited on p. 26, 67, 68, 70, 92, 105, 115)

[77] T. Brixner, J. Stenger, H. M. Vaswani, M. Cho, R. E. Blankenship, and G. R. Fleming.
Two-dimensional spectroscopy of electronic couplings in photosynthesis.
Nature **434**, 625–628 (2005).
(Cited on p. 26)

[78] S. T. Cundiff and S. Mukamel.
Optical multidimensional coherent spectroscopy.
Phys. Today **66**, 44–49 (2013).
URL `http://dx.doi.org/10.1063/PT.3.2047`.
(Cited on p. 26)

[79] J. D. Jackson.
Classical Electrodynamics.
John Wiley & Sons (2002).
(Cited on p. 27)

[80] D. Attwood and A. Sakdinawat.
X-Rays and Extreme Ultraviolet Radiation: Principles and Applications.
Second edition. Cambridge University Press (2017).
(Cited on p. 27, 28)

[81] Deutsches-Elektronen-Synchrotron.
Free-electron laser FLASH.
`https://flash.desy.de/` (retrieved May 05, 2017).
(Cited on p. 29, 31, 32)

[82] I. Vasserman, R. Dejus, P. D. Hartog, E. Moog, S. Sasaki, E. Trakhtenberg, and M. White.
LCLS Undulator Design Development.
Presented at the 26th International Free Electron Laser Conference and 11th Annual FEL User Workshop, Trieste, Italy, 9 Aug -3 Sep 2004 **4**, 814–821 (2004).
(Cited on p. 29)

[83] Deutsches-Elektronen-Synchrotron.
DESY Photon Science - FLASH.
`http://photon-science.desy.de/facilities/flash/index_eng.html` (retrieved May 10, 2017).
(Cited on p. 30)

[84] A. M. Kondratenko and E. L. Saldin.
GENERATING OF COHERENT RADIATION BY A RELATIVISTIC ELECTRON BEAM IN AN ONDULATOR.
Part. Accel. **10**, 207–216 (1980).
(Cited on p. 30)

[85] R. Bonifacio, C. Pellegrini, and L. Narducci.
Collective instabilities and high-gain regime in a free electron laser.
Optics Communications **50**, 373 – 378 (1984).
(Cited on p. 30)

[86] E. L. Saldin, E. A. Schneidmiller, and M. V. Yurkov.
The Physics of Free Electron Lasers.
Springer, Berlin Heidelberg (2000).
(Cited on p. 30, 87, 88)

[87] B. Faatz et al.
Simultaneous operation of two soft x-ray free-electron lasers driven by one linear accelerator.
New Journal of Physics **18**, 062002 (2016).
(Cited on p. 30)

[88] J. Rossbach.
FLASH: The First Superconducting X-Ray Free-Electron Laser, pp. 303–328.
Springer International Publishing, Cham (2016).
URL `http://dx.doi.org/10.1007/978-3-319-14394-1_10`.
(Cited on p. 31)

[89] K. Tiedtke, A. Azima, N. von Bargen, L. Bittner, S. Bonfigt, S. DÃijsterer, B. Faatz, U. FrÃijhling, M. Gensch, C. Gerth, N. Guerassimova, U. Hahn, T. Hans, M. Hesse, K. Honkavaar, U. Jastrow, P. Juranic, S. Kapitzki, B. Keitel, T. Kracht, M. Kuhlmann, W. B. Li, M. Martins, T. NÃžÃśez, E. PlÃűnjes, H. Redlin, E. L. Saldin, E. A. Schneidmiller, J. R. Schneider, S. Schreiber, N. Stojanovic, F. Tavella, S. Toleikis, R. Treusch, H. Weigelt, M. WellhÃűfer, H. Wabnitz, M. V. Yurkov, and J. Feldhaus.
The soft x-ray free-electron laser FLASH at DESY: beamlines, diagnostics and end-stations.
New Journal of Physics **11**, 023029 (2009).
(Cited on p. 32, 90)

[90] M. Wöstmann, R. Mitzner, T. Noll, S. Roling, B. Siemer, F. Siewert, S. Eppenhoff, F. Wahlert, and H. Zacharias.
The XUV split-and-delay unit at beamline BL2 at FLASH.
Journal of Physics B: Atomic, Molecular and Optical Physics **46**, 164005 (2013).
(Cited on p. 31, 38, 43, 46, 47, 103)

[91] K. Tiedtke, J. Feldhaus, U. Hahn, U. Jastrow, T. Nunez, T. Tschentscher, S. V. Bobashev, A. A. Sorokin, J. B. Hastings, S. MÃűller, L. Cibik, A. Gottwald, A. Hoehl, U. Kroth, M. Krumrey, H. SchÃűppe, G. Ulm, and M. Richter.
Gas detectors for x-ray lasers.
Journal of Applied Physics **103**, 094511 (2008).
(Cited on p. 31, 90)

[92] G. Brenner, S. Kapitzki, M. Kuhlmann, E. Ploenjes, T. Noll, F. Siewert, R. Treusch, K. Tiedtke, R. Reininger, M. Roper, M. Bowler, F. Quinn, and J. Feldhaus.
First results from the online variable line spacing grating spectrometer at FLASH.
Nuclear Instruments and Methods in Physics Research Section A: Accelerators, Spectrometers, Detectors and Associated Equipment **635**, S99 – S103 (2011).
PhotonDiag 2010.
(Cited on p. 32, 89, 90)

[93] http://www.femtolasers.com/.
(Cited on p. 32)

[94] C. Ott.
Attosecond multidimensional interferometry of single and two correlated electrons in atoms.
Ph.D. thesis, Universität Heidelberg (2012).
(Cited on p. 32, 40, 43, 45)

[95] P. Raith.
Few-Cycle Multidimensional Laser Control of Attosecond Pulse Generation.
Ph.D. thesis, Universität Heidelberg (2012).
(Cited on p. 32)

[96] A. Kaldun.
Fano Resonances in the Time Domain - understanding and controlling the absorption and emission of light.
PhD Thesis, Universität Heidelberg (2014).
(Cited on p. 32)

[97] P. B. Corkum.
Plasma perspective on strong field multiphoton ionization.
Phys. Rev. Lett. **71**, 1994–1997 (1993).
(Cited on p. 33, 34)

[98] K. J. Schafer, B. Yang, L. F. DiMauro, and K. C. Kulander.
Above threshold ionization beyond the high harmonic cutoff.
Phys. Rev. Lett. **70**, 1599–1602 (Mar 1993).
(Cited on p. 33)

[99] K. C. Kulander, K. J. Schafer, and J. L. Krause.

Dynamics of Short-Pulse Excitation, Ionization and Harmonic Conversion, pp. 95–110.
Springer US, Boston, MA (1993).
(Cited on p. 33)

[100] C. Kan, C. E. Capjack, R. Rankin, and N. H. Burnett.
Spectral and temporal structure in high harmonic emission from ionizing atomic gases.
Phys. Rev. A **52**, R4336–R4339 (Dec 1995).
(Cited on p. 34)

[101] R. López-Martens, K. Varjú, P. Johnsson, J. Mauritsson, Y. Mairesse, P. Salières, M. B. Gaarde, K. J. Schafer, A. Persson, S. Svanberg, C.-G. Wahlström, and A. L'Huillier.
Amplitude and Phase Control of Attosecond Light Pulses.
Phys. Rev. Lett. **94**, 033001 (Jan 2005).
(Cited on p. 34)

[102] M. Chini, K. Zhao, and Z. Chang.
The generation, characterization and applications of broadband isolated attosecond pulses.
Nat Photon **8**, 178–186 (March 2014).
(Cited on p. 34)

[103] K. Varjú, Y. Mairesse, P. Agostini, P. Breger, B. Carré, L. J. Frasinski, E. Gustafsson, P. Johnsson, J. Mauritsson, H. Merdji, P. Monchicourt, A. L'Huillier, and P. Salières.
Reconstruction of Attosecond Pulse Trains Using an Adiabatic Phase Expansion.
Phys. Rev. Lett. **95**, 243901 (Dec 2005).
(Cited on p. 34, 35)

[104] G. Farkas and C. Tóth.
Proposal for attosecond light pulse generation using laser induced multiple-harmonic conversion processes in rare gases.
Physics Letters A **168**, 447 – 450 (1992).
(Cited on p. 34)

[105] P. Agostini and L. F. DiMauro.
The physics of attosecond light pulses.
Reports on Progress in Physics **67**, 813 (2004).
(Cited on p. 35)

[106] M. Lewenstein, P. Balcou, M. Y. Ivanov, A. L'Huillier, and P. B. Corkum.
Theory of High-Harmonic Generation by Low-Frequency Laser Fields.
Phys. Rev. A **49**, 2117–2132 (1994).
(Cited on p. 35)

[107] M. Kohler, T. Pfeifer, K. Hatsagortsyan, and C. Keitel.
Chapter 4 - Frontiers of Atomic High-Harmonic Generation.
In E. A. Paul Berman and C. Lin (Eds.), *Advances in Atomic, Molecular, and Optical Physics*, volume 61 of *Advances In Atomic, Molecular, and Optical Physics*, pp. 159 – 208. Academic Press (2012).
URL `http://www.sciencedirect.com/science/article/pii/B9780123964823000041`.
(Cited on p. 35)

[108] G. Sansone, E. Benedetti, F. Calegari, C. Vozzi, L. Avaldi, R. Flammini, L. Poletto, P. Villoresi, C. Altucci, R. Velotta, S. Stagira, S. De Silvestri, and M. Nisoli.
Isolated Single-Cycle Attosecond Pulses.
Science **314**, 443–446 (2006).
(Cited on p. 37)

[109] Z.-H. Loh, M. Khalil, R. E. Correa, and S. R. Leone.
A tabletop femtosecond time-resolved soft x-ray transient absorption spectrometer.
Review of Scientific Instruments **79**, 073101 (2008).
(Cited on p. 37)

[110] M. Chini, H. Mashiko, H. Wang, S. Chen, C. Yun, S. Scott, S. Gilbertson, and Z. Chang.
Delay control in attosecond pump-probe experiments.
Opt. Express **17**, 21459–21464 (2009).
(Cited on p. 37)

[111] M. Fieß, M. Schultze, E. Goulielmakis, B. Dennhardt, J. Gagnon, M. Hofstetter, R. Kienberger, and F. Krausz.
Versatile apparatus for attosecond metrology and spectroscopy.
Review of Scientific Instruments **81**, 093103 (2010).
(Cited on p. 37)

[112] M. Huppert, I. Jordan, and H. J. Wörner.
Attosecond beamline with actively stabilized and spatially separated beam paths.
Review of Scientific Instruments **86**, 123106 (2015).
(Cited on p. 37)

[113] BengtssonS., L. W., KroonD., CampS., MirandaM., A. L., L'HuillierA., S. J., G. B., RippeL., and MauritssonJ.
Space-time control of free induction decay in the extreme ultraviolet.
Nat Photon **11**, 252–258 (April 2017).
(Cited on p. 37)

[114] M. Sabbar, S. Heuser, R. Boge, M. Lucchini, L. Gallmann, C. Cirelli, and U. Keller.
Combining attosecond XUV pulses with coincidence spectroscopy.
Review of Scientific Instruments **85**, 103113 (2014).
(Cited on p. 37)

[115] S. J. Weber, B. Manschwetus, M. Billon, M. Böttcher, M. Bougeard, P. Breger, M. Géléoc, V. Gruson, A. Huetz, N. Lin, Y. J. Picard, T. Ruchon, P. Salières, and B. Carré.
Flexible attosecond beamline for high harmonic spectroscopy and XUV/near-IR pump probe experiments requiring long acquisition times.
Review of Scientific Instruments **86**, 033108 (2015).
(Cited on p. 37)

[116] M. Drescher, M. Hentschel, R. Kienberger, G. Tempea, C. Spielmann, G. A. Reider, P. B. Corkum, and F. Krausz.
X-ray Pulses Approaching the Attosecond Frontier.
Science **291**, 1923–1927 (2001).
(Cited on p. 37)

[117] F. Böttcher, B. Manschwetus, H. Rottke, N. Zhavoronkov, Z. Ansari, and W. Sandner.
Interferometric long-term stabilization of a delay line: a tool for pump–probe photoelectron–photoion-coincidence spectroscopy on the attosecond time scale.
Applied Physics B **91**, 287–293 (2008).
(Cited on p. 37)

[118] E. Goulielmakis, M. Schultze, M. Hofstetter, V. S. Yakovlev, J. Gagnon, M. Uiberacker, A. L. Aquila, E. M. Gullikson, D. T. Attwood, R. Kienberger, F. Krausz, and U. Kleineberg.
Single-Cycle Nonlinear Optics.
Science **320**, 1614–1617 (2008).
(Cited on p. 37)

[119] M. Schultze, A. Wirth, I. Grguras, M. Uiberacker, T. Uphues, A. Verhoef, J. Gagnon, M. Hofstetter, U. Kleineberg, E. Goulielmakis, and F. Krausz.
State-of-the-art attosecond metrology.
Journal of Electron Spectroscopy and Related Phenomena **184**, 68 – 77 (2011).
(Cited on p. 37)

[120] F. Sorgenfrei, W. F. Schlotter, T. Beeck, M. Nagasono, S. Gieschen, H. Meyer, A. Föhlisch, M. Beye, and W. Wurth.
The extreme ultraviolet split and femtosecond delay unit at the plane grating monochromator beamline PG2 at FLASH.

Review of Scientific Instruments **81**, 043107 (2010).
(Cited on p. 38)

[121] Y. Nabekawa, H. Hasegawa, E. J. Takahashi, and K. Midorikawa.
Production of Doubly Charged Helium Ions by Two-Photon Absorption of an Intense Sub-10-fs Soft X-Ray Pulse at 42 eV Photon Energy.
Phys. Rev. Lett. **94**, 043001 (Jan 2005).
(Cited on p. 38)

[122] F. Campi, H. Coudert-Alteirac, M. Miranda, L. Rading, B. Manschwetus, P. Rudawski, A. L'Huillier, and P. Johnsson.
Design and test of a broadband split-and-delay unit for attosecond XUV-XUV pump-probe experiments.
Review of Scientific Instruments **87**, 023106 (2016).
(Cited on p. 38)

[123] P. Tzallas, D. Charalambidis, N. A. Papadogiannis, K. Witte, and G. D. Tsakiris.
Direct observation of attosecond light bunching.
Nature **426**, 267–271 (November 2003).
(Cited on p. 38)

[124] R. Moshammer, T. Pfeifer, A. Rudenko, Y. H. Jiang, L. Foucar, M. Kurka, K. U. Kühnel, C. D. Schröter, J. Ullrich, O. Herrwerth, M. F. Kling, X.-J. Liu, K. Motomura, H. Fukuzawa, A. Yamada, K. Ueda, K. L. Ishikawa, K. Nagaya, H. Iwayama, A. Sugishima, Y. Mizoguchi, S. Yase, M. Yao, N. Saito, A. Belkacem, M. Nagasono, A. Higashiya, M. Yabashi, T. Ishikawa, H. Ohashi, H. Kimura, and T. Togashi.
Second-order autocorrelation of XUV FEL pulses via time resolved two-photon single ionization of He.
Opt. Express **19**, 21698–21706 (Oct 2011).
(Cited on p. 38, 44, 100)

[125] P. Tzallas, E. Skantzakis, L. A. A. Nikolopoulos, G. D. Tsakiris, and D. Charalambidis.
Extreme-ultraviolet pump-probe studies of one-femtosecond-scale electron dynamics.
Nat Phys **7**, 781–784 (2011).
(Cited on p. 38)

[126] N. Berrah, L. Fang, B. F. Murphy, E. Kukk, T. Y. Osipov, R. Coffee, K. R. Ferguson, H. Xiong, J.-C. Castagna, V. S. Petrovic, S. C. Montero, and J. D. Bozek.
Two mirror X-ray pulse split and delay instrument for femtosecond time resolved investigations at the LCLS free electron laser facility.
Opt. Express **24**, 11768–11781 (May 2016).
(Cited on p. 38)

[127] S. Usenko, A. Przystawik, M. A. Jakob, L. L. Lazzarino, G. Brenner, S. Toleikis, C. Haunhorst, D. Kip, and T. Laarmann.
Attosecond interferometry with self-amplified spontaneous emission of a free-electron laser.
Nature Communications **8**, 15626– (May 2017).
(Cited on p. 38, 88)

[128] S. Roling and H. Zacharias.
Split-and-Delay Units for Soft and Hard X-Rays, pp. 891–925.
Springer International Publishing, Cham (2016).
(Cited on p. 38, 46, 49)

[129] O. Hemmers, S. B. Whitfield, P. Glans, H. Wang, D. W. Lindle, R. Wehlitz, and I. A. Sellin.
High-resolution electron time-of-flight apparatus for the soft x-ray region.
Review of Scientific Instruments **69**, 3809–3817 (1998).
(Cited on p. 38)

[130] A. T. J. B. Eppink and D. H. Parker.
Velocity map imaging of ions and electrons using electrostatic lenses: Application in photoelectron and photofragment ion imaging of molecular oxygen.

Review of Scientific Instruments **68**, 3477–3484 (1997).
(Cited on p. 38)

[131] H. Wang, M. Chini, S. Chen, C.-H. Zhang, F. He, Y. Cheng, Y. Wu, U. Thumm, and Z. Chang.
Attosecond Time-Resolved Autoionization of Argon.
Phys. Rev. Lett. **105**, 143002 (2010).
(Cited on p. 38, 56, 118)

[132] M. Holler, F. Schapper, L. Gallmann, and U. Keller.
Attosecond Electron Wave-Packet Interference Observed by Transient Absorption.
Phys. Rev. Lett. **106**, 123601 (2011).
(Cited on p. 38, 56, 118)

[133] T. Ding.
Time-resolved spectroscopy of autoionizing states in few-electron systems.
Master's thesis, Ruprecht-Karls-Universität, Heidelberg (2013).
(Cited on p. 40, 41, 68)

[134] http://henke.lbl.gov/optical_constants/.
(Cited on p. 42, 48, 101)

[135] *Stefan Kaesdorf, ETF15 Combined Electron TOF / Positive Ion Mass Spectrometer*.
`http://www.kaesdorf.de/ElectronTOF.html` (retrieved September 20, 2017).
(Cited on p. 44)

[136] *Hitachi 001-0640*.
`http://www.hitachi-hightech.com/products/images/9797/ana-grating_05.pdf` (retrieved September 16, 2017).
(Cited on p. 45)

[137] *Princeton Instruments PIXIS XO 400B*.
`http://www.princetoninstruments.com/userfiles/files/assetLibrary/Datasheets/Princeton_Instruments_PIXIS_XO_400B_rev_N2_9_6_2012.pdf` (retrieved September 16, 2017).
(Cited on p. 45)

[138] *2D-Schlitzblende SMS-20-20-S-HV*.
`http://www.smaract.com/products/positioning-systems/` (retrieved September 16, 2017).
(Cited on p. 45)

[139] L. Aufleger.
Measurement of electron dynamics in atoms and molecules with intense XUV FEL radiation.
Master's thesis, Ruprecht-Karls-Universität, Heidelberg (2016).
(Cited on p. 45, 49, 117)

[140] R. Mitzner, B. Siemer, M. Neeb, T. Noll, F. Siewert, S. Roling, M. Rutkowski, A. A. Sorokin, M. Richter, P. Juranic, K. Tiedtke, J. Feldhaus, W. Eberhardt, and H. Zacharias.
Spatio - temporal coherence of free electron laser pulses in the soft x-ray regime.
Opt. Express **16**, 19909–19919 (2008).
(Cited on p. 46)

[141] S. Roling.
private communications.
Part of the Team of Prof. H. Zachrias, University of Münster, Germany.
(Cited on p. 47)

[142] Y. Zhang, K. Meyer, C. Ott, and T. Pfeifer.
Passively phase-stable, monolithic, all-reflective two-dimensional electronic spectroscopy based on a four-quadrant mirror.
Opt. Lett. **38**, 356–358 (2013).
(Cited on p. 48)

[143] *Physik Instrumente, S-325 Piezo Z / Tip / Tilt Platform.*
`https://www.physikinstrumente.de/de/produkte/kippplattformen/piezo-platforms/s-325-piezo-hub-und-kipp-plattform-300650/` (retrieved September 18, 2017).
(Cited on p. 49)

[144] *Physik Instrumente, Hera 622.*
`https://www.physikinstrumente.com/en/products/linear-stages-and-actuators/piezo-stages/p-6201-p-6291-pihera-piezo-linear-stage-202300/` (retrieved September 18, 2017).
(Cited on p. 49)

[145] *Physik Instrumente, H-811.D2 6-Axis Miniature Hexapod.*
`https://www.physikinstrumente.de/de/produkte/hexapoden-parallelkinematiken/hexapoden-mit-motor-spindel-antrieb/h-811d2-6-achsen-miniatur-hexapod-700884/` (retrieved September 19, 2017).
(Cited on p. 49)

[146] F. Bakar.
Design eines Breitband-XUV Gitterspektrometers und numerische Simulationen zur multidimensionalen XUV-Spektroskopie.
Bachelor thesis, Ruprecht-Karls-Universität, Heidelberg (2014).
(Cited on p. 50)

[147] J. Javanainen, J. H. Eberly, and Q. Su.
Numerical simulations of multiphoton ionization and above-threshold electron spectra.
Phys. Rev. A **38**, 3430–3446 (1988).
(Cited on p. 55, 59)

[148] Q. Su and J. H. Eberly.
Model atom for multiphoton physics.
Phys. Rev. A **44**, 5997–6008 (1991).
(Cited on p. 55, 59)

[149] A. H. Zewail.
Laser Femtochemistry.
Science **242**, 1645–1653 (1988).
(Cited on p. 55)

[150] L. R. Khundkar and A. H. Zewail.
Ultrafast Molecular Reaction Dynamics in Real-Time: Progress Over a Decade.
Annual Review of Physical Chemistry **41**, 15–60 (1990).
(Cited on p. 55)

[151] A. H. Zewail.
Femtosecond transition-state dynamics.
Faraday Discuss. Chem. Soc. **91**, 207–237 (1991).
(Cited on p. 55)

[152] A. S. Alnaser, B. Ulrich, X. M. Tong, I. V. Litvinyuk, C. M. Maharjan, P. Ranitovic, T. Osipov, R. Ali, S. Ghimire, Z. Chang, C. D. Lin, and C. L. Cocke.
Simultaneous real-time tracking of wave packets evolving on two different potential curves in $H_2{}^+$ *and* $D_2{}^+$.
Phys. Rev. A **72**, 030702 (Sep 2005).
(Cited on p. 56)

[153] F. Légaré, K. F. Lee, I. V. Litvinyuk, P. W. Dooley, A. D. Bandrauk, D. M. Villeneuve, and P. B. Corkum.
Imaging the time-dependent structure of a molecule as it undergoes dynamics.

Phys. Rev. A **72**, 052717 (Nov 2005).
(Cited on p. 56)

[154] T. Ergler, A. Rudenko, B. Feuerstein, K. Zrost, C. D. Schröter, R. Moshammer, and J. Ullrich.
Spatiotemporal Imaging of Ultrafast Molecular Motion: Collapse and Revival of the D_2^+ *Nuclear Wave Packet*.
Phys. Rev. Lett. **97**, 193001 (Nov 2006).
(Cited on p. 56)

[155] T. Ergler, B. Feuerstein, A. Rudenko, K. Zrost, C. D. Schröter, R. Moshammer, and J. Ullrich.
Quantum-Phase Resolved Mapping of Ground-State Vibrational D_2 *Wave Packets via Selective Depletion in Intense Laser Pulses*.
Phys. Rev. Lett. **97**, 103004 (Sep 2006).
(Cited on p. 56)

[156] A. Rudenko, Y. H. Jiang, M. Kurka, K. U. KÃijhnel, L. Foucar, O. Herrwerth, M. Lezius, M. F. Kling, C. D. SchrÃűter, R. Moshammer, and J. Ullrich.
Exploring few-photon, few-electron reactions at FLASH: from ion yield and momentum measurements to time-resolved and kinematically complete experiments.
Journal of Physics B: Atomic, Molecular and Optical Physics **43**, 194004 (2010).
(Cited on p. 56)

[157] Y. H. Jiang, A. Rudenko, J. F. Pérez-Torres, O. Herrwerth, L. Foucar, M. Kurka, K. U. Kühnel, M. Toppin, E. Plésiat, F. Morales, F. Martín, M. Lezius, M. F. Kling, T. Jahnke, R. Dörner, J. L. Sanz-Vicario, J. van Tilborg, A. Belkacem, M. Schulz, K. Ueda, T. J. M. Zouros, S. Düsterer, R. Treusch, C. D. Schröter, R. Moshammer, and J. Ullrich.
Investigating two-photon double ionization of D_2 *by XUV-pump–XUV-probe experiments*.
Phys. Rev. A **81**, 051402 (May 2010).
(Cited on p. 56)

[158] M. Magrakvelidze, O. Herrwerth, Y. H. Jiang, A. Rudenko, M. Kurka, L. Foucar, K. U. Kühnel, M. Kübel, N. G. Johnson, C. D. Schröter, S. Düsterer, R. Treusch, M. Lezius, I. Ben-Itzhak, R. Moshammer, J. Ullrich, M. F. Kling, and U. Thumm.
Tracing nuclear-wave-packet dynamics in singly and doubly charged states of N_2 *and* O_2 *with XUV-pump–XUV-probe experiments*.
Phys. Rev. A **86**, 013415 (Jul 2012).
(Cited on p. 56, 85)

[159] Y. H. Jiang, A. Rudenko, O. Herrwerth, L. Foucar, M. Kurka, K. U. Kühnel, M. Lezius, M. F. Kling, J. van Tilborg, A. Belkacem, K. Ueda, S. Düsterer, R. Treusch, C. D. Schröter, R. Moshammer, and J. Ullrich.
Ultrafast Extreme Ultraviolet Induced Isomerization of Acetylene Cations.
Phys. Rev. Lett. **105**, 263002 (Dec 2010).
(Cited on p. 56)

[160] J. Mauritsson, T. Remetter, M. Swoboda, K. Klünder, A. L'Huillier, K. J. Schafer, O. Ghafur, F. Kelkensberg, W. Siu, P. Johnsson, M. J. J. Vrakking, I. Znakovskaya, T. Uphues, S. Zherebtsov, M. F. Kling, F. Lépine, E. Benedetti, F. Ferrari, G. Sansone, and M. Nisoli.
Attosecond Electron Spectroscopy Using a Novel Interferometric Pump-Probe Technique.
Phys. Rev. Lett. **105**, 053001 (2010).
(Cited on p. 56)

[161] E. Goulielmakis, Z. H. Loh, A. Wirth, R. Santra, N. Rohringer, V. S. Yakovlev, S. Zherebtsov, T. Pfeifer, A. M. Azzeer, M. F. Kling, S. R. Leone, and F. Krausz.
Real-time observation of valence electron motion.
Nature **466**, 739–7U7 (2010).
(Cited on p. 56, 118)

[162] M. Wu, S. Chen, S. Camp, K. J. Schafer, and M. B. Gaarde.
Theory of strong-field attosecond transient absorption.
Journal of Physics B: Atomic, Molecular and Optical Physics **49**, 062003 (2016).

(Cited on p. 56, 63)

[163] S. R. Leone and D. M. Neumark.
Attosecond science in atomic, molecular, and condensed matter physics.
Faraday Discuss. **194**, 15–39 (2016).
(Cited on p. 56)

[164] E. R. Warrick, W. Cao, D. M. Neumark, and S. R. Leone.
Probing the Dynamics of Rydberg and Valence States of Molecular Nitrogen with Attosecond Transient Absorption Spectroscopy.
The Journal of Physical Chemistry A **120**, 3165–3174 (2016).
PMID: 26862883.
(Cited on p. 56)

[165] Y. Cheng, M. Chini, X. Wang, A. González-Castrillo, A. Palacios, L. Argenti, F. Martín, and Z. Chang.
Reconstruction of an excited-state molecular wave packet with attosecond transient absorption spectroscopy.
Phys. Rev. A **94**, 023403 (Aug 2016).
(Cited on p. 56)

[166] M. F. Jager, C. Ott, P. M. Kraus, C. J. Kaplan, W. Pouse, R. E. Marvel, R. F. Haglund, D. M. Neumark, and S. R. Leone.
Tracking the insulator-to-metal phase transition in VO2 with few-femtosecond extreme UV transient absorption spectroscopy.
Proceedings of the National Academy of Sciences **114**, 9558–9563 (2017).
(Cited on p. 56)

[167] M. Sabbar, H. Timmers, Y.-J. Chen, A. K. Pymer, Z.-H. Loh, S. G. Sayres, S. Pabst, R. Santra, and S. R. Leone.
State-resolved attosecond reversible and irreversible dynamics in strong optical fields.
Nat Phys **13**, 472–478 (May 2017).
(Cited on p. 56, 118)

[168] M. Chini, X. Wang, Y. Cheng, Y. Wu, D. Zhao, D. A. Telnov, S.-I. Chu, and Z. Chang.
Sub-cycle Oscillations in Virtual States Brought to Light.
Sci. Rep. **3**, 1105 (2013).
(Cited on p. 56, 76)

[169] C. Ott, A. Kaldun, P. Raith, K. Meyer, M. Laux, Y. Zhang, S. Hagstotz, T. Ding, R. Heck, and T. Pfeifer.
Quantum Interferometry and Correlated Two-Electron Wave-Packet Observation in Helium.
ArXiv e-prints (2012).
(Cited on p. 58, 72)

[170] Z. Q. Yang, D. F. Ye, T. Ding, T. Pfeifer, and L. B. Fu.
Attosecond XUV absorption spectroscopy of doubly excited states in helium atoms dressed by a time-delayed femtosecond infrared laser.
Phys. Rev. A **91**, 013414 (Jan 2015).
(Cited on p. 59)

[171] T. Ding.
Modellatom mit zwei Elektronen in jeweils einer Raumdimension in Wechselwirkung mit XUV- und IR-Laserfeldern.
Bachelor thesis, Universität Heidelberg (2011).
(Cited on p. 59)

[172] G. D. Borisova.
Einfluss der Elektron-Elektron-Korrelation auf die Ionisation von Atomen in starken, ultrakurzen Laser-Impulsen.
Bachelor thesis, Ruprecht-Karls-Universität, Heidelberg (2015).
(Cited on p. 60)

[173] A. Blättermann, C. Ott, A. Kaldun, T. Ding, and T. Pfeifer.
Two-dimensional spectral interpretation of time-dependent absorption near laser-coupled resonances.
Journal of Physics B: Atomic, Molecular and Optical Physics **47**, 124008 (2014).
(Cited on p. 61, 83)

[174] N. Bloembergen, E. M. Purcell, and R. V. Pound.
Relaxation Effects in Nuclear Magnetic Resonance Absorption.
Phys. Rev. **73**, 679–712 (Apr 1948).
(Cited on p. 61)

[175] E. L. Hahn.
Nuclear Induction Due to Free Larmor Precession.
Phys. Rev. **77**, 297–298 (Jan 1950).
(Cited on p. 61)

[176] E. L. Hahn.
Free nuclear induction.
Physics Today **6**, 4–9 (1953).
(Cited on p. 61)

[177] R. G. Brewer and R. L. Shoemaker.
Optical Free Induction Decay.
Phys. Rev. A **6**, 2001–2007 (Dec 1972).
(Cited on p. 61)

[178] M. Joffre, C. B. a. la Guillaume, N. Peyghambarian, M. Lindberg, D. Hulin, A. Migus, S. W. Koch, and A. Antonetti.
Coherent effects in pump–probe spectroscopy of excitons.
Opt. Lett. **13**, 276–278 (Apr 1988).
(Cited on p. 61)

[179] C. H. B. Cruz, J. P. Gordon, P. C. Becker, R. L. Fork, and C. V. Shank.
Dynamics of spectral hole burning.
IEEE Journal of Quantum Electronics **24**, 261–269 (Feb 1988).
(Cited on p. 61)

[180] W. T. Pollard and R. A. Mathies.
Analysis of Femtosecond Dynamic Absorption Spectra of Nonstationary States.
Annual Review of Physical Chemistry **43**, 497–523 (1992).
PMID: 1463575.
(Cited on p. 61)

[181] S. Bengtsson, E. W. Larsen, D. kroon, C. Arnold, A. L'Huillier, L. Rippe, and J. Mauritsson.
Free Induction Decay in the Extreme Ultraviolet.
In *Frontiers in Optics 2015*, p. FTh3A.2. Optical Society of America (2015).
(Cited on p. 61)

[182] Z. Vardeny and J. Tauc.
Picosecond coherence coupling in the pump and probe technique.
Optics Communications **39**, 396 – 400 (1981).
(Cited on p. 62)

[183] E. P. Ippen and C. V. Shank.
Techniques for measurement, pp. 83–122.
Springer Berlin Heidelberg, Berlin, Heidelberg (1984).
URL `https://doi.org/10.1007/3-540-13493-X_17`.
(Cited on p. 62)

[184] M. Joffre, D. Hulin, J. P. Foing, J. P. Chambaret, A. Migus, and A. Antonetti.
Dynamics and Fourier transform studies of the excitonic optical Stark effect.
IEEE Journal of Quantum Electronics **25**, 2505–2515 (Dec 1989).

(Cited on p. 62)

[185] C.-T. Liao, A. Sandhu, S. Camp, K. J. Schafer, and M. B. Gaarde.
Beyond the Single-Atom Response in Absorption Line Shapes: Probing a Dense, Laser-Dressed Helium Gas with Attosecond Pulse Trains.
Phys. Rev. Lett. **114**, 143002 (Apr 2015).
(Cited on p. 63)

[186] C.-T. Liao and A. Sandhu.
XUV Transient Absorption Spectroscopy: Probing Laser-Perturbed Dipole Polarization in Single Atom, Macroscopic, and Molecular Regimes.
Photonics **4**, – (2017).
(Cited on p. 63)

[187] K. Codling, R. P. Madden, and D. L. Ederer.
Resonances in the Photo-Ionization Continuum of Ne I (20-150 eV).
Phys. Rev. **155**, 26–37 (1967).
(Cited on p. 67, 68, 70, 75)

[188] J. Cooper.
1 Photon interactions with atoms.
In Y. Itikawa (Ed.), *Interactions of Photons and Electrons with Atoms*, volume 17A of *Landolt-Börnstein - Group I Elementary Particles, Nuclei and Atoms*, pp. 1–82. Springer Berlin Heidelberg (2000).
(Cited on p. 68, 69)

[189] W. F. Chan, G. Cooper, X. Guo, and C. E. Brion.
Absolute optical oscillator strengths for the electronic excitation of atoms at high resolution. II. The photoabsorption of neon.
Phys. Rev. A **45**, 1420–1433 (Feb 1992).
(Cited on p. 70)

[190] G. Min, Z. Lin-Fan, L. Cun-Ding, and X. Ke-Zun.
Optically Forbidden Excitations of 2s Electron of Neon Studied by Fast Electron Impact.
Chinese Physics Letters **25**, 3646 (2008).
(Cited on p. 70, 75, 77, 78)

[191] G. Steinmeyer.
Dispersion oscillations in ultrafast phase-correction devices.
IEEE Journal of Quantum Electronics **39**, 1027–1034 (Aug 2003).
(Cited on p. 71)

[192] A. Blättermann, C. Ott, A. Kaldun, T. Ding, V. Stooß, M. Laux, M. Rebholz, and T. Pfeifer.
In situ characterization of few-cycle laser pulses in transient absorption spectroscopy.
Opt. Lett. **40**, 3464–3467 (Aug 2015).
(Cited on p. 72, 81)

[193] A. L'Huillier, L. A. Lompre, G. Mainfray, and C. Manus.
Multiply charged ions induced by multiphoton absorption processes in rare-gas atoms at 1.064Îijm.
Journal of Physics B: Atomic and Molecular Physics **16**, 1363 (1983).
(Cited on p. 72)

[194] C. Smeenk, J. Z. Salvail, L. Arissian, P. B. Corkum, C. T. Hebeisen, and A. Staudte.
Precise in-situ measurement of laser pulse intensity using strong field ionization.
Opt. Express **19**, 9336–9344 (May 2011).
(Cited on p. 72)

[195] J. A. Oteo.
The BakerŰCampbellŰHausdorff formula and nested commutator identities.
Journal of Mathematical Physics **32**, 419–424 (1991).
(Cited on p. 73)

[196] J. C. Slater.
Atomic Shielding Constants.
Phys. Rev. **36**, 57–64 (1930).
(Cited on p. 75)

[197] S. Chen, M. J. Bell, A. R. Beck, H. Mashiko, M. Wu, A. N. Pfeiffer, M. B. Gaarde, D. M. Neumark, S. R. Leone, and K. J. Schafer.
Light-induced states in attosecond transient absorption spectra of laser-dressed helium.
Phys. Rev. A **86**, 063408 (2012).
(Cited on p. 77)

[198] T. Ding, A. Blättermann, V. Stooss, C. Ott, K. Meyer, A. Kaldun, M. Rebholz, P. Birk, M. Hartmann, L. Aufleger, A. Brown, H. van der Hart, and T. Pfeifer.
Towards two-dimensional spectroscopy on inner-shell transitions with XUV and soft-X-ray pulses.
In *International Conference on Ultrafast Phenomena*, p. UF1A.2. Optical Society of America (2016).
(Cited on p. 78, 79)

[199] P. Hamm.
Principles of Nonlinear Optical Spectroscopy: A Practical Approach (2005).
URL `http://www.mitr.p.lodz.pl/evu/lectures/Hamm.pdf`.
(Cited on p. 80)

[200] E. J. Brown, Q. Zhang, and M. Dantus.
Femtosecond transient-grating techniques: Population and coherence dynamics involving ground and excited states.
The Journal of Chemical Physics **110**, 5772–5788 (1999).
(Cited on p. 81)

[201] Z. Wei, J. Li, L. Wang, S. T. See, M. H. Jhon, Y. Zhang, F. Shi, M. Yang, and Z.-H. Loh.
Elucidating the origins of multimode vibrational coherences of polyatomic molecules induced by intense laser fields.
Nature Communications **8**, 735– (2017).
(Cited on p. 81)

[202] M. Kurka, J. Feist, D. A. Horner, A. Rudenko, Y. H. Jiang, K. U. Kühnel, L. Foucar, T. N. Rescigno, C. W. McCurdy, R. Pazourek, S. Nagele, M. Schulz, O. Herrwerth, M. Lezius, M. F. Kling, M. Schöffler, A. Belkacem, S. Düsterer, R. Treusch, B. I. Schneider, L. A. Collins, J. Burgdörfer, C. D. Schröter, R. Moshammer, and J. Ullrich.
Differential cross sections for non-sequential double ionization of He by 52 eV photons from the Free Electron Laser in Hamburg, FLASH.
New J. Phys. **12**, 073035 (2010).
(Cited on p. 85)

[203] A. Kramida, Yu. Ralchenko, J. Reader, and and NIST ASD Team.
NIST Atomic Spectra Database (ver. 5.3), [Online]. Available: `http://physics.nist.gov/asd` [2016, December 22]. National Institute of Standards and Technology, Gaithersburg, MD. (2015).
(Cited on p. 86, 102, 104, 105, 114, 129)

[204] A. E. Livingston, R. Buttner, A. S. Zacarias, B. Kraus, K.-H. Schartner, F. Folkmann, and P. H. Mokler.
Extreme-ultraviolet spectrum of Ne iii.
J. Opt. Soc. Am. B **14**, 522–525 (Mar 1997).
(Cited on p. 87, 102, 104, 105)

[205] G. M. Nikolopoulos and P. Lambropoulos.
Frequency response of an atomic resonance driven by weak free-electron-laser fluctuating pulses.
Journal of Physics B: Atomic, Molecular and Optical Physics **46**, 164010 (2013).
(Cited on p. 88)

[206] Y. H. Jiang, T. Pfeifer, A. Rudenko, O. Herrwerth, L. Foucar, M. Kurka, K. U. Kühnel, M. Lezius, M. F. Kling, X. Liu, K. Ueda, S. Düsterer, R. Treusch, C. D. Schröter, R. Moshammer, and J. Ullrich.
Temporal coherence effects in multiple ionization of N_2 *via XUV pump-probe autocorrelation*.
Phys. Rev. A **82**, 041403(R) (2010).
(Cited on p. 88)

[207] K. Meyer, C. Ott, P. Raith, A. Kaldun, Y. Jiang, A. Senftleben, M. Kurka, R. Moshammer, J. Ullrich, and T. Pfeifer.
Noisy Optical Pulses Enhance the Temporal Resolution of Pump-Probe Spectroscopy.
Phys. Rev. Lett. **108**, 098302 (2012).
(Cited on p. 88)

[208] E. Saldin, E. Schneidmiller, and M. Yurkov.
Statistical properties of radiation from VUV and X-ray free electron laser.
Optics Communications **148**, 383 – 403 (1998).
(Cited on p. 88)

[209] E. L. Saldin, E. A. Schneidmiller, and M. V. Yurkov.
Statistical and coherence properties of radiation from x-ray free-electron lasers.
New Journal of Physics **12**, 035010 (2010).
(Cited on p. 88)

[210] A. Singer, I. A. Vartanyants, M. Kuhlmann, S. Duesterer, R. Treusch, and J. Feldhaus.
Transverse-Coherence Properties of the Free-Electron-Laser FLASH at DESY.
Phys. Rev. Lett. **101**, 254801 (Dec 2008).
(Cited on p. 89)

[211] O. H. Altenmueller, R. R. Larsen, and G. A. Loew.
Investigations of Traveling-Wave Separators for the Stanford Two-Mile Linear Accelerator.
Review of Scientific Instruments **35**, 438–442 (1964).
(Cited on p. 90, 98)

[212] C. Weninger and N. Rohringer.
Transient-gain photoionization x-ray laser.
Phys. Rev. A **90**, 063828 (Dec 2014).
(Cited on p. 95)

[213] M. G. Makris and P. Lambropoulos.
Theoretical interpretation of multiphoton ionization of neon by soft-x-ray intense radiation.
Phys. Rev. A **77**, 023401 (Feb 2008).
(Cited on p. 97)

[214] S. M. Cavaletto.
Private communications . Calculated using Los Alamos National Laboratory Atomic Physics Codes, http://aphysics2.lanl.gov/tempweb., based on R. D. Cowan, Theory of Atomic Spectra (University of California Press, Berkeley, 1981).
Group of Dr. Zoltán Harman, Max-Planck-Institute for Nuclear Physics, Heidelberg, Germany.
(Cited on p. 97, 110, 119, 129)

[215] S. Düsterer.
private communications.
FLASH Photon Diagnostics and Controls, DESY Hamburg, Germany.
(Cited on p. 98)

[216] R. Riedel, A. Al-Shemmary, M. Gensch, T. Golz, M. Harmand, N. Medvedev, M. J. Prandolini, K. Sokolowski-Tinten, S. Toleikis, U. Wegner, B. Ziaja, N. Stojanovic, and F. Tavella.
Single-shot pulse duration monitor for extreme ultraviolet and X-ray free-electron lasers.
Nature Communications **4**, 1731– (April 2013).
(Cited on p. 100)

[217] S. Düsterer, M. Rehders, A. Al-Shemmary, C. Behrens, G. Brenner, O. Brovko, M. DellAngela, M. Drescher, B. Faatz, J. Feldhaus, U. Frühling, N. Gerasimova, N. Gerken, C. Gerth, T. Golz, A. Grebentsov, E. Hass, K. Honkavaara, V. Kocharian, M. Kurka, T. Limberg, R. Mitzner, R. Moshammer, E. Plönjes, M. Richter, J. Rönsch-Schulenburg, A. Rudenko, H. Schlarb, B. Schmidt, A. Senftleben, E. A. Schneidmiller, B. Siemer, F. Sorgenfrei, A. A. Sorokin, N. Stojanovic, K. Tiedtke, R. Treusch, M. Vogt, M. Wieland, W. Wurth, S. Wesch, M. Yan, M. V. Yurkov, H. Zacharias, and S. Schreiber.
Development of experimental techniques for the characterization of ultrashort photon pulses of extreme ultraviolet free-electron lasers.
Phys. Rev. ST Accel. Beams **17**, 120702 (Dec 2014).
(Cited on p. 101)

[218] A. Senftleben, T. Pfeifer, K. Schnorr, K. Meyer, Y. H. Jiang, A. Rudenko, O. Herrwerth, L. Foucar, M. Kurka, K. U. Kühnel, M. Kübel, M. F. Kling, A. Yamada, K. Motomura, K. Ueda, R. Treusch, C. D. Schröter, R. Moshammer, and J. Ullrich.
Characterization of Extreme Ultra-Violet Free-Electron Laser Pulses by Autocorrelation, pp. 61–68.
Springer Berlin Heidelberg, Berlin, Heidelberg (2012).
URL `https://doi.org/10.1007/978-3-642-28948-4_11`.
(Cited on p. 101)

[219] A. Magunia.
Elektronen-Korrelation in Helium unter Einfluss intensiver XUV-Laserpulse.
Bachelor thesis, Ruprecht-Karls-Universität, Heidelberg (2016).
(Cited on p. 105, 115, 117)

[220] Z. Liu, S. M. Cavaletto, C. Ott, K. Meyer, Y. Mi, Z. Harman, C. H. Keitel, and T. Pfeifer.
Phase Reconstruction of Strong-Field Excited Systems by Transient-Absorption Spectroscopy.
Phys. Rev. Lett. **115**, 033003 (Jul 2015).
(Cited on p. 111)

[221] N. Rohringer and R. Santra.
Multichannel coherence in strong-field ionization.
Phys. Rev. A **79**, 053402 (May 2009).
(Cited on p. 111)

[222] A. N. Artemyev, L. S. Cederbaum, and P. V. Demekhin.
Impact of intense laser pulses on the autoionization dynamics of the $2s2p$ *doubly excited state of He.*
Phys. Rev. A **96**, 033410 (Sep 2017).
(Cited on p. 115)

[223] Z. H. Loh, C. H. Greene, and S. R. Leone.
Femtosecond induced transparency and absorption in the extreme ultraviolet by coherent coupling of the He 2s2p (P-1(o)) and 2p(2) (S-1(e)) double excitation states with 800 nm light.
Chem. Phys. **350**, 7–13 (2008).
(Cited on p. 118)

[224] P. Lambropoulos and P. Zoller.
Autoionizing states in strong laser fields.
Phys. Rev. A **24**, 379–397 (Jul 1981).
(Cited on p. 119)

[225] A. R. Attar, L. Piticco, and S. R. Leone.
Core-to-valence spectroscopic detection of the CH2Br radical and element-specific femtosecond photodissociation dynamics of CH2IBr.
The Journal of Chemical Physics **141**, 164308 (2014).
(Cited on p. 120)

[226] E. Ferrari et al.

Widely tunable two-colour seeded free-electron laser source for resonant-pump resonant-probe magnetic scattering.
Nature Communications **7**, 10343– (January 2016).
(Cited on p. 120)

Danksagung

Es ist ja vollkommen klar, dass solche aufwändigen Experimente nicht von einer Person alleine realisiert werden können. Ganz wichtige Zutaten dafür sind Teamwork und insbesondere eine super Stimmung in der Arbeitsgruppe im heimischen Labor und/oder in der FLASH-Halle, aber auch im Büro und bei privaten Aktivitäten. Danke Euch allen dafür, liebe "*InterATTOs*" und "*X-Musicians*"!

Ganz speziell möchte ich mich bei *Thomas Pfeifer* bedanken, für die Gelegenheit, Teil des X-MuSIC Projektes von Anfang an sein zu können, aber auch für die zahlreichen Diskussionen, für die Zeit, die Du Dir genommen hast bei Fragen und Problemen und für die Übernahme des Erstgutachtens dieser Arbeit. Danke für die tolle Betreuung!

Bei Professor *Andreas Wolf* möchte ich mich für die Übernahme des Zweitgutachtens dieser Arbeit bedanken.

Außerdem möchte ich mich ganz besonders bei *Christian Ott* bedanken. Danke für die vielen hilfreichen Email- und Skype-Konversationen in der Anfangsphase des Projektes als Du noch in Berkeley warst, aber gerade auch für die außergewöhnliche Unterstützung im Labor, die vielen Ideen und Ratschläge, und die zahlreichen lehrreichen Gespräche in den letzten 1,5 Jahren seit dem Du Gruppenleiter bist.

Ganz besonders möchte ich mich auch bei *Marc Rebholz*, dem zweit-dienstältesten X-Musician, bedanken für die unermüdliche Unterstützung im Labor von Anfang an. Genauso möchte ich aber auch *Lennart Aufleger*, dem dritt-dienstältesten X-Musician, danken, der das Kernteam der Strahlzeit 2016 vervollständigte. Ich fand besonders auch die Arbeitsatmosphäre mit Euch beiden super! Danke auch den "X-MuSIC Nachzüglern" *Carina Da Costa Castanheira* und *Patrick Rupprecht*. Es macht viel Spaß mit Euch zusammenzuarbeiten.

Weiterhin möchte ich natürlich auch allen anderen Kollegen für die schöne Zeit persönlich Danke sagen. Fangen wir mal mit unserem Großraumbüro an: *Alexander Blättermann*, *Paul Birk*, *Veit Stooß*, *Martin Laux*, *Gergana Borisova*, *Arso Ivanovic*. Weiter geht es mit *Maximilian Hartmann*, *Yonghao Mi*, *Anne Harth* und *Stephan Goerttler*.

Ich möchte meinen beiden Bachelorstudenten, die ich betreuen durfte, *Faiq Bakar* und *Alexander Magunia*, ganz besonders danken. Das war eine riesen Hilfe und es hat sehr viel Spaß gemacht, mit Euch zusammenzuarbeiten!

Ebenso möchte ich allen ehemaligen Gruppenmitgliedern, die zur tollen Arbeitsatmosphäre in unserer Gruppe beigetragen haben, Danke sagen. Insbesondere: *Kristina Meyer*, *Zuoye Liu*, *Yizhu Zhang*, *Andreas Kaldun*, *David Wachs* und *Sandra Marrek*.

Außerdem möchte ich mich bei *Bernd Knape*, *Claus-Dieter Schröter* und *Christian Kaiser* für die technische Unterstützung im Labor und insbesondere am FLASH bedanken.

Auch *Stefano Cavaletto* gebührt ein riesen Dank für die zahlreichen Diskussionen und die Unterstützung bei der Analyse der FEL-Daten. Danke!

Ein großer Dank geht auch an die *Zentrale Feinwerkmechanik* unter der Leitung von Herrn Spranz, die die zahlreichen benötigten Komponenten für die experimentellen Aufbauten (bei oft akuter Dringlichkeit) anfertigten.

Auch unseren Kollaborationspartnern aus Belfast, *Hugo Van Der Hart* und *Andrew Brown*, möchte ich an dieser Stelle nochmals danken für die schöne Zusammenarbeit.

Ganz besonders möchte ich mich bei meiner *Familie*, *Christina* und *Emma* bedanken für die Geduld – es war ja doch alles etwas zeitintensiv.